Two-phase spectral wave explicit Navier-Stokes equations method for wave-structure interactions

Zhaobin Li

▶ **To cite this version:**

Zhaobin Li. Two-phase spectral wave explicit Navier-Stokes equations method for wave-structure interactions. Engineering Sciences [physics]. École centrale de Nantes, 2018. English. NNT : . tel-02109058

HAL Id: tel-02109058
https://hal.science/tel-02109058

Submitted on 24 Apr 2019

HAL is a multi-disciplinary open access archive for the deposit and dissemination of scientific research documents, whether they are published or not. The documents may come from teaching and research institutions in France or abroad, or from public or private research centers.

L'archive ouverte pluridisciplinaire **HAL**, est destinée au dépôt et à la diffusion de documents scientifiques de niveau recherche, publiés ou non, émanant des établissements d'enseignement et de recherche français ou étrangers, des laboratoires publics ou privés.

UNIVERSITE BRETAGNE SCIENCES LOIRE POUR L'INGENIEUR

CENTRALE NANTES

THESE DE DOCTORAT DE

L'ÉCOLE CENTRALE DE NANTES
COMUE UNIVERSITE BRETAGNE LOIRE

ECOLE DOCTORALE N° 602
Sciences pour l'Ingénieur
Spécialité : Mécanique des Milieux Fluides

Par
Zhaobin LI

TWO-PHASE SPECTRAL WAVE EXPLICIT NAVIER-STOKES EQUATIONS METHOD FOR WAVE-STRUCTURE INTERACTIONS

Thèse présentée et soutenue à Nantes, le 27 Novembre 2018
Unité de recherche : Laboratoire d'Hydrodynamique, Energétique et Environnement Atmosphérique (LHEEA), CNRS UMR 6598

Rapporteurs avant soutenance :

M. Harry B. BINGHAM	Professeur, Université Technique du Danemark, Danemark
M. Hrvoje JASAK	Professeur, Université de Zagreb, Croatie

Composition du Jury :

Président :	M. Pierre LUBIN	Professeur, Université de Bordeaux
Examinateurs :	Mme. Jun ZANG	Maître de Conférences HDR, Université de Bath, Royaume-Uni
	M. Charles MONROY	Ingénieur de Recherche, Bureau Veritas
Dir. de thèse :	M. Pierre FERRANT	Professeur, Ecole Centrale de Nantes
Co-encadrant :	M. Guillaume DUCROZET	Maître de Conférences, École Centrale de Nantes
	M. Lionel GENTAZ	Maître de Conférences, École Centrale de Nantes

Acknowledgement

At this moment - after finishing this thesis through a long journey which lasts for more than three years and is full of trials and errors, tears and laughter - I realize how many people have helped and supported me to make this work possible, and I really owe them a large amount of thanks.

Firstly, I would like to express my sincere gratitude to my examining committee. My thanks go to Prof. Pierre LUBIN from University of Bordeaux, France, the president of my jury. My thanks also go to Prof. Harry BINGHAM from Technical University of Denmark and Prof. Hrvoje JASAK from University of Zagreb, Croatia for examining attentively my thesis as "rapporteurs" and providing me with numerous precious comments, which help me a lot to clarify my ideas and better present the work in this thesis. I would like also to express my gratitude to Dr. Jun ZANG from University of Bath, United Kingdom and Dr. Charles MONROY from Bureau Veritas, France for being my jury members and coming to my defense from far. I really appreciate the discussion with them, which are very helpful to improve the quality of the present work.

Next, I would like to express my gratitude to people who have accompanied me during my three-year journey as a "doctorant". (I love this French word meaning "PhD candidate", because it makes me feel that "doctor" is a verb and a PhD candidate is a person who is "doctoring".)

Firstly, my sincere gratitude and respect go to my advisors.

I would like to thank Prof. Pierre FERRANT, my thesis director. It is Pierre who proposes this interesting subject to me and gives me a constant confidence during the three years. As the director, he is always able to provides useful guide for my research and is very supportive and encouraging. He also accompanied me to Dalian for my first international conference, the 32nd IWWWFB.

My gratitude also goes to Dr. Guillaume DUCROZET, Dr. Lionel GENTAZ, my co-supervisors. They are the first persons that I turn to whenever I got stuck on problems. They are always ready for help and are indeed very helpful. The discussion with them always shed new lights on my research. The help from Guillaume with the HOS wave models is particularly appreciated. His expertise with the method and the codes help me solve numerous problems regarding the generation of waves in the present work. They are also the first audiences of my presentations and the first readers of my manuscripts. I really appreciated the time they spend and their patience with me when they have to read my drafts containing numerous spell, grammar and style errors. I even received a hand-corrected paper from Lionel, sending to me by the post office, during the famous "french summer vacation" . Thanks to their comments, the quality of the papers is significantly improved.

Besides, I would also express my thanks to researchers at LHEEA lab who are not officially in my advisory committee but contributes their intelligence to the present work. The

first person to name is Dr. Benjamin BOUSCASSE. Benjamin is the project coordinator of the Chaire Hydrodynamique et Structure Marines CENTRALE NANTES - BUREAU VERITAS, a research project in which my work takes part, and the leader of our research team. Benjamin arrived in the second year of my PhD, and helps me with my research since then. Many of his suggestions have been adopted and integrated in this thesis. We went together to different meetings and conferences, including several meetings with BV in Paris, once OMAE in Madrid, and once IWWWFB in Lorient (he drove his small Ford kA with Youngmyung and me). Secondly, my thanks go to Prof. David LE TOUZE, the head of our research group (H2i). Although I do not work directly with David, he still spends much time in reading and correcting my papers. He participates several times in my progress meeting and his comments are always insightful. He once impressed me by saying "Only having nice results cannot make you a PhD. Having nice results is better than having bad results, but in the end, it is the philosophy that makes you a PhD." Thirdly, I would like to express my gratitude to Dr. Ganbo DENG for his interest in my work and his help with the CALM buoy test case. Thanks to his suggestion, we are able to work together and submit an abstract to the OpenFOAM workshop at Shanghai and finally submitted a journal paper.

I would like also to express my thanks to my colleagues. First, the OpenFOAM team: Youngmyung CHOI and Youngjun KIM, both working with OpenFOAM and in the CN-BV project. They are the persons I turn to for specific OpenFOAM questions, and the discussion with them is really helpful. Secondly, the SWENSE community: Gabriel RELIQUET, Yang ZHANG, and Théo DESCAMPS. And all my office colleagues of D001: Razvan ALAMIAN, Pierre-Yves WUILLAUME, Louis VITTOZ, Vincent LEROY, Wenjin CAO, Laetitia PERNOD, and Lucas LETOURNEL.

I would like also express my thanks to the team of OpenFOAM in Bureau Veritas including Dr. Sopheak SENG and Dr. Charles MONROY. They provide me with a well-validated CFD solver, foamStar, to be used in my thesis for developing foamStarSwense and also serves as my reference of standard CFD solvers.

Moreover, I owe a debt of gratitude to Dr. Vuko Vukčević from University of Zagreb. Vuko developed the first version of two-phase SWENSE method in his PhD and I have learned a lot from his work. It is during the short visit to his university that my research plan became clearer. Thanks to his development of Ghost Fluid Method in OpenFOAM, my development of GFM method in SWENSE is not struggle with excessive programming difficulties.

I would also express my gratitude to all the contributors to the open source projects of OpenFOAM, HOS-Ocean, HOS-NWT, and Grid2Grid. It is only based on their work that the implementation of the two-phase SWENSE method has been done and has been continuously improved by benefiting from the progress of all these codes.

The financial support from China Scholarship Council and the Chaire Hydrodynamique et Structure Marines CENTRALE NANTES - BUREAU VERITAS are also gratefully acknowledged.

In the end, I would like to express my deepest gratitude to my parents. This thesis would not have been possible without their constant love and support. My last thanks go to my girlfriend, Yujie CUI ♡. Her warm love and radiant smiles ignite a flame in my heart, spark my life, and are able to turn any pain in life into a sweet "pain au chocolat".

D206, Ecole Centrale de Nantes
February 2019

Contents

List of Figures

List of Tables

Chapter 1

Introduction and Objectives

1.1 General introduction

The accurate prediction of wave-structure interaction is of vital importance in ship hydrodynamics and ocean engineering. For ocean-going vessels, the wave-induced loads are an essential feature for analyzing ships' seakeeping property, the resistance in waves, and the structural integrity in extreme sea states. In ocean engineering, the calculation of wave-structure interaction helps to optimally design offshore structures, for example, oil and gas facilities or marine renewable-energy devices.

Huge waves crash against swaying North Sea oil rig
(www.youtube.com/bbcnews)

Figure 1.1: Wave-structure interaction

Nowadays, the wave structure-interaction problem can be assessed by various approaches. Empirical formulations, model tests in wave tanks and numerical simulation methods are all frequently used. The numerical simulation approach for the wave-structure interaction problem refers to the use of computer software and numerical analysis methods to solve and analyze the fluid flow and its interaction with the structure. The numerical simulation methods have been developed since they are able to assess complex problems where no empirical formulations exist, and their cost is often much less than a wave tank test.

A large variety of software packages exist for the wave-structure interaction problem, such as commercial software packages WAMIT [11], ANSYS [1], SIMULIA [9], STAR-CCM+ [10], FINE/Marine [2]; in-house computational codes CFDShip-Iowa [12], ReFRESCO [8], ICARE [15]; and open source codes NEMOH [6] and OpenFOAM [7], *etc.* The methods for the fluid simulation behind these software packages can be distinguished into two general groups by whether the viscosity of the fluid is considered or not. Potential theory is widely used if the fluid is assumed to be inviscid. Otherwise, the viscous flow is modeled by Navier-Stokes (NS) equations and solved with Computational Fluid Dynamics (CFD) approaches.

Historically, the numerical study on wave-structure interaction problem has been first carried out by potential-theory-based methods. It assumes that the flow is irrotational, and represents the velocity with the gradient of a scalar function: the velocity potential. Potential theory based wave models are widely developed to describe water wave problems. When taking the structure into account, the Boundary Element Method (BEM) [17, 18, 94] is the prevailing numerical solution technique for the potential flow. Since it distributes the unknowns on the boundaries only, the complexity of the problem is reduced by one dimension. Other approaches have also been developed to solve the velocity potential inside the entire domain, such as Finite Element Method (FEM) [132], Finite Difference Method (FDM) [21], Finite Volume Method (FVM) [86], Harmonic Polynomial Cells (HPC) [114], *etc.* The potential flow solvers are efficient and accurate when the geometry of the structure is smooth and the viscous effects are negligible. However, the irrotational flow assumption of potential theory can lead to numerical difficulties in realistic wave-structure interaction scenario when the flow separation happens.

For this reason, numerous viscous flow solvers with the Computational Fluid Dynamics (CFD) approach are developed to assess the wave-structure interaction problem by solving NS equations. The viscous flow solvers are not limited by the irrotational flow assumption. However, the number of unknown variables in this method is much larger than in potential theory. To solve the wave-structure interaction problem in a viscous CFD solver, the flow is either treated as a single-phase problem containing only the water with a moving free surface [23, 85, 103] or modeled as a two-phase flow containing both the water and the air with a common interface [26, 70, 101]. The position of the interface can be identified by the interface tracking technologies with a free-surface-fitted mesh [15, 88, 121] or with interface capturing algorithms such as Volume Of Fluid (VOF) method [65], Level-Set method [97], Marker and Cell method (MAC) [62] *etc.* These solvers, together with specific wave generation and absorption techniques [59, 64, 73], are able to reproduce open sea and experimental conditions. Numerous validations have proved that viscous CFD solvers are able to provide high fidelity results for a wide variety of applications [118]. However, due to the unsteady nature of the water wave problem and the moving free surface, good quality of both the temporal and the spatial discretization is mandatory in CFD solvers to simulate wave-related problems accurately. Moreover, practical marine and ocean engineering applications need sufficiently long simulation time. For example, in regular waves cases, simulations of several wave periods are needed to get rid of the transient flow regime in the beginning of the simulations and to obtain a periodic state; in irregular sea state, simulations of three-hour physical time are required by classification societies to determine the extreme load on an offshore structure [33]. The result is a prohibitive computational cost that must be reduced before the CFD solvers can be applied as a practical design tool.

The objective of this thesis is to develop an accurate and efficient numerical method to simulate the wave-structure interaction problem by coupling the viscous and the potential flow models. The new method shall combine the advantage of each method, *i.e.*, the efficiency of the potential flow models and the ability to treat complex flow of the viscous CFD solvers.

1.2 Literature review: coupling of viscous and potential flow

The methods of coupling viscous and potential flow models in the literature can be divided, depending on the way the total problem is decomposed, into two groups:

- Domain decomposition (DD): the computational domain is divided into a potential region and a viscous region.
- Functional decomposition (FD): the solution in the viscous computational region is decomposed into a potential part and a viscous part.

Figure 1.2 illustrates these two different decomposition strategies.

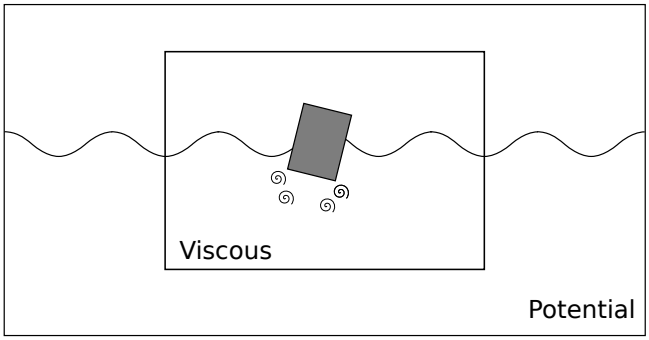

(a) Domain Decomposition

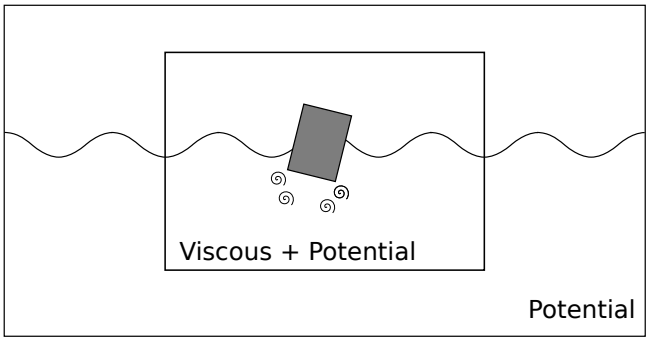

(b) Functional Decomposition

Figure 1.2: Potential and viscous flow coupling methods

1.2.1 Domain decomposition

The domain decomposition (DD) methods split the computational domain into several parts, and in each part, use the appropriate solver with the best efficiency and accuracy. From a physical point of view, the complex interaction, *e.g.*, viscous effects and violent free-surface deformation, only appears in the vicinity of the structure; in the far-field, the viscous effects can often be neglected. For this reason, it is feasible to split the computational domain into a viscous inner sub-domain and an inviscid outer sub-domain. The flows in the two sub-domains can be solved by viscous CFD solvers and potential flow solvers respectively. Information is

exchanged on the common boundary, either in a two-way interactive fashion or a one-way forcing manner.

For two-way coupling: Campana *et al.* [22] proposed a coupling of a RANS solver and a BEM solver with linearized free surface conditions to study free surface ship flows. The matching condition between the RANS solver and the BEM solver was iterated until convergence in an overlapping region. Chen and Lee [25] proposed a similar method as in [22] to couple a RANS and a BEM solver with non-linear free surface conditions to study non-linear waves induced by surface piercing bodies. Colicchio *et al.* [31] coupled a two-phase NS with Level-Set method and a two-phase BEM solver to investigate violent fluid structure interaction, *e.g.*, dam break and green water problem. An overlapping zone was used to guarantee the matching conditions between the two domain. Zhang *et al.* [133] proposed a coupling between a single-phase FEM NS solver and a BEM potential flow solver with nonlinear free surface boundary conditions. Two solvers were connected with a sharp interface. Siddiqui *et al.* [116] presented a coupling of a two-phase RANS solver and the Harmonic Polynomial Cells (HPC) method with non-linear free surface boundary condition to study damaged ship hydrodynamics in forced motion. The two solvers were matched on a sharp interface instead of an overlapping zone. The boundary conditions were passed alternately from one solver to the other in time steps. Lu *et al.* [80] coupled a two-phase VOF NS solver and a single-phase potential flow solver with an overlapping zone. Both solvers were based on the Finite Volume Method. Hamilton and Yeung [61] presented a general matching technique of a linear viscous and a linear inviscid three-dimensional flows utilizing shell function. The above-mentioned works all allow the decomposition interface to intersect the free surface, which is very suitable to study free-surface piercing structures. Other works using fully submerged interface [24, 69] also exist. The two-way coupling is beneficial since the size of the computational domain of the viscous solver can be drastically reduced. But it requires iterations between the two sub-domains on the common interface. To prevent the reflections on the interface, an overlapped blending region is applied sometimes.

Different from the two-way coupling, the alternative one-way forcing manner propagates the information from the potential region to the viscous CFD region. Guignard *et al.* [58] coupled a BEM potential solver with a two-phase viscous solver to study the shoaling and breaking waves in nearshore areas. The potential BEM solution was used to provide boundary conditions for the viscous solver on the coupling interface. Lachaume *et al.* [78], Biausser *et al.* [20] and Grilli *et al.* [57] applied the same coupling method and studied nearshore wave breaking problem. For the wave-structure interaction problem, Christensen *et al.* [30] used the Boussinesq wave model to provide boundary condition for a two-phase viscous solver to calculate wave loads on monopiles. Jacobsen *et al.* [73] proposed a general one-way coupling method to combine potential wave theories and two-phase viscous solvers in OpenFOAM. Relaxation zones were defined on coupling boundaries to gradually blend the viscous results to the incident waves given by the potential wave theories, *i.e.*, to absorb the difference between the two solutions (scatter waves, viscous effects). This method has been widely used by the OpenFOAM community for the simulation of wave-structure interactions [26, 99, 110]. Higuera *et al.* [64] proposed a potential-viscous coupling method similar to Jacobsen *et al.* [73] but used a sharp interface instead of the relaxation zone. The advantage of the one-way coupling is its simplicity. In terms of the efficiency, no iterations between viscous and potential solutions are needed. However, a larger viscous domain is required, compared to the two-way coupling, to avoid the influence of the boundaries.

1.2.2 Functional decomposition

The functional decomposition (FD) approaches split the total problem into a potential component and a viscous component that co-exist in the same computational domain. These components are modeled with different governing equations and solved with potential flow solvers and viscous CFD solvers.

Dommermuth [34] proposed to use the Helmholtz's decomposition to separate the velocity field into an irrotational part and a vortical part to study the free surface flow. Since such decomposition is not unique, multiple choices exist in the literature. The FD methods for fluid-structure interaction problems can be divided into two categories according to whether the structure is considered by the potential flow solution or not. When the structure is taking into account, the fluid-structure interaction problem is divided into a potential part and a viscous part: the entire problem is firstly solved by a potential solver and then corrected by adding the viscous contribution calculated with a viscous solver. Otherwise, the structure is ignored in the potential solution. The total problem is divided into an incident and a complementary part: the incident flow is used as the potential part of the solution, leaving all the remainder to be calculated by the viscous solver as the complementary part.

For the methods in the first category : Kim *et al.* [77] proposed complementary RANS equations to study steady incompressible, turbulent flows around a fixed structure. The irrotational part was solved by a BEM potential solver, representing the potential flow solution of the total flow problem, and the vortical part was solved by a viscous CFD solver. They proved that the functional decomposition was able to reduce the computational cost by using coarse mesh in the far field. Edmund *et al.* [43] improved the method of Kim *et al.* [77] by applying viscous boundary condition of the potential solution on the body-wall. With this method, a better potential solution was obtained and the computational domain of the viscous solver was drastically reduced as long as it encompasses the vortical region. This method has been applied to solve 2D steady incompressible lifting problems by Rosemurgy *et al.* [106] and has been extended to solve 3D unsteady flow by Chen and Maki [27]. The above-mentioned Helmholtz's decomposition remains in the single-phase problem. The extension to free surface flow problem was not straightforward. An attempt to extend this method to solve the 3D flow about a free surface piercing structure was reported by White *et al.* [131]. Janssen *et al.* [74] proposed a perturbation Lattice Boltzmann Method (LBM) where a BEM solver for the potential part and an LBM solver for the viscous effects were coupled with complementary RANS equations. The advantage of these methods is that the viscous solver needs only to focus on the viscous effects in the vortical region, which is confined near the structure and in the wake. However, the potential solver is required to solve the fluid-structure interaction problem as the direct potential flow method does. The same numerical difficulties will be encountered by the potential solver when the structure and the flow are complex.

The second FD decomposition strategy decomposes the total field into an incident and a complementary part. Ferrant *et al.* [49] coupled a single phase viscous CFD solver with the stream function wave theory [105] and studied the interaction of regular waves with a fully submerged 2D structure. The influence of the structure and the viscosity on the incident waves is governed by a complementary RANS equation and solved by the viscous CFD solver. This approach was named as Spectral Wave Explicit Navier-Stokes Equations (SWENSE) method in the work of Luquet *et al.* [82]. This approach was developed and applied to study the interaction of a 3D surface piercing cylinder with regular waves first in the work of Gentaz *et al.* [52]. The method has been validated by Luquet *et al.* [81] with a US Navy Combatant DTMB in waves. The approach was applied to simulate a TLP platform in uni-directional

irregular waves by Luquet *et al.* [83], ship motions in arbitrary waves by Ferrant *et al.* [48] and Monroy *et al.* [91]. The single-phase Level-Set method has been developed to treat complex free surface phenomena by Reliquet *et al.* [103]. Vukčević *et al.* [126, 127] proposed a first two-phase SWENSE formulation to extend this method for two-phase viscous solvers. The advantage of using the incident wave solution as the potential solution part is its simplicity and robustness: no more numerical difficulties are expected in the potential part since it is given directly by wave models. However, the computational domain of the viscous CFD solver shall be larger to attenuate the scattered waves. But since these scattered waves in the far from the structure is not of interest, coarse mesh can be used in the far-field to reduce the computational cost. The original single-phase SWENSE method reduced the CPU time by a factor of 50 compared with direct CFD method for an equivalent precision [83].

1.2.3 Summary

Table 1.1 compares the different potential-viscous coupling methods and the direct simulation method in the context of the wave structure interaction problem.

Comparing with simulating the entire problem with the viscous solver, the coupling methods help to reduce the computational efforts of the viscous solver, by leaving one part of the problem to the potential flow solver. Ideally, the larger portion of problem is solved by the potential flow solver the less viscous computational efforts is needed.

For this reason, many works in the literature use the potential solvers to calculate the incident waves and a part of the scattered waves, leaving the viscous solver to solve a small region. These methods include all the two-way domain decomposition methods, and a part of functional decomposition methods. However, such methods require more potential solution efforts and sometimes iterations between the potential and the viscous solvers.

On the contrary, when the potential flow solution takes only the incident wave solution into account, the couplings are much simpler. Although a larger computational domain is used to attenuate the scattered waves, such coupling does not require the iterations between the viscous and the potential flow solvers and thus is also able to reduce the computational effort. Moreover, the functional decomposition which divides the entire problem into an incident part and a complementary part (*e.g.*, SWENSE) is able to use coarse mesh away from the structure and can thus reduce the computational cost.

Solution Strategy		Potential Solution	Viscous Domain	Viscous Mesh
Direct		-	Large	Fine
Domain Decomposition	Two-way	Incident + Scattered	Small	Fine
	One-way	Incident	Medium	Fine
Functional Decomposition	Potential + Viscous	Incident + Scattered	Small	Fine
	Incident + Complementary	Incident	Medium	Fine: near-field Coarse: far-field

Table 1.1: Comparison the coupling strategies of potential and viscous flow models for wave-structure interaction

1.3 Motivation

Nowadays, two-phase flow solvers with interface capturing technique are widely used to simulate the wave structure interactions. Many two-phase solvers use the one-way domain decomposition strategy to generate and absorb waves on the CFD computational boundaries [64, 73, 87]. However, this method is still computational resource demanding since a fine mesh is required everywhere in the viscous computational domain to obtain a good simulation of incident waves.

The success of the SWENSE method to speed up single-phase CFD solvers encourages researchers to extend the method for two-phase solvers to enhance their performance on wave related problems. However, such work requires the coupling between a two-phase CFD solver with single-phase potential wave models and is not straightforward since the definition domain of the two solvers are not identical.

The coupling of a single-phase potential solver and a two-phase viscous solver exists in the literature, but mostly remains in the domain decomposition category. For example, a variety of strategies have been proposed to force the two-phase viscous solution to be equal to the single-phase potential solution [30, 31, 64, 73, 80, 116] in the far-field. However, such a strategy cannot be applied to the functional decomposition methods, since differences between the total solution and the potential wave solution should be kept to represent the complementary field. For this reason, the work on the functional decomposition with a single-phase potential solver and a two-phase viscous solver is rare in the literature. This difficulty had limited the development of two-phase SWENSE method for a longtime. The first attempt to develop a two-phase SWENSE method was made by Vukčević *et al.* [126, 127]. However, their method is different from the original SWENSE method and still requires refined mesh to keep the incident wave accurate. The reason of this will be elaborated later in this thesis.

The motivation of the present research is to develop a new two-phase SWENSE method following the original method, *i.e.*, making the new method able to use coarse mesh for the incident wave propagation to enhance the viscous solvers' performance. This proposed method should be general and can be used by most of two-phase CFD solvers with interface capturing techniques.

Secondly, the present work also takes parts in the long-term cooperation between l'Ecole Centrale de Nantes and Bureau Veritas (Chaire Hydrodynamique et Structure Marines CENTRALE NANTES - BUREAU VERITAS). One objective of the cooperation is to develop cutting-edge numerical simulation software. Bureau Veritas provides a two-phase viscous CFD solver *foamStar* [92], which is developed with the open-source CFD package OpenFOAM [14]. *foamStar* is able to simulate the wave-structure interaction problem with the one-way domain decomposition strategy. A new solver *foamStar-SWENSE*, shall be developed in this thesis with the two-phase SWENSE method to improve the efficiency of *foamStar*.

1.4 Present contribution

In order to achieve the objectives, the thesis makes the following specific contributions in the coupling of viscous and potential method for the wave-structure interaction problem:

- New mathematical models of the SWENSE method are derived for two-phase CFD solvers with interface capturing techniques. The governing equations are proposed in three forms, including:
  - Non conservative form

  - Conservative form
  - Ghost Fluid Method (GFM) form

  The first two forms use standard numerical discretization schemes and can be adopted by most two-phase solvers with minimal efforts. The GFM form is an improvement of the previous two forms to enhance the interface accuracy and stability. It relies on specific discretization operators to handle the interface discontinuity [127].

- An improved reconstruction technique to map the results of Higher-Order Spectral (HOS) wave models onto the CFD grid is proposed. This technique improves the quality of the reconstructed incident wave field at the reconstruction stage, without increasing the computational cost of the HOS simulations. The reconstruction efficiency is guaranteed by using the Fast Fourier Transform algorithm.

The above mentioned methods are implemented in *foamStar-SWENSE* with the open-source CFD package OpenFOAM for demonstration and validation purposes. Three validation cases are used, including:

- a simulation of progressive wave propagation;
- a calculation of high order loads on a fixed cylinder in deep water regular waves;
- a simulation of a captive Catenary Anchor Leg Mooring (CALM) buoy in regular and irregular waves.

1.5 Thesis outline

The thesis is divided into six chapters and is organized as follows.

Chapter 1 presents the background and objectives of the research. An overview of the literature on the coupling of the CFD solvers with potential theory for the wave-structure interaction is provided.

Chapter 2 provides a background of the mathematical models and the numerical methods before developing the two-phase SWENSE method. It outlines the principle of the single-phase SWENSE method, the incident wave modeling, and the conventional two-phase CFD solvers.

In Chapter 3 the two-phase SWENSE method is developed. The difficulties and challenges in straightforwardly extending the single-phase SWENSE method for two-phase CFD solvers are explained. The new mathematical model of the two-phase SWENSE method is then derived with intermediate steps to overcome each of the difficulties. The governing equations are provided in three forms: the conservative form, the non-conservative form, and a Ghost Fluid Method form. These three forms are implemented in OpenFOAM and tested with a regular wave propagation case.

Chapter 4 explains how to reconstruct the incident wave solution from spectral wave models on CFD solvers. After analyzing existing reconstruction strategies to transfer the results of Higher-Order Spectral (HOS) wave models to the CFD mesh, a new reconstruction technique is proposed to improve the reconstruction accuracy.

The validation and application cases are shown in Chapter 5, including the calculation of higher-order loads on a vertical cylinder in regular waves, and a Catenary Anchor Leg Mooring (CALM) buoy in regular and irregular waves. The numerical results obtained with the two-phase SWENSE method are validated by comparison with reference data. The efficiency of

the proposed method is demonstrated by comparing with a conventional two-phase NS solver on the same problems. The vertical cylinder test case also serves to compare the three sets of two-phase SWENS equations on their convergence and efficiency.

Chapter 6 presents the summary and the conclusions of the thesis. The perspectives for future research are also briefly discussed.

Chapter 2

Basic mathematical models and numerical methods

The aim of this chapter is to provide a minimum background of the mathematical models and the numerical methods for developing the SWENSE method for two-phase CFD solvers.

Section 2.1 explains the idea of the SWENSE method and its advantage in dealing with wave-structure interactions. The principal idea of SWENSE is described as a functional decomposition which separates the total problem into an incident and a complementary problem. The notations and the nomenclature in the SWENSE method are defined. Next, a demonstrative case is used to show how the SWENS equations are derived following the functional decomposition procedure. The advantages of the SWENS equations over the Navier-Stokes (NS) equations are explained.

Section 2.2 reviews the mathematical models and the numerical techniques used by spectral wave models, which provide incident wave information for SWENSE solvers. Two spectral wave models are considered in this work to simulate regular and the irregular incident waves. The advantages and the limitations of the wave models are discussed.

Section 2.3 explains the mathematical models of two-phase CFD solvers, including interface capturing techniques and the two-phase NS equations. The Ghost Fluid Method (GFM), which is often applied in two-phase CFD solvers to improve the accuracy and the stability near the free surface, is also described. In the end, the relaxation zone technique for wave generation and absorption is explained.

Section 2.4 analyzes *foamStar*, a two-phase NS solver developed by Bureau Veritas and Ecole Centrale de Nantes based on OpenFOAM. The understanding of its implementation details is helpful for the development of two-phase SWENSE solvers further in this thesis. *foamStar* is also used as a representative two-phase NS solver in the comparison with SWENSE solvers.

2.1 Introduction of SWENSE method

The Spectral Wave Explicit Navier Stokes Equations (SWENSE) method [49] is proposed to speed up Navier-Stokes (NS) solvers for wave-structure interaction problems because simulating incident wave propagation accurately in NS solvers costs much computational resources. Instead, the SWENSE method uses the potential wave models to obtain the incident wave solution efficiently and couples it with a viscous solver. Consequently, the viscous solver is only responsible to solve a *complementary fields* (the difference from the incident wave solution

caused by the structure, and the viscosity). The governing equations of the complementary fields are called the Spectral Wave Explicit Navier Stokes Equations (SWENSE).

In this section, the principal idea of the SWENSE method is presented, as follows:

1. The functional decomposition procedure to separate the total problem into an incident wave problem and a complementary problem is explained.

2. The SWENS equations are derived in a simple single-phase scenario as an illustrative example.

3. The properties of the single-phase SWENS equations are examined to show its advantages.

2.1.1 Functional decomposition

The SWENSE method defines three notions:

1. Total field: the total field represents real flow in the computational domain, *i.e.*, the final solution of the wave-structure interaction problem. The viscosity of the fluid is taken into account. The flow is governed by the incompressible Navier-Stokes equations.

2. Incident field: the incident wave part concerns the propagation of the incident waves in the computational domain without structures. The viscosity of fluid is neglected and the flow is assumed to be irrotational so that this part is solved by potential theory with dedicated non-linear spectral wave models. The solution of this part satisfies the incompressible Euler equations.

3. Complementary field: the complementary part represents the difference between the total field and the incident field. This field is generated due to the structures and the viscosity of the fluid. The complementary variables are governed by the Spectral Wave Explicit Navier-Stokes Equations (SWENSE), which are to be derived.

With these notions, a primitive field of the flow χ (pressure, velocity, and free surface elevation) is divided into an incident part χ_I and a complementary part χ_C (see Eqn.(2.1.1)). χ_I is explicitly evaluated by the wave model; χ_C shall be calculated by the viscous CFD solver implementing the SWENS equations, as follows.

$$\chi = \chi_I + \chi_C \tag{2.1.1}$$

In this thesis, variables without subscript denote the total field, subscript I denotes the incident waves parts, and subscript C denotes the complementary fields.

This functional decomposition shall not modify the final solution, requiring that the total field reconstructed by summing up the incident field and the complementary field is still the solution of the total Navier-Stokes equations. In order to guarantee this property, the governing equations of the SWENSE method are derived mathematically from the Navier-Stokes equations and the Euler equations, as illustrated by Fig. 2.1.

In Fig. 2.1, a V-shape structure illustrates the functional decomposition. In the first row, the total field represents the final solution of the wave-structure interaction. The Navier-Stokes equations govern this flow. The total solution χ is written as a sum of the incident field and the complementary field ($\chi = \chi_I + \chi_C$). The second row presents the incident wave propagation in the computational domain, without structures. The flow is assumed to be inviscid and

irrotational, so that is can be solved with spectral wave models based on potential theory. The potential wave solution satisfies the incompressible Euler equations. The last row shows the complementary field χ_C, *i.e.*, the influence of the structure on the incident wave field. This field is governed by the SWENS equations. The left half of this V-shape structure shows the derivation procedure. Assuming the NS equations and the Euler equations have the same definition zone, it is possible to use the Navier-Stokes equations minus the Euler equations. Rewriting the remainder with the variable χ_C results in the SWENS equations. The right half shows the reconstruction step, where the complementary field χ_C is added to the incident solution χ_I to reconstruct the total solution χ.

This procedure ensures the equivalence between the direct solution of the NS equations and the reconstructed solution from the functional decomposition.

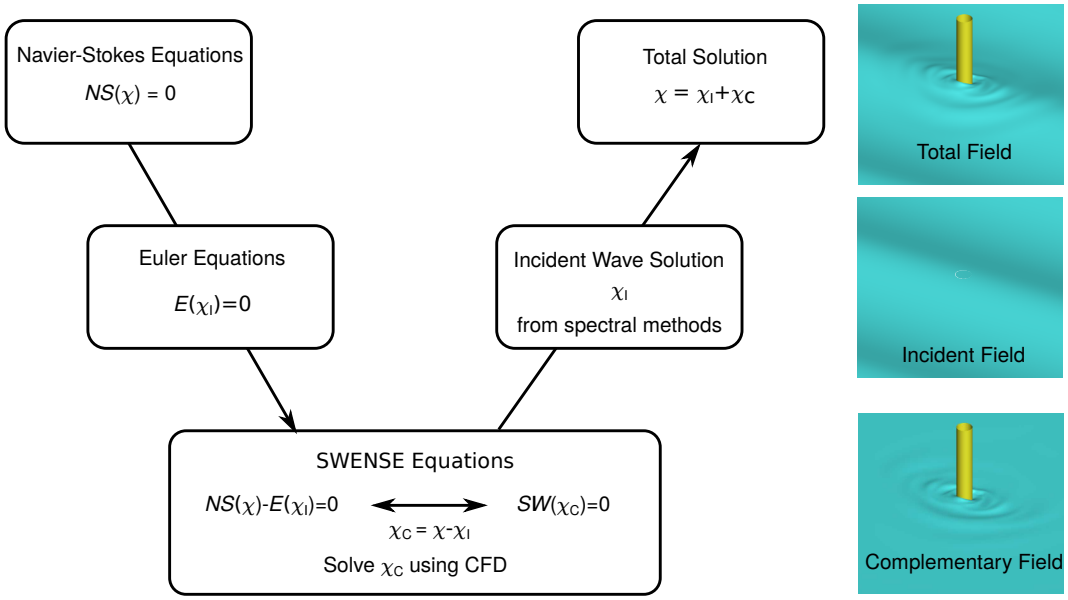

Figure 2.1: The SWENSE method decomposes the total field into an incident and a complementary field.

2.1.2 Derivation of the single-phase SWENS equations

In this section, a simplified version of single-phase SWENS equations is derived to demonstrate the functional decomposition procedure. For simplicity, the free surface is not considered. The entire computational domain is fully occupied by water.

Navier-Stokes Equations

The NS equations for an incompressible, Newtonian fluid are:

$$\nabla.\mathbf{u} = 0 \tag{2.1.2}$$

$$\frac{\partial \mathbf{u}}{\partial t} + \mathbf{u}.\nabla\mathbf{u} = -\frac{\nabla p}{\rho} + \mathbf{g} + \nu\nabla^2\mathbf{u} \tag{2.1.3}$$

where $\mathbf{u}$ is the velocity, p is the pressure. $\rho = \rho_w$ stands for the density of water and ν stands for the kinematic viscosity. $\mathbf{g}$ stands for the gravitational acceleration.

Euler Equations

The incident wave solution obtained from potential theory satisfies the incompressible Euler equations, as follows:

$$\nabla.\mathbf{u}_I = 0 \tag{2.1.4}$$

$$\frac{\partial \mathbf{u}_I}{\partial t} + \mathbf{u}_I.\nabla\mathbf{u}_I = -\frac{\nabla p_I}{\rho_I} + \mathbf{g} \tag{2.1.5}$$

where $\rho_I = \rho_w$.

SWENS equations

Subtracting the Euler equations from the NS equations, we obtain:

$$\nabla.(\mathbf{u} - \mathbf{u}_I) = 0 \tag{2.1.6}$$

$$\begin{aligned} &\frac{\partial(\mathbf{u} - \mathbf{u}_I)}{\partial t} + (\mathbf{u} - \mathbf{u}_I).\nabla(\mathbf{u} - \mathbf{u}_I) + (\mathbf{u} - \mathbf{u}_I).\nabla\mathbf{u}_I + \mathbf{u}_I.\nabla(\mathbf{u} - \mathbf{u}_I) \\ &= -\frac{\nabla(p - p_I)}{\rho} + \nu\nabla^2(\mathbf{u} - \mathbf{u}_I) + \nu\nabla^2\mathbf{u}_I \end{aligned} \tag{2.1.7}$$

where $\rho = \rho_I = \rho_w$. The last term vanishes as $\nabla^2\mathbf{u}_I = 0$ when the velocity field $\mathbf{u}_I$, derived from potential theory, is solenoidal and irrotational [76, 117] since

$$\begin{aligned} \nabla^2\mathbf{u}_I &= \nabla(\nabla.\mathbf{u}_I) - \nabla \times (\nabla \times \mathbf{u}_I) \\ &= \nabla(\cancelto{0}{\nabla.\mathbf{u}_I}) - \nabla \times (\cancelto{0}{\nabla \times \mathbf{u}_I}) \\ &= 0 \end{aligned} \tag{2.1.8}$$

Noting $\mathbf{u}_C = \mathbf{u} - \mathbf{u}_I$ and $p_C = p - p_I$, the governing equations of the single-phase SWENSE method read:

$$\nabla.\mathbf{u}_C = 0 \tag{2.1.9}$$

$$\frac{\partial \mathbf{u}_C}{\partial t} + \mathbf{u}_C.\nabla\mathbf{u}_C + \mathbf{u}_C.\nabla\mathbf{u}_I + \mathbf{u}_I.\nabla\mathbf{u}_C = -\frac{\nabla p_C}{\rho} + \nu\nabla^2\mathbf{u}_C \tag{2.1.10}$$

2.1.3 Properties of the single-phase SWENS equations

An interesting property of the SWENSE momentum equation (Eqn.(2.1.10)) is that it keeps the accuracy of the incident wave kinematics regardless of the mesh quality.

Take an incident wave propagation as an example. If the computational domain is fully submerged in the water and there is no structure in the computational domain (see Fig 2.2), no disturbance is expected in this scenario. The simulation results of CFD should be equal to the incident wave solution given by potential theory since:

- No structure appears in the computational domain to generate the diffracted waves,
- The viscosity of fluid has no effects on the incident velocity field (see Eqn.(2.1.8)).

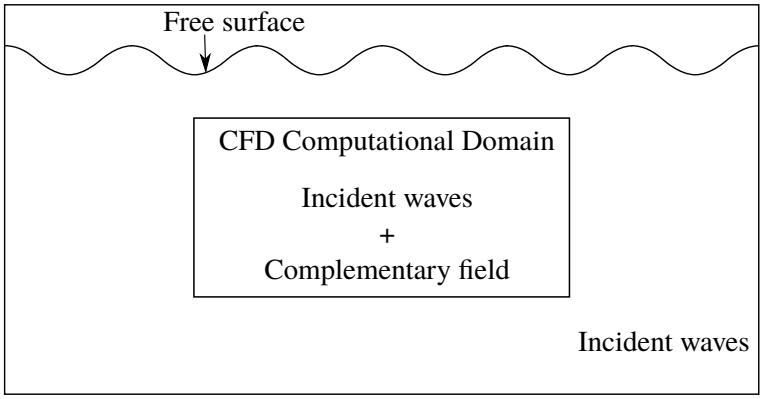

Figure 2.2: Propagation of incident waves in a fully submerged computational domain.

However, in a conventional NS solver, the incident wave information is only available on the boundaries. The internal flow needs to be calculated by solving the NS equations. In this way, both the temporal and the spatial discretization need to be fine to avoid numerical dissipation.

On the contrary, the SWENSE method is very suitable to maintain the incident wave kinematics provided by the wave theory. As the SWENSE method treats the incident wave separately, maintaining the total solution equal to the incident solution is equivalent to keeping the complementary field equal to zero. The following part proves this ability of the SWENS equations.

Take an example where a pure incident wave simulation starts with zero complementary fields

$$\mathbf{u}_C = 0 \tag{2.1.11}$$

$$p_C = 0 \tag{2.1.12}$$

Substitute this initial condition into the SWENSE momentum equation (Eqn.(2.1.10)), yielding:

$$\frac{\partial \mathbf{u}_C}{\partial t} + \cancelto{0}{\mathbf{u}_C \cdot \nabla \mathbf{u}_C} + \cancelto{0}{\mathbf{u}_C \cdot \nabla \mathbf{u}_I} + \cancelto{0}{\mathbf{u}_I \cdot \nabla \mathbf{u}_C} = \cancelto{0}{-\frac{\nabla p_C}{\rho}} + \cancelto{0}{\nu \nabla^2 \mathbf{u}_C} \tag{2.1.13}$$

The result is that the time derivative of the complementary velocity is equal to zero.

$$\frac{\partial \mathbf{u}_C}{\partial t} = 0 \tag{2.1.14}$$

So the complementary fields remains zero in the entire computational domain. The total field is consequently equal to the incident wave. This results will not be affected by the numerical resolution.

Thanks to this property, in a realistic wave-structure interaction problem, coarse mesh in the far-field can be used by the SWENSE method since the incident waves are already provided and are not affected by the CFD resolution. The mesh needs to be refined in the area of interest only (often in the region close to the structure) to capture the complementary field accurately. The total number of CFD cells can be reduced for a given level of accuracy.

2.2 Incident wave modeling with spectral methods

Although the incident waves propagation problem is no more treated by the CFD solvers in the SWENSE method, it still needs to be solved by external solvers. These external solvers should be more accurate and more efficient than the viscous CFD solvers in calculating incident waves, so that the overall efficiency can be improved. In the present work, the incident waves are obtained with spectral wave models, since they are both accurate and efficient. Moreover, their incident wave solution can be easily extended above the incident free surface. Such a property are very helpful for the SWENSE method, when the incident and the total free surfaces are different.

This section presents the theoretical background of spectral wave models. First, the single-phase incompressible Euler equations are presented as the governing equations for the inviscid water wave problem. The second part presents the potential theory and the general principle of the spectral methods. Thirdly, the stream-function wave theory is presented to model uni-directional regular waves. In the last, the Higher Order Spectral (HOS) method for the multi-directional irregular waves modeling is outlined. In the end, the advantages and the limitation associated with the spectral wave models are examined.

2.2.1 Single-phase incompressible Euler equations

The Euler equations give a mathematical description of inviscid flow. The incompressible version of the Euler equations is widely used in the modeling of water waves, since in such phenomenon the viscosity are negligible. When the air above the free surface is also neglected, the single-phase incompressible Euler equations can be established in the water only. The water free surface is considered as a moving boundary (see Fig. 2.3).

The moving free surface is defined by a time dependent free-surface elevation function, as follows

$$z = \eta_I(\mathbf{x}, t) \tag{2.2.1}$$

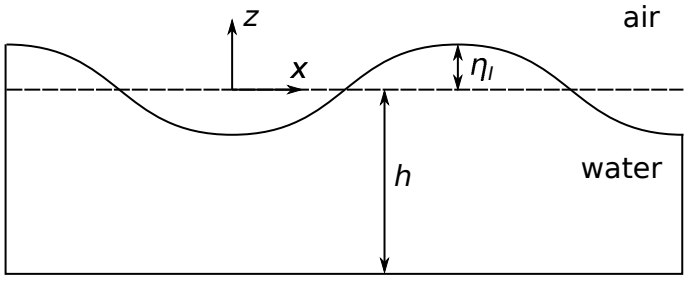

Figure 2.3: Water waves are modeled as a single-phase problem with a deforming free surface.

The water beneath the free surface is modeled with the incompressible Euler equations for inviscid fluid. Recalling Eqn.((2.1.4) and (2.1.5) as follows,

$$\begin{aligned} \nabla.\mathbf{u}_I &= 0 \\ \frac{\partial \mathbf{u}_I}{\partial t} + \mathbf{u}_I.\nabla\mathbf{u}_I &= -\frac{\nabla p_I}{\rho_I} + \mathbf{g} \end{aligned}$$

where $\rho_I = \rho_w$. The subscript I represents "*incident*" field, and w is for "*water*". The boundary conditions are:

$$\frac{\partial \eta_I}{\partial t} + u_I \frac{\partial \eta_I}{\partial x} + v_I \frac{\partial \eta_I}{\partial y} - w_I = 0 \quad at \quad z = \eta_I(\mathbf{x}, t) \tag{2.2.2}$$

$$p_I = 0 \quad at \quad z = \eta_I(\mathbf{x}, t) \tag{2.2.3}$$

$$w_I = 0 \quad at \quad z = -h \tag{2.2.4}$$

with $\mathbf{u}_I = (u_I, v_I, w_I)$, $\mathbf{x} = (x, y)$.

2.2.2 Potential theory and spectral solution methods

Assuming ideal fluid and irrotational flow, it is possible to define a velocity potential ϕ, so that

$$\mathbf{u}_I = \nabla \phi \tag{2.2.5}$$

The Euler equations can be written in an equivalent form with ϕ, as follows,

$$\Delta \phi = 0, \tag{2.2.6}$$

$$\frac{\partial \eta_I}{\partial t} + \frac{\partial \phi}{\partial x}\frac{\partial \eta_I}{\partial x} + \frac{\partial \phi}{\partial y}\frac{\partial \eta_I}{\partial y} - \frac{\partial \phi}{\partial z} = 0 \quad at \quad z = \eta_I(\mathbf{x}, t) \tag{2.2.7}$$

$$\frac{\partial \phi}{\partial t} + \frac{1}{2}(\nabla \phi)^2 + gz = 0 \quad at \quad z = \eta_I(\mathbf{x}, t) \tag{2.2.8}$$

$$\frac{\partial \phi}{\partial z} = 0 \quad at \quad z = -h \tag{2.2.9}$$

Spectral methods are used to solve this non-linear potential flow problem. The spectral methods decompose the free surface elevation $\eta_I(\mathbf{x}, t)$ and the velocity potential $\phi(\mathbf{x}, z, t)$ using a set of basis functions. An example of an uni-directional wave case is shown as follows

$$\eta_I(x, t) = \sum_i A_i^{\eta}(t)\psi_i(x) \tag{2.2.10}$$

$$\phi(x, z, t) = \sum_i A_i^{\phi}(t)\frac{\cosh(k_i(z+h))}{\cosh(k_i h)}\psi_i(x) \tag{2.2.11}$$

where A_i is the modal amplitudes, k_i is the wave numbers, and $\psi_i(x)$ is the horizontal basis functions (sine and cosine functions or their complex exponential equivalents).

In this work, two fully non-linear spectral methods are adopted. The first is based on the stream function theory [105] for 2D regular waves. The second is the Higher Order Spectral (HOS) method [37, 38] for 2D/3D arbitrary waves in open seas or in experimental wave tanks.

2.2.3 Regular waves: stream function theory

For 2D regular nonlinear waves, an algorithm based on the stream function wave theory has been adopted [41, 105]. This algorithm is able to generate accurate solution of steadily progressing periodic waves over a horizontal seabed for a wide range of depths, amplitudes and wavelengths. The method is briefly described in the following paragraph, the reader can find more information in the reference [41, 105].

The method decomposes the free surface elevation and the velocity potential using basis functions as shown in Eqn.(2.2.10) and (2.2.11). The basis function $\psi_i(\mathbf{x})$ is replaced by $\psi_i(x - ct)$, with c the phase velocity, to obtain constant modal amplitudes A_i^η and A_i^ϕ.

The dynamic boundary condition and the stream function on the free surface are discretized to solve for the coefficients A_i^η an A_i^ϕ. Once the coefficients are obtained, the incident velocity field $\mathbf{u}_I$ is calculated with Eqn.(2.2.5), and the pressure is obtained with the Bernoulli equation.

Figure 2.4 illustrates the velocity field calculated by the stream function wave theory. The wave period is equal to 0.7017s, the wave height is equal to 0.0575m, and the water depth is equal to 0.6m ($ka = 0.24$, $kh = 4.91$).

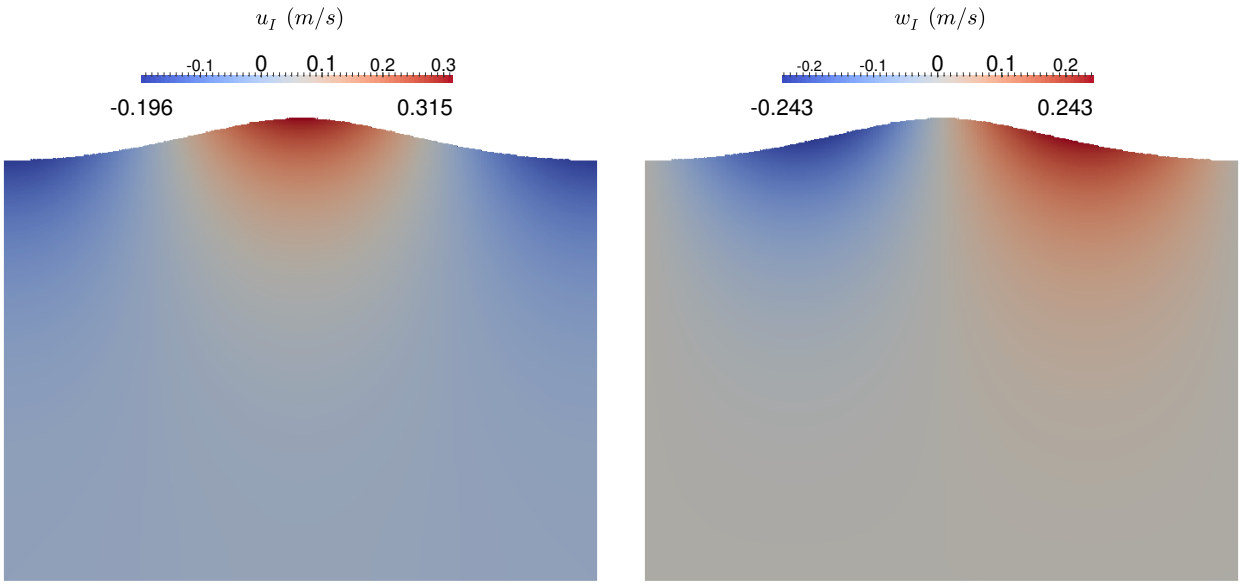

(a) Horizontal velocity

(b) Vertical velocity

Figure 2.4: Velocity field calculated by the stream function wave theory ($T = 0.7017s, H = 0.0575m, h = 0.6m$).

2.2.4 Arbitrary waves: Higher Order Spectral method

The Higher-Order Spectral (HOS) method is adopted for modeling arbitrary incident waves. HOS models are widely used for the study of wave propagation in open domains [35, 130]. It considers the full non-linearity of the free surface up to the wave breaking limit and exhibits high efficiency and accuracy thanks to its pseudo-spectral formalism. Two open-source solvers developed in LHEEA Lab (ECN/CNRS), *HOS-Ocean* [37] and *HOS-NWT* [38], are used to solve arbitrary incident waves in open domains and experimental wave tanks, respectively. The idea of the HOS method is briefly described in the following paragraphs. The reader is referred to the original works for more details.

For simplicity, only *HOS-Ocean* in a 2D case is presented.

Using Eqn.(2.2.11), the HOS methods transform the velocity potential into a sum of basis functions, which is defined with as follows,

$$\psi_i(x) = \exp(ik_i x) \tag{2.2.12}$$

where x is the horizontal coordinate. A variable $\tilde{\phi}$ representing the velocity potential on the free surface is defined, as follows,

$$\tilde{\phi}(x,t) = \phi\left(x, z = \eta_I(x,t), t\right) \tag{2.2.13}$$

The free surface quantities η_I is decomposed with Eqn.(2.2.10). $\widetilde{\phi}$ is decomposed in the spectral domain with the following equation

$$\tilde{\phi}(x,t) = \sum_i A_i^{\tilde{\phi}}(t) \exp(ik_i x) \tag{2.2.14}$$

.

The time evolution of the previous free surface quantities (η_I and $\tilde{\phi}$) is calculated by the following free surface boundary conditions,

$$\frac{\partial \eta_I}{\partial t} = \left(1 + \left(\frac{\partial \eta_I}{\partial x}\right)^2\right) w_I - \frac{\partial \tilde{\phi}}{\partial x}.\frac{\partial \eta_I}{\partial x} \tag{2.2.15}$$

$$\frac{\partial \tilde{\phi}}{\partial t} = -g\eta_I - \frac{1}{2}\left(\frac{\partial \tilde{\phi}}{\partial x}\right)^2 + \frac{1}{2}\left(1 + \left(\frac{\partial \eta_I}{\partial x}\right)^2\right) w_I^2 \tag{2.2.16}$$

.

The vertical velocity $w_I = \dfrac{\partial \phi}{\partial z}$ at the free surface is calculated by expressing the velocity potential $\tilde{\phi}$ and the vertical velocity W as a truncated series of components. $\phi = \sum_{m=1}^{M} \phi^{(m)}$ and $w_I = \sum_{m=1}^{M} w_I^{(m)}$. M stands for the order of nonlinearity, which is arbitrary. The free surface velocity potential and the vertical velocity is then expanded as a Taylor series with respect to the mean water level.

Figure 2.5, reproduced from Ducrozet *et al.* [39], gives an example of an irregular waves simulation conducted by *HOS-Ocean*. The computational domain and duration are made to be large to investigate the extreme wave events.

Besides *HOS-Ocean*, the second solver, *HOS-NWT* (Numerical Wave Tank), is used to reproduce the experimental conditions. The basis functions and the numerical schemes are adapted to reproduce a rectangular wave tank with a wave-maker, an absorbing zone, and perfectly reflective side walls.

2.2.5 Advantages and limitations of the spectral methods

Advantages

One difficulty in the coupling of two free surface flow solvers is that the free surface position calculated by the two solvers may be different. In the context of the SWENSE method, this problem is more notable, since the structure will definitely make the incident and the total free surface elevation different. Figure 2.6 shows such a scenario. The incident wave free surface position is shown as η_I, the total free surface is shown as η. For a single-phase viscous solver, the computational domain contains all the area under the total free surface position η. When

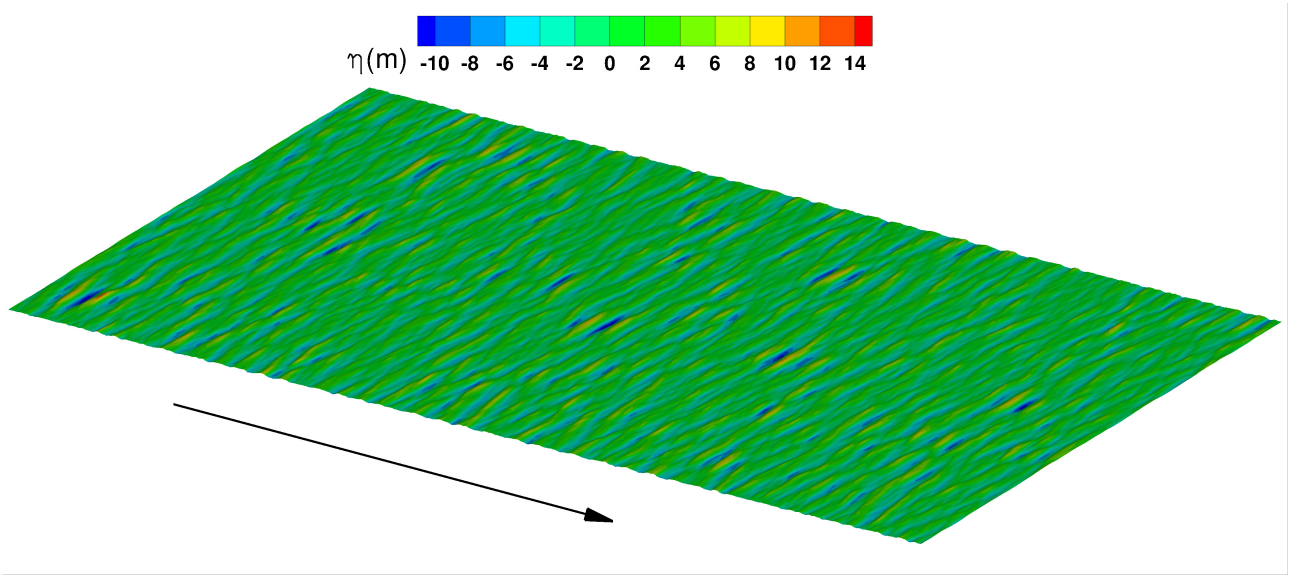

Figure 2.5: Free-surface elevation of a *HOS-Ocean* simulation with JONSWAP spectrum ($H_s = 11m, T_p = 12.5s, \gamma = 5$). The size of computational domain is $(Lx, Ly) = (40\lambda_p, 20\lambda_p) \approx 50km^2$. The picture is reproduced from the work of Ducrozet *et al.* [39].

$\eta > \eta_I$, an extension of the incident solution is necessary, so that the same SWENS equations can be used in the entire computational domain.

The main advantage of the spectral wave methods, is that they can provide incident wave fields even above the incident wave free surface. In fact, Eqn.(2.2.11) can provide incident wave solution satisfying the Euler equations at arbitrary position. In Fig. 2.7, the velocity field calculated by the stream function wave theory is extended above the incident wave free surface position (white line). This advantage of spectral wave models helps the SWENSE method to adjust the definition zone of the incident wave, so that the same functional decomposition can be used in the entire CFD computational domain.

Limitations

Although the spectral wave models (stream function, and HOS) are able to reproduce a large variety of non-linear water waves encountered in the marine and offshore applications, they do have some limitations.

- Rectangular computational domain: Spectral methods are limited to simulate the waves in a rectangular computational domain. This limitation is associated with the Fourier transform used by the spectral method, *i.e.*, the computational domain should be periodic or symmetric. The stream function wave theory is only able to calculate regular waves in a constant water depth. The HOS solvers can either use a large rectangular domain with periodic boundary conditions to mimic the open-sea condition (*HOS-Ocean*), or simulate a rectangular wave tank with fully reflective side walls (*HOS-NWT*). The standard open source version of *HOS-Ocean* and *HOS-NWT* require constant water depth. In a more advanced in-house version, the HOS solvers are able to deal with variable bathymetry [54–56].

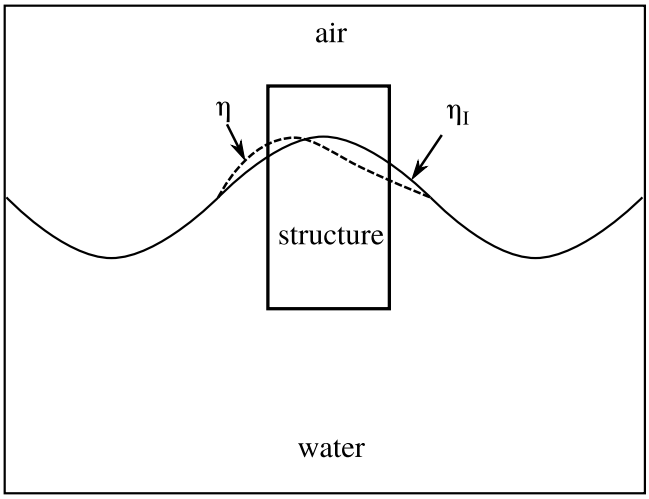

Figure 2.6: Difference between the incident and the total free surface position.

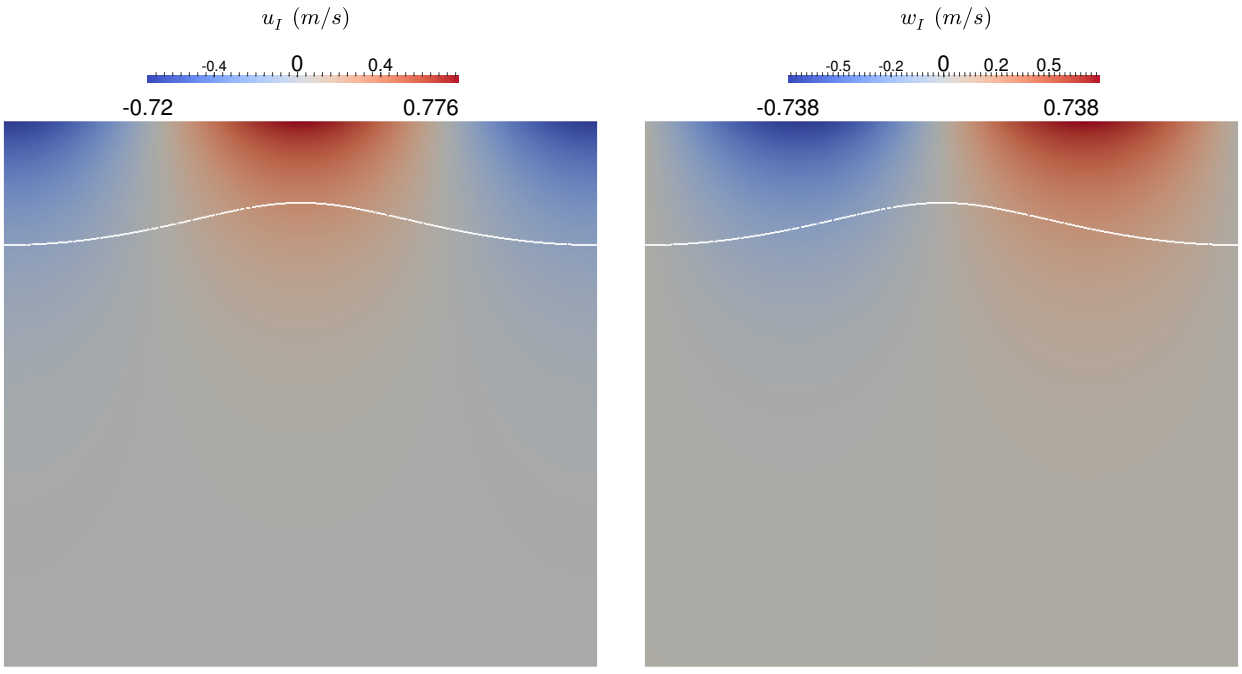

(a) Horizontal velocity

(b) Vertical velocity

Figure 2.7: Extended velocity field calculated by the stream function wave theory. The incident free surface is represented by the white line. ($T = 0.7017s, H = 0.0575m, h = 0.6m$).

- Non-breaking incident waves: Spectral methods are not able to simulate the breaking wave events. This limitation is associated with the single-value free surface position function. With this limitation the overturning free surface of the breaking waves can not be reproduced. In the HOS models, the effects of wave breaking of the incident waves can be approximated through specific models. When a wave breaking even appears, such models extract energy from the wave system to represent the natural energy dissipation and to stabilize the numerical simulation. Promising recent developments may overcome this limitation [111, 112]. Note that the non-breaking limitation applies only on the incident waves. The breaking wave caused by a structure can be captured as the complementary fields in the SWENSE method.

2.3 Mathematical models for two-phase flows

This section describes the mathematical and the numerical models for simulating the water-wave phenomenon with conventional two-phase CFD solvers. In these models, the flow is assumed to be incompressible for classical marine and offshore applications.

First, interface capturing techniques used by two-phase solvers are explained.

Secondly, the incompressible Navier-Stokes (NS) equations to describe the two-phase viscous flow is shown. In this formulation, the two-phase flow is described by a single set of governing equations. Both conservative and non-conservative forms of the NS equations are presented.

Thirdly, the mathematical description of the Ghost Fluid Method (GFM) for the two-phase flow is outlined. This method is used to improve the accuracy and the stability on the air-water interface.

Lastly, the wave generation and absorption techniques via relaxation zones [73, 92] are presented. Such techniques enable the two-phase CFD solvers to reproduce open sea and experimental conditions by generating waves and preventing the reflections at the boundaries of the computational domain.

2.3.1 Interface capturing techniques

The two most popular interface capturing techniques in the literature are the Volume of Fluid (VOF) [65] and the Level-Set (LS) method [97].

The VOF method defines a scalar to represent the volume fraction of one fluid in a computational cell. The LS method uses a signed distance field to represent the distance of one cell to the nearest interface.

One advantage of the VOF method is its mass conservation. The LS method tends to lose mass [119, 120] unless it is coupled with other interface capturing techniques [113]. Another advantage of the VOF method is its simplicity. The volume fraction field can be advected with the flow velocity as a passive scalar directly. The LS method is more complicated: an extension of velocity and a re-distancing procedure are often required to maintain the signed distance function [53].

The drawbacks of the VOF method are that the interface position can not be accurately given and the computation of geometric quantities such as curvature is not straightforward. On the contrary, the LS method is able to provide this information with ease. Such information is important in the calculation of the surface tension. However, in marine and offshore applications, the surface tension is often negligible.

The present work adopts the VOF method as the interface capturing technique, considering its advantages in the mass conservation and simplicity.

Volume of Fluid Method

The VOF method defines a scalar field $\alpha \in [0, 1]$ indicating the volume fraction of water phase in a computational cell: it is equal to 1 if the cell is full of water, and is equal to 0 if the cell is full of air. The cells intersected by the free surface has a VOF value between 0 and 1. Figure 2.8 illustrates the definition of the VOF field α.

$$\alpha = \begin{cases} 0 & \text{in the air} \\ \in (0,1) & \text{on the interface} \\ 1 & \text{in the water} \end{cases} \tag{2.3.1}$$

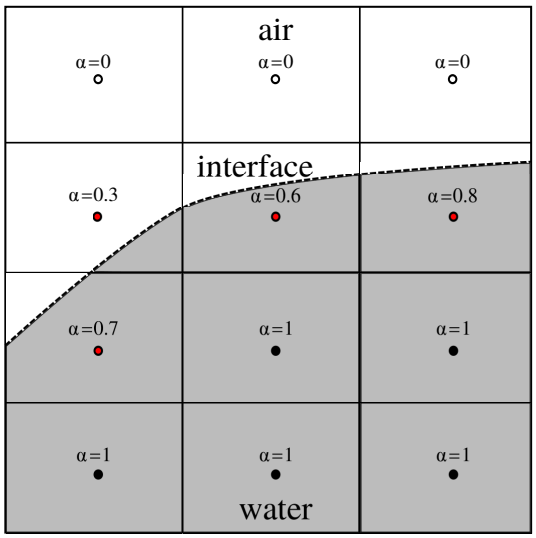

Figure 2.8: VOF method represents the interface by the volume fraction field α

The volume fraction field is convected by the velocity field $\mathbf{u}$, as follows,

$$\frac{\partial \alpha}{\partial t} + \mathbf{u}.\nabla\alpha = 0 \tag{2.3.2}$$

2.3.2 Two-phase Navier-Stokes equations: one-fluid form

The two-phase Navier-Stokes (NS) equations are defined in a zone containing both water and air (see Fig. 2.9).

In the one-fluid form two-phase NS equations (also called as aggregated-fluid approach [129]), the fluid in this computational zone is considered as one mixture fluid. The fluid properties are defined with the VOF function α as a mixture of the two fluids. The fluid properties are defined as a linear combination of the air and the water. The α is used as the weight. For example, the fluid density and the fluid viscosity in a computational cell are defined as follows.

$$\rho = \alpha\rho_w + (1-\alpha)\rho_a \tag{2.3.3}$$

$$\mu = \alpha\mu_w + (1-\alpha)\mu_a \tag{2.3.4}$$

where ρ is the density of the fluid; μ is the dynamic viscosity. The subscripts a and w represent the property of air and water, respectively.

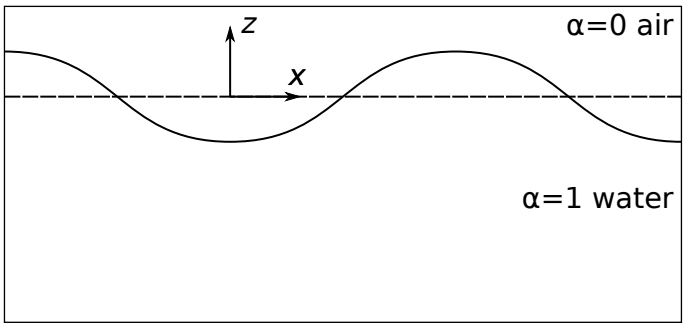

Figure 2.9: The two-phase Navier-Stokes equations are defined in a large zone containing both water and air. The fluid in this zone is considered as a single mixture fluid.

Continuity equation

In marine and offshore applications, both the air and the water are usually considered as incompressible. The continuity equation for this mixture fluid reads,

$$\nabla.\mathbf{u} = 0 \tag{2.3.5}$$

Momentum equation

The momentum equation for the mixture fluid, in the non-conservative form [31, 95, 124] reads:

$$\frac{\partial \mathbf{u}}{\partial t} + \mathbf{u}.\nabla\mathbf{u} = -\frac{\nabla p}{\rho} + \mathbf{g} + \frac{\nabla.(\mu(\nabla\mathbf{u} + \nabla\mathbf{u}^T))}{\rho} \tag{2.3.6}$$

where p is the pressure field; $\mathbf{g}$ is the gravitational acceleration; μ is the dynamic viscosity. The surface tension is neglected for the classical marine and offshore applications. The above equation can be also written in a conservative form [108, 123] as follows,

$$\frac{\partial \rho\mathbf{u}}{\partial t} + \nabla.(\rho\mathbf{u}\mathbf{u}) = -\nabla p + \rho\mathbf{g} + \nabla.(\mu(\nabla\mathbf{u} + \nabla\mathbf{u}^T)) \tag{2.3.7}$$

In some works [26, 64, 73, 92, 100], the NS momentum equation is written with the hydrodynamic pressure $p_{-\rho gh} = p + \rho g z$, where g is the magnitude of $\mathbf{g}$ and z is the vertical coordinate.

In non conservative form

$$\frac{\partial \mathbf{u}}{\partial t} + \nabla.(\mathbf{u}\mathbf{u}) = -\frac{\nabla p_{-\rho gh}}{\rho} + gz\frac{\nabla\rho}{\rho} + \frac{\nabla.(\mu(\nabla\mathbf{u} + \nabla\mathbf{u}^T))}{\rho} \tag{2.3.8}$$

In conservative form

$$\frac{\partial \rho\mathbf{u}}{\partial t} + \nabla.(\rho\mathbf{u}\mathbf{u}) = -\nabla p_{-\rho gh} + gz\nabla\rho + \nabla.(\mu(\nabla\mathbf{u} + \nabla\mathbf{u}^T)) \tag{2.3.9}$$

The use of the dynamic pressure $p_{-\rho gh}$ avoids the numerical integration of the gravity term $\rho\mathbf{g}$ in the entire computational domain. It produces more accurate results when the mesh

quality is poor [16]. The additional source term related to the interface ($gz\nabla\rho$) appears to take into account the restoring force when the free surface is deformed from the hydrostatic equilibrium, *i.e.*, $gz \neq 0$.

Remark on the one-fluid form of the two-phase NS equations

The one-fluid form of NS equations is implemented by many two-phase flow solvers [66, 108, 122, 129]. Good results have been shown.

However, the numerical solvers encounter difficulties in capturing the discontinuous nature at the interface. In a mathematical point of view, the following discontinuities should appear in the exact solution:

- In Eqn.(2.3.6) and (2.3.7), the difference between the fluid densities across the interface leads to a discontinuity on the gradient of the pressure field. The gradient of pressure (∇p) is approximately 1000 times larger in the water than in the air.
- In Eqn.(2.3.9), a discontinuity of the dynamic pressure $p_{-\rho gh}$ also appears. This discontinuity is due to the gradient of density term $\nabla\rho$. This term only has non-zero values on the interface. The consequence is a jump of ρgz in the dynamic pressure $p_{-\rho gh}$ field on the interface.

In the numerical solution, the sharp discontinuity is smeared in a transition zone with several cells where the solution changes from one phase to the other. A common problem caused by the smearing interface is the spurious air velocity near the free surface, which affects the accuracy and the stability of the simulation [29, 73].

2.3.3 Ghost-Fluid Method for two-phase flow

The Ghost Fluid Method (GFM) [45, 67, 96] can be used to remove the numerical smearing caused by the one-fluid form NS equations and improve the accuracy and the stability near the interface. This section is adapted from the Ph.D. thesis of Vukčević [126], to explain the mathematical model of the GFM.

Unlike the one-fluid form NS equations, which are obtained directly for the entire mixture fluid, the GFM Navier-Stokes equations are established in two steps:

- Establish separately in each fluid the Navier-Stokes equations with the corresponding properties of the fluid;
- Connect the variables (pressure, velocity) in the two set of equations on the common interface.

In the water

The Navier-Stokes equations in the water are written as follows,

$$\nabla.\mathbf{u} = 0 \tag{2.3.10}$$

$$\frac{\partial \mathbf{u}}{\partial t} + \mathbf{u}.\nabla\mathbf{u} = -\frac{\nabla p_{-\rho gh}}{\rho_w} + \nu_w \nabla^2 \mathbf{u} \tag{2.3.11}$$

where $p_{-\rho gh} = p + \rho_w gz$.

In the air

The Navier-Stokes equations in the air are written as follows,

$$\nabla.\mathbf{u} = 0 \tag{2.3.12}$$

$$\frac{\partial \mathbf{u}}{\partial t} + \mathbf{u}.\nabla\mathbf{u} = -\frac{\nabla p_{-\rho gh}}{\rho_a} + \nu_a \nabla^2 \mathbf{u} \tag{2.3.13}$$

where $p_{-\rho gh} = p + \rho_a g z$.

Interface Conditions

Define $[\chi] = \chi_a - \chi_w$ the jump at interface for any quantity χ. Following [126], the pressure p is continuous at the interface, so that

$$[p] = 0 \tag{2.3.14}$$

$$[p_{-\rho gh}] = [\rho] g z \tag{2.3.15}$$

Subtract Eqn.(2.3.11) from Eqn.(2.3.13) on the common interface, yielding,

$$\left[\frac{\partial \mathbf{u}}{\partial t} + \mathbf{u}.\nabla\mathbf{u}\right] = -\left[\frac{\nabla p_{-\rho gh}}{\rho}\right] + (\nu_a \nabla^2 \mathbf{u} - \nu_w \nabla^2 \mathbf{u}) \tag{2.3.16}$$

Following the work of Vukčević [126], the unsteady term and the convective term are considered to be continuous, so that the fluid in both side of the interface shares the same acceleration, yielding

$$\left[\frac{\partial \mathbf{u}}{\partial t} + \mathbf{u}.\nabla\mathbf{u}\right] = 0 \tag{2.3.17}$$

The viscous term is assumed to be continuous for convenience

$$\nu_a \nabla^2 \mathbf{u} - \nu_w \nabla^2 \mathbf{u} = 0 \tag{2.3.18}$$

This approximation is valid in classical marine and offshore applications, where the viscous effects on the interface is of minor importance compared with the pressure and gravity contribution.

Substitute the above mentioned equation in Eqn.(2.3.16), yielding,

$$\left[\frac{\nabla p_{-\rho gh}}{\rho}\right] = 0 \tag{2.3.19}$$

This equation signifies that the gradient of the dynamic pressure is proportional to the density of the fluid, *i.e.*, in the water, the pressure gradient is approximately 1000 times larger than in the air.

Combined Equations

The combined equations are written as follows,

$$\nabla.\mathbf{u} = 0 \tag{2.3.20}$$

$$\frac{\partial \mathbf{u}}{\partial t} + \mathbf{u}.\nabla\mathbf{u} = -\frac{\nabla p_{-\rho gh}}{\rho} + \nu\nabla^2\mathbf{u} \tag{2.3.21}$$

Note that Eqn.(2.3.21) doesn't contain the density gradient term $gz\dfrac{\nabla\rho}{\rho}$ as in Eqn. (2.3.8). This term is absorbed by the interface jump condition of $p_{-\rho gh}$ given in Eqn. (2.3.15). Special discretization operators are needed to take into account the discontinuity of the dynamic pressure and its gradient (Eqn.(2.3.15) and (2.3.19)) [126].

The free surface position is required in the GFM to apply the interface discontinuity conditions. However, the VOF method cannot explicitly give the exact position of the free surface. In this scenario, the $\alpha = 0.5$ contour of the VOF field is used to represent the free surface. The density (ρ) and the viscosity (ν) of the fluid are defined with the VOF field (α) as follows,

$$\rho = \begin{cases} \rho_w & \alpha > 0.5 \\ \rho_a & \alpha < 0.5 \end{cases} \tag{2.3.22}$$

and

$$\nu = \begin{cases} \nu_w & \alpha > 0.5 \\ \nu_a & \alpha < 0.5 \end{cases} \tag{2.3.23}$$

2.3.4 Wave generation and absorption

The two-phase CFD solvers described previously are able to construct virtually a numerical water tank. However, they still lack specific methods to generate realistic waves for real marine and offshore applications. Moreover, the numerical wave tank requires also dedicated wave absorption methods to prevent wave reflections at the boundaries of the computational domain. Without wave absorption techniques, the reflecting waves may travel back to the area of interest and pollute the simulation result.

The straightforward idea of the wave generation and absorption is to mimic the experimental wave tank, by using a moving boundary to reproduce mechanical wave-makers and modeling the wave absorbing beach to prevent the wave reflections. However, the computational cost can be prohibitive. For this reason, the coupling of potential theory and CFD solvers with the one-way domain decomposition strategy is often used [64, 73, 87].

The simplest one-way domain decomposition method for wave generation and absorption is to impose wave velocity and free surface elevation from the potential wave theories at the inlet and outlet boundaries of the CFD domain [64]. Such approach may suffer from wave reflection problems. A commonly used alternative is the relaxation zone technique [73, 87, 92], in which a blending zone is defined near the boundary to gradually blend the CFD result to the target value.

Relaxation Zone

The relaxation zone technique defines regions where the computed value is gradually blended to the target value using a space-dependent weight function ω as shown in Fig.2.10. The value in

these regions is relaxed as a linear combination of the numerical solution χ_{CFD} and the target value χ_{target}, as follows:

$$\chi = \omega\chi_{target} + (1-\omega)\chi_{CFD} \tag{2.3.24}$$

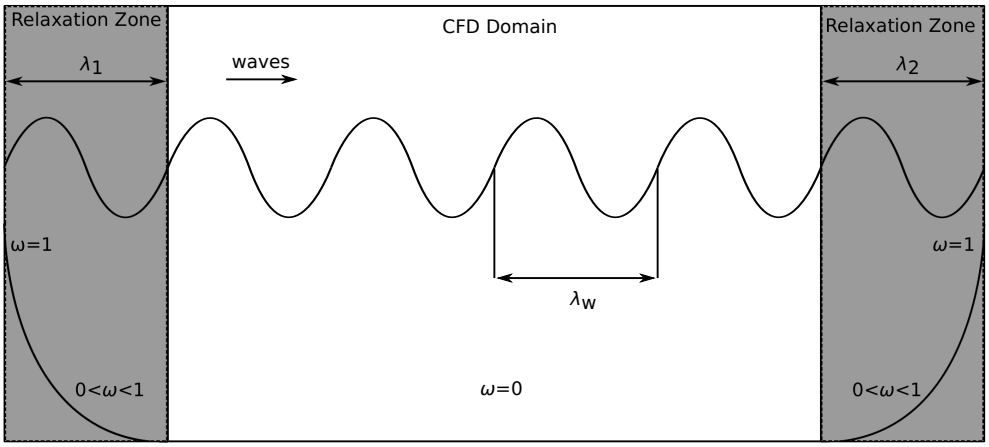

Figure 2.10: Relaxation Zone

The weight function is defined in a way where it is equal to 1 on the boundary and is equal to 0 in the full CFD domain. The present implementation follows the work of Monroy *et al.* [92]. The weight function reads,

$$\omega = -2x^3 + 3x^2 \tag{2.3.25}$$

where x is the non-dimensional distance to the inner boundary of the relaxation zone. $x = 1$ corresponds to the outer boundary of the relaxation zone. $x = 0$ corresponds to the interface between the pure CFD and the relaxation zone.

In the relaxation zone, the values are explicitly relaxed to the target values. The velocity field $\mathbf{u}$ and the VOF field α are blended to their target values. The pressure is not relaxed by this method since pressure is solved at each step to verify the continuity equation.

$$\mathbf{u} = \omega\mathbf{u}_{target} + (1-\omega)\mathbf{u}_{CFD} \tag{2.3.26}$$
$$\alpha = \omega\alpha_{target} + (1-\omega)\alpha_{CFD} \tag{2.3.27}$$

This technique is able to generate incident waves in the wave generation zone, where the target values are set to be the values of incident waves.

It can also be used to prevent wave reflections at the outlet if the target value is set accordingly [29].

- If target values is set to no waves, the entire wave field is damped.
- If the target value is set to the incident waves, the relaxation zone allows the incident wave part travel away at the outlet boundary, and damps the scattered waves to avoid the reflection.

2.4 Two-phase solvers implemented in OpenFOAM

The open source CFD software package OpenFOAM [**?**] is used in the present study. OpenFOAM contains advanced discretization and solution techniques for partial differential equations. Developing new solvers based on the OpenFOAM package allows the use of the state-of-the-art CFD techniques and reduce the developing time drastically.

In this section, the numerical techniques related to developing two-phase flow solvers in OpenFOAM are presented. It first contains the Finite Volume discretization procedure of the governing equations. Secondly, the segregated algorithm to obtain a converged solution of the inter-dependent VOF, momentum, and continuity equations are presented. These techniques are the standard practice of OpenFOAM, and have been already implemented in the native two-phase solver *interFoam*. Many customized two-phase solvers for marine and offshore applications in OpenFOAM, *e.g.*, *waves2Foam* [73] and *foamStar* [92], share the same basic routine but add specific features.

This section uses the two-phase CFD solver *foamStar* as an example. The solver implements the two-phase NS equation. The momentum equation is written in the conservative form with the hydrodynamic pressure (Eqn.(2.3.9)). VOF method is used for the interface capturing.

2.4.1 Finite Volume discretization

This section describes the discretization process in OpenFOAM. It consists of two steps:

- A space discretization step to divide the computational domain into control volumes;
- An equation discretization step to transform the governing equations into an equivalent system of linear algebra equations.

Space discretization

OpenFOAM discretizes the computational domain into unstructured non-overlapped polyhedral control volumes (or cells). Each control volume is closed by an arbitrary number of faces. Each face should be flat and may have an arbitrary number of points and edges(see Fig. 2.11). Each face connects only two neighboring cells or only one if the face locates on the boundary.

OpenFOAM uses a collocated variable arrangement. All the variables are located in the center of the control volumes. After the domain discretization, the continuous field is transformed into a finite number of discretized variables, which are often written as a vector. Each element of a variable vector corresponds to the value in the center of one control volume.

Equation discretization

This section describes briefly how the governing equations are discretized with the standard Finite Volume Method in OpenFOAM. More details can be found in the literature [50, 93].

For convenience purposes, in this section, the sign $\{\cdot\}$ is used to indicate that the terms enclosed are treated implicitly. Otherwise, the terms are evaluated explicitly.

foamStar is presented as example.

VOF equation

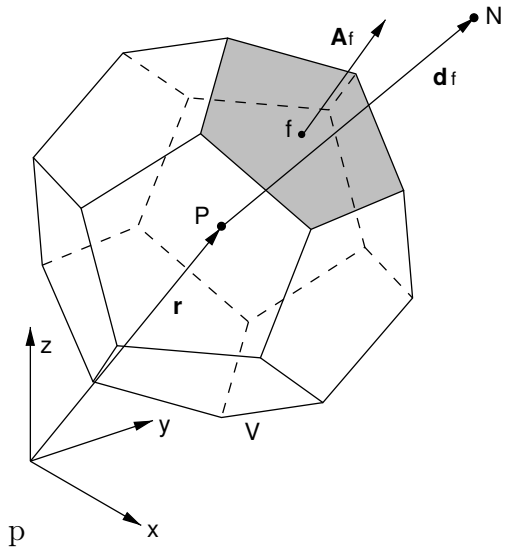

Figure 2.11: A polyhedral control volume (reproduced from the Ph.D. thesis of Vukčević [126])

Equation (2.3.2) is re-written in its conservative form. Both the time derivative term and the convective term are discretized implicitly.

$$\left\{\frac{\partial \alpha}{\partial t}\right\} + \{\nabla.(\mathbf{u}\alpha)\} = 0 \tag{2.4.1}$$

In OpenFOAM, an artificial compression term is added to Eqn.(2.4.1) to avoid the interface smearing [19, 109]. The MUlti-dimensional Limiter for Explicit Solution (MULES) method is used to keep the boundedness of the α field. These techniques are also adopted in the present implementation. The readers are referred to the literature for the implementation details [32].

Momentum equation

The discretized form of the momentum equation (Eqn.(2.3.9)) reads:

$$\left\{\frac{\partial \rho \mathbf{u}}{\partial t}\right\} + \{\nabla.(\rho \mathbf{u}\mathbf{u})\} = -\nabla p_{-\rho g h} + gz\nabla\rho + \{\nabla.(\mu\nabla\mathbf{u})\} + \nabla\mathbf{u}.\nabla\mu \tag{2.4.2}$$

The transient, the convection, and the diffusion terms are discretized implicitly. Leaving the other three terms on the R.H.S. of the equation to be explicitly evaluated.

Note that the pressure terms ($\nabla p_{-\rho g h}$, $gz\nabla\rho$) are evaluated on the cell faces and reconstructed in the cell center. This method is used to improve the pressure-velocity coupling in the collocated variable arrangement in OpenFOAM by mimicking the staggered variable arrangement [109].

Using Eqn.(2.4.2), a linear system is assembled for the velocity variable in each control volume.

$$a_P \mathbf{u}_P + \sum_N a_N \mathbf{u}_N = \mathbf{S} - \nabla p_{-\rho g h} \tag{2.4.3}$$

where the subscript P and N represent the value of the current control volume and the values of its neighbors. The coefficients of the discretized system are a_P and a_N. $\mathbf{S}$ represents the source terms, which contains

- Old time step contribution coming from the time derivative term,
- Explicit source terms besides the pressure gradient
- Possible non-orthogonal correction in the diffusion term.

In OpenFOAM, the solution of Eqn.(2.4.3) is called the momentum prediction. However, the predicted velocity is not guaranteed to be solenoidal. A correction is required using the pressure equation.

Pressure equation

The pressure equation of incompressible flow is not given in the NS equations. It is derived from the continuity equation as follows.

According to Jasak [75], the momentum equation (Eqn.(2.4.3)) is written in a semi-discretized form as

$$a_P \mathbf{u}_P = H(\mathbf{u}) - \nabla p_{-\rho g h} \tag{2.4.4}$$

where the pressure term $\nabla p_{-\rho g h}$ is not discretized at this step following the work of Rhie and Chow [104]. The $H(\mathbf{u})$ contains all the off-diagonal coefficients in the momentum equation matrix multiplied by the neighboring velocity and the source term $\mathbf{S}$ in Eqn.(2.4.3).

$$H(\mathbf{u}) = -\sum_N a_N \mathbf{u}_N + \mathbf{S} \tag{2.4.5}$$

Dividing a_P from both sides of Eqn.(2.4.4) the velocity in the cell center is expressed as:

$$\mathbf{u}_P = \frac{H(\mathbf{u})}{a_P} - \frac{1}{a_P} \nabla p_{-\rho g h} \tag{2.4.6}$$

By interpolating the cell centered velocity $\mathbf{u}_P$, the velocity at the cell face is written as:

$$\mathbf{u}_f = \overline{\mathbf{u}_P} = \overline{\left(\frac{H(\mathbf{u})}{a_P}\right)} - \overline{\left(\frac{1}{a_P}\right)} \{\nabla p_{-\rho g h}\}_f \tag{2.4.7}$$

where $\overline{\cdot}$ symbol denotes the interpolated value on the cell face. Note that the pressure gradient $\nabla p_{-\rho g h}$ is implicitly expressed on the cell face f by using the center pressure of the two neighbor cells, following Rhie and Chow [104].

By integrating the continuity equation (Eqn.(2.3.5)) in a Control Volume (CV), it becomes

$$\int_{CV} \nabla . \mathbf{u} dV = \sum_f \mathbf{A}_f . \mathbf{u}_f = 0 \tag{2.4.8}$$

where $\mathbf{A}_f$ represent the vector of the free surface area.

Using Eqn.(2.4.7) to replace $\mathbf{u}_f$, it becomes

$$\sum_f \mathbf{A}_f . \left(\overline{\left(\frac{H(\mathbf{u})}{a_P}\right)} - \overline{\left(\frac{1}{a_P}\right)} \{\nabla p_{-\rho g h}\}_f \right) = 0 \tag{2.4.9}$$

Finally, by putting the implicit terms on the left side, the pressure equation is written as

$$\sum_f \mathbf{A}_f . \left(\overline{\left(\frac{1}{a_P}\right)} \{\nabla p_{-\rho g h}\}_f \right) = \sum_f \mathbf{A}_f . \overline{\left(\frac{H(\mathbf{u})}{a_P}\right)} \tag{2.4.10}$$

After the $p_{-\rho gh}$ is obtained, the velocity flux F_f at the cell face is corrected to be conservative with

$$F_f = \mathbf{A}_f . \left(\overline{\left(\frac{H(\mathbf{u})}{a_P} \right)} - \overline{\left(\frac{1}{a_P} \right)} \left(\nabla p_{-\rho gh} \right)_f \right) \tag{2.4.11}$$

This conservative velocity flux ($\sum_f F_f = 0$) is used to reconstruct the velocity field $\mathbf{u}$ in the cell center.

2.4.2 Segregated solution algorithm

The three discretized equations (VOF, momentum, and pressure) have inter-dependent matrix coefficients. In OpenFOAM, this inter-equation coupling is treated by a segregated iterative approach called PIMPLE [93]. The PIMPLE algorithm comprises two loops. The inner loop solves the velocity-pressure coupling with the PISO algorithm [71]. The outer loop follows the idea of SIMPLE algorithm [50, 98] to deal with the nonlinear dependency between the velocity field and the free surface position.

Figure 2.12 explains the implementation of the PIMPLE algorithm in the two-phase solver *foamStar*.

1. At the beginning of each time step, one step related to the wave generation is used to update the incident wave properties $\mathbf{u}_{target}$ and α_{target} from external wave models before entering the PIMPLE loop.

2. In the PIMPLE loop, the Volume of Fluid field α (Eqn.(2.3.2)) is solved; the fluid properties are updated using the new VOF field (Eqn. (2.3.3) and (2.3.4)).

3. In the PISO loop:

   a) The velocity field is solved (Eqn.(2.4.3)) in the momentum predictor step.

   b) The pressure equation of $p_{-\rho gh}$ (Eqn.(2.4.10)) is solved.

   c) The velocity field is updated from the conservative velocity flux.

4. The solution is blended to the target values in the relaxation zones to attenuate the scattered waves in the far-field (Eqn. (2.3.26) and (2.3.27))

5. Outer iterations are made to achieve the convergence of the VOF, the velocity, and the pressure before stepping to the next time.

2.5 Closure

This chapter has provided a basic theoretical background before developing the two-phase SWENSE method in Chapter 3.

The principal idea of the Spectral Wave Explicit Navier-Stokes Equations (SWENSE) method has been explained. In this method, the total flow is decomposed into an incident and a complementary field via the functional decomposition. The complementary field represents the influence caused by the structure and the viscous effects. The complementary variables are governed by the SWENS equations, which is derived from the Navier-Stokes equations and the Euler equations. The single-phase SWENS equations in a fully submerged computational

domain has been derived to show the mathematical procedure. The advantage of the SWENSE method in maintaining the incident wave kinematics is proved by examining the mathematical property of the single-phase SWENS equations.

The spectral wave models have been shown. The stream-function wave theory and the Higher-Order Spectral (HOS) method are selected to simulate the regular and irregular incident waves. The ability of the spectral wave models to provide the incident wave solution satisfying the Euler equations at an arbitrary position (even above the incident free surface), has been highlighted as the key advantage in the context of the SWENSE method. This advantage helps to adjust the definition zone of the incident wave problem according to the total free surface position so that a single set of SWENS equations can be applied in the entire CFD computational domain. The limitations of the spectral methods have been pointed out, including the requirement of a rectangular computational domain and the limitation on the non-breaking incident wave.

In the end, the mathematical models of the two-phase flow and their implementation in a CFD solver *foamStar* have been explained. The mathematical models include the Volume of Fluid method for the interface capturing and the two-phase Navier-Stokes (NS) equations. At first, the NS equations have been presented in the one-fluid form, with both the conservative and the non-conservative versions. The Ghost Fluid Method to model the two fluids separately to improve the accuracy and stability at the interface has also been reviewed. The implementation of the mathematical models in *foamStar* has been shown, explaining the standard Finite Volume method and the segregated solution algorithm PIMPLE.

The above mentioned mathematical models and numerical techniques constitute the theoretical foundation of the present work and shall be used in the development of the new two-phase SWENSE method. These new developments will be presented in Chapter 3.

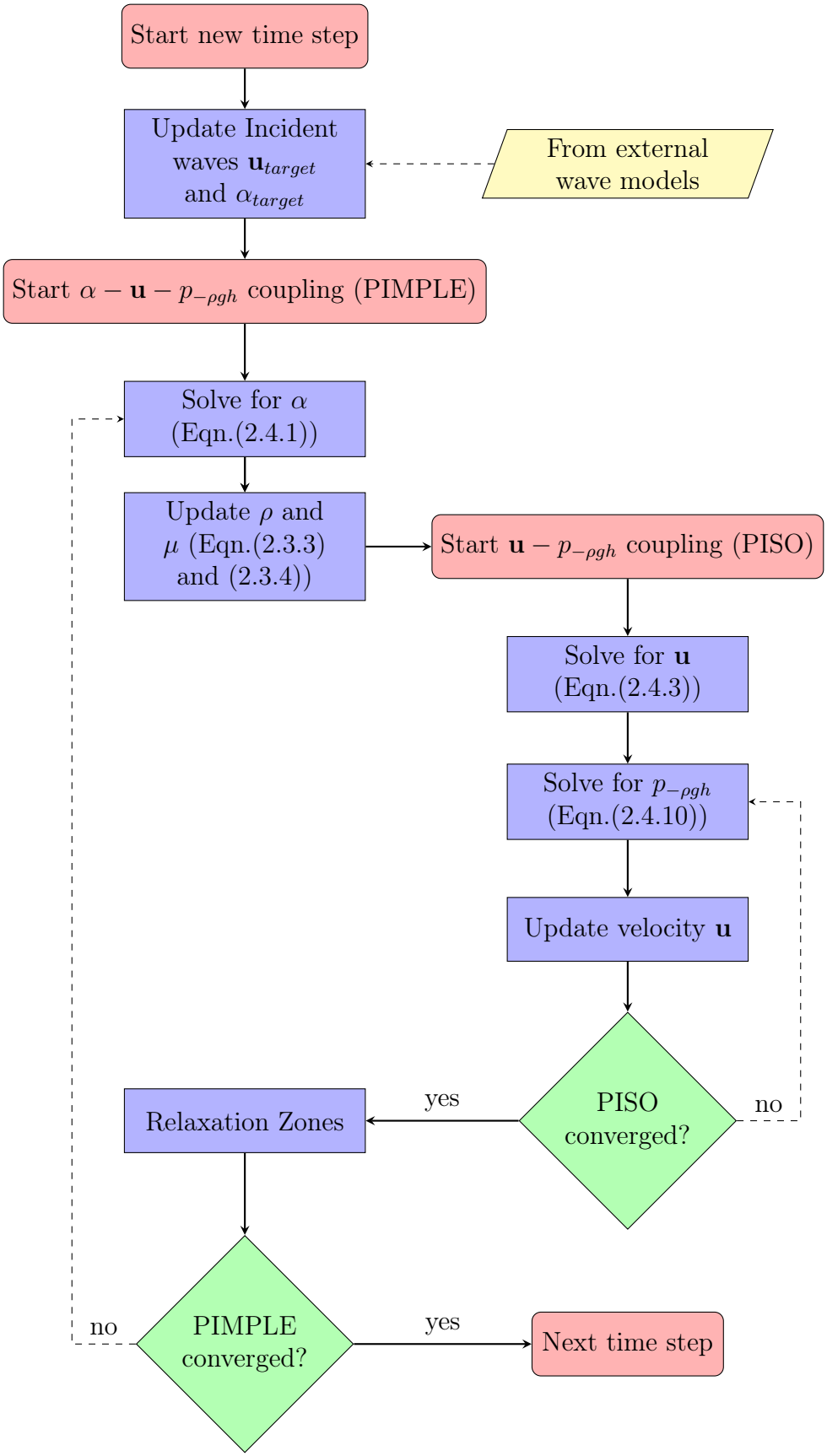

Figure 2.12: PIMPLE algorithm in *foamStar*

Chapter 3

Two-phase SWENSE method

This chapter presents the main research efforts in this thesis regarding the development of the two-phase SWENSE method. This chapter is divided into three parts, including

- Sections 3.1 - 3.6: the mathematical models of the two-phase SWENSE method;
- Section 3.8: the implementation of two-phase SWENSE solvers in OpenFOAM;
- Section 3.9: an illustrative wave propagation test case.

Firstly, the mathematical models of the two-phase SWENSE method are presented in Section 3.1 - 3.6. This part explains the difficulties in extending the original SWENSE method (single-phase) to two-phase and proposes solution to overcome these difficulties.

In Section 3.1, the differences between a single-phase CFD solver and a two-phase one are listed. The requirements and challenges on developing the mathematical models for the two-phase SWENSE method are explained.

In Section 3.2, a first attempt to develop the two-phase SWENS equations is shown, where the functional decomposition procedure of the single-phase SWENSE method is applied directly. However, the resulting equations fails to keep the benefit of the SWENSE method and thus is abandoned. Then, the reason of such a failure is analyzed.

In order to overcome the difficulties, Section 3.3 proposes an extra step before applying the functional decomposition. In this step, the Euler equations, describing the incident wave fields, are reformulated in a modified version.

In Section 3.4 the two-phase SWENS equations are derived, both in the conservative and the non-conservative form. The properties of the derived governing equations are analyzed.

In Section 3.5, the Ghost Fluid Method (GFM) is applied to improve the interface stability, deriving a third set of governing equations.

Section 3.6 explains the boundary condition used in the two-phase SWENSE method. Most boundary conditions are the same with the single-phase method. Only the atmosphere boundary condition is new, since it is not required by the single-phase method. Different possible definitions of such a boundary condition and their influence are discussed.

These sections (Section 3.1-3.6) explain the development of the mathematical models of the two-phase SWENSE method in this thesis. In Section 3.7, the proposed method is compared with another two-phase SWENSE method, developed previously by Vukčević *et al.* [127].

The second part contains only Section 3.8. In this section, the mathematical models are implemented in OpenFOAM to develop a two-phase SWENSE solver, *foamStar-SWENSE*.

The last part of this chapter (Section 3.9) tests the two-phase SWENSE method with an illustrative wave propagation test case. *foamStar-SWENSE* is compared with *foamStar* and a reference potential flow solution. A comparison between the conservative form, the non-conservative form, and the GFM form of the two-phase SWENS equations is also provided.

3.1 Problem statement: from single-phase to two-phase

The original SWENSE method proposed by Ferrant *et al.* [49] only considered the single-phase case. It was implemented in a single-phase RANSE solver *ICARE* developed in LHEEA Lab, using the Finite Difference method. *ICARE* models the water under the free surface only. The free surface is either tracked with the free surface elevation function [83, 90], or captured by the Level-Set method [102]. The free surface is treated as a deforming boundary where the free surface boundary conditions are applied.

The difficulties hindering the direct use of single-phase SWENS method with two-phase solvers lie in the fact that the two-phase solvers use different computational domains and boundary conditions. These differences are shown in Fig. 3.1:

- Computational domain: In the single-phase SWENSE method, the governing equations are defined under the free surface only (the gray region); In the two-phase SWENSE method, the computational domain also contains the air phase.

- Boundary condition: In the single-phase SWENSE method, free surface boundary conditions are applied on the real free surface position (on the dashed curve η). In a two-phase solver, it is no more possible to define a free surface boundary condition. An atmosphere boundary condition should be applied on the top of the domain to mimic a connected-to-air boundary.

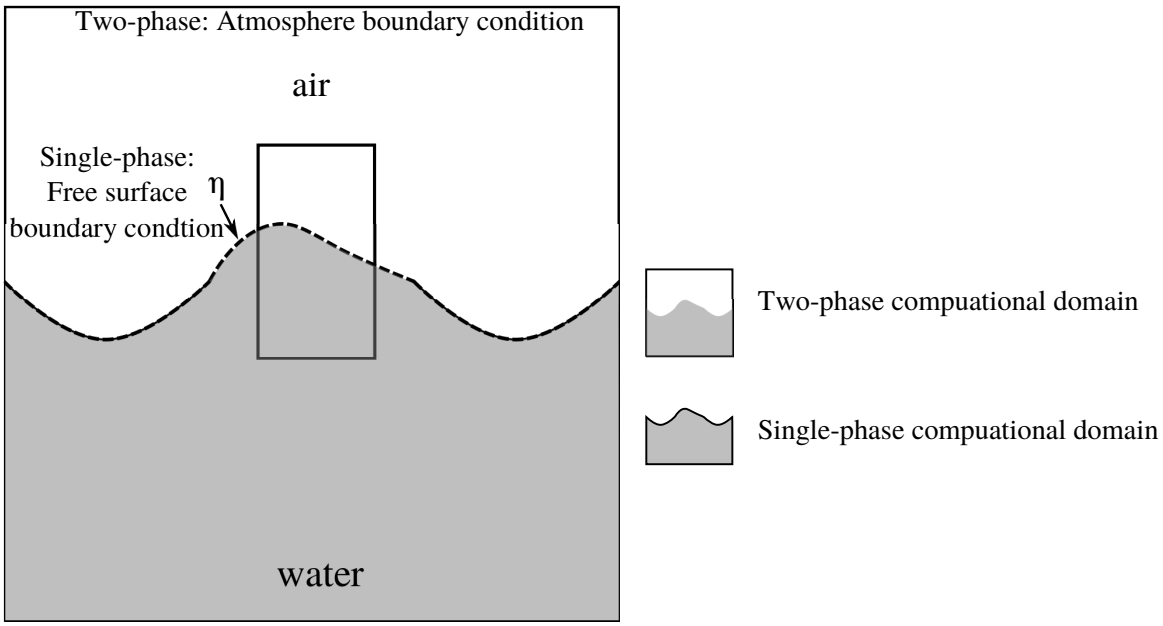

Figure 3.1: Difference on the computational domain of a single-phase and a two-phase solver. The dashed black curve represents the water free surface.

As a result, the development of the two-phase SWENSE method consists of (1) an extension of the computational domain and (2) a definition of a new atmosphere boundary condition.

The first work, *i.e.*, the extension of the computational domain, requires a definition in the air of the three fields used by the SWENSE method (the total fields, the incident fields, and the complementary fields), as well as their governing equations.

- For the total field: the two-phase NS equations are already defined in both water and air and do not need any extension. The total field can be constructed in the entire domain once the incident and the complementary fields are obtained.

- For the incident field: both the incident field and the Euler equations are defined in the water. Fortunately, the spectral methods can extend them to an arbitrary domain (see Section 2.2.5). In single-phase SWENSE method, the incident fields are extended to the total free surface position; in the present two-phase method, they are extended in the air. Such extension provides a smooth incident velocity across the free surface, but will lead to unrealistic incident fields in the air, *e.g.*, oscillating *incident wind* velocity. This choice is valid as long as the air effects are negligible, which is true for most wave-structure problems.

- For the complementary field: The SWENS equations can be obtained from the two-phase NS equations and the extended Euler equations. CFD solvers are used to find the complementary fields by solving the SWENS equations.

Secondly, an additional atmosphere boundary condition should be defined so that the SWENS equations can be solved with the CFD solvers.

3.1.1 Objective

The capacity use coarse mesh for incident wave propagation need to be kept in the new two-phase SWENSE method to speed up the CFD solvers.

As has been explained in Sect. 2.1.3, this property is ensured by the governing equations in the single-phase SWENSE method. More specifically, the source terms in the SWENS momentum equation are equal to zero in pure incident wave propagation cases. No complementary velocity or pressure will be generated. As a result, the total velocity field is equal to the incident potential wave solution, regardless of the CFD mesh.

To make the two-phase SWENSE method able to use coarse mesh, its governing equations requires the same property: the source terms of the momentum equation should be equal to zero for pure incident wave propagation. As a result, this requirement guided the development of the two-phase method, whenever a choice should be made.

3.2 Direct extension

This section shows an attempt to derive the two-phase SWENS equations by applying the functional decomposition procedure directly.

In this example, the one-fluid form two-phase NS equations in non-conservative form is used as the governing equations for the total field.

3.2.1 Two-phase Navier-Stokes equations

The two-phase NS equations in non-conservative form are recalled as follows,

$$\begin{aligned}
\rho &= \alpha\rho_w + (1-\alpha)\rho_a \\
\mu &= \alpha\mu_w + (1-\alpha)\mu_a \\
\frac{\partial\alpha}{\partial t} + \mathbf{u}.\nabla\alpha &= 0 \\
\nabla.\mathbf{u} &= 0 \\
\frac{\partial\mathbf{u}}{\partial t} + \mathbf{u}.\nabla\mathbf{u} &= -\frac{\nabla p}{\rho} + \mathbf{g} + \frac{\nabla.\left(\mu\left(\nabla\mathbf{u} + \nabla\mathbf{u}^T\right)\right)}{\rho}
\end{aligned}$$

where w and a stand for the properties in the water and in the air respectively and the α denotes the VOF field. Note that the total pressure p is used here instead of the dynamic pressure $p_{-\rho gh}$, since the pressure p shall be subtracted later by the incident pressure p_I, which contains also the hydrostatic part.

3.2.2 Extended Euler equations

With the spectral methods, the incident wave fields are extended in the entire computational domain directly. After this extension, the Euler equations (Eqn. (2.1.4) and (2.1.5)) are valid in the entire computational domain, which is recalled as follows,

$$\begin{aligned}
\rho_I &= \rho_w \\
\nabla.\mathbf{u}_I &= 0 \\
\frac{\partial\mathbf{u}_I}{\partial t} + \mathbf{u}_I.\nabla\mathbf{u}_I &= -\frac{\nabla p_I}{\rho_I} + \mathbf{g}
\end{aligned}$$

3.2.3 SWENS equations

Since the two-phase NS equations and the extended Euler equations are both defined in the entire computational domain, it is possible to apply the functional decomposition procedure to derive the SWENS equations, by subtracting the Euler equations from the two-phase NS equations. The resulting equations are,

$$\nabla.\mathbf{u}_C = 0 \tag{3.2.1}$$

$$\frac{\partial\mathbf{u}_C}{\partial t} + \mathbf{u}_C.\nabla\mathbf{u}_C + \mathbf{u}_C.\nabla\mathbf{u}_I + \mathbf{u}_I.\nabla\mathbf{u}_C = -\frac{\nabla p_C}{\rho} + \frac{\nabla.\left(\mu\left(\nabla\mathbf{u} + \nabla\mathbf{u}^T\right)\right)}{\rho} + \frac{\nabla p_I}{\rho_I} - \frac{\nabla p_I}{\rho} \tag{3.2.2}$$

with the notation of $\mathbf{u}_C = \mathbf{u} - \mathbf{u}_I$ and $p_C = p - p_I$.

The viscous stress term can be decomposed as follows,

$$\nabla.\left(\mu\left(\nabla\mathbf{u} + \nabla\mathbf{u}^T\right)\right) = \nabla.\left(\mu\left(\nabla\mathbf{u}_C + \nabla\mathbf{u}_C^T\right)\right) + \nabla.\left(\mu\left(\nabla\mathbf{u}_I + \nabla\mathbf{u}_I^T\right)\right) \tag{3.2.3}$$

and can be simplified with $\nabla.\mathbf{u}_I = 0$ and $\nabla\times\mathbf{u}_I = 0$, to make it

$$\begin{aligned}
\nabla.\left(\mu\left(\nabla\mathbf{u}_I + \nabla\mathbf{u}_I^T\right)\right) &= 2\nabla.\left(\mu\nabla\mathbf{u}_I^T\right) \\
&= 2\left(\mu\nabla\left(\nabla.\mathbf{u}_I\right) + \nabla\mathbf{u}_I.\nabla\mu\right) \\
&= 2\nabla\mathbf{u}_I.\nabla\mu.
\end{aligned} \tag{3.2.4}$$

The resulting momentum equation is written as,

$$\frac{\partial \mathbf{u}_C}{\partial t}+\mathbf{u}_C.\nabla\mathbf{u}_C+\mathbf{u}_C.\nabla\mathbf{u}_I+\mathbf{u}_I.\nabla\mathbf{u}_C=-\frac{\nabla p_C}{\rho}+\frac{\nabla.\left(\mu\left(\nabla\mathbf{u}_C+\nabla\mathbf{u}_C^T\right)\right)}{\rho}+\underbrace{\frac{2\nabla\mathbf{u}_I.\nabla\mu}{\rho}}+\underline{\underline{\frac{\nabla p_I}{\rho_I}-\frac{\nabla p_I}{\rho}}} \tag{3.2.5}$$

Extra terms in this momentum equation, comparing with the single-phase SWENSE momentum equation, are underlined. The influence of them will be examined.

3.2.4 Influence of the extra viscous term

The extra viscous term

$$\frac{2\nabla\mathbf{u}_I.\nabla\mu}{\rho} \tag{3.2.6}$$

is generally not zero mathematically, since a viscosity gradient may exist ($\nabla\mu \neq \mathbf{0}$). In a two-phase flow of Newtonian fluids, this term has non-zero values only at the interface, since

$$\nabla\mu \begin{cases} = \mathbf{0} & \text{out of the interface} \\ \neq \mathbf{0} & \text{on the interface} \end{cases} \tag{3.2.7}$$

However, this term is dropped off in the present work, for the following reasons:

- In the point of view of the SWENSE method, if this source term is kept, it makes the source term in the momentum equations not equal to zero in a pure incident wave propagation case, and thus fails to meet the requirement of the SWENSE method, *i.e.*, the source terms in the SWENSE momentum equation should be equal to zero in a pure incident wave propagation case. (see Section 2.1.3).
- Dropping off this term will not have a large influence on the simulation result becasue the effects of the interface viscous term is much smaller than the pressure and gravity contribution and does not need to be well resolved (For example, two-phase CFD simulations for classical marine and offshore applications often do not require meshes to capture the free surface boundary layer).

3.2.5 Influence of the extra pressure terms

The extra pressure terms

$$\frac{\nabla p_I}{\rho_I}-\frac{\nabla p_I}{\rho} \tag{3.2.8}$$

have different values in water and in air:

- In water, these terms are equal to zero and the resulting governing equation is the same with the single-phase version, since

$$\rho_I = \rho = \rho_w \text{ (in the water)} \tag{3.2.9}$$

- In air, these terms are equal to non-zero values. Since the extended incident density equals to the water density, and the ρ in two-phase flow depends on the free surface position.

If we assume the density ratio of water and air equals to 1000, the underline terms are equal to:

$$\begin{aligned}\frac{\nabla p_I}{\rho_I} - \frac{\nabla p_I}{\rho} &= \frac{\nabla p_I}{\rho_w} - \frac{\nabla p_I}{\rho_a} \\ &= \frac{1}{1000}\frac{\nabla p_I}{\rho_a} - \frac{\nabla p_I}{\rho_a} \\ &= -\frac{999}{1000}\frac{\nabla p_I}{\rho_a} \text{ (in the air)}\end{aligned} \tag{3.2.10}$$

The non-zero values in air of these underlined terms make this governing equation less interesting, since:

- Firstly, the source terms themselves need a good CFD mesh to be evaluated accurately.
- Secondly, the value of these source terms is so large that the simulation may be unstable. It equals approximately 1000 times the acceleration of a water particle given by the potential wave theory.

$$\frac{999}{1000}\frac{\nabla p_I}{\rho_a} \approx \frac{\nabla p_I}{\rho_a} = 1000\frac{\nabla p_I}{\rho_I} = -1000(\frac{D\mathbf{u}}{Dt} - \mathbf{g}) \tag{3.2.11}$$

- Thirdly and the most importantly, for a pure incident wave propagation problem, the source term in the SWENSE momentum equation is non-zero in the air, which fails to meet the expectation of the SWENSE method (see Section 2.1.3). Moreover, the flow in the air can also influence the simulation results in the water, so that the incident waves can be affected.

To conclude, these extra pressure terms show that the direct extension of incident field in the air is unsuitable for the two-phase SWENSE method.

3.3 Modified Euler equations

In the previous section, it is found that a serious problem of extending the incident wave field in the air directly is that the density is mismatched in the Euler equations and in the two-phase Navier-Stokes equations. This density mismatch makes the underlined pressure source terms in Eqn. (3.2.5) cannot be canceled out.

In this section, we propose an approach to modify the Euler equations to use the density according to the actual free surface position, to vanish the underlined source terms in Eqn. (3.2.5).

Define a modified incident pressure p_I^* is introduced, as follows,

$$p_I^* = \rho\frac{p_I}{\rho_I} \tag{3.3.1}$$

where ρ is the density field in the two-phase flow, and ρ_I is the density of incident waves (water).

Take the gradient on both side, yielding:

$$\nabla p_I^* = \nabla(\frac{\rho}{\rho_I}p_I) = \frac{p_I}{\rho_I}\nabla\rho + \frac{\rho}{\rho_I}\nabla p_I \tag{3.3.2}$$

and

$$\frac{\nabla p_I}{\rho_I} = \frac{\nabla p_I^*}{\rho} - \frac{p_I}{\rho_I}\frac{\nabla \rho}{\rho} \tag{3.3.3}$$

The Euler momentum equation (Eqn. (2.1.5)) is then written in a modified version with p_I^*. It reads :

$$\frac{\partial \mathbf{u}_I}{\partial t} + \mathbf{u}_I.\nabla \mathbf{u}_I = -\frac{\nabla p_I^*}{\rho} + \frac{p_I}{\rho_I}\frac{\nabla \rho}{\rho} + \mathbf{g} \tag{3.3.4}$$

In this modified version, the Left-Hand Side (L.H.S.) has the same form as its original version (Eqn. (2.1.5)). The right hand side (R.H.S.) is modified. It contains a term related to the pressure gradient, a term related to the gradient of the density, and a gravity acceleration term.

- The pressure gradient term $\frac{\nabla p_I^*}{\rho}$ is written with the modified incident pressure p_I^*. The denominator of this term is written with the real density ρ of the two-phase flow.
- The term related to the gradient of the density $\frac{p_I}{\rho_I}\frac{\nabla \rho}{\rho}$. In incompressible two-phase flow, this term equals to zero in both phases, and has non-zero value on the interface only.

The modified momentum equation (Eqn. (3.3.4)) are mathematical equivalent to the original one (Eqn. (2.1.5)). So the solution of the original Euler equations ($\mathbf{u}_I$, p_I) still satisfy the modified Euler equations. The incident pressure (p_I) is then transformed to p_I^* using Eqn. (3.3.1). In this modified Euler momentum equation, the denominator of the pressure gradient term is in accordance with the two-phase Navier-Stokes equations, which overcomes the problem of the mismatched density when developing the two-phase SWENS equations.

3.4 Two-phase SWENS equations: one-fluid form

In this section, the one-fluid form of two-phase SWENS equations is developed. Similar to the one-fluid form of two-phase NS equations, the two-phase flow is modeled as a single mixture fluid of both water and air. The equations are derived both in the conservative and the non-conservative form. The properties of the derived governing equations are analyzed in the end.

3.4.1 Non-conservative two-phase SWENS equations

This part develops the two-phase SWENS equations in its non-conservative form.

The non-conservative form two-phase Navier-Stokes equations and the non-conservative form Euler equations (modified form) are used in this part.

Continuity Equation

The same continuity equation is obtained as in single-phase SWENSE method.

$$\nabla.\mathbf{u}_C = 0 \tag{3.4.1}$$

Momentum Equation

The momentum equation is derived by subtracting the momentum equation of the modified Euler equations (Eqn. (3.3.4)) from the Navier-Stokes momentum equation (Eqn. (2.3.6)).

Subtract Eqn. (3.3.4) from Eqn. (2.3.6) and use the notion of $p_C = p - p_I^*$, the two-phase SWENSE momentum equation written with the complementary variables is obtained as:

$$\frac{\partial \mathbf{u}_C}{\partial t} + \mathbf{u}.\nabla\mathbf{u}_C + \mathbf{u}_C.\nabla\mathbf{u}_I = -\frac{\nabla p_C}{\rho} - \frac{p_I}{\rho_I}\frac{\nabla\rho}{\rho} + \frac{\nabla.\left(\mu\left(\nabla\mathbf{u}_C + \nabla\mathbf{u}_C^T\right)\right)}{\rho} \tag{3.4.2}$$

The viscous term is obtained with the simplification mentioned in Section 3.2.4.

3.4.2 Conservative two-phase SWENS equations

The conservative two-phase SWENS equations can be obtained in a similar procedure. However, an additional step is necessary to transform the modified Euler equations.

Euler Equations

Take the non-conservative momentum equation of the modified Euler equation and multiply by ρ on both sides, yielding:

$$\rho(\frac{\partial \mathbf{u}_I}{\partial t} + \mathbf{u}_I.\nabla\mathbf{u}_I) = -\nabla p_I^* + \frac{p_I}{\rho_I}\nabla\rho + \rho\mathbf{g} \tag{3.4.3}$$

Momentum equation

The conservative form Navier-Stokes equations for two-phase flow is recalled here

$$\frac{\partial \rho\mathbf{u}}{\partial t} + \nabla.(\rho\mathbf{u}\mathbf{u}) = -\nabla p + \rho\mathbf{g} + \nabla.\left(\mu\left(\nabla\mathbf{u} + \nabla\mathbf{u}^T\right)\right) \tag{3.4.4}$$

The L.H.S. of the Euler equation (Eqn. (3.4.3)) can be transformed to

$$\rho(\frac{\partial \mathbf{u}_I}{\partial t} + \mathbf{u}_I.\nabla\mathbf{u}_I) = \frac{\partial \rho\mathbf{u}_I}{\partial t} - \mathbf{u}_I\frac{\partial\rho}{\partial t} + \nabla.(\rho\mathbf{u}_I\mathbf{u}_I) - \mathbf{u}_I\nabla.(\rho\mathbf{u}_I) \tag{3.4.5}$$

Use the L.H.S. of Eqn. (3.4.4) minus Eqn. (3.4.5), yielding:

$$\begin{aligned}
&\frac{\partial \rho\mathbf{u}}{\partial t} + \nabla.(\rho\mathbf{u}\mathbf{u}) - \frac{\partial \rho\mathbf{u}_I}{\partial t} + \mathbf{u}_I\frac{\partial\rho}{\partial t} - \nabla.(\rho\mathbf{u}_I\mathbf{u}_I) + \mathbf{u}_I\nabla.(\rho\mathbf{u}_I) \\
=&\frac{\partial \rho\mathbf{u}_C}{\partial t} + \nabla.(\rho\mathbf{u}\mathbf{u}_C) + \rho\mathbf{u}_C.\nabla\mathbf{u}_I + \mathbf{u}_I\left(\frac{\partial\rho}{\partial t} + \nabla.(\rho\mathbf{u}_I) + \nabla.(\rho\mathbf{u}_C)\right) \\
=&\frac{\partial \rho\mathbf{u}_C}{\partial t} + \nabla.(\rho\mathbf{u}\mathbf{u}_C) + \rho\mathbf{u}_C.\nabla\mathbf{u}_I
\end{aligned} \tag{3.4.6}$$

The simplification of Eqn. (3.4.6) is achieved with the mass conservation

$$\frac{\partial\rho}{\partial t} + \nabla.(\rho\mathbf{u}) = 0 \tag{3.4.7}$$

Subtract the R.H.S of Eqn. (3.4.4) and Eqn. (3.4.3), yielding:

$$\begin{aligned} &-\nabla p+\rho\mathbf{g}+\nabla.\left(\mu\left(\nabla\mathbf{u}+\nabla\mathbf{u}^{T}\right)\right)-\left(-\nabla p_{I}^{*}+\frac{p_{I}}{\rho_{I}}\nabla\rho+\rho\mathbf{g}\right)\\ =&-\nabla p_{C}-\frac{p_{I}}{\rho_{I}}\nabla\rho+\nabla.\left(\mu\left(\nabla\mathbf{u}_{C}+\nabla\mathbf{u}_{C}^{T}\right)\right)\end{aligned} \tag{3.4.8}$$

The viscous term is obtained with the simplification mentioned in Section 3.2.4.

$$\frac{\partial\rho\mathbf{u}_{C}}{\partial t}+\nabla.(\rho\mathbf{u}\mathbf{u}_{C})+\rho\mathbf{u}_{C}.\nabla\mathbf{u}_{I}=-\nabla p_{C}-\frac{p_{I}}{\rho_{I}}\nabla\rho+\nabla.\left(\mu\left(\nabla\mathbf{u}_{C}+\nabla\mathbf{u}_{C}^{T}\right)\right) \tag{3.4.9}$$

3.4.3 Volume of Fluid transport equation

The VOF field is not decomposed in the present method. Since splitting the VOF field into an incident and a complementary part is not straightforward. It is especially difficult to define the bound of the complementary field so that the total VOF field is bounded between 0 and 1. The transport equation for VOF is the same as the two-phase Navier-Stokes equations. It reads

$$\frac{\partial\alpha}{\partial t}+\mathbf{u}.\nabla\alpha=0 \tag{3.4.10}$$

where $\mathbf{u}$ is the total velocity solution reconstructed by using $\mathbf{u}=\mathbf{u}_{I}+\mathbf{u}_{C}$.

The fluid properties are defined with the VOF field in a standard manner:

$$\rho=\alpha\rho_{w}+(1-\alpha)\rho_{a} \tag{3.4.11}$$

$$\mu=\alpha\mu_{w}+(1-\alpha)\mu_{a} \tag{3.4.12}$$

3.4.4 Properties of the two-phase SWENS equations

This part discusses the property of the proposed two-phase SWENSE method. Two properties of the governing equation is mathematically proven. They are :

1. The ability to regress to the Navier-Stokes equations.
2. The ability to keep the total solution equal to the incident wave solution when no structure is present in the computational domain, regardless of the mesh used.

Since the conservative and the non-conservative forms are equivalent. These two properties are only demonstrated with the non-conservative form as follows.

Proposition 1. *The SWENSE momentum equation (Eqn.* (3.4.2)*) is equivalent to Navier-Stokes momentum equation (Eqn.* (2.3.8)*) if the incident wave part is defined to be no waves.*

Proof. Let the incident wave field to be zero, i.e.,

$$\mathbf{u}_{I}=0 \tag{3.4.13}$$

and the incident pressure is equal to the hydrostatic pressure

$$\frac{p_{I}}{\rho_{I}}=-gz \tag{3.4.14}$$

Thus, Eqn. (3.4.2) can be written as:

$$\frac{\partial \mathbf{u}_C}{\partial t} + \mathbf{u}_C.\nabla \mathbf{u}_C = -\frac{\nabla p_C}{\rho} + gz\frac{\nabla \rho}{\rho} + \frac{\nabla.\left(\mu\left(\nabla \mathbf{u}_C + \nabla \mathbf{u}_C^T\right)\right)}{\rho} \tag{3.4.15}$$

transform this equation with the relations below

$$\mathbf{u}_C = \mathbf{u} - \mathbf{u}_I = \mathbf{u} \tag{3.4.16}$$

$$p_C = p_{\_\rho gh} \tag{3.4.17}$$

yielding,

$$\frac{\partial \mathbf{u}}{\partial t} + \mathbf{u}.\nabla \mathbf{u} = -\frac{\nabla p_{\_\rho gh}}{\rho} + gz\frac{\nabla \rho}{\rho} + \frac{\nabla.\left(\mu\left(\nabla \mathbf{u} + \nabla \mathbf{u}^T\right)\right)}{\rho} \tag{3.4.18}$$

Eqn. (3.4.18) and (2.3.8) are identical, showing the SWENSE momentum equation (3.4.2) can regress to the two-phase Navier-Stokes equation (2.3.8) if there is no incident waves.

□

Proposition 2. *The incident wave kinematics is maintained by using Eqn.* (3.4.2)*, i.e., in the case where incident waves propagate without any obstacle in the computational domain,* $\mathbf{u}_C$ *and* p_C *remain zero.*

Proof. In the case of pure incident wave simulation, the initial value of the complementary fields are zero, *i.e.*,

$$\mathbf{u}_C(\mathbf{x}, t=0) = 0 \tag{3.4.19}$$

$$p_C(\mathbf{x}, t=0) = 0 \tag{3.4.20}$$

The last term in Eqn. (3.4.2) is equal to zero in the entire computational domain.

$$\frac{p_I}{\rho_I}\frac{\nabla \rho}{\rho} = 0 \tag{3.4.21}$$

	On the incident free surface	elsewhere
p_I	0	non-zero
$\nabla\rho$	non-zero	0
$\frac{p_I}{\rho_I}\frac{\nabla\rho}{\rho}$	0	0

Using the above conditions, Eqn. (3.4.2) is simplified to

$$\frac{\partial \mathbf{u}_C}{\partial t} + \cancelto{0}{\mathbf{u}.\nabla \mathbf{u}_C} + \cancelto{0}{\mathbf{u}_C.\nabla \mathbf{u}_I} = -\frac{\nabla p_C}{\rho}^{0} - \frac{p_I}{\rho_I}\frac{\nabla \rho}{\rho}^{0} + \frac{\nabla.\left(\mu\left(\nabla \mathbf{u}_C + \nabla \mathbf{u}_C^T\right)\right)}{\rho}^{0} \tag{3.4.22}$$

$$\frac{\partial \mathbf{u}_C}{\partial t} = 0 \tag{3.4.23}$$

The complementary velocity field $\mathbf{u}_C$ remains zero, and so does the pressured field p_C. Eqn. (3.4.2) maintains the kinematics of the incident waves, regardless of CFD mesh quality.

□

The proof of the second properties also justifies the choice of dropping off the extra viscous term ($\frac{2\nabla \mathbf{u}_I.\nabla \mu}{\rho}$) in Section 3.2.4. If that term is kept, the second properties is no more valid.

3.5 SWENS equations: Ghost Fluid Method

In the previous section, the two-phase SWENS equations are written in the one-fluid form. Similar to the two-phase NS equations, the exact solutions of these equations contain discontinuities due to the sharp interface, including,

- A discontinuity on the gradient of the pressure field due to the difference between the fluid densities across the interface. The gradient of pressure (∇p_C) should be approximately 1000 times smaller in the air phase than that on the water side.
- A discontinuity in the dynamic pressure p_C also appears. This discontinuity is due to the gradient of density $\nabla\rho$. This term is non-zero on the interface, and results in a jump of $\frac{p_I}{\rho_I}$ on the dynamic pressure field p_C at the interface position.

In this thesis, the two-phase SWENS equations are also proposed in a Ghost Fluid Method (GFM) form, to help the CFD solver keep the discontinuities in the numerical solution. In this section, the governing equations of the two-phase SWENSE method are derived in the GFM framework with two steps.

- Establish separately in each fluid the SWENS equations with the corresponding properties of the fluid;
- Connect the variables (pressure, velocity) in the two set of equations on the common interface.

3.5.1 Single-phase SWENS equations in each phase

In the water

The SWENS equations are obtained by subtracting the Euler equations from the single-phase Navier-Stokes equations. It yields,

$$\nabla.\mathbf{u}_C = 0 \tag{3.5.1}$$

$$\frac{\partial \mathbf{u}_C}{\partial t} + \mathbf{u}_C.\nabla\mathbf{u}_C + \mathbf{u}_C.\nabla\mathbf{u}_I + \mathbf{u}_I.\nabla\mathbf{u}_C = -\frac{\nabla p_C}{\rho_w} + \nu_w\nabla^2\mathbf{u}_C \tag{3.5.2}$$

where $\mathbf{u}_C = \mathbf{u} - \mathbf{u}_I$ and $p_C = p - p_I = p - p_I^*$, since $p_I = p_I^*$ in the water. The viscous term is obtained by cancel out the incident part $\nu\nabla^2\mathbf{u}_I = 0$ (see Section 2.1.2).

In the air

The Euler equations in the air are modified with the notion of p_I^*.

$$p_I^* = \rho_a\frac{p_I}{\rho_w} \tag{3.5.3}$$

The Euler equations are modified as

$$\nabla.\mathbf{u}_I = 0 \tag{3.5.4}$$

$$\frac{\partial \mathbf{u}_I}{\partial t} + \mathbf{u}_I.\nabla\mathbf{u}_I = -\frac{\nabla p_I^*}{\rho_a} + \mathbf{g} \tag{3.5.5}$$

The term related to the interface disappears since it is assumed that the computational domain contains only air.

Subtract the modified Euler equations from the single-phase Navier-Stokes equations in the air, yielding:

$$\nabla.\mathbf{u}_C = 0 \tag{3.5.6}$$

$$\frac{\partial \mathbf{u}_C}{\partial t} + \mathbf{u}_C.\nabla\mathbf{u}_C + \mathbf{u}_C.\nabla\mathbf{u}_I + \mathbf{u}_I.\nabla\mathbf{u}_C = -\frac{\nabla p_C}{\rho_a} + \nu_a\nabla^2\mathbf{u}_C \tag{3.5.7}$$

where $\mathbf{u}_C = \mathbf{u} - \mathbf{u}_I$ and $p_C = p - p_I^*$.

3.5.2 Interface conditions

Define $[\chi] = \chi_a - \chi_w$ the jump at interface for any quantity χ. Following [127], we assume the pressure p is continuous at the interface, so that

$$[p] = 0 \tag{3.5.8}$$

$$[p_C] + [p_I^*] = 0 \tag{3.5.9}$$

$$[p_C] = -[p_I^*] = -p_I\frac{[\rho]}{\rho_w} = p_I\frac{\rho_w - \rho_a}{\rho_w} \tag{3.5.10}$$

Comparing with the GFM two-phase Navier-Stokes equations, the only difference is the term gz in the Navier-Stokes equations is replaced by $-\frac{p_I}{\rho_I}$ in the SWENSE method.

Similar to the GFM two-phase Navier-Stokes equations, the pressure gradient over the density is considered to be continuous across the free surface.

$$\left[\frac{\nabla p_C}{\rho}\right] = 0 \tag{3.5.11}$$

This equation signifies that the gradient of the complementary pressure is proportional to the density of the fluid. In the water phase, the gradient of pressure is approximately 1000 times larger than that in the air phase.

3.5.3 Combined equations

The combined equations are written as follows,

$$\nabla.\mathbf{u}_C = 0 \tag{3.5.12}$$

$$\frac{\partial \mathbf{u}_C}{\partial t} + \mathbf{u}.\nabla\mathbf{u}_C + \mathbf{u}_C.\nabla\mathbf{u}_I = -\frac{\nabla p_C}{\rho} + \nu\nabla^2\mathbf{u}_C \tag{3.5.13}$$

The free surface position is required in the GFM to apply the interface discontinuity conditions. However, the VOF method cannot explicitly give the exact position of the free surface. In this scenario, the contour of the VOF field with the volume fraction equals 0.5 is used to represent the free surface. The density (ρ) and the viscosity (ν) of the fluid are defined with the VOF field (α) as follows,

$$\rho = \begin{cases} \rho_w & \alpha > 0.5 \\ \rho_a & \alpha < 0.5 \end{cases} \tag{3.5.14}$$

and

$$\nu = \begin{cases} \nu_w & \alpha > 0.5 \\ \nu_a & \alpha < 0.5 \end{cases} \tag{3.5.15}$$

The discontinuities conditions (Eqn. (3.5.10) and (3.5.11)) on the free surface are taken into account by special GFM discretization operators similar to Section 2.3.3. The numerical implementation of these operators are adopted from the work of Vukčević [126].

3.6 Boundary Conditions

In order to guarantee the uniqueness of the numerical solution of the governing equations, boundary conditions need to be specified at the boundaries of the CFD domain [125]. This section describes the boundary conditions commonly used by the two-phase SWENSE method, which are shown in Fig. 3.2.

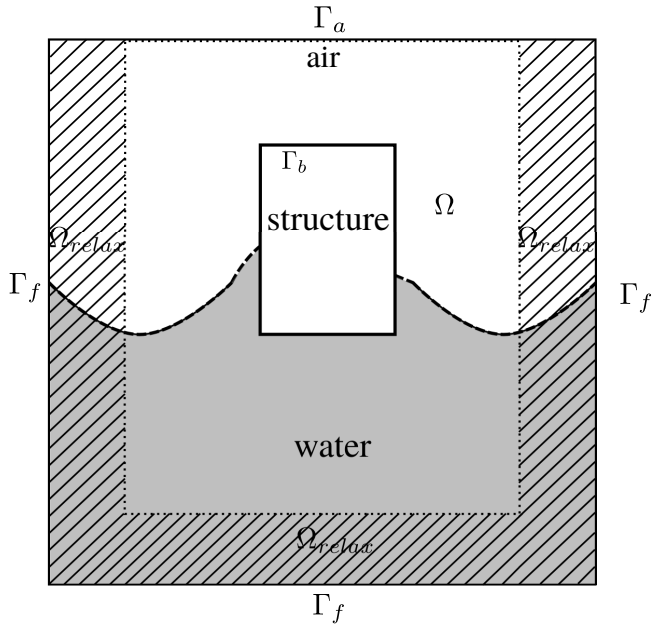

Figure 3.2: Computational domain and boundary condition in two-phase SWENSE method.

These boundaries include

- the far-field boundary (Γ_f),
- the body wall boundary (Γ_b),
- the atmosphere boundary (Γ_a).

Among them, the far-field and the body wall conditions were already defined in the single-phase SWENSE method; their definitions are slightly modified to be used by the two-phase method. The atmosphere boundary condition is specific to the two-phase SWENSE method. Several possibilities to define this boundary condition are discussed.

3.6.1 Far-field

The far-field(Γ_f), in the context of wave-structure interaction, refers to the region far away from the structure. The SWENSE method assumes that the complementary fields vanish in the far-field. The total wave fields are consequently equal to the incident wave fields on this boundary. With this assumption, the far-field boundary condition is defined as:

$$\mathbf{u}_C = 0 \tag{3.6.1}$$

$$\frac{\partial p_C}{\partial n} = 0 \tag{3.6.2}$$

$$\alpha = \alpha_I \tag{3.6.3}$$

where n stands for the local normal direction of the boundary. The two-phase SWENSE method in this thesis also adopts the relaxation zone method to attenuate the complementary fields. This zone is shown as Ω_{relax} in Fig. 3.2. The relaxation zone gradually blends the complementary velocity ($\mathbf{u}_{C,CFD}$) to zero and the VOF field (α_{CFD}) to the target values in the far-field.

$$\mathbf{u}_C = (1-\omega)\mathbf{u}_{C,CFD} \tag{3.6.4}$$

$$\alpha = \omega\alpha_I + (1-\omega)\alpha_{CFD} \tag{3.6.5}$$

where the ω is the weight function (see Section 2.3.4). No relaxation on the complementary pressure field p_C is given, since the pressure field needs to be directly calculated to enforce the continuity equation.

3.6.2 Body wall

The body wall boundary (Γ_b) in the present work refers to a stationary wall of a structure. The total velocity of the fluid is equal to zero on this boundary. The normal gradient of the VOF field is defined to be zero following the common practice in a two-phase solver.

In the context of the two-phase SWENSE formulations, these boundary conditions are defined as

$$\mathbf{u}_C = -\mathbf{u}_I \tag{3.6.6}$$

$$\frac{\partial p_C}{\partial n} = 0 \tag{3.6.7}$$

$$\frac{\partial \alpha}{\partial n} = 0 \tag{3.6.8}$$

where n stands for the local normal direction of the boundary.

3.6.3 Atmosphere

The atmosphere boundary (Γ_a) in a two-phase CFD solver refers to the uppermost boundary of the computational domain. This boundary is usually only in contact with the air phase. This boundary can be modeled in different ways in a conventional CFD solver. For example, it can be modeled as

- A stationary wall: the velocity is equal to zero; the pressure is given according to the velocity boundary condition; the normal gradient of the VOF field is equal to zero.

- An open boundary connecting to the atmosphere: the normal gradient of the velocity field equals to zero; the pressure has a fixed value; the normal gradient of the VOF field is equal to zero.

In this section, these two options are both adapted and compared in the SWENSE framework.

Stationary wall

The stationary wall requires the total velocity to be zero on the boundary surface. It is the same boundary condition of a stationary body wall. It requires the complementary velocity field to be the opposite of the incident velocity field on the boundary, the normal gradient of the VOF field is equal to zero:

$$\mathbf{u}_C = -\mathbf{u}_I \tag{3.6.9}$$

$$\frac{\partial p_C}{\partial n} = 0 \tag{3.6.10}$$

$$\frac{\partial \alpha}{\partial n} = 0 \tag{3.6.11}$$

where n stands for the local normal direction of the boundary.

In the present method, the incident velocity field $\mathbf{u}_I$ is defined as the extended wave velocity in the air. So on the atmosphere boundary, the incident velocity field is non-zero. The stationary wall leads to a non-zero boundary value of the complementary velocity field. Even in pure incident wave propagation, this boundary condition requires the CFD solver to solve a complementary velocity field opposite to the incident wave velocity. In fact, this boundary condition does not only affect the boundary region, as the pressure field propagates the effects of this boundary condition in the entire computational domain.

Figure 3.3 shows a simulation with this boundary condition. It simulates a fully nonlinear regular wave propagating in a periodic domain. The black curves illustrate the free surface position.

- The left figure shows the initial condition, where the complementary velocity field $\mathbf{u}_C = 0$ in everywhere.

- The right figure shows the complementary velocity field after the first time step. A significant complementary velocity field $\mathbf{u}_C$ appears the air phase, down to the free surface, and may modify the wave solutions.

To conclude, modeling the uppermost boundary of the computational domain as a stationary wall is not suitable in the two-phase SWENSE method, since it loses the property of the SWENSE method in keeping the complementary field zero in incident wave propagation cases.

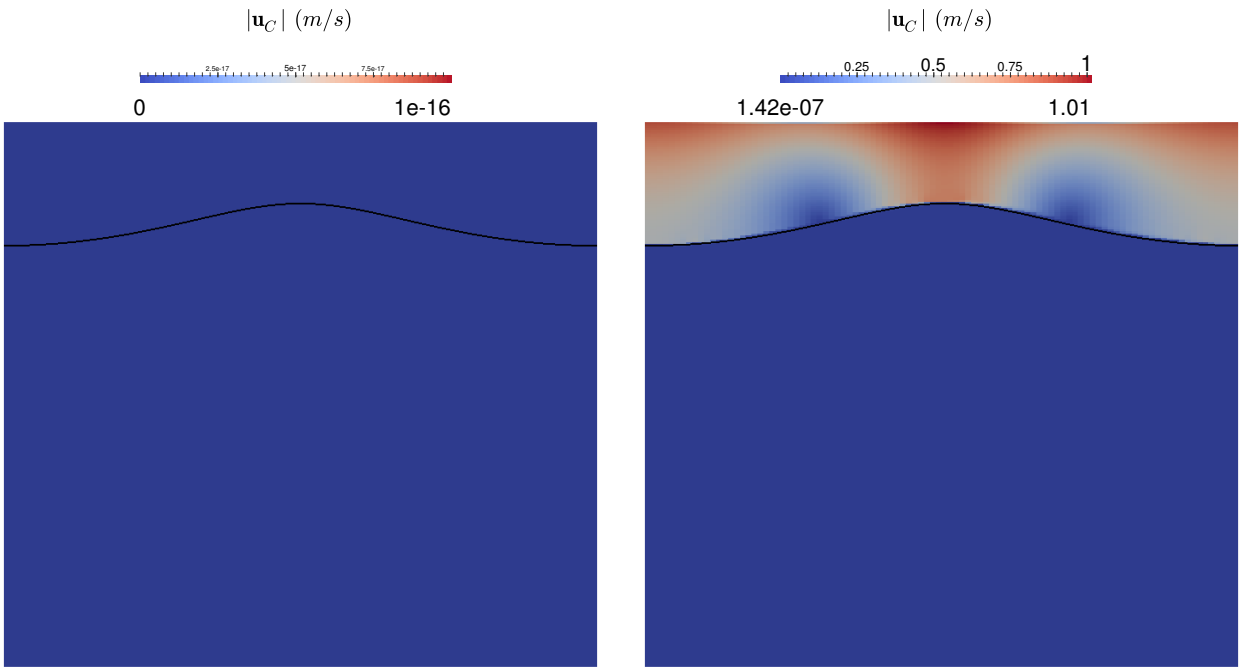

(a) $t = 0$ (b) $t = \Delta t$

Figure 3.3: Complementary velocity fields with the stationary wall boundary condition on the top of the computational domain.

Open boundary

A second way is to define this boundary as an open boundary like in a conventional two-phase solver. The open boundary defines velocity field to have zero normal gradients. The momentum is able to cross the open boundary. In the SWENSE method, we apply this condition on the complementary velocity field, so that the complementary momentum is able to move across the open boundary freely. The complementary pressure field is set to a fixed reference value on this boundary. The reference pressure is often defined to be zero.

$$\frac{\partial \mathbf{u}_C}{\partial n} = \mathbf{0} \tag{3.6.12}$$

$$p_C = p_{Ref} = 0 \tag{3.6.13}$$

$$\frac{\partial \alpha}{\partial n} = 0 \tag{3.6.14}$$

where n stands for the local normal direction of the boundary.

In theory, this boundary condition does not influence the complementary velocity field for the incident wave propagation problem. Both the initial value and the boundary value of the complementary velocity field are zero. In this case, no complementary field is expected (see Section 3.4.4).

Figure 3.4 shows a simulation with the open boundary condition. The same regular wave as in Fig. 3.3 is simulated. The black curves illustrate the free surface position.

- The left figure shows the initial condition, where the complementary field $\mathbf{u}_C = 0$ in everywhere.

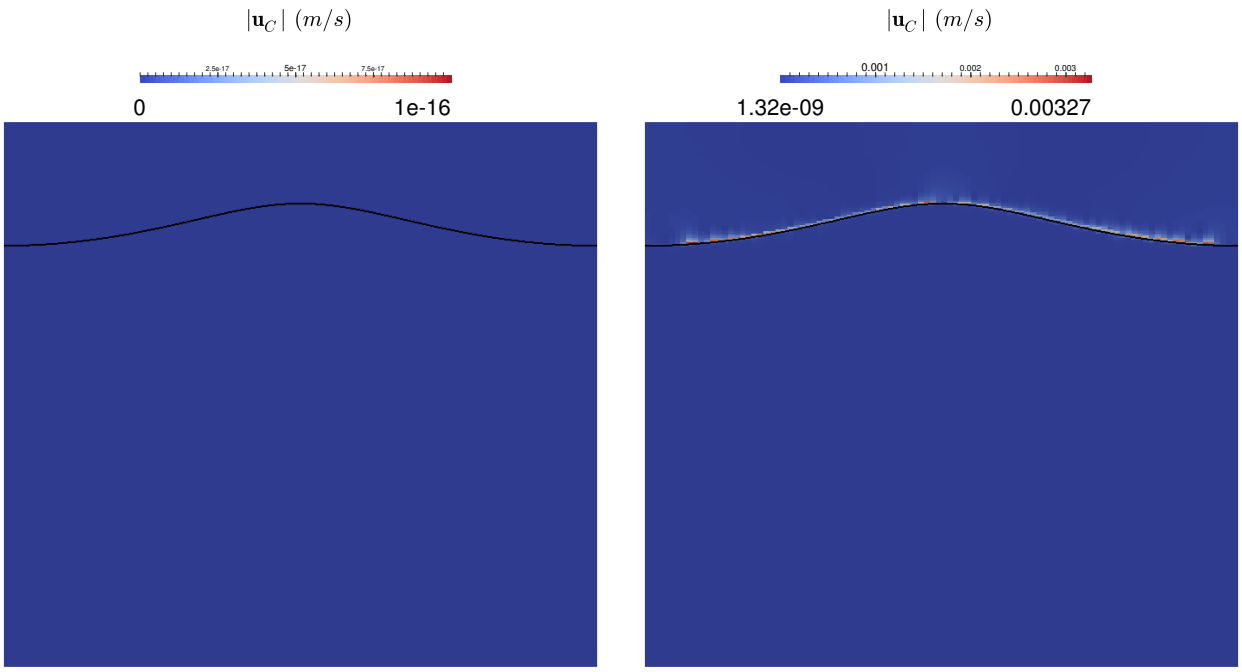

(a) $t = 0$ (b) $t = \Delta t$

Figure 3.4: Complementary velocity fields with the open boundary condition on the top of the computational domain.

- The right figure shows the complementary velocity field after the first time step. The complementary velocity field $\mathbf{u}_C$ in the present simulation is almost zero everywhere in the computational domain.

This result implies that the total wave field is equal to the incident wave, which is the expected situation for a pure incident wave propagation problem. However, a small complementary velocity field is generated near the free surface. The reason of these non-zero values shall be discussed in the last section of this chapter. Here, modeling the uppermost boundary of the computational domain as an opening to the atmosphere is considered to be appropriate.

3.7 Comments on the mathematical models

This part firstly discusses the difference between the present work and the work of Vukčević *et al.* [127]. Those authors have indeed developed a first implementation of the two-phase SWENSE method within OpenFOAM. However, several discrepancies between the original method have been identified and will be discussed in this section. Secondly, the influence on imposing the incident wave velocity in the air in the present work is discussed.

3.7.1 Main differences with Vukčević *et al.* [127]

In the work of Vukčević *et al.* [127], the authors evaluate numerically the quantities related to the incident waves by the CFD solvers. For example, the continuity equation used in [127] reads,

$$\nabla.\mathbf{u}_C = -\nabla.\mathbf{u}_I \tag{3.7.1}$$

Although the R.H.S. equals zero in the wave theory, Vukčević *et al.* [127] evaluated this term by the CFD solver, to consider the errors coming from:

- the spectral solution techniques;
- the mapping of incident velocity on the CFD mesh;

Vukčević *et al.* emphasized the necessity to compensate the errors with the complementary field. However, in the present work, we choose to ignore these errors and cancel out the R.H.S. term with the theoretical relation $\nabla.\mathbf{u}_I = 0$ for incompressible flow. The reasons for this choice are:

- The potential flow methods are accurate for water wave problems. The numerical error in a converged spectral potential flow result is often negligible. Compensating this error by CFD solvers may not be beneficial because this correcting step may introduce larger numerical errors itself.
- The mapping technique of incident field on CFD mesh is improved in this work (see Chapter 4), so that the numerical error related to the mapping procedure is drastically reduced.
- The precision of the numerical evaluation of the incident quantities relies on a fine Finite Volume discretization. This is not consistent with the objective of the SWENSE method, *i.e.*, to be able to use coarse mesh in the far-field for the incident wave propagation problem.

The momentum equation in [127] (provided with the GFM formulation) is not simplified either with the analytic relation of the incident variables provided by the Euler equations, it reads.

$$\frac{\partial \mathbf{u}_C}{\partial t} + \mathbf{u}.\nabla\mathbf{u}_C - \nu\nabla^2\mathbf{u}_C = -\frac{\partial \mathbf{u}_I}{\partial t} - \mathbf{u}.\nabla\mathbf{u}_I + \nu\nabla^2\mathbf{u}_I - \frac{\nabla p_{-\rho g h}}{\rho} \tag{3.7.2}$$

This treatment requires a fine CFD mesh to evaluate accurately the source terms related to the incident fields. Otherwise, their numerical errors will influence the total solution (even in the far-field). The present work chooses to follow the original single-phase SWENSE method, *i.e.*, to simplify the incident quantities as much as possible to avoid such errors.

3.7.2 Incident solution in the air

In this part, the influence of extending the incident wave velocity in the air is discussed.

In the present work, the incident velocity in the air is directly evaluated by the spectral wave theory. The result is a smooth transition near the free surface, which is beneficial in the numerical aspect.

The drawback of such an extension is that it generates an oscillating *incident wind* field in the air. For a pure wave propagation problem, the complementary field is expected to be zero in the entire domain, so this *incident wind* solution resides finally in the total field. The total solution in the air is not physically correct. Figure 3.5 shows the total velocity field in a two-phase SWENSE simulation. The white curves represent the free surface position. Above the free surface, the oscillatory *incident wind* velocity field is significant. This *incident wind*

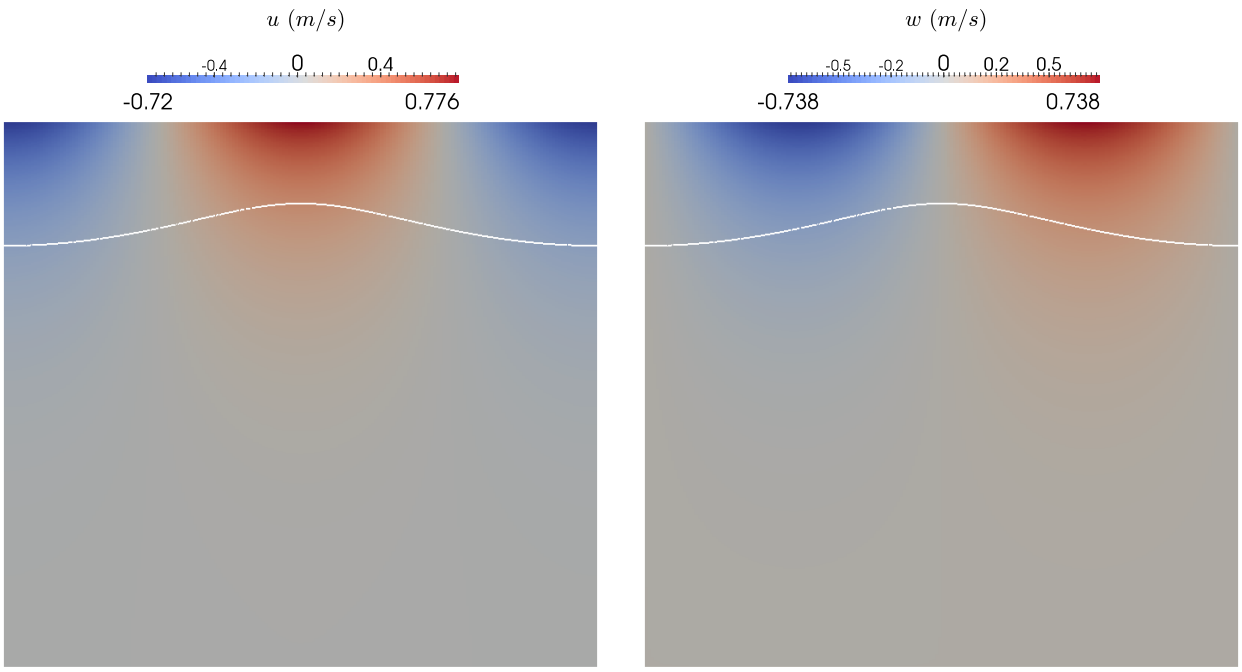

(a) Horizontal velocity

(b) Vertical velocity

Figure 3.5: Total velocity field in a regular wave propagation case by two-phase SWENSE method.

field depends on the result of Euler equation and may not represent the true air flow in an ordinary wave propagation case. The scenario represented by such a simulation is a traveling water wave with the oscillating wind blowing on top of it.

Besides this choice, most of the literature regarding the coupling potential flow and two-phase viscous flow solvers (mostly with domain decomposition method) [30, 64, 73, 80, 116] ignores the air velocity in the potential problem and regards it as zero, assuming the air velocity has little influence on the total solution for the wave-structure interaction problem. This choice results in a discontinuity in the potential velocity solution across the free surface, which is inconsistent with the two-phase CFD methods assuming the continuous velocity field. In this case, using the potential theory to calculate the air velocity may be a better solution. Such work has been done by Colicchio *et al.* [31] who used a two-phase BEM solver to find the potential flow solution in the air and coupled it with a two-phase viscous solver. However, the velocity given by the two-phase BEM solver still had a discontinuity. Considering such a discontinuity in the SWENSE method may require complicated numerical treatments in the CFD solver and is not straightforward.

In the present work, the adopted compromise is to use the spectral method to provide a continuous velocity field and accept this oscillatory wind in the air as a side effect. In most wave-structure interaction problems, the air-effects are often very weak compared with the contribution of the water part. This non-physical *incident wind* field in the air is often acceptable. This assumption shall be checked by the validation cases later in the thesis.

3.8 Implementation in OpenFOAM

The mathematical models developed in the previous sections are general and can be applied to the two-phase solvers with interface capturing techniques. In this thesis, these mathematical models are implemented in OpenFOAM for validation purposes.

The solver developed in the present thesis is named *foamStar-SWENSE*. It has three versions with three different sets of governing equations (conservative, non-conservative, GFM). The implementation is achieved by modifying an existing two-phase solver in OpenFOAM (*foamStar* [92]). The original governing equations (two-phase NS equations) used by *foamStar* are replaced by the two-phase SWENS equations developed in the present work. The GFM version of the code is developed with the contribution of Vukčević *et al.* from University of Zagreb on the Ghost Fluid Method. Their code was developed in the navalHydroPack [13] in the foam-extend version. It has been adapted in the OpenFOAM environment in this work. Since the three versions of SWENS equations are similar, only the non-conservative version is described in this part. The other two versions are implemented in similar ways.

Since the implementation of *foamStar-SWENSE* is very similar to the implementation of *foamStar* (see Section 2.4), this parts only outlines the main procedures.

3.8.1 Equation discretization

Same as in Section 2.4, the sign $\{\cdot\}$ is used to indicate that the terms enclosed are treated implicitly. Otherwise, the terms are evaluated explicitly.

VOF equation

Eqn. (3.4.10) is written in a conservative form and discretized as, which is the same as Eqn. 2.4.1 :

$$\left\{\frac{\partial \alpha}{\partial t}\right\} + \{\nabla.\mathbf{u}\alpha\} = 0 \tag{3.8.1}$$

Note that the total velocity is used in this equation, which is reconstructed with $\mathbf{u} = \mathbf{u}_I + \mathbf{u}_C$.

Momentum equation

The discretized form of Eqn. (3.4.2) reads:

$$\left\{\frac{\partial \mathbf{u}_C}{\partial t}\right\} + \{\nabla.(\mathbf{u}\mathbf{u}_C)\} + \nabla.(\mathbf{u}_C\mathbf{u}_I) = -\frac{\nabla p_C}{\rho} - \frac{p_I}{\rho_I}\frac{\nabla \rho}{\rho} + \frac{\{\nabla.(\mu\nabla\mathbf{u}_C)\} + \nabla\mathbf{u}_C.\nabla\mu}{\rho} \tag{3.8.2}$$

The time derivative, the convection, and the diffusion terms of the $\mathbf{u}_C$ are discretized implicitly. The source terms on the R.H.S. and the $\nabla.\mathbf{u}_C\mathbf{u}_I$ is explicitly evaluated.

Same as the discretized NS momentum equation (Eqn. 2.4.2), the pressure terms ($\frac{\nabla p_C}{\rho}$, $\frac{p_I}{\rho_I}\frac{\nabla \rho}{\rho}$) are evaluated on the cell faces and reconstructed in the cell center.

Using Eqn. (3.8.2), a linear equation for each control volume is assembled:

$$a_P\mathbf{u}_{C,P} + \sum_N a_N\mathbf{u}_{C,N} = \mathbf{S} - \frac{\nabla p_C}{\rho} \tag{3.8.3}$$

Pressure equation

The discretized pressure equation of the SWENSE solver is derived in the same way in as in standard incompressible flow solvers(see Section 2.4).

The final form of the discretized pressure equation is written as,

$$\sum_f \mathbf{A}_f . \left(\overline{\left(\frac{1}{a_P} \right)} \frac{\{\nabla p_C\}_f}{\overline{\rho}} \right) = \sum_f \mathbf{A}_f . \overline{\left(\frac{H(\mathbf{u}_C)}{a_p} \right)} \tag{3.8.4}$$

with

$$H(\mathbf{u}_C) = -\sum_N a_N \mathbf{u}_{C,N} + \mathbf{S} \tag{3.8.5}$$

The sign $\overline{\cdot}$ denotes interpolated value on the cell face. The complementary pressure gradient $(\nabla p_C)_f$ is discretized on the cell face with the value of the current cell and its neighbors, following the work of Rhie and Chow [104], to avoid the check-board decoupling problem. This Poisson equation is solved to determine the complementary pressure field p_C and to correct the complementary velocity flux $F_{C,f}$.

$$F_{C,f} = \mathbf{u}_{C,f} . \mathbf{A}_f = \overline{\left(\frac{H(\mathbf{u}_C)}{a_P} \right)} . \mathbf{A}_f - \overline{\left(\frac{1}{a_P} \right)} \frac{(\nabla p_C)_f}{\overline{\rho}} . \mathbf{A}_f \tag{3.8.6}$$

The cell-centered $\mathbf{u}_C$ is reconstructed from the face-flux $F_{C,f}$.

3.8.2 Solution algorithm

PIMPLE algorithm is adopted to solve the VOF-velocity-pressure coupling. The structure of the SWENSE solver is provided in the flowchart (see Fig. 3.6).

1. At the beginning of each time step, incident wave properties $\mathbf{u}_I$ and p_I are updated from potential wave solvers and mapped to the CFD mesh. The total velocity is reconstructed with $\mathbf{u} = \mathbf{u}_I + \mathbf{u}_C$.
2. The Volume of Fluid field α (Eqn. (3.8.1))is solved; the fluid properties are updated using the new VOF field (Eqn. (3.4.11) and (3.4.12)). The modified incident wave pressure (p_I^*) is updated with the new density field (Eqn. (3.3.1)).
3. The PISO algorithm is adopted to solve the velocity and pressure coupling. In the PISO loop:
   a) The complementary velocity field is solved (Eqn. (3.8.2)) at the momentum prediction step.
   b) The complementary pressure p_C (Eqn. (3.8.4)) is solved, and the flux is updated with (Eqn. (3.8.6)).
   c) The complementary velocity field $\mathbf{u}_C$ at the cell center are reconstructed from the face flux.
4. The solution is then blended to the target values in the relaxation zones to attenuate the scattered waves in the far-field (Eqns. (3.6.4) and (3.6.5))
5. PIMPLE loop iterates to achieve the convergence of the VOF, the velocity, and the pressure before stepping to the next time.

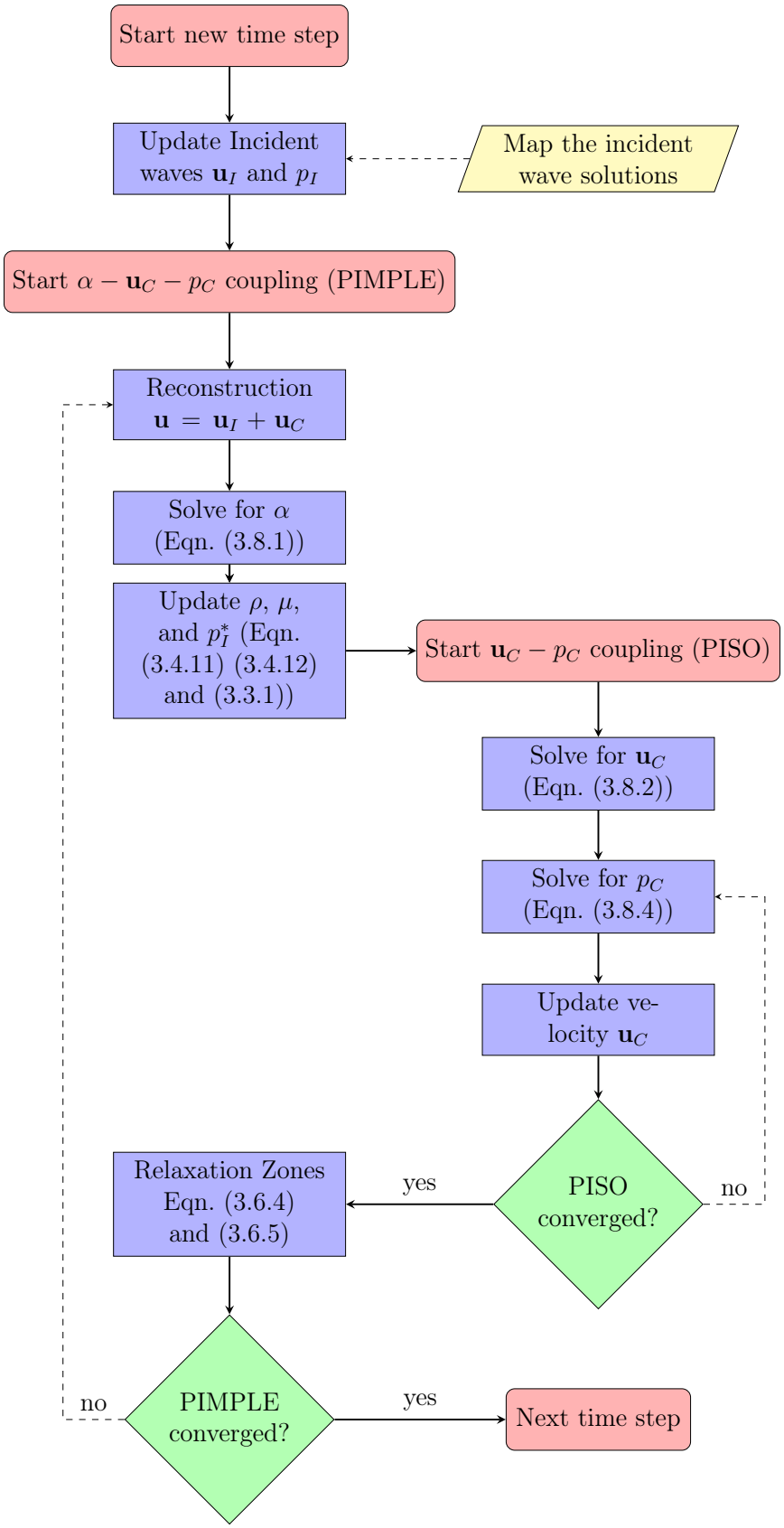

Figure 3.6: Solution Algorithm of the SWENSE method

3.9 Test case: regular wave propagation

One attractive feature of the SWENSE method is its ability to maintain an accurate incident wave field with relatively small computational resources. In this section, this ability of the two-phase SWENSE method is tested by a simple illustrative test case.

The test case concerns a pure regular wave propagation (*i.e.*, without any structure in the computational domain). Different time and space discretizations are used. All the three versions of *foamStar-SWENSE* are tested (conservative, non-conservative, and Ghost Fluid Method). Comparative simulations with *foamStar* are also conducted. The result of the SWENSE methods are first validated by the analytical wave theory solution and then compared with the result of *foamStar*.

The aim of this section is to study:

- the performance of the proposed method in wave propagation problems;
- the advantages of the SWENSE solvers (*foamStar-SWENSE*) over the conventional solver (*foamStar*);
- the differences between the three SWENSE formulations;
- the sources of error in the SWENSE solvers and their influence.

3.9.1 Case setup

This test case simulates the fully-nonlinear regular wave propagation in a 2D computational domain. To focus on the wave propagation problem, the periodic boundary conditions at the inlet and the outlet are used to get rid of the wave generation and absorption issue. In order to demonstrate the stability and the accuracy of the method, this test case is intentionally designed to have a big computational domain and to last for a sufficiently long time in order to increase the numerical difficulties. Steady-state propagating waves with a moderately high wave steepness ($ka = 0.24$) and deep water depth ($kh = 4.71$) are simulated. The incident wave information is obtained by the stream function wave theory [41, 105]. The wave characteristics are listed in Table 3.1.

Parameter	Value
Wave period (T)	$0.7017\,s$
Wave height ($H = 2a$)	$0.0575\,m$
Water depth (h)	$0.6000\,m$
Wave steepness (ka)	0.2235
Relative water depth (kh)	4.6645

Table 3.1: Wave characteristics for the 2D wave propagation case

A two-dimensional rectangular computational domain is used, as illustrated by Fig. 3.7. The waves travel from the left to the right. Periodic boundary conditions are applied on the inlet and the outlet boundaries. The origin of the coordinate system is located at the left of the computational domain on the free surface position at rest. The axis x points right and the

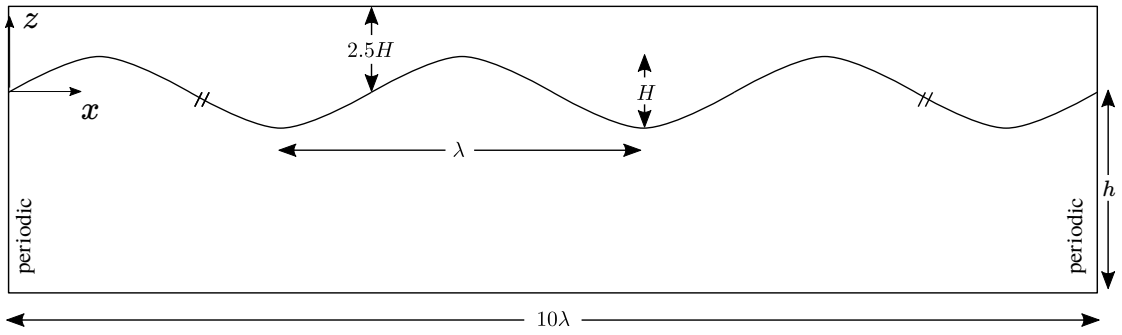

Figure 3.7: Computational Domain for the 2D wave propagation case.

axis z points up. The length of the computational domain is equal to ten wave lengths (λ), and the height of the computational domain equals to the water depth (h) plus 2.5 times the wave height (H). The simulation lasts for 20 wave periods.

The waves are initialized everywhere in the computational domain at the beginning of the simulation.

For *foamStar-SWENSE*, the initial values of the complementary velocity field and the complementary pressure field are set to zero, and the VOF field is set according to the stream function wave theory in the beginning. The simulation with *foamStar* is initialized with the velocity field ($\mathbf{u}$) and the VOF field (α) set according to the stream function wave theory. The initial VOF field is shown in Fig. 3.8.

Figure 3.8: Initial VOF field of the regular wave propagation test case.

Four sets of numerical discretization are used (see Tab. 3.2). The mesh is uniform everywhere in the computational domain. From a coarser discretization to a finer discretization, a constant refinement ratio of 2 is applied in both space and time. Figure 3.9 shows the local mesh near the free surface (over one wave length) of all the four discretization. The medium discretization corresponds to the typical configuration used by two-phase VOF solvers for wave-structure interaction problems, while the very coarse discretization is expected to produce inaccurate results with the original two-phase Navier-Stokes solver.

Parameter	Fine	Medium	Coarse	Very coarse
Mesh size ($\Delta x, \Delta z$)	$\lambda/200, H/40$	$\lambda/100, H/20$	$\lambda/50, H/10$	$\lambda/25, H/5$
Time step (Δt)	$T/800$	$T/400$	$T/200$	$T/100$

Table 3.2: Discretizations for the regular wave propagation case.

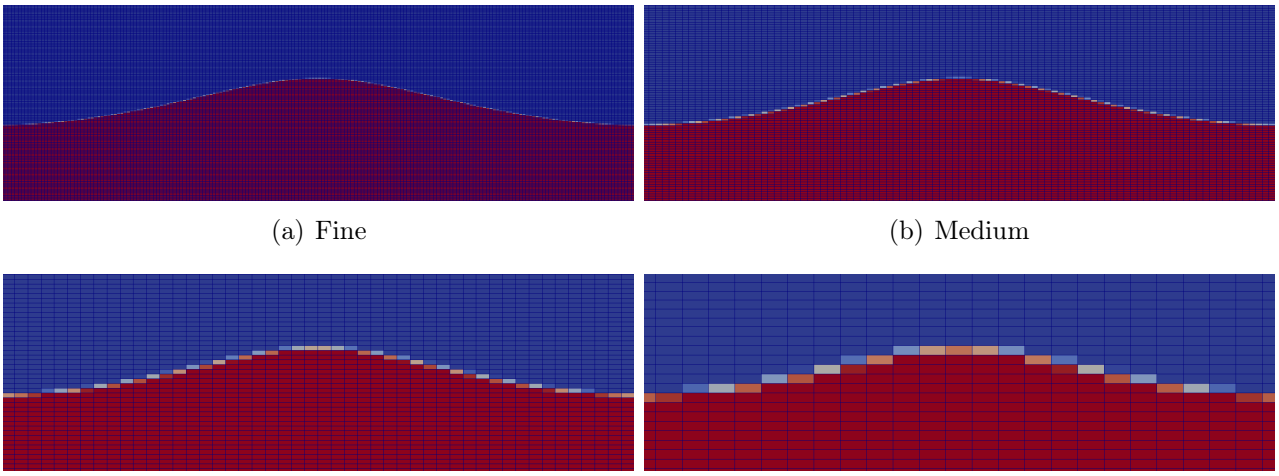

(a) Fine (b) Medium

(c) Coarse (d) Very Coarse

Figure 3.9: Zoom of local mesh near the free surface of the regular wave propagation test case.

3.9.2 Results: free surface shape on the medium mesh

This part compares the free surface shape obtained by *foamStar-SWENSE* and by *foamStar* on the medium discretization ($\Delta x = \lambda/100$,$\Delta t = T/400$), which represents the typical configuration used by two-phase VOF solvers. This part will give an intuitive impression on different methods. More quantitative results will be given in the next section.

In Fig. 3.10, the free surface elevation (η) is plotted against the distance from the inlet (x). The surface elevation is non-dimensionalized by the incident wave amplitude ($a = H/2$), and the distance is non-dimensionalized by the wave length (λ).

- The stream function solution is plotted with the solid black line;
- *foamStar-SWENSE* is plotted with the red dashed line. The three SWENSE solvers have very close results with this discretization, thus only one curve (obtained with the non-conservative formulation) is used to present all of them;
- *foamStar* is plotted with the blue point-dashed lines.

The first plot corresponds to the initial condition of the simulation at $t = 0$. The time interval between each subfigures is five wave periods.

- The first figure plots the initial condition. All the three curves superpose.
- The second figure shows the result of $t = 5T$. The three results are almost identical. No visible difference can be found at this moment. Both the wave amplitudes and the phases are well-kept.
- At $t = 10T$, a small discrepancy may be observed between the results of *foamStar* and the other two results. The discrepancy becomes more visible at $t = 15T$ and $t = 20T$. A loss of wave amplitude is observed in *foamStar*, whereas *foamStar-SWENSE* is still in good agreement with the stream function wave theory.

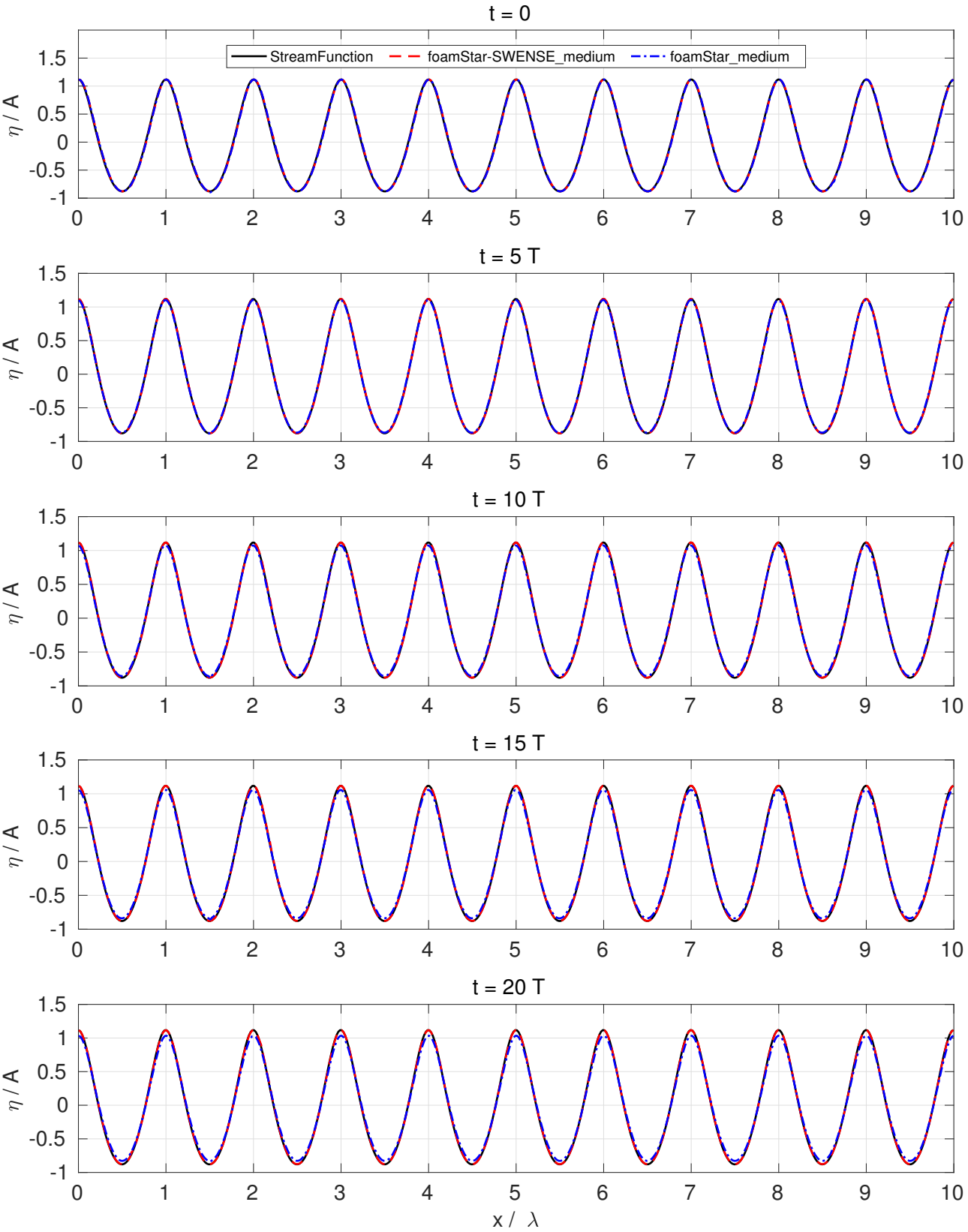

Figure 3.10: Free surface shape for regular wave propagation test case with the medium discretization ($\Delta x = \lambda/100$,$\Delta t = T/400$).

3.9.3 Results: Wave elevation in the center of the domain

In this section, the free surface elevations in the center of the domain are measured to analyze the behavior of the three SWENSE formulations and compare them with the conventional two-phase Navier-Stokes (NS) solver. Results obtained with these methods are referred to as:

- SWENSE-Conservative: the result of *foamStar-SWENSE* with conservative momentum equation;
- SWENSE-Non-Conservative: the result of *foamStar-SWENSE* with non conservative momentum equation;
- SWENSE-GFM: the result of *foamStar-SWENSE* with the Ghost Fluid Method;
- NS-Conservative: the result of *foamStar* with two-phase NS equations;
- Stream Function: the reference solution of the stream function wave theory.

The time histories of the free surface elevation (η) and the amplitude of the first harmonic component ($\eta^{(1)}$) are plotted in Figs. (3.11 - 3.14). Each figure compares the results of different CFD methods on the same discretization. The four figures together show the influence of the discretization (from the finest to the coarsest) on the simulation results. The vertical axes are non-dimensionalized by the first harmonic amplitude given by the stream function wave theory ($\eta^{(1)}_{SF}$). The abscissas (t) are non-dimensionalized by the wave period (T). Please note the vertical axis of Fig 3.14 has a different scale comparing with the others, since the loss of amplitude is severe in this case.

The following text describes the observations from Figs. (3.11 - 3.14). A quantitative analyse shall be given in Tab. 3.3 to Tab. 3.6 afterwards.

- Figure 3.11 shows the result of the fine resolution $(\Delta x, \Delta z, \Delta t) = (\lambda/200, H/40, T/800)$. The free surface (η) shows barely any difference between the CFD results and the stream function solution. The first harmonic amplitudes ($\eta^{(1)}$) reveal tiny differences between the numerical methods. SWENSE-Conservative and SWENSE-GFM lose slightly the wave amplitudes, while SWENSE-Non-Conservative generates a bit larger amplitudes. The wave damping in NS-Conservative is the largest in all the CFD results. However, the differences between the numerical results and the reference value are all very small (within 3%).
- Figure 3.12 shows the result of the medium resolution $(\Delta x, \Delta z, \Delta t) = (\lambda/100, H/20, T/400)$. In the free surface elevation (η), a very small discrepancy may be observed between the result of NS-Conservative and the others. The first harmonic amplitudes ($\eta^{(1)}$) shows that the SWENSE results are very close to the reference value (differences are less than 2%), while the wave amplitude is diminished in NS-Conservative. At the end of simulation, the waves are about 7% smaller than the reference value.
- The result of the coarse resolution $(\Delta x, \Delta z, \Delta t) = (\lambda/50, H/10, T/200)$ is illustrated by Fig. 3.13. In the free surface elevation, the discrepancy between the numerical results and the reference solutions are visible. The waves simulated with *foamStar* are damped, while the SWENSE results are also smaller than the reference solution. The first harmonic amplitudes reveal that for the first 10 wave periods, the three SWENSE solvers have similar performances, which are only 1.8% smaller than the reference value, while the

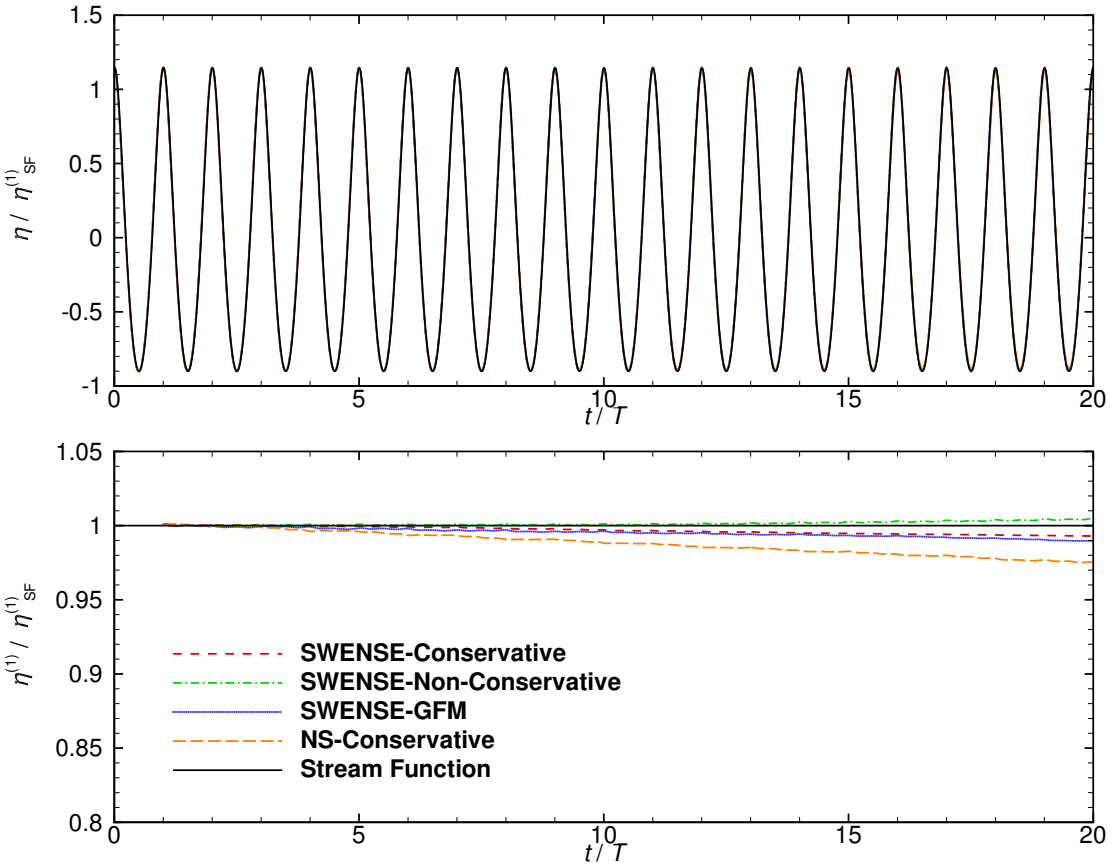

Figure 3.11: Comparing the three SWENS equations ($\Delta x = \lambda/200$, $\Delta t = T/800$).

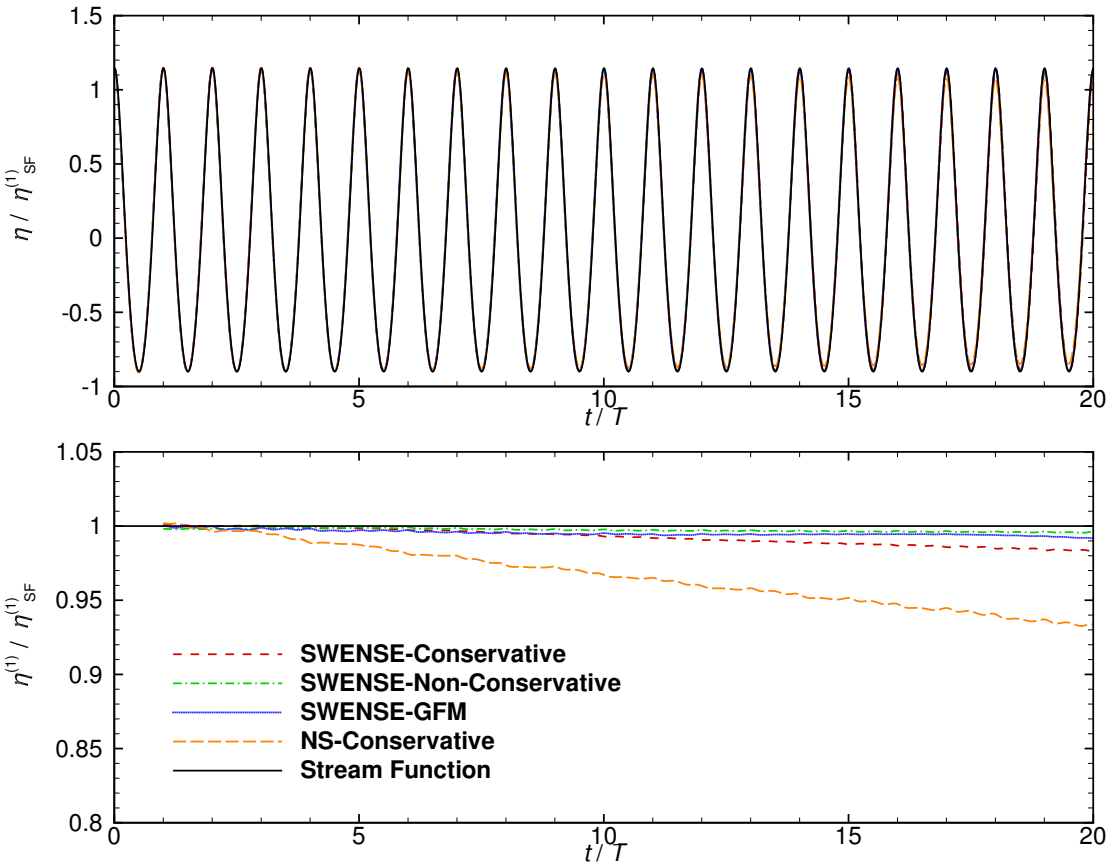

Figure 3.12: Comparing the three SWENS equations ($\Delta x = \lambda/100$, $\Delta t = T/400$).

result of NS_Conservative is 10% smaller. In the end of the simulation, SWENSE-GFM has the best accuracy, followed by SWENSE-Conservative, and SWENSE-Non-Conservative. NS-Conservative loses about 20% of the wave amplitude.

- The result of the very coarse resolution $(\Delta x, \Delta z, \Delta t) = (\lambda/25, H/5, T/100)$ is illustrated by Fig. 3.14. This configuration is very coarse, to set difficulties for the SWENSE solvers. With this configuration, the differences between the numerical results and the reference solution are apparent. The first harmonic amplitudes reveal that for that the SWENSE solvers also face the wave damping problem on this very coarse discretization, however the problem is much smaller in the SWENSE method than in the NS method.

Table 3.3 to 3.6 provide the first harmonic amplitudes ($\eta^{(1)}$) in a more quantitative way.

$\eta^{(1)}/\eta^{(1)}_{SF}$	5T	10T	15T	20T
SWENSE-conservative	99.98%	99.71%	99.48%	99.30%
SWENSE-Non-conservative	100.09%	100.12%	100.27%	100.48%
SWENSE-GFM	99.83%	99.62%	99.34%	98.97%
NS-Conservative	99.59%	98.83%	98.26%	97.55%

Table 3.3: First harmonic amplitude of waves on the fine mesh

$\eta^{(1)}/\eta^{(1)}_{SF}$	5T	10T	15T	20T
SWENSE-conservative	99.85%	99.30%	98.77%	98.30%
SWENSE-Non-conservative	99.92%	99.77%	99.68%	99.60%
SWENSE-GFM	99.73%	99.52%	99.46%	99.19%
NS-Conservative	98.74%	96.71%	95.15%	93.38%

Table 3.4: First harmonic amplitude of waves on the medium mesh

$\eta^{(1)}/\eta^{(1)}_{SF}$	5T	10T	15T	20T
SWENSE-conservative	99.33%	98.10%	96.81%	95.46%
SWENSE-Non-conservative	99.57%	98.39%	95.97%	90.78%
SWENSE-GFM	98.89%	98.39%	98.20%	97.55%
NS-Conservative	95.92%	90.15%	85.51%	81.04%

Table 3.5: First harmonic amplitude of waves on the coarse mesh

$\eta^{(1)}/\eta^{(1)}_{SF}$	5T	10T	15T	20T
SWENSE-conservative	96.54%	90.73%	81.85%	66.89%
SWENSE-Non-conservative	97.34%	93.61%	88.79%	83.22%
SWENSE-GFM	99.13%	98.26%	97.10%	95.55%
NS-Conservative	85.91%	71.52%	61.58%	53.62%

Table 3.6: First harmonic amplitude of waves on the very coarse mesh

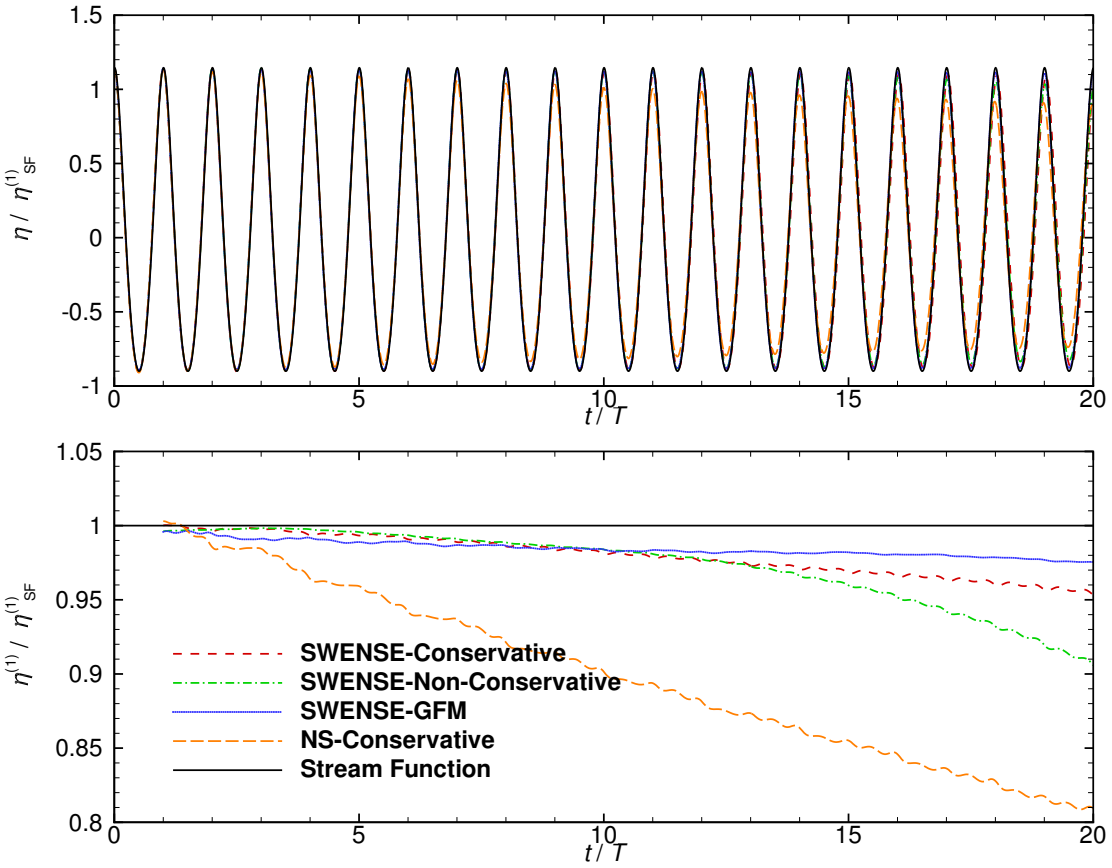

Figure 3.13: Comparing the three SWENS equations ($\Delta x = \lambda/50$, $\Delta t = T/200$).

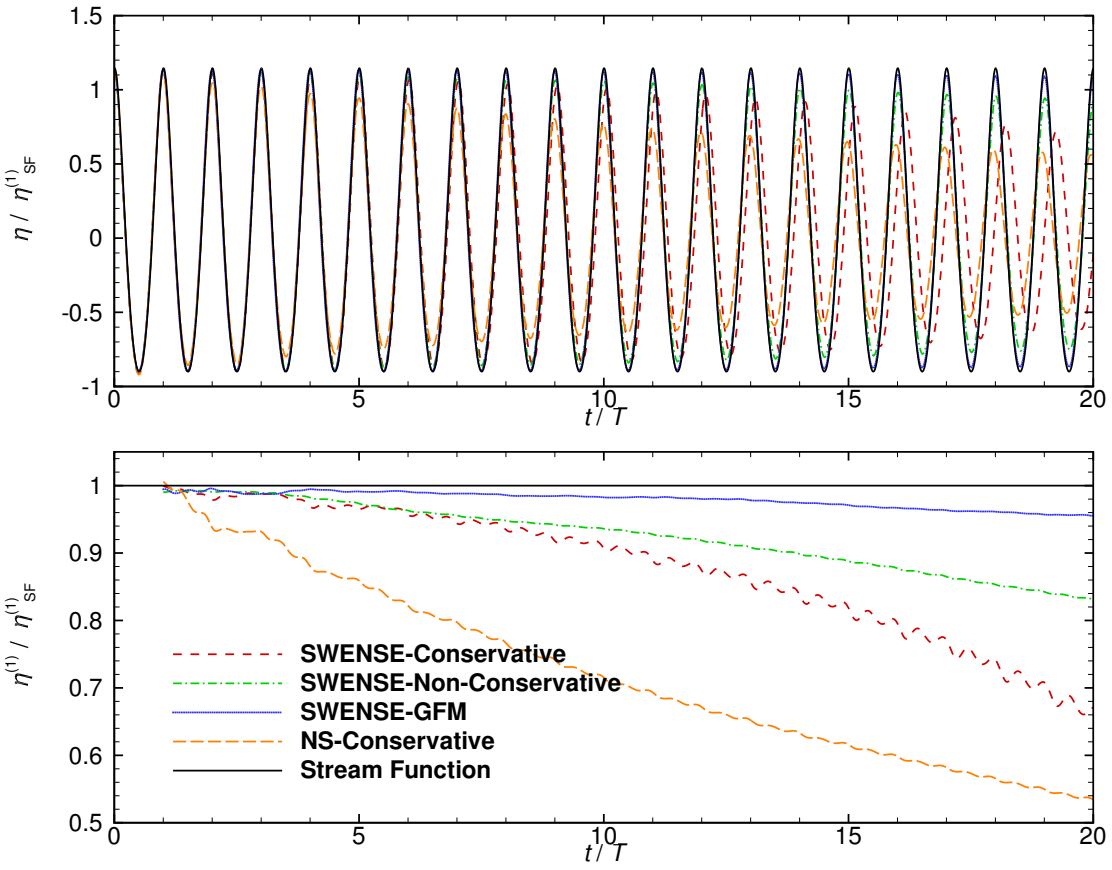

Figure 3.14: Comparing the three SWENS equations ($\Delta x = \lambda/25$, $\Delta t = T/100$).

Conclusion

The results reveal that:

- *foamStar-SWENSE* (implementing any of the three SWENSE formulations) is able to propagate the waves more accurately than *foamStar* (conventional two-phase NS solver) on any given discretization set. With the fine and the medium discretization setups, all the SWENSE formulations keep errors below 2% on the wave amplitude even after 20 wave periods. With the two coarser discretizations, the SWENSE solvers are able to keep the first several wave periods accurate before the waves get damped. On the contrary, the conventional NS solver diminishes the waves from the very beginning of the simulation.
- The numerical results of the SWENSE solvers are different from the stream function wave solution, showing that the theoretical ability of the SWENSE method to keep the incident wave unchanged (complementary field equals to zero) is not completely held in the present implementation. With the fine and the medium resolution, the SWENSE solver is able to give results very close to the potential theory; However, the SWENSE methods, especially the ones without GFM method suffer also from wave damping on coarser mesh (although less severe than the NS solver). The reason of this will be discussed in 3.9.4.
- In the present case, all the SWENSE formulations are able to produce a good incident wave during the first several periods, even with coarse mesh. This behavior is useful for a real wave-structure simulation. Since in such case, wave generation and absorption boundaries are used, the CFD solver needs to propagate waves only for several wave lengths. The behavior of the SWENSE method with wave generation and absorption boundaries shall be tested in Section 3.9.5.

3.9.4 Discussion: sources of errors

Section 3.4.4 proved the theoretical property of the two-phase SWENSE method in maintaining the complementary field zero for the pure incident wave propagation problem, *i.e.*, the results of SWENSE solvers will be the same as the waves models. However, in the present test case, the numerical results and the incident wave solution show discrepancies, indicating that the theoretical property is not completely reproduced by the numerical implementations. The following content discusses the cause of this different behavior.

Numerical error on the interface pressure source term

In Section 3.4.4, the property of the two-phase SWENSE method in maintaining the complementary field zero for the pure incident wave propagation problem. This property is valid since the interface pressure source term of the momentum equation is equal to zero in such scenario. Take the non-conservative SWENSE method as an example, the interface pressure source term:

$$\frac{p_I}{\rho_I}\frac{\nabla\rho}{\rho} = 0 \tag{3.9.1}$$

This relation has two requirements:

1. $p_I = 0$ on the free surface;
2. $\nabla\rho = 0$ out of the free surface.

However, the numerical implementation may not respect the second requirement, *i.e.*, numerical evaluation of $\nabla\rho$ may result in non-zero values outside the *interface cells*. To elaborate, Fig. 3.15 illustrates the numerical evaluation of $\nabla\rho$ in OpenFOAM by the standard Finite Volume Method.

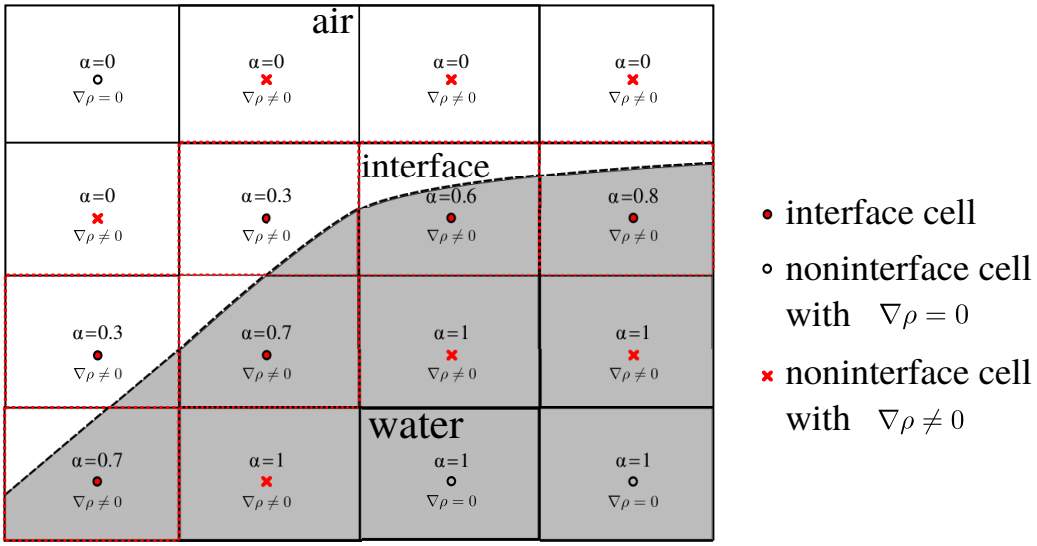

Figure 3.15: Numerical evaluation of the density gradient with the standard Finite Volume Method.

- The *interface* is represented by a black dashed line.
- The *interface cells* are the cells intersect with the interface ($0 < \alpha < 1$). They are represented by the red circles. The other cells are *non-interface cells*.
- The cells with non-zero density gradient ($\nabla\rho \neq 0$) are represented by:
  - the red circles in *interface cells*;
  - the red crosses in *non-interface cells*;
- The cell edges with non-zero density gradient ($\nabla\rho \neq 0$) are represented by the red dashed lines.

In theory, in the *non-interface cells*, the density gradient is equal to zero ($\nabla\rho = 0$), and they have no contribution to the momentum equation. However, in the numerical implementation the *non-interface cells* with red crosses contain non-zero density gradient, resulting in non-zero source terms in the SWENSE momentum equation. The complementary fields are generated in consequence and are responsible for the discrepancies of the SWENSE results and the reference value. It is worth mentioning that the consequence is more serious in the air than in the water, since the air density is much smaller ($\rho_a \ll \rho_w$). In two-phase flow, this problem is well-known as the spurious (or parasitic) velocity [51, 63, 108, 115]. The spurious velocity problem can be alleviated by using the Ghost Fluid Method operators [126], since the GFM takes into account the density jump explicitly and ensures that jump only in the *interface-cells*.

Figure 3.16 shows the interface pressure gradient evaluated using the three SWENSE formulations at the beginning of the simulation with the coarse discretization ($\lambda/\Delta x = 50, H/\Delta z = 10$). Note the fields are scaled by the maxiume value in each figure.

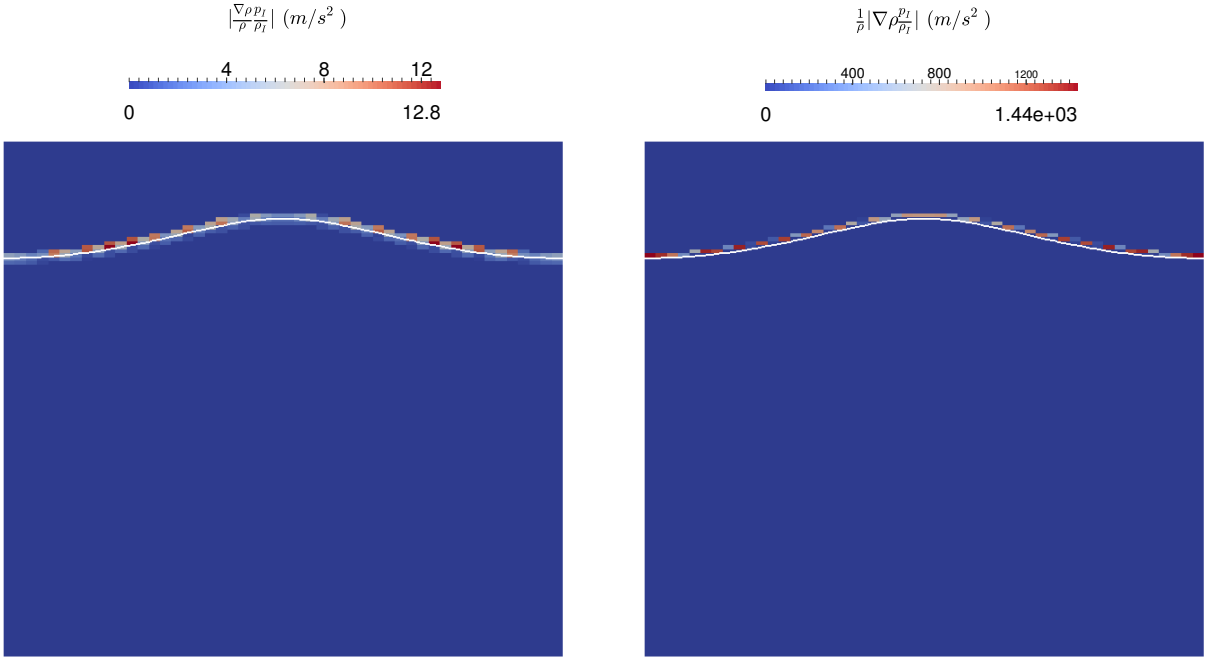

(a) SWENSE-Non-Conservative

(b) SWENSE-Conservative

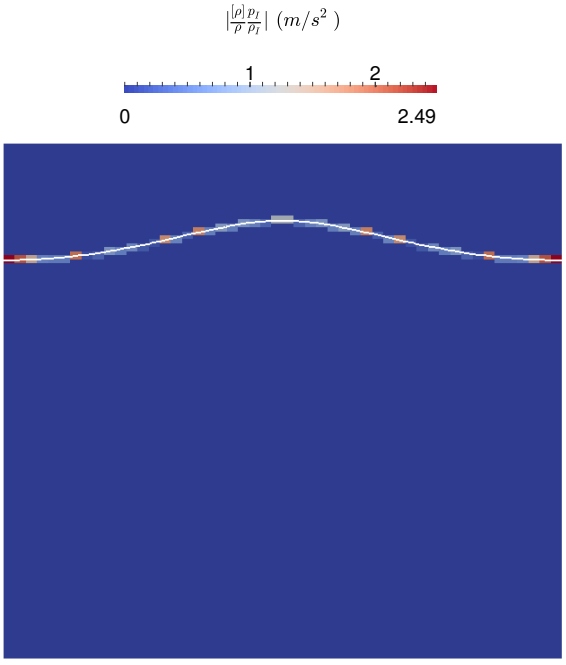

(c) SWENSE-GFM

Figure 3.16: Interface pressure source term at the beginning of the wave propgation case.

This value should be equal to zero in the theory, the numerical results show the numerical errors in each formulations. Note the difference between the non-conservative and the conservative formulations (Fig. 3.16(a) and 3.16(b). The difference is caused by the diffrent evalution of the reversed density term $(\frac{1}{\rho})$.

- In the SWENSE-Non-Conservative: the reversed density $\frac{1}{\rho}$ is evaluated together with the others terms in the interface pressure term to calculate $\frac{p_I}{\rho_I}\frac{\nabla\rho}{\rho}$ at the cell faces and then reconstructed in the cell center.
- In the SWENSE-Conservative: $\frac{p_I}{\rho_I}\nabla\rho$ is evaluated at the cell faces and then reconstructed in the cell center, and then divided by the density ρ in that cell, which makes the result more significant in the air.

A one dimensional case in Fig. 3.17 is used to illustrate this difference. Since the $\frac{p_I}{\rho_I}$ is calculated in the same way, the figure only illustrates the difference in the calculation of $\frac{\nabla\rho}{\rho}$. Note the result of $\frac{\nabla\rho}{\rho}$ in the air cell is equal to 2 in the non conservative formulation while it is equal to 499 in the conservative formulation. With this comparison, it is clear that conservative formulation creates larger numerical errors on the in the air phase than the non conservative formulation.

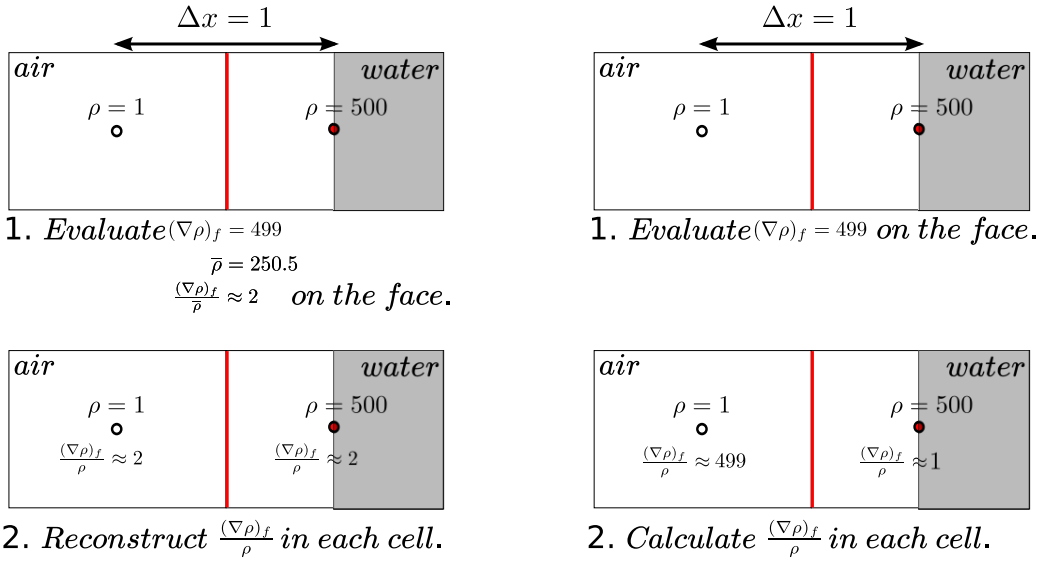

(a) Non conservative (b) Conservative

Figure 3.17: Comparison of the non conservative and the conservative formulation on the evaluation of the the interface pressure term.

The SWENSE-GFM formulation produces the smallest interface pressure source term. The small error in the GFM formulation is due to the approximation of the interface with the $\alpha = 0.5$ contour. This contour is not the exact position of the incident wave free surface, so the incident wave pressure p_I at on this contour may have values different from zero. With this

reduced error, the GFM is able to maintain the incident waves better even with the very coarse discretization.

3.9.5 Wave generation and absorption boundary condition

The periodic boundary condition in the present test case represents the less favorable situation for the wave simulation by the CFD solvers: without any wave generation or absorption condition, the CFD solvers are not able to correct its solution with external wave information; all numerical errors accumulate in the computational domain.

However, in a real wave-structure interaction problem, the far-field boundaries can provide wave generation and absorption conditions. With such boundary conditions, the numerical errors may be eliminated on the boundaries, so that the simulation may produce smaller errors and obtain better accuracy.

To test it, an incident wave propagation case with wave generation and absorption boundaries is carried out. The coarsest discretization ($(\Delta x, \Delta z, \Delta t) = (\lambda/25, H/5, T/100)$) is used. The total computational domain is reduced to 6 wave length long, with 1.5 wave-length-long relaxation zones at both the inlet and the outlet boundaries. Such a configuration is typically used in wave-structure interaction applications. The computational domain is illustrated in Fig. 3.18.

The wave travels from the left to the right. In the relaxation zone, the complementary velocity field ($\mathbf{u}_C$) is gradually blended to zero, and the VOF field is blended to the target VOF field. All the three SWENSE formulations are used in this case. The simulations last for 30 wave periods. The free surface elevation is measured in the center of the computational domain. Its time history and the first harmonic amplitude are plotted in Fig. 3.19.

The time history of the free surface elevation shows a good agreement between all the numerical results and the reference value.

The first harmonic amplitude analysis show that the three solvers produce stable simulation results after a transient stage of about 4 wave periods. The results at the 30th wave period are shown in Tab 3.7. In the table, the first harmonic amplitude of the wave simulation ($\eta^{(1)}$) is normalized by the first harmonic amplitude given by the stream function wave theory ($\eta(1)_{SF}$).

Method	$\eta^{(1)}/\eta^{(1)}_{SF}$
SWENSE-Conservative	98.51%
SWENSE-Non-Conservative	100.85%
SWENSE-GFM	97.92%
NS-Conservative	-

Table 3.7: First harmonic amplitudes of waves over 30 wave periods with the wave generation and absorption boundaries.

The result with *foamStar* cannot be provided with the same configuration. Indeed, the simulation of *foamStar* stopped quickly due to a stability problem in the relaxation zone.

3.10 Closure

In this chapter, the novel two-phase SWENSE method has been proposed. It follows the functional decomposition procedure from the original single-phase SWENSE method, and is

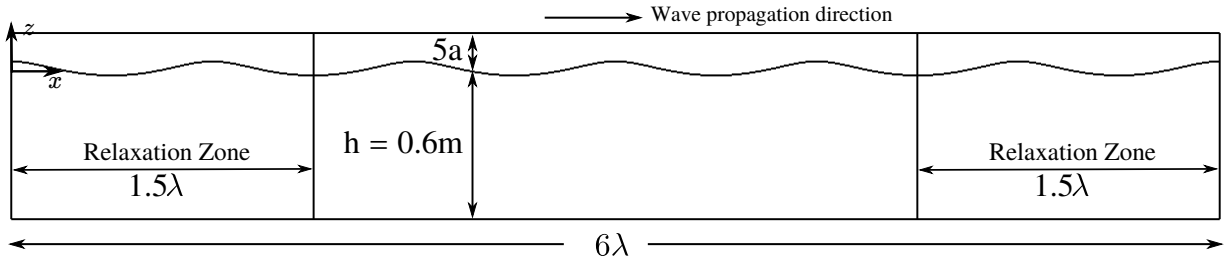

Figure 3.18: Computational domain for the regular wave propagation case with wave generation and absorption boundaries.

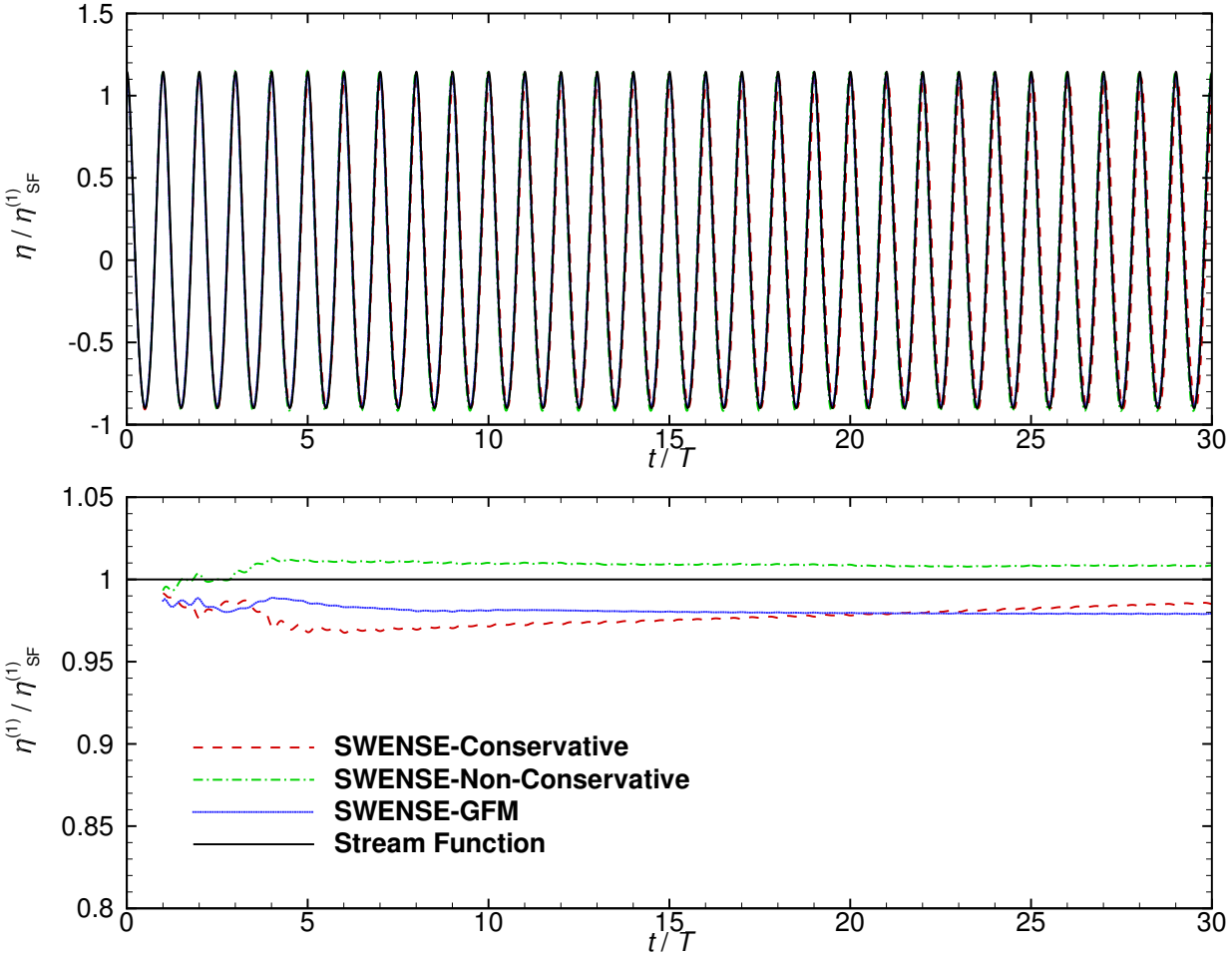

Figure 3.19: Comparison of the three SWENSE formulations with wave generation and absorption conditions.

extended for two-phase CFD solvers.

The differences between the single-phase and the two-phase SWENSE methods have been discussed. Two main differences lie in the computational domain and the treatment of the free surface boundary condition. These differences require an extension of the incident field in the air-phase and the development of new governing equations and new boundary conditions.

Extension of the incident field in the air

The spectral wave models can extend the incident fields and the definition zone of Euler equations to an arbitrary domain (see Section 2.2.5). In the present two-phase method, they are extended in the air. Such extension provides a smooth incident velocity across the free surface, but will lead to unrealistic incident fields in the air, *e.g.*, oscillating *incident wind* velocity. This choice is valid as long as the air effects are negligible, which is the case for most wave-structure problems.

Modified Euler equations

A modified Euler equation has been introduced to overcome the difficulty of the mismatched density in a two-phase solver and the single-phase wave model. A modified incident pressure is defined with the actual density of the two-phase flow ρ and the incident density ρ_I, as follows:

$$p_I^* = \rho \frac{p_I}{\rho_I}$$

Three sets of two-phase SWENS equations

Three sets of governing equations have been derived for the two-phase SWENSE method. All the three sets of governing equations share the same VOF transport equations and the same continuity equation, as follows:

$$\frac{\partial \alpha}{\partial t} + \mathbf{u}.\nabla\alpha = 0$$
$$\nabla.\mathbf{u}_C = 0$$

The momentum equation is provided in the non-conservative form, the conservative form and the Ghost Fluid Method (GFM) form.

The non-conservative form:

$$\frac{\partial \mathbf{u}_C}{\partial t} + \mathbf{u}.\nabla\mathbf{u}_C + \mathbf{u}_C.\nabla\mathbf{u}_I = -\frac{\nabla p_C}{\rho} - \frac{p_I}{\rho_I}\frac{\nabla\rho}{\rho} + \frac{\nabla.\left(\mu\left(\nabla\mathbf{u}_C + \nabla\mathbf{u}_C^T\right)\right)}{\rho}$$

The conservative form:

$$\frac{\partial \rho\mathbf{u}_C}{\partial t} + \nabla.(\rho\mathbf{u}\mathbf{u}_C) + \rho\mathbf{u}_C.\nabla\mathbf{u}_I = -\nabla p_C - \frac{p_I}{\rho_I}\nabla\rho + \nabla.\left(\mu\left(\nabla\mathbf{u}_C + \nabla\mathbf{u}_C^T\right)\right)$$

The GFM form:

$$\frac{\partial \mathbf{u}_C}{\partial t} + \mathbf{u}.\nabla\mathbf{u}_C + \mathbf{u}_C.\nabla\mathbf{u}_I = -\frac{\nabla p_C}{\rho} + \nu\nabla^2\mathbf{u}_C$$

All the three momentum equations have the theoretical ability to keep the incident wave kinematics with coarse CFD mesh, since the source terms are equal to zero for the incident wave propagation problem.

Boundary conditions for two-phase SWENSE method

The boundary conditions for the two-phase SWENSE method has been defined. They are summarized in Tab 3.8, where n is the normal direction on the boundary surface.

	body wall	atmosphere	far-field
α	$\frac{\partial \alpha}{\partial n} = 0$	$\frac{\partial \alpha}{\partial n} = 0$	$\alpha = \alpha_I$
$\mathbf{u}_C$	$\mathbf{u}_C = -\mathbf{u}_I$	$\frac{\partial \mathbf{u}_C}{\partial n} = \mathbf{0}$	$\mathbf{u}_C = \mathbf{0}$
p_C	$\frac{\partial p_C}{\partial n} = 0$	$p_C = 0$	$\frac{\partial p_C}{\partial n} = 0$

Table 3.8: Boundary conditions for the two-phase SWENSE method

Implementation in OpenFOAM

The proposed governing equations have been implemented in a two-phase solver *foamStar-SWENSE*, in the framework of OpenFOAM. The standard Finite Volume method is used to discretize the governing equations. The coupling of VOF-velocity-pressure is solved with the PIMPLE algorithm. The Ghost Fluid Method is adapted from the work of Vukčević [126].

Regular wave propagation test case

A regular wave propagation test case has been used to test the proposed SWENSE formulations. Four discretizations have been compared. The finest mesh contains 200 cells in one wave length, and the coarsest mesh contains only 25 cells per wave length. The comparison shows the SWENSE methods can always produce more accurate results than the conventional Navier-Stokes solver (*foamStar*). However, the wave damping problem happens also in the SWENSE solvers after a few wave periods on the coarsest mesh. This observation is contradictory to the theoretical properties of the SWENSE equations.

The cause of this wave damping has been investigated. It is found that the numerical error of the interface pressure term in the momentum equations creates non-zero complementary fields. This numerical error generates spurious complementary velocity field in the air phase. This problem is the most serious with the conservative form govering equations. The use of the Ghost Fluid Method is able to reduce this numerical error, and thus its results are much closer to the reference value even on the coarsest discretization.

Although the two-phase SWENSE solvers are not able to keep the incident wave accurate in a periodical computational domain due to the accumulation of the numerical errors, they are still very advantageous when the wave generation and absorption boundary conditions are applied. These boundary conditions are able to absorb the numerical error on the boundaries and avoid it from accumulating. In a wave propagation test case with the wave generation and absorption boundary conditions, all the three SWENSE formulations are able to produce accurate incident wave results for a long simulation time. With a very coarse mesh (25 cells per wave length and 5 cells per wave height), the SWENSE methods are able to produce waves with less than 2% difference from the reference value.

Chapter 4

Incident field reconstruction on CFD mesh

This chapter focuses on the reconstruction of spectral waves models' results on the CFD mesh. Such a reconstruction is used in

- the SWENSE method for providing incident wave solutions in the whole computational domain;
- one-way viscous and potential flow coupling for providing incident wave fields at the boundary regions.

This reconstruction procedure is necessary since the spectral wave models express the unknowns with their modal description, while the CFD solvers need the spatial information on the CFD mesh. The reconstruction of the incident wave fields on the CFD mesh can be done in two approaches:

- Analytical evaluation: the incident wave information in a CFD cell is evaluated by substituting the time and the coordinates into the modal functions;
- Interpolation: the results of the spectral wave models are firstly transformed via Inverse Fast Fourier Transform on a coarse rectangular grid and then interpolated to the CFD mesh.

These approaches have been already used in the LHEEA Lab for coupling CFD solvers and spectral waves models [29, 36, 83, 90]. The best practice is to apply the analytical method to reconstruct regular waves given by the stream function wave theory and to use the interpolation method to reconstruct arbitrary waves given by the Higher-Order Spectral (HOS) methods.

This chapter explains these methods and suggests an improvement on the interpolation method. It contains four sections.

The first section outlines the two approaches and compares their efficiency. This comparison will clarify why the analytical method is suitable for reconstructing stream function waves and the interpolation method is suitable for HOS solvers.

The second section focuses on the accuracy of the reconstruction approaches. A special attention is paid on the error of the velocity divergence field ($\nabla.\mathbf{u}_I$) after the reconstruction. This quantity is important to the Volume of Fluid (VOF) method, since the VOF field needs to be convected with a divergence free velocity field. It is found that the interpolation method creates large divergence error and thus needs to be improved.

The third section proposes an improvement on the interpolation method to reduce the velocity divergence error.

The fourth section shows an irregular wave propagation case with *foamStar-SWENSE* coupling with the improved interpolation method.

4.1 Reconstruction of incident wave information from the result of spectral methods

The spectral wave models used in the present work (stream function wave theory, *HOS-Ocean* and *HOS-NWT*) store the incident wave information in the spectral form. Recalling Eqn. (2.2.10) and (2.2.11), the free surface elevation ($\eta_I(\mathbf{x}, t)$) and the velocity potential ($\phi(\mathbf{x}, z, t)$) are expressed as a linear combination of basis functions.

An example of a 2D case in *HOS-Ocean* is shown as follows

$$\eta_I(x,t) = \sum_i A_i^{\eta}(t)\psi_i(x) \tag{4.1.1}$$

$$\phi(x,z,t) = \sum_i A_i^{\phi}(t)\frac{\cosh(k_i(z+h))}{\cosh(k_i h)}\psi_i(x) \tag{4.1.2}$$

where A_i are the complex modal amplitudes, k_i is the wave numbers, and $\psi_i(x)$ are the horizontal basis functions,

$$\psi_i(x) = \exp(jk_i x) \tag{4.1.3}$$

where j is the unit imaginary number $j^2 = -1$.

The incident velocity is calculated by taking the derivative of the velocity potential, as follows

$$\mathbf{u}_I(x,z,t) = \nabla\phi(x,z,t) \tag{4.1.4}$$

which can also be written in the modal form. For example, the velocity ($\mathbf{u}_I = (u_I, w_I)$) can be written as,

$$u_I(x,z,t) = \sum_i A_i^{\phi}(t) jk_i \frac{\cosh(k_i(z+h))}{\cosh(k_i h)}\psi_i(x) \tag{4.1.5}$$

$$w_I(x,z,t) = \sum_i A_i^{\phi}(t) k_i \frac{\sinh(k_i(z+h))}{\cosh(k_i h)}\psi_i(x) \tag{4.1.6}$$

Since the basis functions are standard, only the modal coefficients ($A_i^{\eta}(t)$, $A_i^{\phi}(t)$) are stored and communicated to CFD solvers. The CFD solvers shall use these modal coefficients to reconstruct the incident wave information on the CFD mesh.

Two reconstruction methods are commonly used:

- The analytical evaluation: the incident wave field is calculated for each CFD cell by substituting its coordinates into the basis functions. Since in each CFD cell, one needs to calculate all the N Fourier components, this method is only suitable when the number of modes N is small. In practice, this method is used in regular wave cases only, which use classically $O(10)$ modes for η_I and ϕ.

- Interpolation method: the modal amplitudes of incident wave information are firstly transformed onto uniformly-spaced discretized points by the Inverse Fast Fourier Transform (IFFT) and then interpolated into the CFD meshes. This method takes the advantage of the IFFT so that the evaluation of the basis function is done in an efficient way. This method is suitable work with HOS methods, since the number of modes needed by a HOS solver is often large ($O(10^2) \sim O(10^3)$ for 2D cases and $O(10^4) \sim O(10^6)$ for 3D cases).

4.1.1 Analytical evaluation for the stream function wave theory

The 2D regular waves are calculated with the stream function wave theory [41, 105]. The free surface elevation η_I and the velocity potential ϕ can be written as:

$$\eta_I(x,t) = \sum_{i=1}^{N_1} A_i^{\eta} \psi_i(x - ct) \tag{4.1.7}$$

$$\phi(x,z,t) = \sum_{i=1}^{N_2} A_i^{\phi} \frac{\cosh(k_i(z+h))}{\cosh(k_i h)} \psi_i(x - ct) \tag{4.1.8}$$

where the modal coefficients (A_i^{η} and A_i^{ϕ}) are constant in time. Since the solution of the stream function wave theory often converges with a small number of Fourier modes ($N_1 \approx O(10)$ and $N_2 \approx O(10)$), the analytical evaluation is possible without excessive computational efforts. To evaluate the incident wave information, it just needs to substitute the time (t) and the CFD cell's position (x, z) into Eqn. (4.1.7) and (4.1.8).

An example of a reconstructed regular wave field is shown in Fig. 4.1. The wave is the same as in the previous test case. It has a medium steepness ($ka = 0.24$) and is propagating in deep water condition ($kh = 4.71$). For this case, the stream function wave theory converges with only 9 Fourier components ($N_2 = 9$) for the velocity potential. The CFD mesh contains 100 cells in one wave length and 20 cells in one wave height (corresponding to the medium mesh used in Section 3.9).

4.1.2 Interpolation method for the HOS wave models

The result of HOS wave models (or example, 2D *HOS-Ocean*) can be written as:

$$\eta_I(x,t) = \sum_{i}^{N} A_i^{\eta}(t) \psi_i(x) \tag{4.1.9}$$

$$\phi(x,z,t) = \sum_{i}^{N} A_i^{\phi}(t) \frac{\cosh(k_i(z+h))}{\cosh(k_i h)} \psi_i(x) \tag{4.1.10}$$

Contrary to the stream function wave theory, the HOS wave models use large computation domain (stream function wave theory use only 1/2 wave length) and the modal coefficients ($A_i^{\eta}(t)$ and $A_i^{\phi}(t)$) are time dependent. This nature makes the reconstruction procedure for the HOS wave models more complicated and more time-consuming than the stream function wave theory.

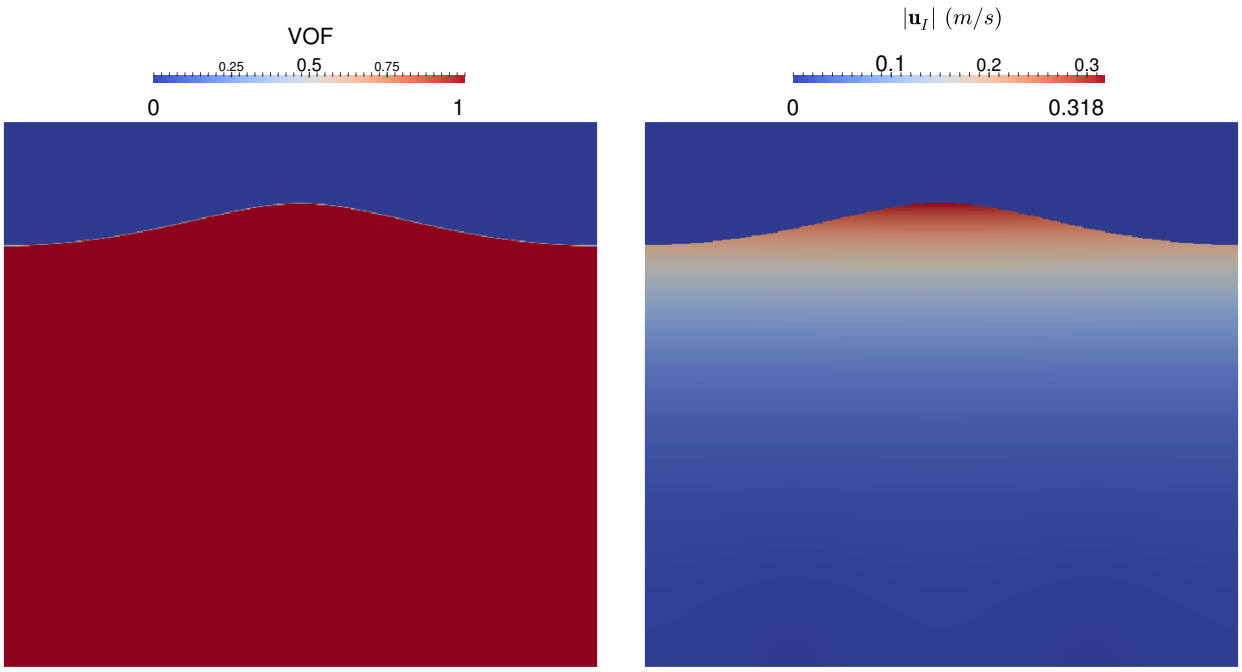

(a) VOF field

(b) Velocity field

Figure 4.1: Reconstructed velocity field from the stream function wave theory. The wave has a steepness of $ka = 0.24$ and the relative depth $kh = 4.71$.

The first difficulty is the large number of Fourier modes (N), which is related to the large computational domain. The number of modes (N) needed by HOS methods is typically $O(10^2) \sim O(10^3)$ in 2D cases and $O(10^4) \sim O(10^6)$ in 3D cases. Evaluating all the Fourier components in every CFD cell is inefficient, especially in multi-directional 3D wave cases.

The second difficulty is that the HOS results are time-dependent, *i.e.*, the coefficients of the Fourier modes ($A_i^\eta(t)$, $A_i^\phi(t)$) change in time, and the time step used by HOS method is often larger than the CFD. An extra temporal interpolation is then required.

For this reason, the HOS wave fields is not reconstructed by the analytical evaluation. Interpolation is used both in the spatial and the temporal domain. Since the interpolation in the temporal domain is trivial, the remainder of this section focuses only on the spatial interpolation.

The interpolation procedure to reconstruct the HOS results on CFD cells is proposed by Ducrozet [36]. The procedure firstly reconstructs the wave information on a coarse rectangular HOS grid via the Inverse Fast Fourier Transform (IFFT) and then interpolates it on the CFD mesh. This procedure can be divided into two steps.

1. IFFT: This step translates the spectral information into spatial domain via the Inverse Fast Fourier Transform (IFFT). After the IFFT, the wave information is available on uniformly spaced points. The number of points is equal to the number of Fourier modes (N) used in the HOS computation. The distance between two points is equal to the shortest wave length of the basis function ($2\pi/k_N$). Take a 2D case as an example:

    - For the free surface elevation ($\eta_I(x,t)$), IFFT transforms A_i^η to N uniformly distributed points in the x direction (see Figure 4.2).

- The reconstruction of the velocity ($\mathbf{u}_I(x, z, t)$) field is done similarly. But since the velocity field also depends on the vertical direction (z), several IFFTs are used. Each IFFT transforms A_i^ϕ to the velocity on N horizontally uniformly distributed points with a given vertical position (z). After this reconstruction, the velocity field is available on a coarse rectangular grid (referred as the HOS grid hereafter) with several horizontal layers. Each horizontal layer contains N uniformly distributed points. Note that the vertical position of these layers can be arbitrarily given, so that a vertical refinement near the free surface is possible.

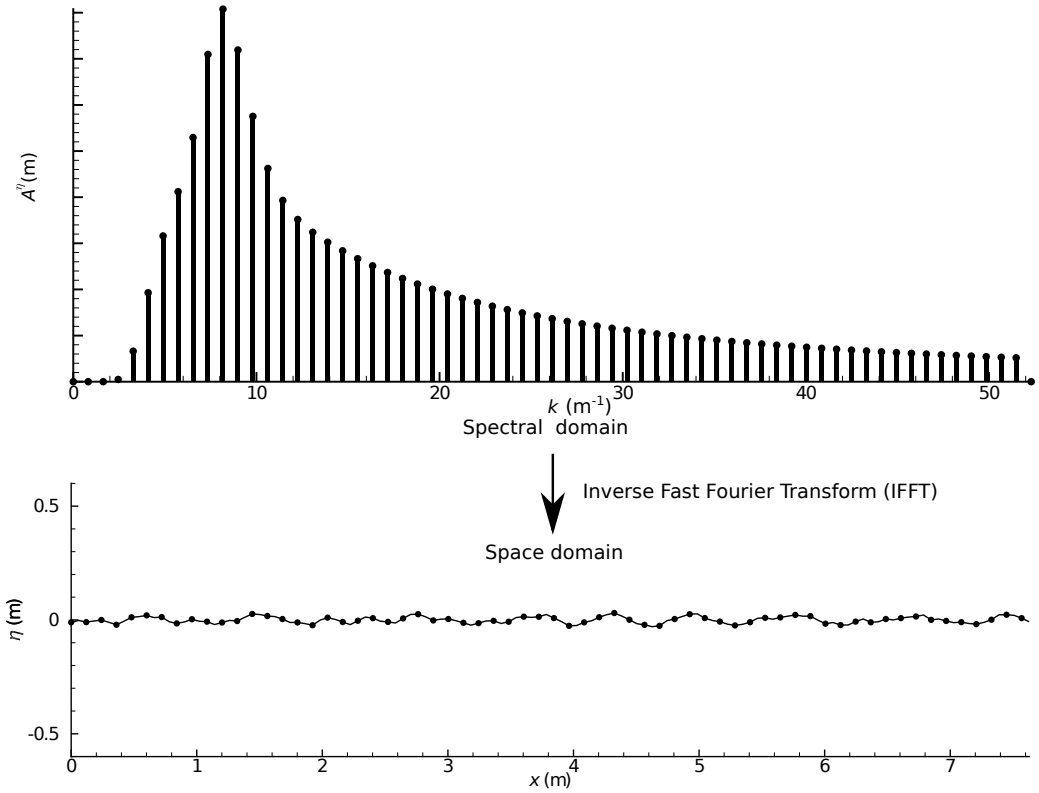

Figure 4.2: Reconstruction of the incident wave solution on the HOS grid. The figure on top illustrates the free surface elevation (η_I) stores in spectral domain as the amplitudes of the Fourier components. The abscissa denotes the wave number k and the amplitudes (A^η) are shown with bars. At bottom, the modal information is transformed in the spatial domain with the Inverse Fast Fourier Transform (IFFT) on uniformly-spaced points.

2. Interpolation: the incident wave information is mapped from the HOS grid on the CFD mesh. This step is necessary since the HOS grid is often different from a CFD mesh. For example, a typical HOS simulation uses 10 points per peak wave length, while CFD solvers usually use around 100 cells. Figure 4.3 shows a comparison of a typical HOS grid (on the left) and a CFD mesh (on the right). The figure is colored by the velocity magnitude. The result on the CFD mesh is interpolated from the HOS grid behind it with the spline scheme.

An example of the interpolation result is shown in Fig. 4.4. The VOF field (on the top) is reconstructed from the free surface elevation (η_I). The velocity field is shown at the bottom. The waves are simulated by *HOS-Ocean* (JONSWAP wave spectrum with $T_p = 0.701s, H_s = 0.028m, \gamma = 3.3$). The HOS simulation contains 10 peak wave lengths with 128 Fourier components.

4.2 Divergence of the reconstructed velocity field

This section analyzes the error caused by the two reconstruction methods. The velocity divergence is used to represent the error. If the reconstruction is accurate, the velocity divergence is equal to zero, since the flow is incompressible. The physical significance of the velocity divergence is the volume change rate. Its unit is s^{-1}. Having $\nabla.\mathbf{u}_I = a(s^{-1})$ means that the cell will have a relative volume change of a in one second.

The VOF method is very sensitive to the velocity divergence. If a velocity field with large divergence is used to convect the VOF field, the boundedness of the VOF field will be strongly violated, and will cause instability problems in the simulation.

In theory, the velocity divergence is equal to zero in the results of the wave models,

$$\nabla.\mathbf{u}_I = 0 \tag{4.2.1}$$

After reconstructed on the Finite Volume mesh, this quantity is calculated by

$$\nabla.\mathbf{u}_I = \sum_f \mathbf{u}_{I,f}.\mathbf{A}_f/\Delta V \tag{4.2.2}$$

where f represents the cell faces of a control volume, $\mathbf{u}_{I,f}$ represents the incident velocity field reconstructed on the cell face center, $\mathbf{A}_f$ the surface vector of the cell face f, and ΔV the volume of the control volume. This value may contains numerical error coming from:

1. Approximating the face-averaged value by the face-center value ($\mathbf{u}_{I,f} \approx \mathbf{u}_I(\mathbf{x}_{cf})$), where $\mathbf{x}_{cf}$ is the face center coordinates.

2. Evaluation of $\mathbf{u}_I(\mathbf{x}_{cf})$ with interpolation.

The first source of error is due to the use of the second-order Finite Volume Method, which affects both the analytical method and the interpolation method. The second source of error is unique for the interpolation method.

4.2.1 Analytical evaluation for the stream function wave theory

Regular waves are reconstructed with the analytical method. So the error comes from approximating the face-averaged value by the face-center value ($\mathbf{u}_{I,f} \approx \mathbf{u}_I(\mathbf{x}_{cf})$) only. This error is related to the use of the second-order accurate Finite Volume Method in OpenFOAM and can be reduced with fine CFD meshes.

To verify this statement, Fig. 4.5 shows the divergence of the incident wave velocity on four different CFD meshes. The wave ($T = 0.7017s$, $H = 0.0575m$) and the meshes are the same with the waves used in Section 3.9. Please note that the figures are plotted with different scales, which are adjusted by the maximum value of each figure.

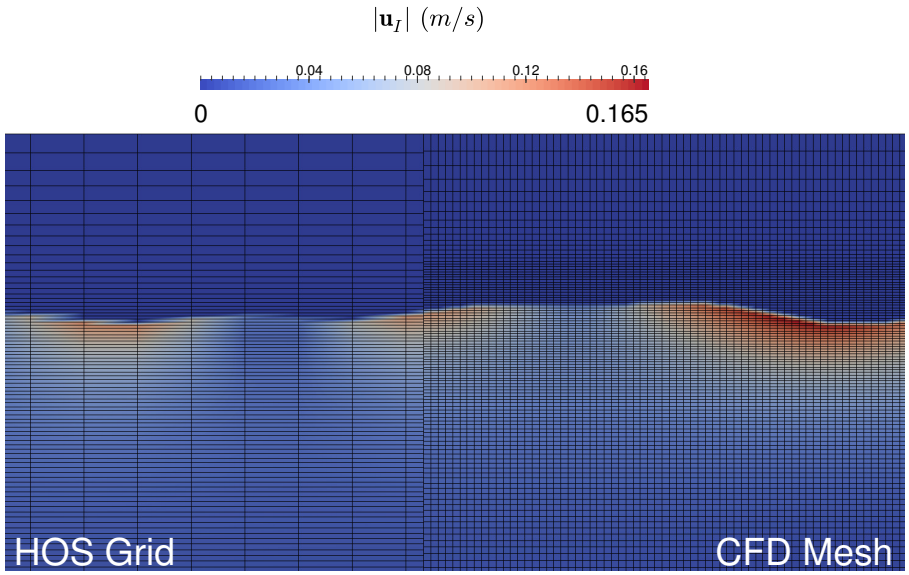

Figure 4.3: Comparison of a typical mesh of an HOS solver (left) and a CFD solver (right).

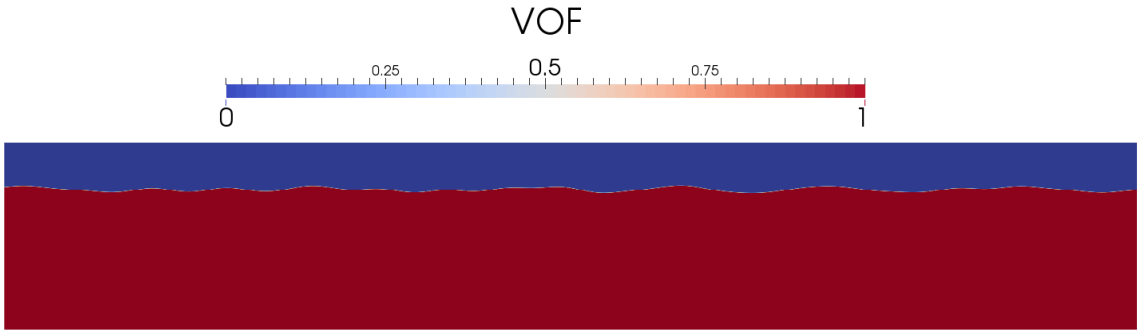

(a) Volume of Fluid Field

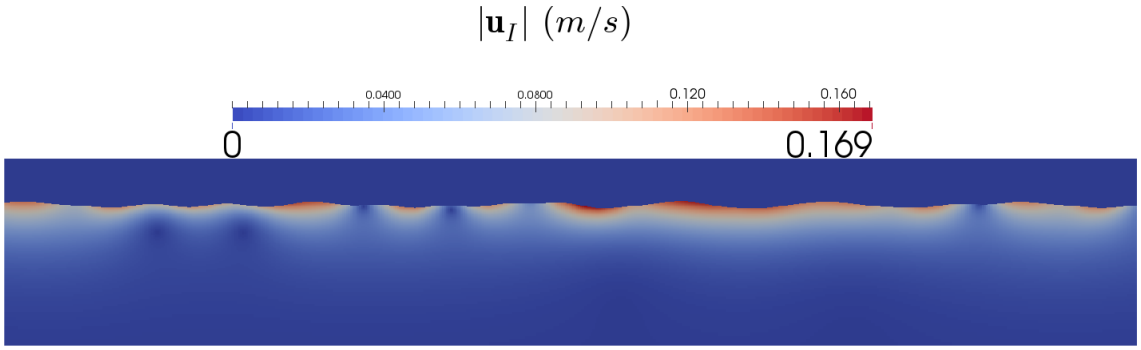

(b) Interpolated velocity field under the free surface

Figure 4.4: Irregular wave field interpolated from the Higher Order Spectrum (HOS) method on the CFD mesh.

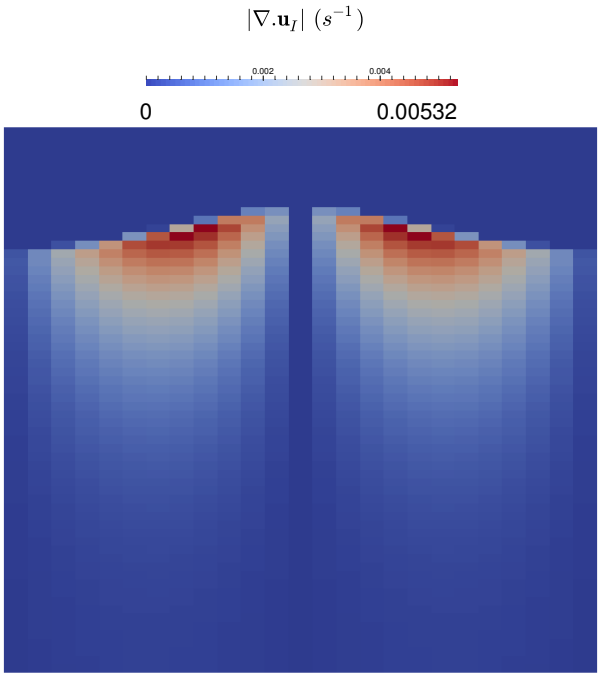

(a) Very Coarse $(\Delta x, \Delta z) = (\lambda/25, H/5)$

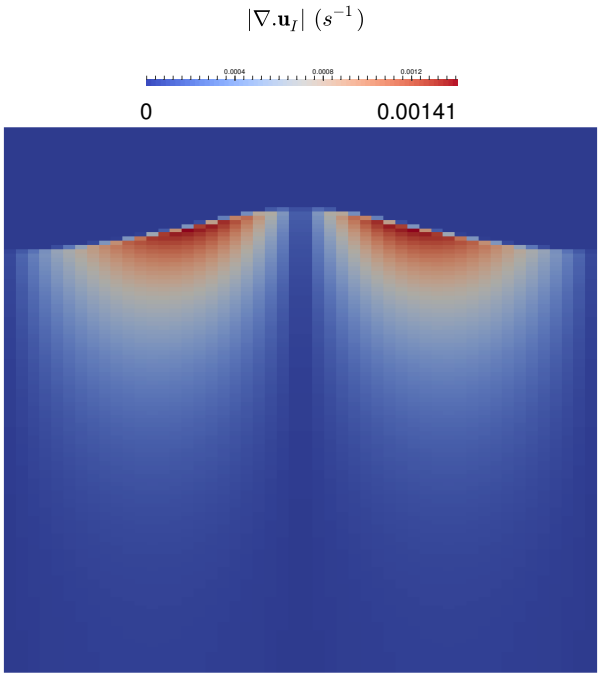

(b) Coarse $(\Delta x, \Delta z) = (\lambda/50, H/10)$

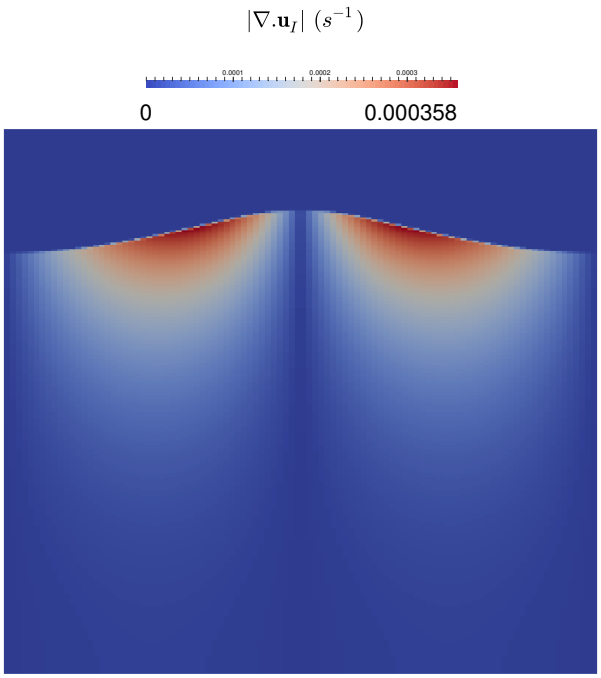

(c) Medium $(\Delta x, \Delta z) = (\lambda/100, H/20)$

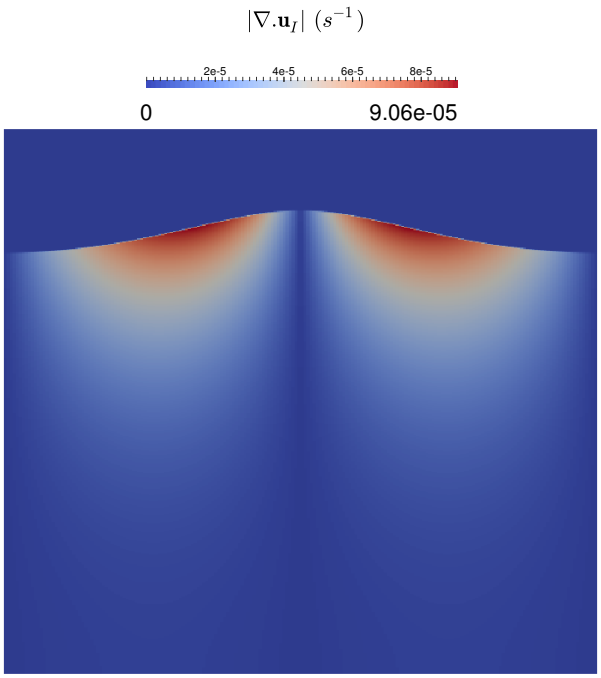

(d) Fine $(\Delta x, \Delta z) = (\lambda/200, H/40)$

Figure 4.5: Divergence of the incident velocity field $(\nabla.\mathbf{u}_I)$ on the CFD mesh reconstructed from the stream function wave theory.

In the figures, it is found that the divergence error is reduced with the mesh refinement. The maximum divergence happens on the *very coarse* mesh. Its value is equal to 5×10^{-3}. This value implies the VOF field will change relatively 5×10^{-3} in one second. Such a magnitude of error is often not harmful to the VOF field, since the time step used by a CFD solver is very small ($\Delta t \ll 1s$). The VOF field convected with this velocity field after 40 wave periods are shown in Fig. 4.6. Note that the maximum and minimum values of the VOF field are very close to 0 and 1. The reconstructed velocity field with the analytical method is often accurate enough to be used with the VOF method.

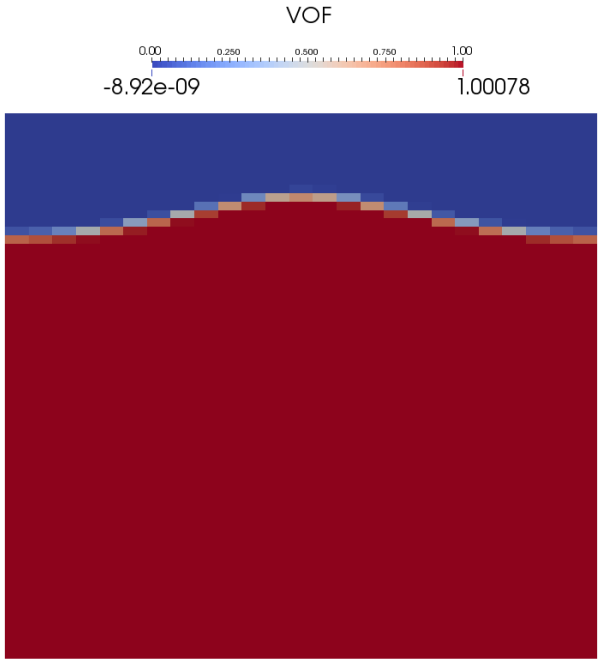

Figure 4.6: Volume of Fluid Field after 40 wave periods with the very coarse mesh configuration.

4.2.2 Interpolation method for the HOS wave models

In the reconstruction of irregular waves, $\mathbf{u}_I(\mathbf{x}_{cf})$ is interpolated from the HOS grid. Extra interpolation error is expected and can not be reduced by refining only the CFD meshes.

Fig. 4.7 plots the divergence of the velocity field reconstructed from a HOS simulation. The irregular waves (JONSWAP wave spectrum with $T_p = 0.701s, H_s = 0.028m, \gamma = 3.3$) are the same with Fig. 4.4. Three different mesh densities are used to check the influence of the CFD mesh. Please note the figures are plotted with different color scales, which are adjusted by the maximum value of each figure. From the figure, it can be observed that

- The velocity divergence is much larger compared to the regular waves (comparing the maximum values: $0.46 \gg 0.005$).

- The error is not reduced with the refinement of the CFD mesh. All the three meshes produce the velocity divergence levels of the same order of magnitude. On the refined mesh, this error is even larger than on the coarse mesh.

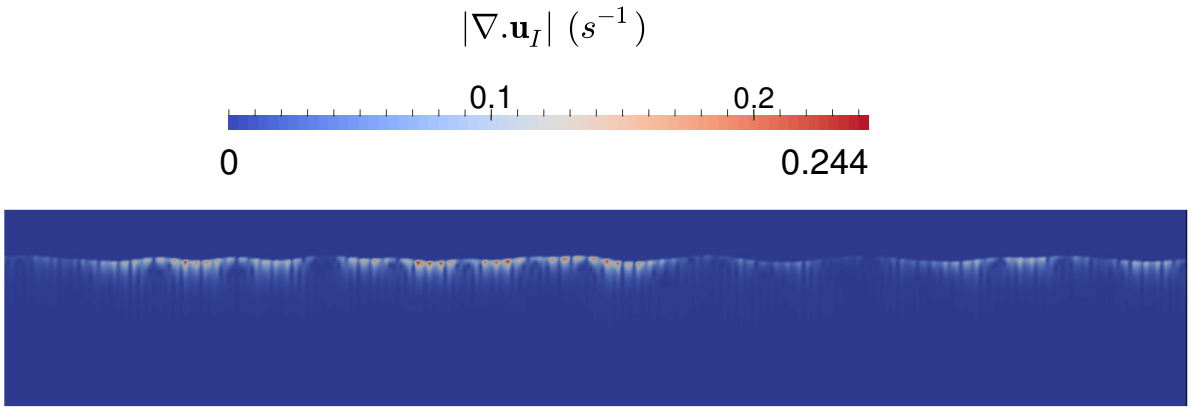

(a) Coarse $(\Delta x, \Delta z) = (\lambda_p/50, Hs/10)$

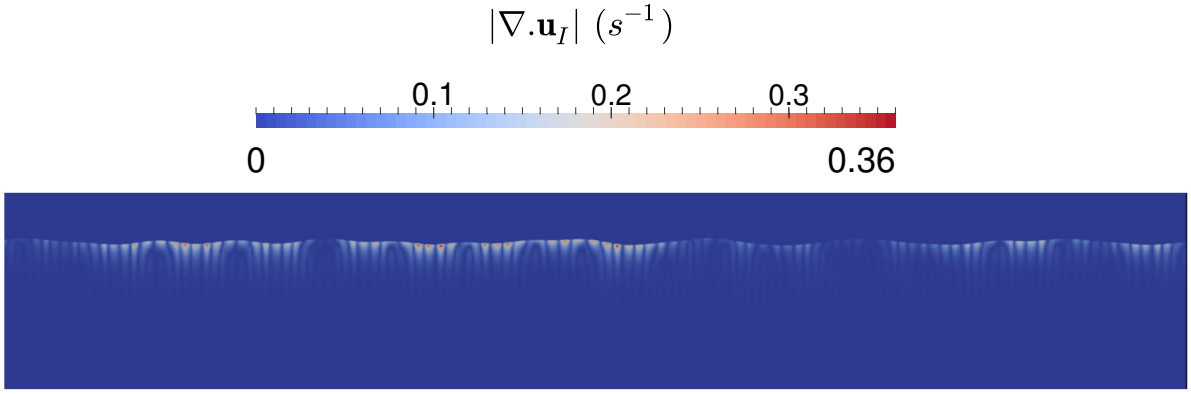

(b) Medium $(\Delta x, \Delta z) = (\lambda_p/100, Hs/20)$

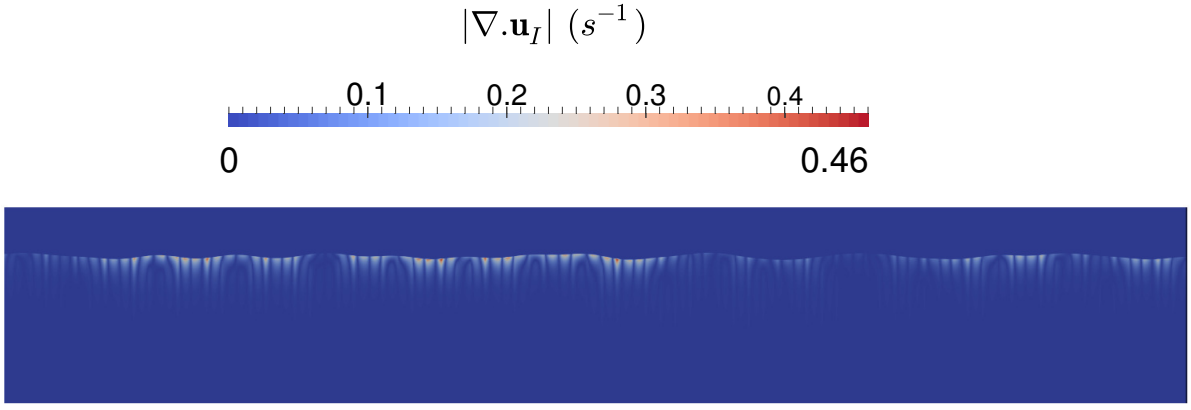

(c) Fine $(\Delta x, \Delta z) = (\lambda_p/200, Hs/40)$

Figure 4.7: Divergence of the incident velocity field $(\nabla.\mathbf{u}_I)$ on the CFD mesh reconstructed from HOS method.

If this velocity field is used to convect the VOF field, it leads to non-physical compression and inflation on the VOF field. In consequence, the calculation of fluid properties (density, viscosity) is affected and may make the simulation unstable. This problem is illustrated in Fig. 4.8. This figure shows a simulation of *foamStar-SWENSE*, in which the interpolation method is used to reconstruct the irregular waves. The medium mesh is used ($(\Delta x, \Delta z) = (\lambda_p/100, Hs/20)$).

- Fig. 4.8(a) shows the initial VOF field calculated from the HOS wave free surface elevation. The initial value is bounded between 0 and 1;
- Fig. 4.8(b) shows the VOF field after one peak periods. The VOF field has some strips with brighter colors in the water side, where the VOF value is smaller or larger than one.

Such a result shows that the interpolation method is unable to provide an accurate enough velocity field for the VOF method. An improvement of the interpolation method is needed.

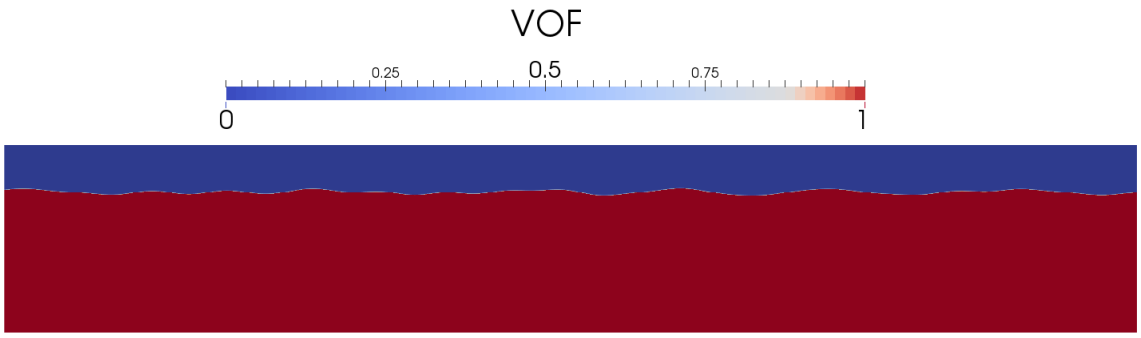

(a) Volume of Fluid Field at $t = 0$

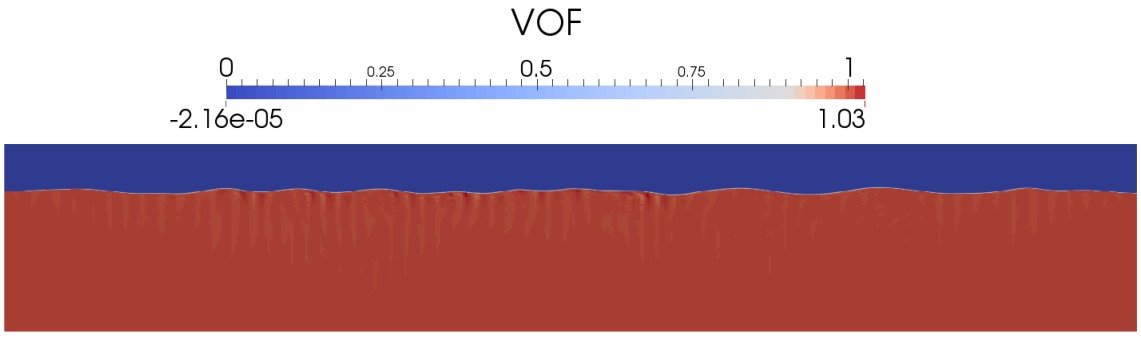

(b) Volume of Fluid Field at $t = T_p$

Figure 4.8: VOF field convected by the irregular wave field interpolated from the Higher Order Spectrum (HOS) method.

4.3 Improvement of the interpolation accuracy with zero-padding technique

In the previous section, it has been proven that the interpolation from HOS grids to CFD meshes is not accurate enough. One of the consequence is that the interpolated velocity field

has a large divergence, which breaks the boundedness of the VOF field and causes instability problems.

The interpolation accuracy issue has been addressed in previous studies at LHEEA Lab. In the PhD thesis of Monroy [90], various interpolation techniques were tested. However, even sophisticated interpolation schemes fail to reduce the error effectively.

Indeed, the vital challenge against an accurate interpolation is the large space interval between two HOS points. As has been mentioned, a typical HOS simulation uses $O(10)$ points per peak wave length, while CFD solvers usually use $O(100)$ cells (see Figure 4.3 for a comparison). It is hard to require the interpolated information to be accurate with such large intervals.

The first reflection is to reduce the interval by using more collocation points in the HOS computation (and more modes as well). However, the nature of the HOS method makes this refinement difficult: an over-refined grid is unnecessary in a physical point of view and may lead to instability problems in the computation [40].

To overcome this difficulty, we propose to refine the HOS grid at the postprocessing stage, *i.e.*, to use a coarse HOS grid for the computation and to use a refined grid only for the reconstruction. The refinement is independent of the HOS computation. It takes the HOS results as input and refines the grid to a user defined level.

The refinement is achieved with a *zero-padding* step in the spectral domain (see Figure 4.9) before the IFFT. After reading the amplitudes of Fourier components from the HOS results, extra modes are added in the end of the spectrum to extend it. The additional modes have zero amplitudes, so that the solution is not influenced by the zero-padding. Moreover, according to the relation between the spectral and the spatial domain in the FFT algorithm, additional Fourier components result in extra spatial points. If the spectrum is extended 2^N times, the distance between two HOS points can be reduced by 2^N times. Note that the factor 2^N is necessary to end up with the original spatial points plus $2^N - 1$ additional points between two original points. In this way, the incident result is available on a finer HOS grid. The interpolation error on the velocity can be reduced consequently. The efficiency is still greatly enhanced compared to the analytical evaluation, since this method still allows the use of IFFT.

To demonstrate the improvement on the interpolation accuracy, a comparison between the original interpolation method and the proposed *zero-padding* refinement method is shown in Fig. 4.10. The CFD mesh has 100 cells per peak wave length and 20 cells per wave height, which is a typical discretization for the wave-structure interaction (the same as the medium mesh in Fig. 4.7). The HOS simulation has 128 computational points in a total length of 10 peak wave-length.

- The direct interpolation method reconstructs the wave information on the original HOS grid with 128 points.

- The zero-padding method reconstructs the result on a grid with 512 points by extending 4 times the number of Fourier modes,*i.e.*, 3 extra points between two original HOS grid points.

Fig. 4.10(a) and Fig. 4.10(b) compare the reconstructed velocity field under the free surface. No difference is observed at this level. However, a clear improvement is observed on the divergence of the velocity field, as shown in the two figures at the bottom. Note the different color scales, showing the maximum divergence in each figure.

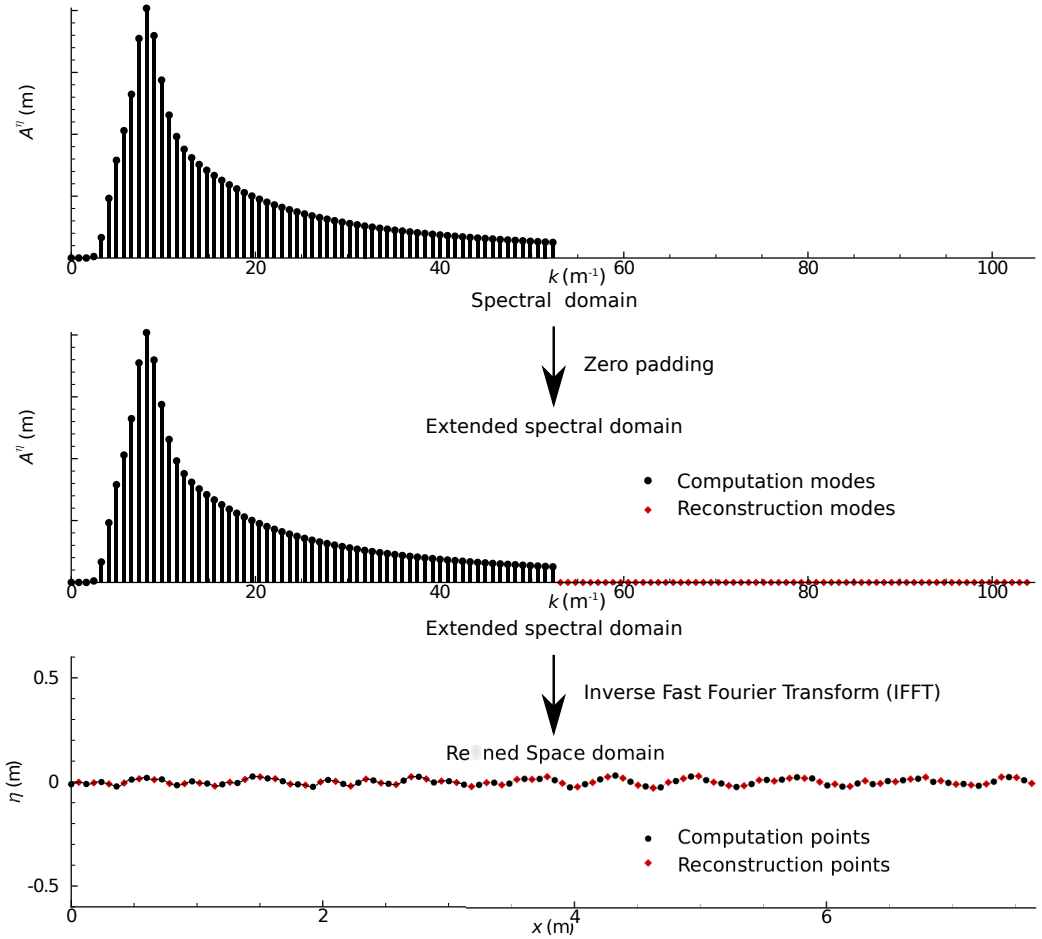

Figure 4.9: Zero-padding procedure for increasing the spatial resolution of the HOS results. The original spectrum of the HOS results (on the top) is extended by adding extra modes of zero amplitudes in the end (in the middle). It results in extra points in the space domain, and thus the HOS mesh is refined.

- In Fig. 4.10(c), the maximum velocity divergence generated by the direct interpolation is equal to 0.36.
- In Fig. 4.10(d), this error is reduced to 0.00451 after the *zero-padding* refinement procedure. The divergence of the interpolated velocity field is reduced by almost 2 orders of magnitude.

This improvement is very beneficial for the VOF method. Figure 4.11 compares the simulation results with the original and the improved interpolation methods. The VOF field is plotted at the same simulation time ($t = T_p$) using the same HOS result as the incident waves. Note the different scales of the legends, which are adjusted by the maximum and the minimum value of the field.

- In Fig. 4.11(a) the reconstruction is done with the direct interpolation. 128 HOS points are used for 10 peak wave length.
- In Fig. 4.11(b) the reconstruction is done with the *zero-padding*. 512 HOS reconstruction points are used for 10 peak wave lengths.

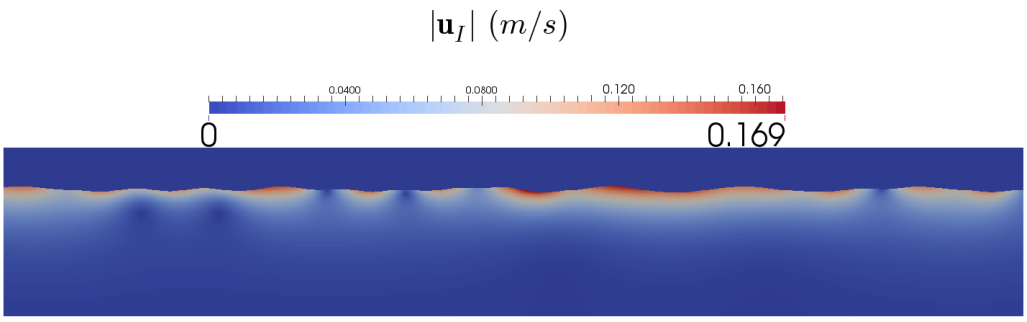

(a) Velocity field: HOS reconstruction mesh with 128 points

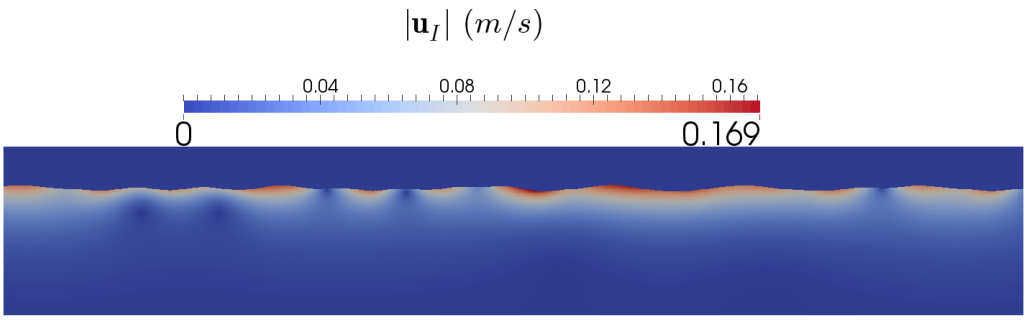

(b) Velocity field: HOS reconstruction mesh with 512 points

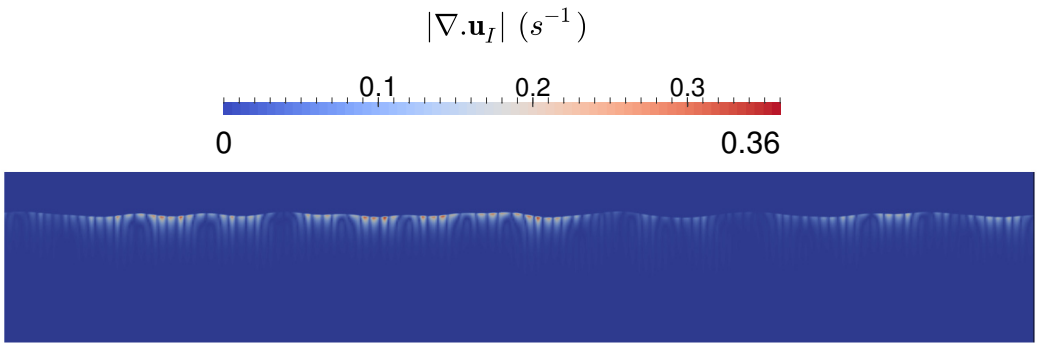

(c) Velocity divergence: HOS reconstruction mesh with 128 points

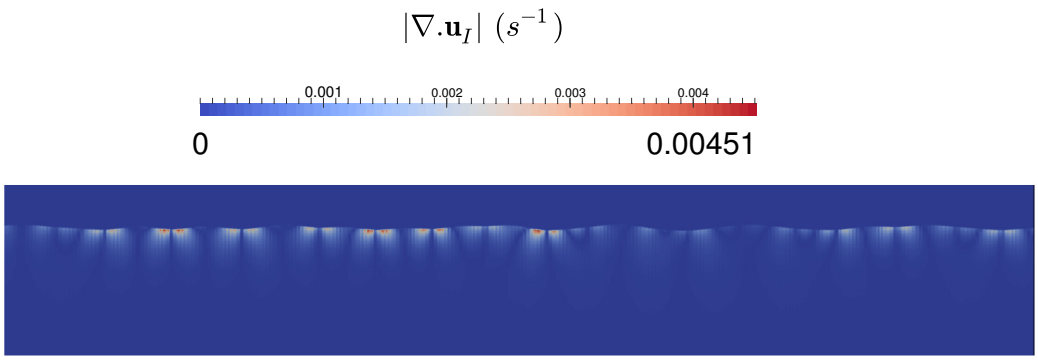

(d) Velocity divergence: HOS reconstruction mesh with 512 points

Figure 4.10: Comparison of the interpolated velocity obtained with the original and a refined HOS grid.

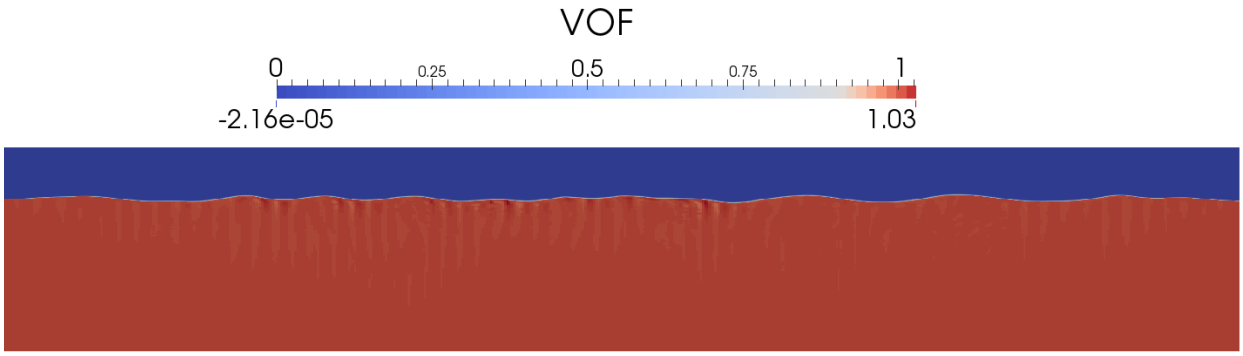

(a) VOF at $t = T_p$: HOS reconstruction mesh with 128 points

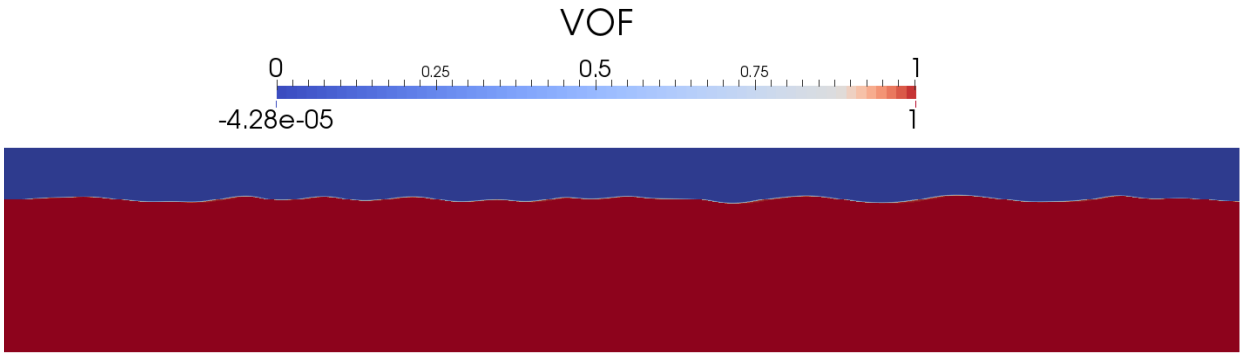

(b) VOF at $t = T_p$: HOS reconstruction mesh with 512 points

Figure 4.11: VOF field before and after the improvement. The same HOS simulation result is used as input.

The quality of the VOF field shows a clear improvement. With this improvement, the two-phase SWENSE method is able to simulate irregular waves. A test case shall be presented in the next section.

4.4 Irregular waves with the two-phase SWENSE method

With the help of the *zero-padding* refinement, the two-phase SWENSE method is able to simulate irregular incident waves just like regular ones. An illustrative test case with *foamStar-SWENSE* (non-conservative form governing equations) is shown in this part.

Test case setup

The test case concerns the propagation of irregular incident waves in a 2D computational domain.

On the incident wave modeling side: the incident waves are generated with *HOS-Ocean* to reproduce the open sea condition. The waves are generated with the JONSWAP wave spectrum with

- $T_p = 0.701s$,

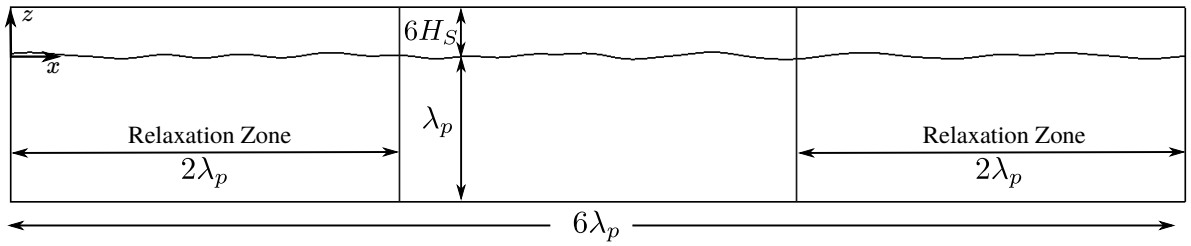

Figure 4.12: Computational domain of the 2D irregular wave propagation test cases.

Parameter	Value
Δt	$T_p/200$
Δx	$\lambda_p/100$
Δz	$H_s/20$

Table 4.1: Numerical discretization for the 2D irregular wave propagation test case

- $H_s = 0.028m$,
- $\gamma = 3.3$.

The *HOS-Ocean* simulation is done with a computational domain of ten peak wavelengths (λ_p). The domain is discretized with 128 HOS computational points, and reconstructed with 512 HOS reconstruction points.

On the CFD simulation side: the computation is conducted with *foamStar-SWENSE* with the non-conservative governing equations. The computational domain (see Fig. 4.12) is representative to the ones used in classical wave-structure interaction problems. It covers the center of the HOS simulation region and contains $6\lambda_p$. The waves travel from the left to the right. At the inlet and outlet boundaries, relaxation zones with $2\lambda_p$ long are used. The origin of the coordinate system is located at the left of the computational domain on the free surface position at rest. The axis x points right and the axis z points up. The water depth is equal to λ_p, the uppermost boundary of the computational domain is located at $z = 6H_s$. The detail of numerical discretization is listed in Tab. 4.1. This configuration has been tested, and considered able to provide converged results.

The VOF field is initialized according to the HOS result. A zero complementary velocity field is given in the beginning. The boundary conditions of the inlet, the outlet, and the bottom are set as far-field, and the atmosphere boundary condition is applied to the uppermost boundary.

Numerical result

The results of *foamStar-SWENSE* is compared with the solution given by *HOS-Ocean*. Figure 4.13 compares the time history of the free surface elevation in the center of the computational domain. The denotes the non-dimensional simulation time, which is defined as t/T_p. In total, 100 peak wave periods are simulated. The vertical axis denotes the non-dimensionalized free

surface elevation. It is defined as the free surface elevation (η) divided the significant wave height (H_s).

Figure 4.13(a) gives an overview of the total 100 peak wave periods. Figure 4.13(b) and 4.13(c) focuses on the first and the last 25 peak wave periods. A good agreement between the result of *foamStar-SWENSE* and the result of *HOS-Ocean* can be observed. Both the wave amplitude and the wave phase are well-kept by *foamStar-SWENSE*. Even after 100 peak wave periods, the simulated waves are still in good agreement with the reference HOS value. This result demonstrates that the combination of the zero-padding procedure and the two-phase SWENSE method is able to simulate long-time irregular waves generated by the HOS wave models.

Discussion

The result of *foamStar-SWENSE* is generally in good agreement with the result of *HOS-Ocean*, illustrating the capacity to simulate irregular waves with the SWENSE method. The simulation is stable, showing that the interpolation error in the reconstructed incident field is acceptable with the help of the *zero-padding* technique. Figure 4.14 shows the VOF field at $t = 100T_p$. The boundedness of VOF is still well maintained.

Besides the general good agreement, Figure 4.13 also reveals small discrepancies when large waves appear (e.g., $t \approx 6.5T_p$, $t \approx 19T_p$, $t \approx 69T_p$). The result of *foamStar-SWENSE* seems to over predict the crests of such waves. Other discrepancies are also observed in small-amplitude waves (*e.g.*, from $75T_p$ to $80T_p$). The reasons leading to the discrepancies are discussed as follows.

- The over prediction of the wave crest position may be associated to the over prediction of the wave crest velocity in the HOS reconstruction. In the present work, the incident wave velocity is reconstructed from the velocity potential to ensure an isovolume velocity field. However, this approach overpredicts the velocity of wave crests, especially when the wave is steep [36].

- The differences related with the small amplitude waves may be due to the relatively low CFD resolution. The CFD mesh may not be fine enough to capture accurately small waves, since the mesh is given as ($\Delta z = H_s/20$). For example, a wave with $H = 0.4H_s$ has only 8 cells per wave height in the vertical direction in the present test case, while a wave whose wave height is equal to H_s contains 20 cells in the vertical direction.

4.5 Closure

The reconstruction of incident wave field given by the spectral wave models on the CFD mesh has been addressed.

Two existing reconstruction approaches are outlined in the first section. Considering the computational cost, the wave obtained by the stream function wave theory is reconstructed by the analytical reconstruction approach, while waves obtained by the HOS method is reconstructed by the interpolation method.

The reconstruction error associated with these two methods has been examined in the second section. The attention has been paid on the divergence of the incident velocity field ($\nabla.\mathbf{u}_I$), since this quantity is crucial for the boundedness of the VOF field. The analytical evaluation gives a minor reconstruction error caused by the Finite Volume Method, which is

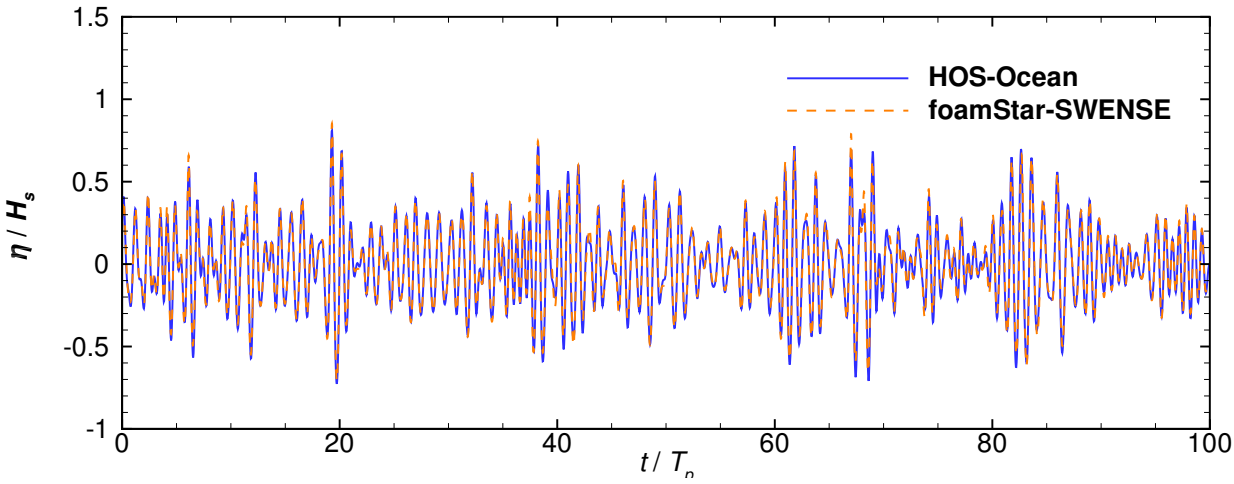

(a) $0 - 100T_p$

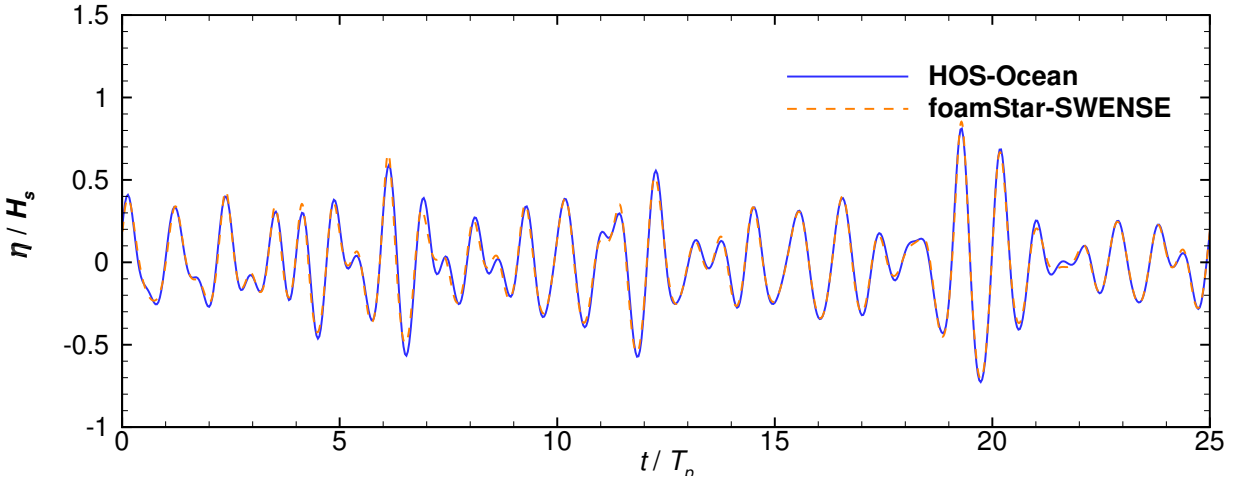

(b) The first 25 wave periods

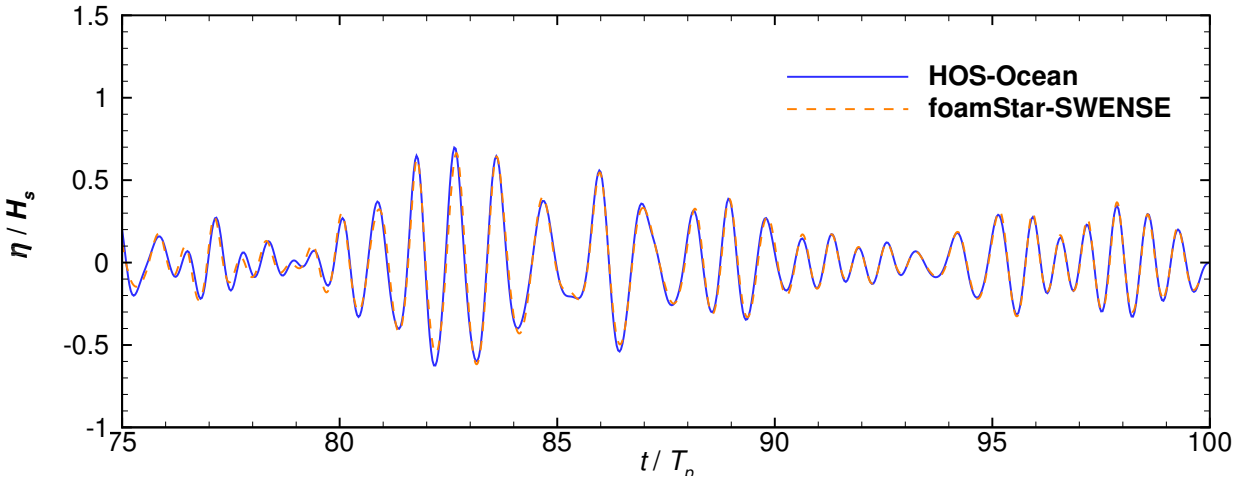

(c) The last 25 wave periods

Figure 4.13: Comparison of the free surface elevation time history obtained with *foamStar-SWENSE* and *HOS-Ocean* (JONSWAP wave spectrum with $T_p = 0.701s, H_s = 0.028m, \gamma = 3.3$.)

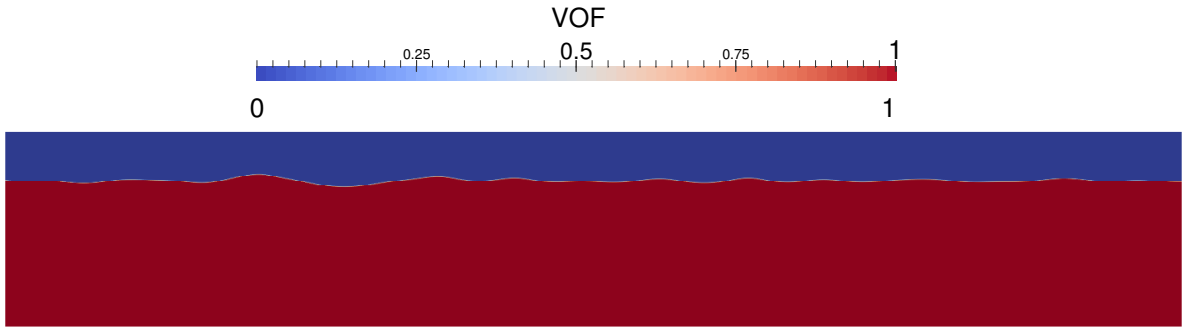

Figure 4.14: Volume of Fluid field at $t = 100T_p$ in the irregular wave propagation case.

negligible. The interpolation method generate a large reconstruction error, caused by the large space intervals of the HOS grid.

A *zero-padding* technique has been proposed to improve the interpolation accuracy. It refines the HOS grid at the postprocessing stage, by extending the modal spectrum and translating the spectrum to a refined HOS grid with the Inverse Fast Fourier Transform algorithm. With this method, the velocity divergence is drastically reduced. The problem of unboundedness of VOF field is much alleviated.

These reconstruction methods are summarized in Tab. 4.2.

	Stream Function	HOS	
Wave type	2D regular wave	2D/3D (ir)regular wave	
Mode number	$\sim O(10)$	2D: $O(10^2 \sim 10^3)$/3D: $O(10^4 \sim 10^6)$	
Time interval	steady	$\Delta t_{HOS} > \Delta t_{CFD}$	
Reconstruction Method	Analytical	Interpolation	Interpolation+zero padding
Reconstruction Error	Small	Large	Small

Table 4.2: Reconstruction method for the stream function wave theory and the HOS solvers.

The above mentioned interpolation technique is made available to the public in an open-source library *Grid2Grid* [28]. The library is developed by the LHEEA Lab at Ecole Centrale de Nantes to connect CFD solvers with *HOS-Ocean* and *HOS-NWT*. It is published with the GNU General Public License v3.0. It can be downloaded from the url: `https://github.com/LHEEA/Grid2Grid`.

The ability to simulate irregular waves by the two-phase SWENSE method is tested with an irregular wave case. The incident waves are obtained from the *HOS-Ocean*. The simulation lasts for 100 peak wave periods. The CFD simulation is stable even though the simulation time is long. The result is also in good agreement with the reference value.

Chapter 5

Validation and applications

After showing the capacity of the proposed two-phase SWENSE method on the propagation of incident waves in Chapter 3 and Chapter 4, this chapter aims at proving the validity and efficiency of the novel two-phase SWENSE method on solving the wave-structure interaction problem.

The main difference between a wave-structure interaction problem and the incident wave propagation is that structures appear in the computational domain and disturbs the incident wave field. Non-zero complementary fields are expected. The two-phase SWENSE method should able to calculate the complementary fields correctly.

Two cases are used to test the present two-phase SWENSE method. The first test case is a simple and classical wave-structure interaction problem. It calculates the higher-order wave forces on a bottom mounted vertical cylinder. This test case is used to:

- Investigate and compare the convergence behaviors of the three two-phase formulations proposed in this thesis;
- Compare the computational time of the three two-phase formulations;
- Validate the two-phase SWENSE method by comparing the results of the SWENSE simulations with experimental data and other numerical results.

The second test case represents a real application scenario. The structure studied is a Catenary Anchor Leg Mooring (CALM) buoy [107]. The simulation reproduces the experimental condition where the buoy is fixed in its hydrostatic position and is exposed to both regular and irregular waves. Violent free surface deformations and viscous effects are expected. This test case is used to :

- Validate and test the robustness of the SWENSE method when dealing with a complex geometry;
- Demonstrate the efficiency of the two-phase SWENSE method by comparing with the conventional two-phase Navier-Stokes method;
- Validate the two-phase SWENSE method by comparing the flow details with the conventional two-phase Navier-Stokes method;
- Validate the irregular wave modeling with the HOS wave model.

5.1 Higher-order wave forces on a vertical cylinder

The calculation of higher-order wave forces on the cylinder is a classical problem in offshore engineering. The engineering background is a so-called "ringing" phenomenon. It is associated with the vibration of the structure excited by the higher-order components of the wave force, since the higher-order components have frequencies close to the natural frequency of the structure. This problem has been addressed in numerous researches with different approaches. Previous studies include asymptotic analytic solutions [44, 84], experiments [68], and numerical simulations with fully nonlinear potential flow approaches [46, 47, 114], *etc.* Since the higher-order forces are often two to five orders of magnitudes smaller than the first order force, these small components are suitable to validate the CFD solvers in detail.

This test case contains two parts.

- A comparative study of the three two-phase SWENSE formulations (the non conservative form, the conservative form, and the Ghost Fluid Method form), using a rather steep wave condition ($ka = 0.24$). It contains:
  - a comparison of the convergence behavior on the inline wave force,
  - a comparison of the computational time,
  - a comparison of the flow details.
- A series of simulations covering eight different wave steepness ($0.06 < ka < 0.24$), with the non conservative SWENSE formulation. The results are compared with the reference data to validate the approach.

5.1.1 Test case setup

The simulation reproduces the experiment of Huseby and Grue [68], where a thin cylinder is exposed to regular waves in deep water. The cylinder has a radius of $R = 0.03m$, being fixed in the water tank with a water depth of $h = 0.6m$. The incident wave frequency f is equal to $1.425Hz$. The experiment setup is illustrated by Fig. 5.1. Different wave amplitudes (a) are used in the experiment, and the data is available for a series of wave steepnesses in the range of $ka \in [0.03, 0.24]$.

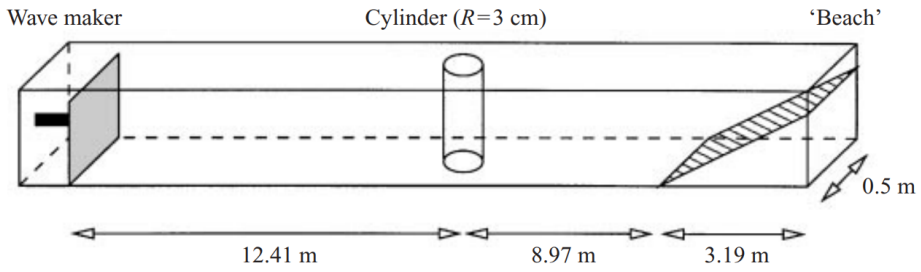

Figure 5.1: The experiment setup, reproduced from the article of Huseby and Grue [68] with permission, copyright Cambridge University Press.

For convenience, the experimental wave tank is not modeled by the simulation. Instead, a cylindrical mesh is used as depicted in Fig.5.2. The cylinder is located in the center of the

domain. The generation of the regular incident waves is achieved by using the stream function wave theory, with the far-field boundary condition in the far-field. This configuration is identical to an ideal experimental condition, where the wave generation is perfectly controlled with no wave reflections on the wave tank boundaries, and no generation of spurious free waves from the wavemaker.

The mesh is adapted to the SWENSE methodology, since the fine mesh is located only near the structure to capture the complementary fields accurately. Coarse cells in the far field contribute to the reduction of the computational cost.

The origin of the coordinate system coincides the cylinder's center-line and is located at the free surface position of the water at rest, axis x points to the incident wave propagation direction and axis z points upward. The domain's radius equals to 2 wave length ($L_r = 2\lambda$). The mesh is refined near the cylinder, and gradually enlarged along the radius direction. In the far-field, the relaxation zone with a length of 1.5λ is used to absorb the disturbed wave field, leaving a pure CFD zone with one wave length $(-0.5\lambda, 0.5\lambda)$. Along the vertical axis, the computational domain extends from the tank bottom at $z = -0.60m$ until $z = 5a$ in the air. In this direction, the meshes are uniform in the zone near the air-water interface. Depending on the incident wave amplitude, the size of this zone is $z \in (-1.5a, 1.5a)$. Out of this refined zone, the cell size increases gradually. A longitudinal symmetry plane is used to simulate only half of the domain. The setup information is summarized in Tab. 5.1. The boundary conditions are listed as follows,

- far-field: $\mathbf{u}_C = 0$, $\alpha = \alpha_I$, and $\dfrac{\partial p_C}{\partial n} = 0$;
- cylinder: body-wall boundary condition, $\mathbf{u}_C = -\mathbf{u}_I$,$\dfrac{\partial \alpha}{\partial n} = 0$, and $\dfrac{\partial p_C}{\partial n} = 0$;
- bottom: free slip boundary condition, $\dfrac{\partial \mathbf{u}_C}{\partial n} = \mathbf{0}$, $\dfrac{\partial \alpha}{\partial n} = 0$, and $p_C = 0$;
- atmosphere: atmosphere boundary condition, $\dfrac{\partial \mathbf{u}_C}{\partial n} = \mathbf{0}$, $\dfrac{\partial \alpha}{\partial n} = 0$, and $p_C = 0$;

Parameter	Value
Cylinder radius (R)	$0.03\,m$
Water depth (h)	$0.60\,m$
Wave frequency (f)	$1.425\,Hz$
Domain size ($L_r \times L_\theta \times L_z$)	$2\lambda \times 180^o \times (h + 5a)$
Relaxation Zone Length (L_{relax})	1.5λ

Table 5.1: Parameters for test case cylinder in waves

5.1.2 Comparison of the three two-phase SWENSE formulations

This section investigates and compares the three two-phase SWENSE formulations, *i.e.*

- Non conservative form

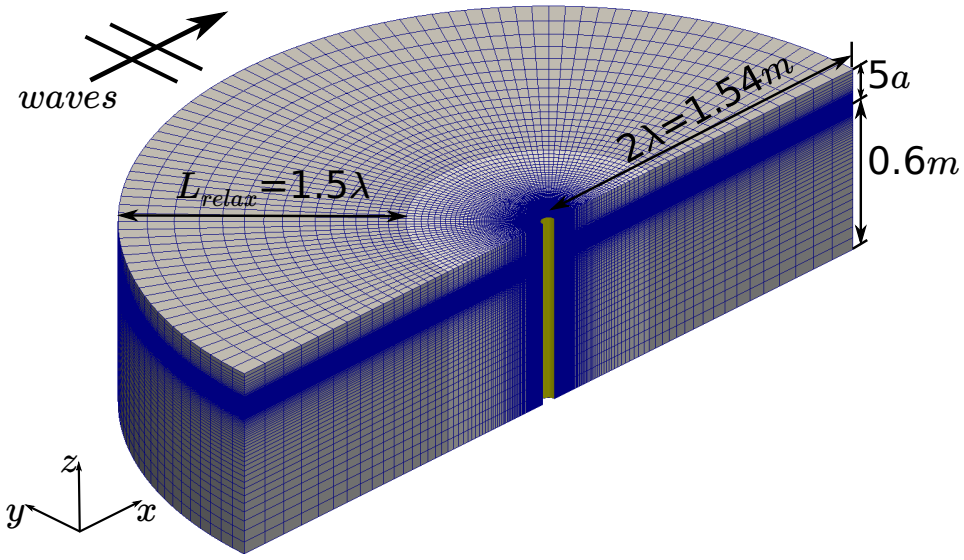

Figure 5.2: CFD mesh used for test case cylinder in waves.

- Conservative form
- Ghost Fluid Method (GFM) form

A systematic convergence study is conducted. Six discretizations are defined to test and compare the three formulations. A rather steep incident waves ($ka = 0.24$) is simulated. The convergence study is conducted with up to the fourth harmonic components of the inline wave force. The flow details and computational time are also presented to compare the different formulations.

Spatial and temporal discretizations

Six discretizations are used in this section. The meshes are changed simultaneously in radial, tangential and vertical directions so that the same topology is kept. The time step is varied with the mesh size, to maintain an identical CFL number in all the simulations. The discretization details are summarized in Table 5.2.

Index	Number of cells in				Time step
	radial direction	tangential direction	a wave amplitude	total	$T/\Delta t$
1	50	40	6	88,000	200
2	60	48	7	155,520	240
3	71	56	9	246,512	285
4	100	80	12	668,000	400
5	140	112	17	1,881,600	560
6	200	160	24	5,504,000	800

Table 5.2: Parameters for the convergence study of the cylinder in waves case

Inline force result

Figure 5.3 plots the time histories of the inline force obtained with the non conservative formulation using the discretization from 1 to 6. The figure consists two parts. The top part plots the inline force from the beginning of the simulation to the 7th wave period. The abscissa denotes the normalized time t/T. The bottom part shows a zoom between the fourth and the fifth wave period. The following statements may be observed from the figure.

- A periodic regime appears after the second wave period in all the three figures.
- The inline force amplitudes gradually increase with the mesh and time step refinement; a converging trend is shown.
- The difference between the coarsest discretization (No.1) and the finest discretization (No.6) is not very significant.

Figures 5.4 and 5.5 are similar to Figure 5.3, but plot the results of the conservative and the GFM form respectively.

Figure 5.6 compares the three SWENSE formulations on a same discretization (No.4), showing a good agreement.

For a better comparison, the time history of the force is transformed to the frequency domain by the moving window harmonic analysis with Fast Fourier Transform (FFT).

Figure 5.7 illustrates this procedure with the result of non conservative SWENSE formulation. The time history of inline wave force (on the top) is transformed to the amplitudes of harmonic components (at the bottom, only the first four amplitudes are plotted). The base frequency is given by the incident wave frequency ($f = 1.425Hz$). Following [68], the harmonic amplitudes are normalized using:

$$F_n^{'} = \frac{F_n}{\rho g R^3} \cdot \left(\frac{R}{A}\right)^n \tag{5.1.1}$$

Note that the first harmonic amplitude is divided by 10 to be plotted in the same figure.

It can be observed that after the transient regime in the beginning, the amplitudes become almost constant (after $t = 3T$). It is then possible to average these values over the last three periods and study the convergence behavior of the solver with them.

This process is done for all the simulations. The raw results are summarized in Tab. 5.3. The relative errors shall be given in Tab. 5.5 after the convergence study.

Estimate the convergence rates

In Table 5.3, each harmonic amplitude is provided with values obtained with six discretizations. These six values are used to estimate the convergence rates of the solvers. The estimation is done with the method proposed by Eça and Hoekstra [42]. It assumes that the discretization error is expressed in a power series of the mesh and time-step size, as follows

$$\epsilon_i = \phi_i - \phi_0 = \alpha(\Delta x)^{p_x} + \beta(\Delta t)^{p_t} \tag{5.1.2}$$

where ϵ_i is the discretization error of the simulation result ϕ_i, while ϕ_0 denotes the exact solution of the mathematical equations. Δx and Δt stand for the characteristic mesh and the time-step size. The five parameters: ϕ_0, α, p_x, β, p_t are determined by the least squares method, *i.e.*, by minimizing the following function, using the six simulation results,

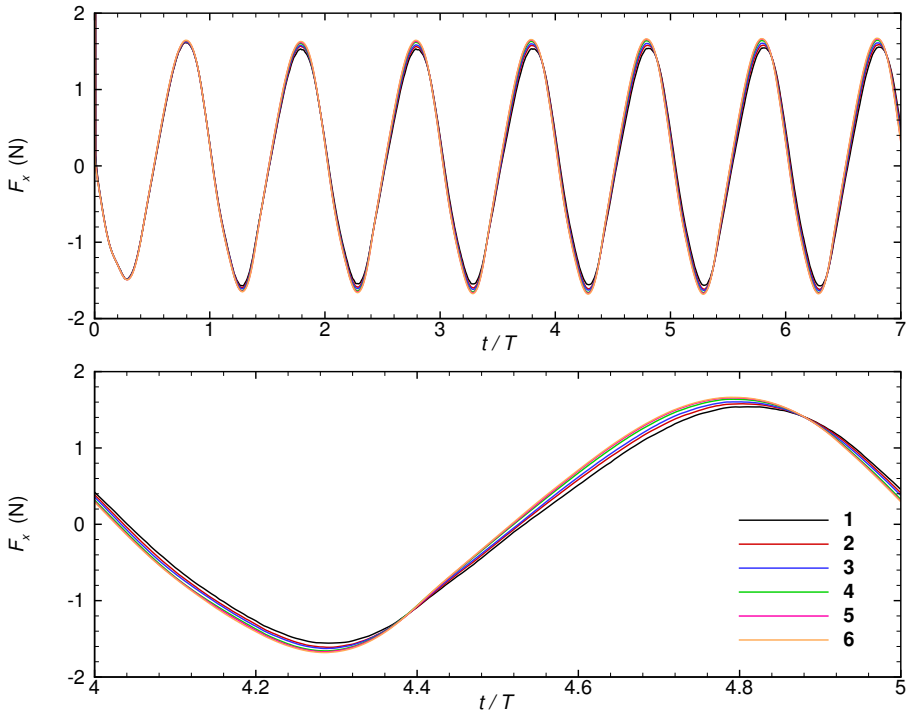

Figure 5.3: Comparison of the time history of inline wave force with different discretizations using the non conservative SWENSE formulation

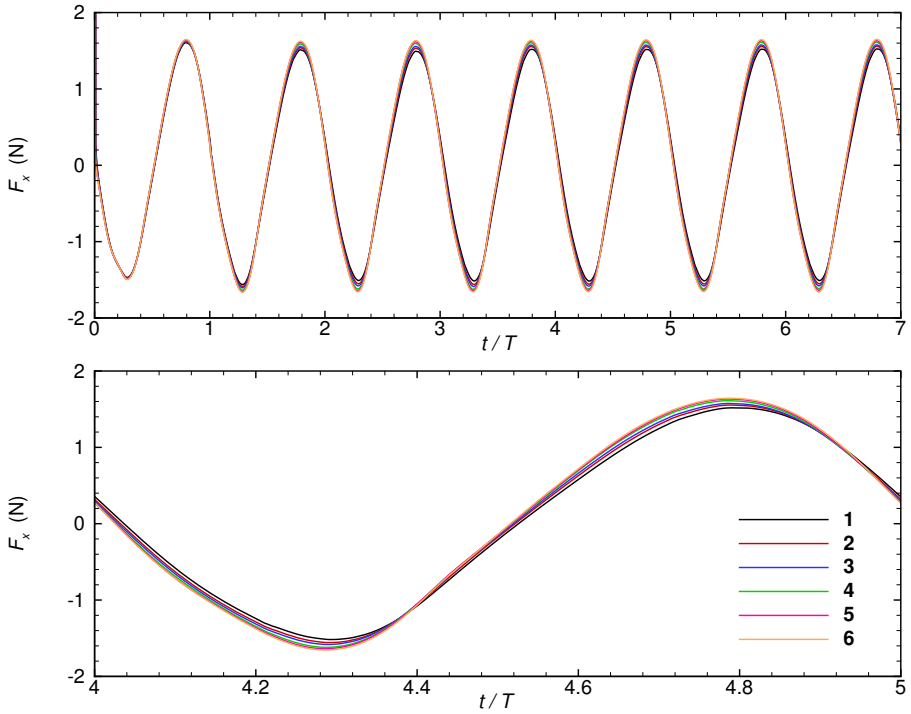

Figure 5.4: Comparison of the time history of inline wave force with different discretizations using the conservative SWENSE formulation

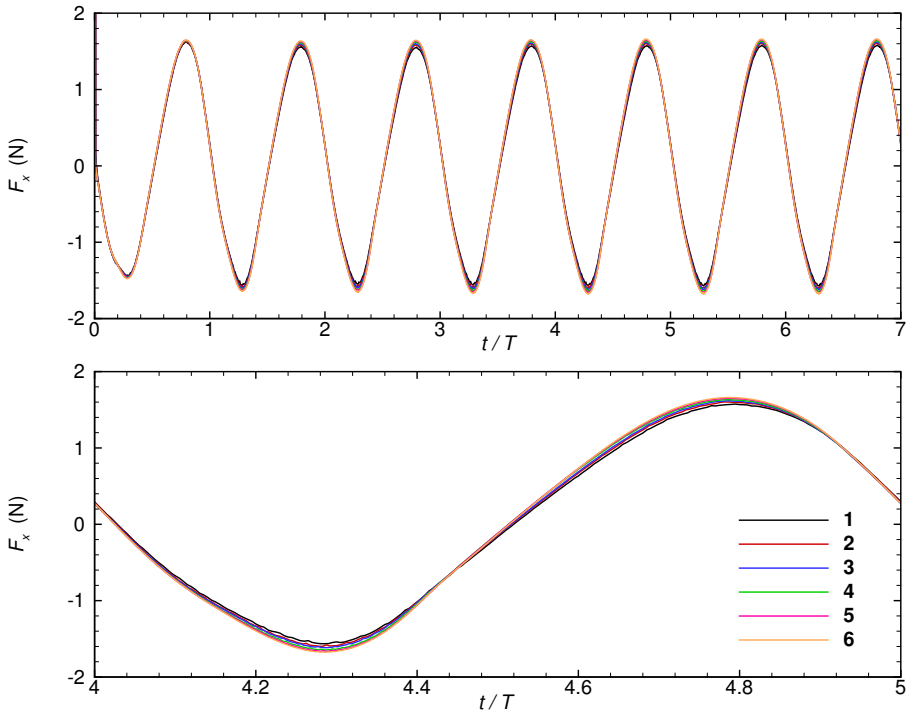

Figure 5.5: Comparison of the time history of inline wave force with different discretizations using the Ghost Fluid Method SWENSE formulation

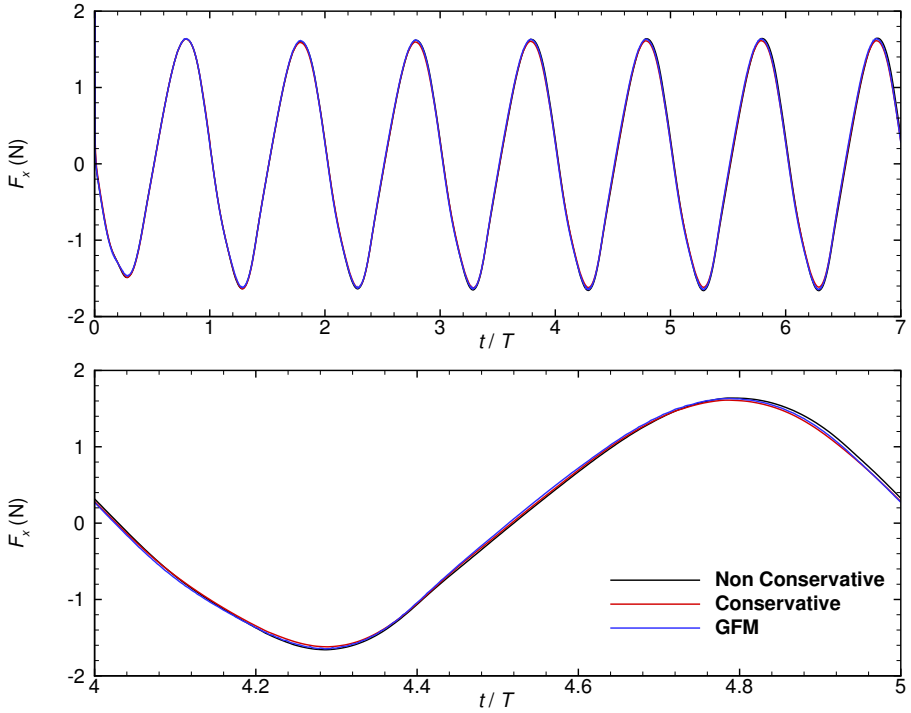

Figure 5.6: Comparison of the inline wave force time history using three two-phase SWENSE formulations with the discretization No. 4

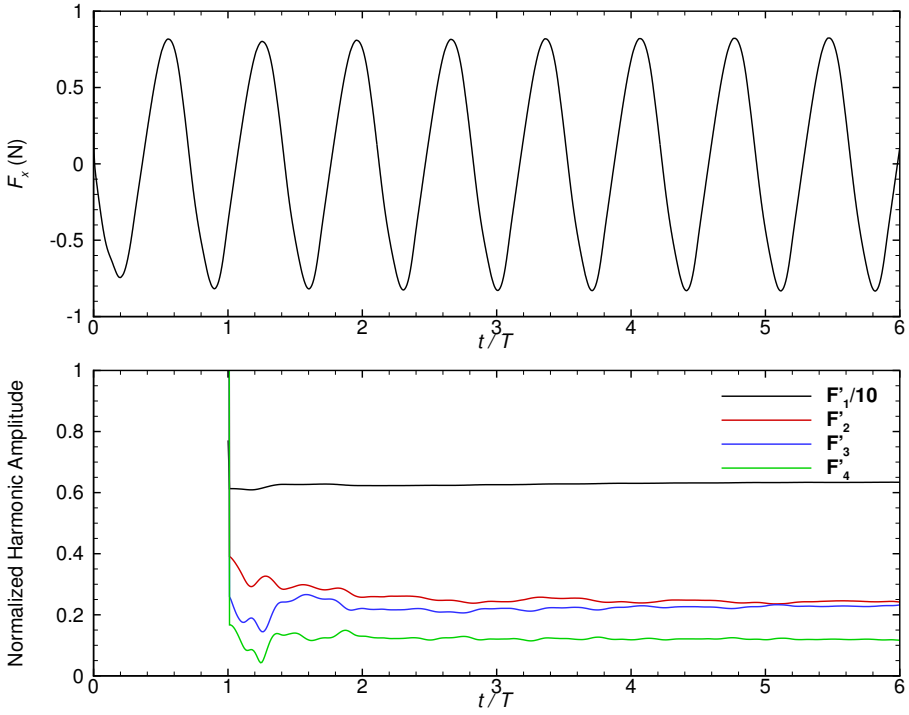

Figure 5.7: Fast Fourier Transform from the force time history (on the top) to the amplitudes of harmonic components (at the bottom). Example of non conservative formulation with Discretization No.4.

$$S_{RE}(\phi_0, \alpha, \beta, p_x, p_t) = \sqrt{\sum_{i=1}^{n_g} (\phi_i - (\phi_0 + \alpha(\Delta x)^{p_x} + \beta(\Delta t)^{p_t}))^2} \tag{5.1.3}$$

This procedure provides the extrapolated *exact* solution ϕ_0 and the order of accuracy in space and time p_x and p_t. These results listed in Tab. 5.4.

Figure 5.8 compares the convergence behavior of the three two-phase SWENSE formulations. The four figures plot the first to the fourth harmonic amplitudes of the horizontal wave force with the time step refinement. Please be aware of the difference scales of the vertical axis. The horizontal axis represents the number of time steps per wave period. Since the mesh size and the time step size are changed proportionally, it also demonstrates the convergence with the mesh refinement. In each figure, the solid lines represent the simulation results obtained by the three SWENSE formulations. The solid lines are extended to the extrapolated *exact* value (ϕ_0) located at the right border.

For the first harmonic amplitude, all the simulation results increase with the mesh and time step refinement. The extrapolated *exact* value (ϕ_0) of the three formulations are very close. In Tab. 5.4, the convergence order of all the three methods are between 1 and 2. In theory, the second-order Finite Volume discretization schemes used in OpenFOAM can provide second order convergence rate. In reality, this order is smaller than two due the combined Euler and Crank-Nicolson schemes in the temporal discretization, and the MULES limiter in the VOF equation, *etc.*

The second harmonic amplitude shows different convergence behaviors of the three SWENSE

Harmonic amplitude	SWENSE formulation	Discretization					
		1	2	3	4	5	6
F_1'	non conservative	5.970	6.127	6.201	6.320	6.381	6.419
	conservative	5.860	5.998	6.079	6.208	6.286	6.351
	GFM	6.020	6.137	6.195	6.297	6.366	6.404
F_2'	non conservative	0.298	0.279	0.257	0.244	0.223	0.220
	conservative	0.189	0.203	0.209	0.221	0.227	0.233
	GFM	0.222	0.220	0.207	0.207	0.202	0.205
F_3'	non conservative	0.176	0.194	0.205	0.226	0.231	0.236
	conservative	0.144	0.163	0.179	0.208	0.227	0.236
	GFM	0.206	0.219	0.227	0.240	0.247	0.242
F_4'	non conservative	0.099	0.115	0.122	0.120	0.117	0.114
	conservative	0.080	0.094	0.101	0.116	0.118	0.122
	GFM	0.113	0.119	0.121	0.124	0.125	0.125

Table 5.3: Harmonic amplitudes of inline wave force obtained with different discretizations.

Harmonic amplitude	SWENSE formulation	Extrapolated Value	Order of convergence	
		(ϕ_0)	space (p_x)	time (p_t)
F_1'	non conservative	6.450	1.9	1.9
	conservative	6.447	1.3	1.3
	GFM	6.461	1.5	1.5
F_2'	non conservative	0.216	1.8	1.8
	conservative	0.241	1.4	1.4
	GFM	0.201	1.8	1.8
F_3'	non conservative	0.241	1.9	2.0
	conservative	0.259	1.2	1.2
	GFM	0.256	1.6	1.6
F_4'	non conservative	0.097	1.0	2.0
	conservative	0.124	2.0	1.9
	GFM	0.125	1.8	1.6

Table 5.4: Estimated exact value and order of convergence for the first to fourth harmonic amplitudes

formulations. The results of the non conservative and the GFM formulations decrease with the refinement, while the conservative formulation increases. The extrapolated value of the three formulations are 0.216, 0.241, and 0.201. A difference of 16% is found between the GFM and the conservative formulations. The difference between the GFM and the non conservative formulations is 7%. The result on the second harmonic amplitude is less accurate than the first harmonic component. This behavior is reasonable since the nature of the wave force at the double incident wave frequency makes the result more sensible to the incident wave quality and the calculated diffracted field [89].

The convergence behavior of the third harmonic amplitude is similar with the first harmonic amplitude. All the simulation results increase with the refinement. The extrapolated values

(ϕ_0) has a maximum 7% difference. The convergence order is also between 1 and 2.

For the fourth harmonic amplitude, the convergence behaviors of the three formulations are different again. The non conservative formulation shows an oscillatory behavior. The results increase with mesh refinement from the discretization No.1 to discretization No.3, and starts to decrease from discretization No.3 to discretization No.6. This oscillatory behavior leads to difficulties in estimating the convergence rate. The verification program provided by [42] gives 1 and 2 as the estimated convergence order, using complex weighting procedures, which make the results on the fourth harmonic amplitude not very reliable. However, the other two formulations show a monotonic convergence behavior and obtain very close extrapolated value.

Relative Errors

Table 5.5 presents the relative error on different discretizations. The relative error is defined with the following equation, according to [42].

$$\delta_i = \frac{|\phi_i - \phi_0|}{|\phi_0|} \tag{5.1.4}$$

Harmonic amplitude	SWENSE formulation	Relative error on discretization (%)					
		1	2	3	4	5	6
F_1'	non conservative	7.4	5.0	3.9	2.0	1.1	0.5
	conservative	9.1	7.0	5.7	3.7	2.5	1.5
	GFM	6.8	5.0	4.1	2.5	1.5	0.9
F_2'	non conservative	38.0	29.1	19.0	13.0	3.2	1.9
	conservative	21.6	15.8	13.3	8.3	5.8	3.3
	GFM	10.4	9.5	3.0	3.0	0.5	2.0
F_3'	non conservative	27.0	19.5	14.9	6.2	4.2	2.1
	conservative	44.4	37.1	30.9	19.7	12.4	8.9
	GFM	19.5	14.5	11.3	6.3	3.5	5.5
F_4'	non conservative*	20.8	8.0	2.4	4.0	6.4	8.8
	conservative	35.5	24.2	18.5	6.5	4.8	1.6
	GFM	9.6	4.8	3.2	0.8	0.0	0.0

*Note: the relative errors of the fourth harmonic amplitude with the non conservative formulation are calculated with the *exact* value of GFM method.

Table 5.5: Relative errors with different discretizations

Table 5.5 shows:

- For the first harmonic amplitude, all the three SWENSE formulations are able to obtain converged results with fine discretizations. Note that when the coarse discretizations are used, the SWENSE method is able to produce results closed to the converged value. When the coarsest discretization is used, the relative errors of the three SWENSE methods are all below 10%. The non conservative and the GFM formulations have smaller errors compared with the conservative formulation.

- For higher-order components, the numerical errors also decrease with the mesh and time step refinement. In general, the GFM formulation produces smaller errors than the other

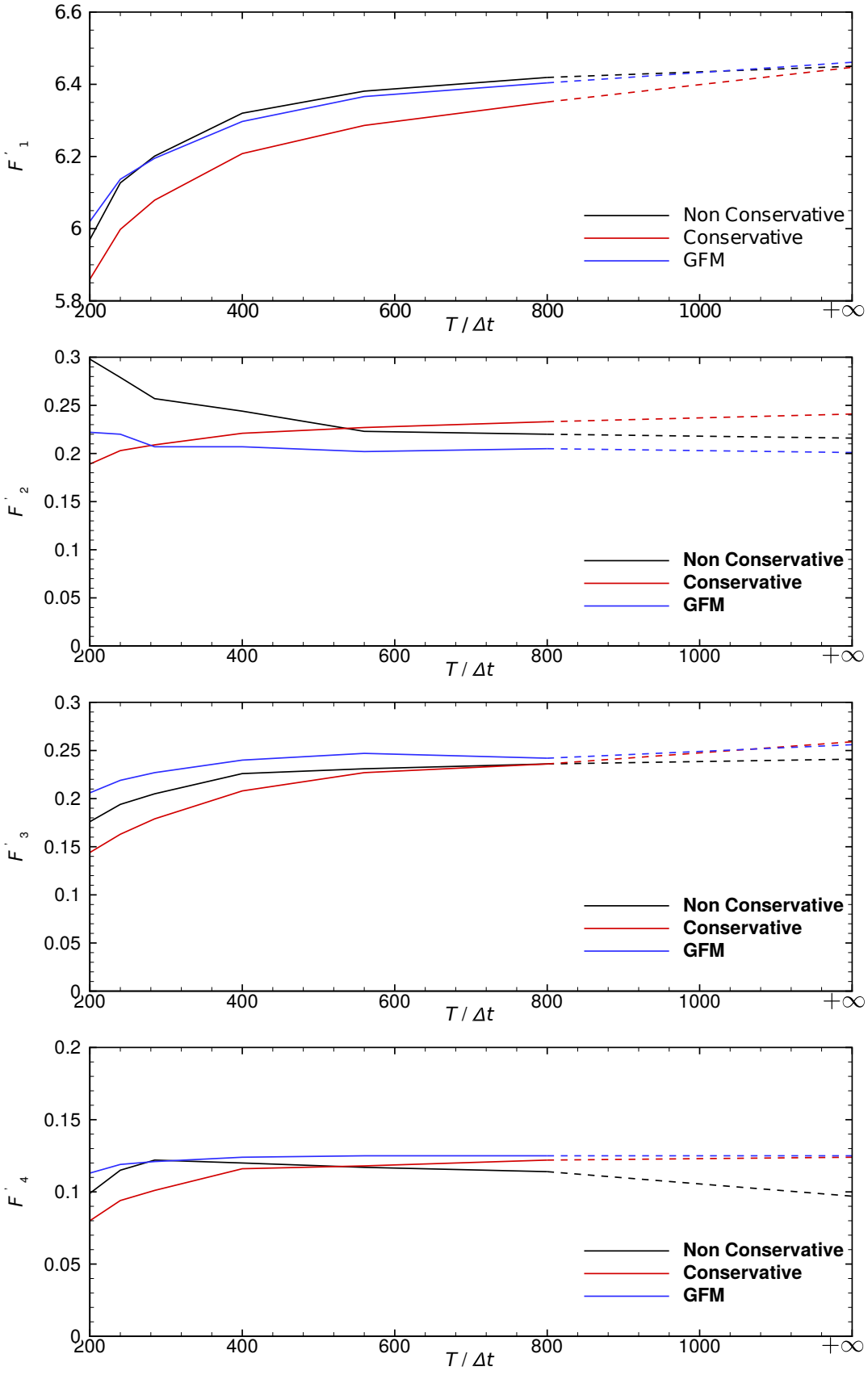

Figure 5.8: Comparison of the convergence behavior of different two-phase SWENSE formulations.

two SWENSE formulations. The higher-order amplitudes contain larger numerical errors than the first harmonic amplitude. This behavior is reasonable since the accurate computation requires more refined discretization. In a practical application case, the mesh does not need to be refined everywhere as in this section; local refinement near the structure can help the SWENSE solvers to capture better this higher order components with a limited increase of total cell number.

Flow details

Figure 5.9 to 5.14 compare the flow details obtained with the three two-phase SWENSE formulations. The figures are snapped from the simulation with the discretization No. at $t = 7T$, when the crest of the incident wave passes the center-line of the cylinder. The solid white line represents the position of the free surface, which is reconstructed by the 0.5 contour of the VOF field ($\alpha = 0.5$). In all the figures the wave travels from the left to the right.

The total velocity ($\mathbf{u}$) is compared in Figure 5.9, it is observed that

- The velocities in the air increase with the height in all the numerical results. This is because the incident wave field is extended in the air. The incident velocity increases with the height.
- The result of the conservative formulation has larger velocity in the air, and the velocity field is much more disturbed than the others. This is due to the different treatment of the interface pressure term in the momentum equation, which as been explained in Section 3.9.4. This large velocity in the air is also a common problem of the two-phase solvers with the conservative momentum equation [29, 126, 129].
- As the air effect is negligible in classical wave-structure interaction cases, it is more significant to focus on the solution in the water only to avoid the distraction. Figure 5.10 compares the velocity field in the water obtained by multiplying the velocity field by the VOF field. A good agreement is observed.

The complementary velocity ($\mathbf{u}_C$) *in the water* is compared in Fig. 5.11 and Fig. 5.12 (zoom). The field is obtained multiplying by the VOF field to get rid of the air part.

- The complementary velocity fields are large near the structure and vanish in the far-field. This is in accordance with the assumption of the SWENSE method.
- The complementary velocity fields obtained by the three SWENSE formulations agree well near the cylinder.

The complementary pressure fields p_C are compared in Fig. 5.13 and Fig 5.14 (zoom). Note that the field in the air is *not* multiplied with the VOF field.

- The complementary pressure fields are remarkable only in the water. In the air, there is almost no visible variation of p_C, since the density of the air is much smaller than the water.
- The complementary pressure fields are large near the structure and vanish in the far-field. This is in accordance with the assumption of the SWENSE method.

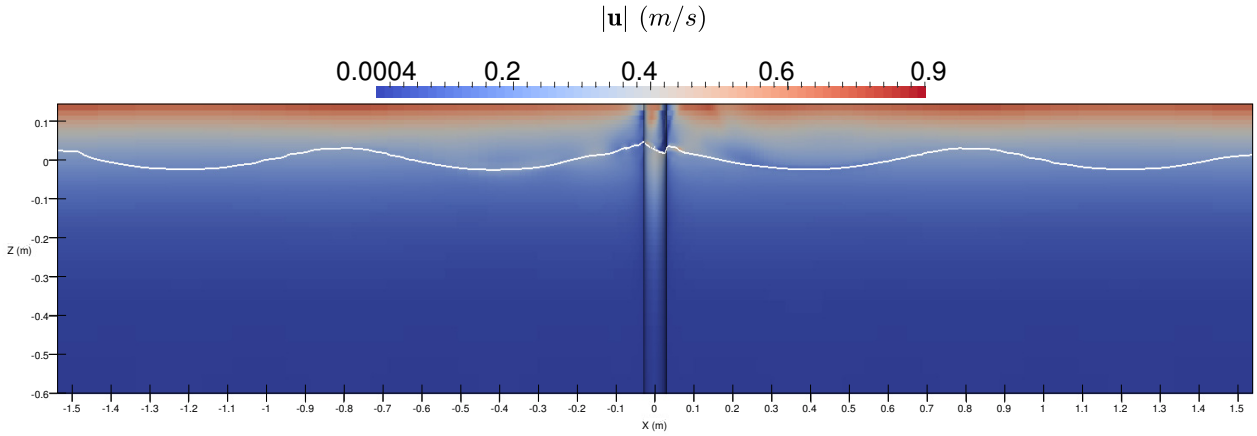

(a) Non Conservative

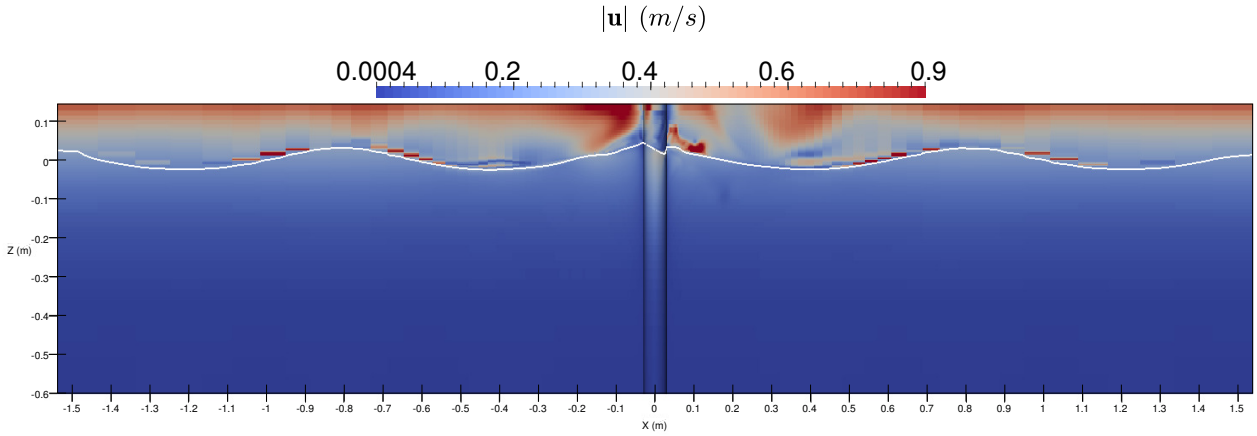

(b) Conservative

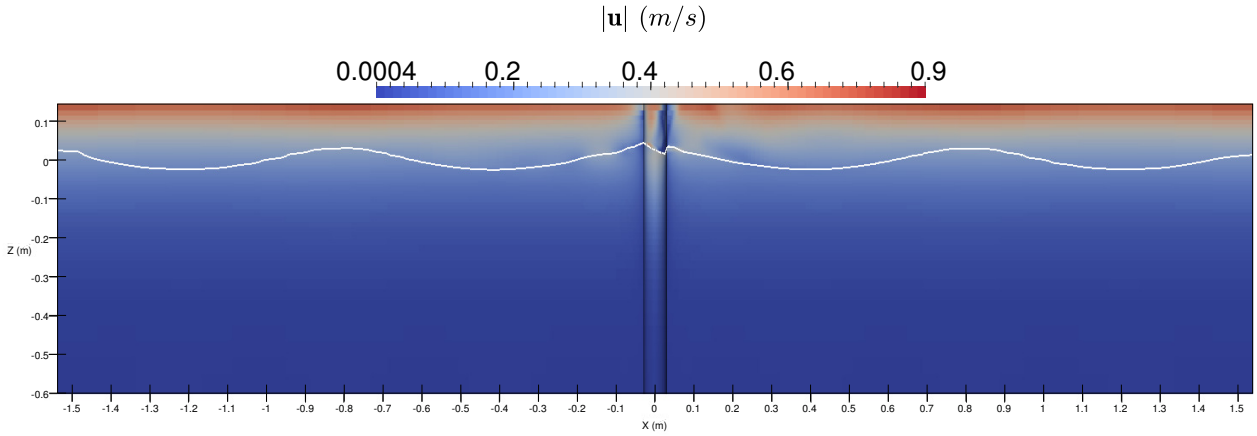

(c) GFM

Figure 5.9: Total velocity fields when a wave crest pass the cylinder ($t = 7T$) obtained by different SWENSE formulations on the discretization No.4.

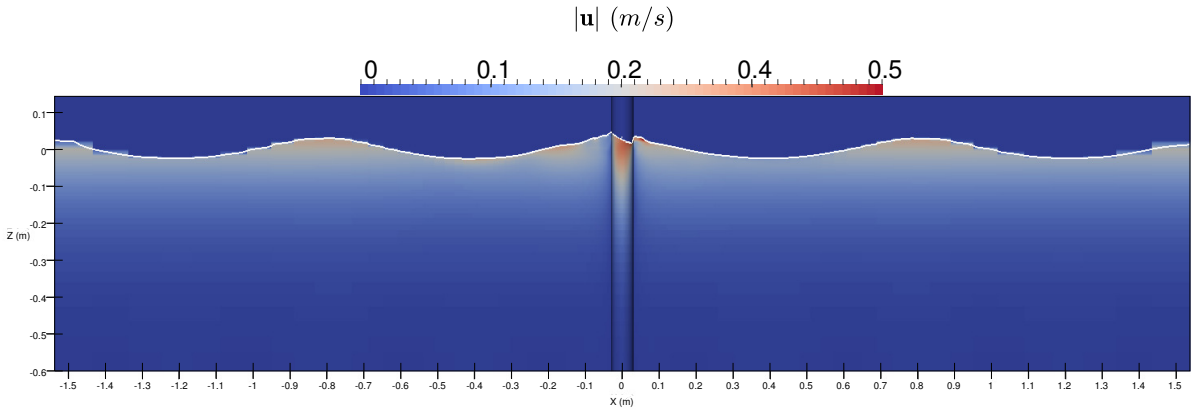

(a) Non Conservative

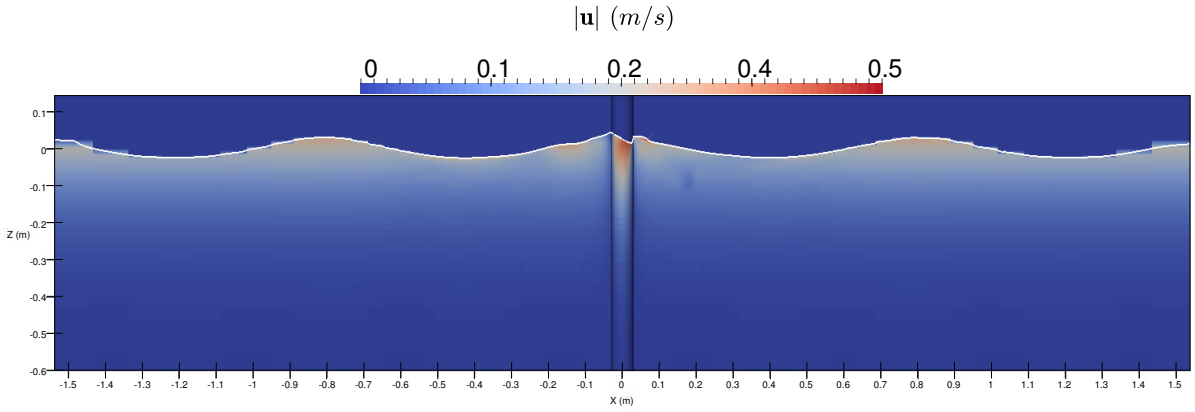

(b) Conservative

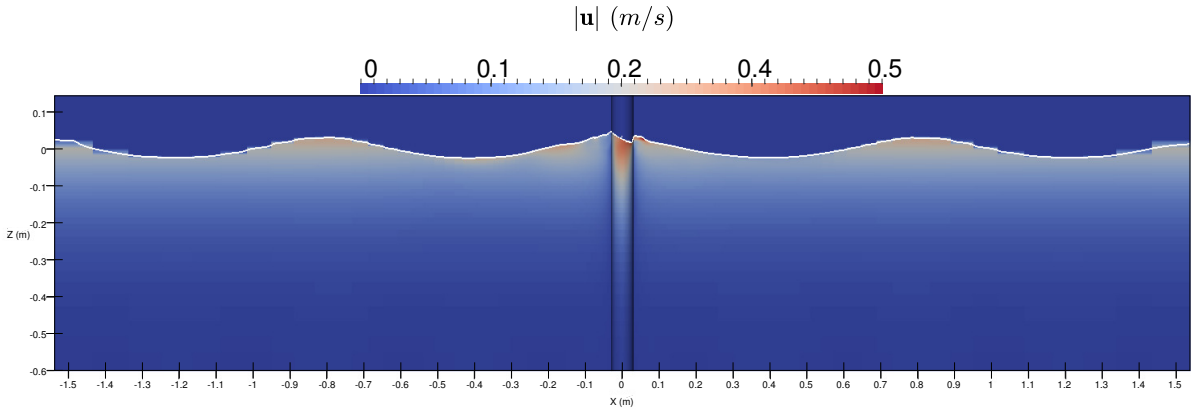

(c) GFM

Figure 5.10: Total velocity fields in the water when a wave crest pass the cylinder ($t = 7T$) obtained by different SWENSE formulations on the discretization No.4.

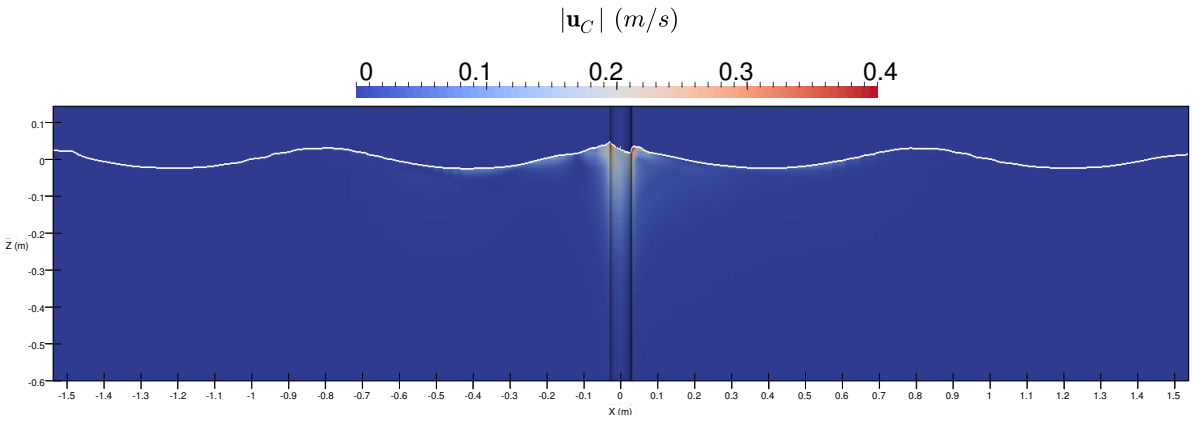

(a) Non Conservative

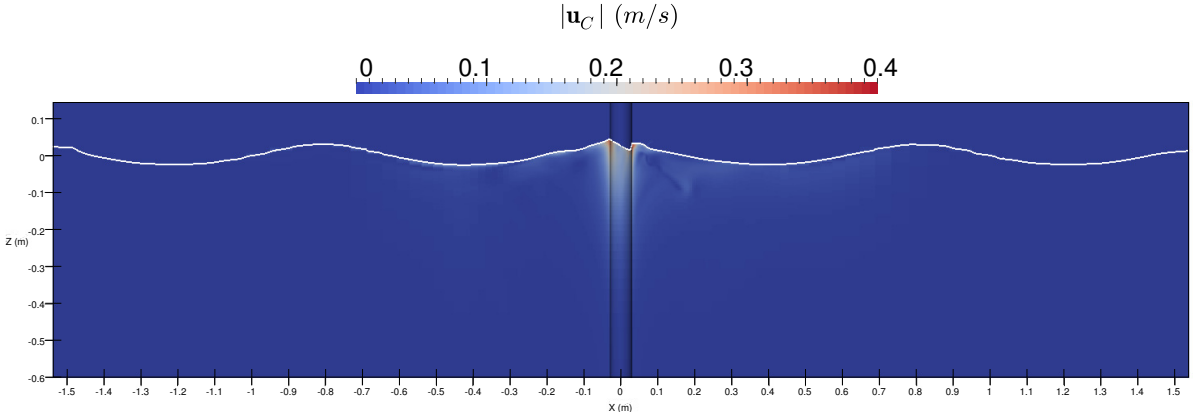

(b) Conservative

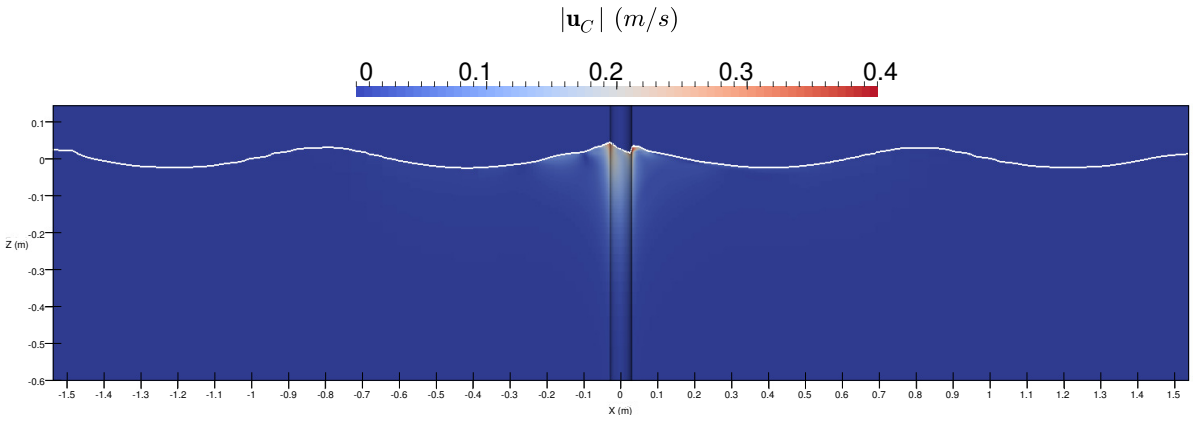

(c) GFM

Figure 5.11: Complementary velocity fields in the water when a wave crest pass the cylinder ($t = 7T$) obtained by different SWENSE formulations on the discretization No.4.

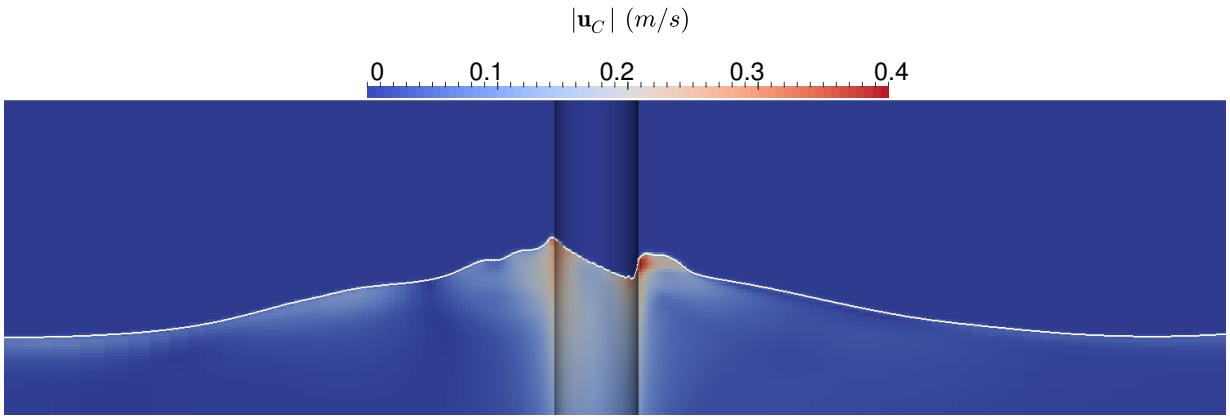

(a) Non Conservative

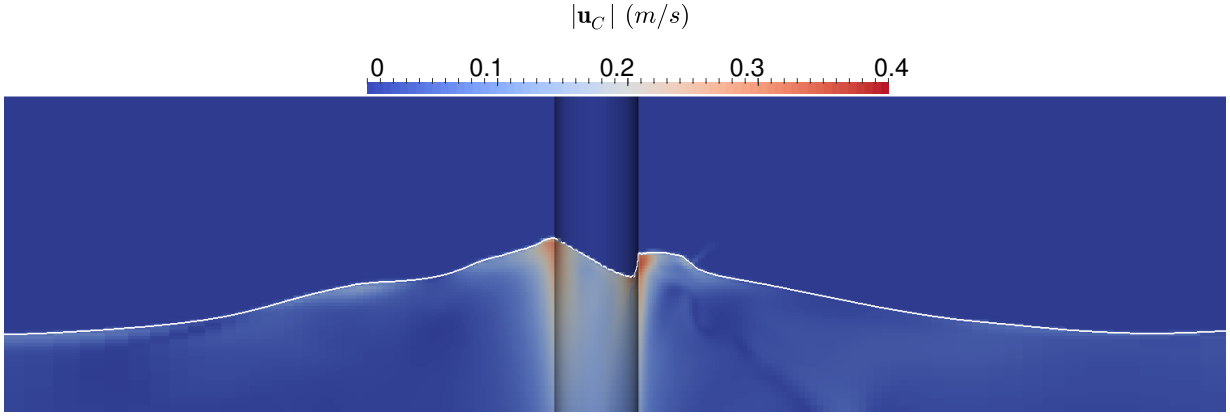

(b) Conservative

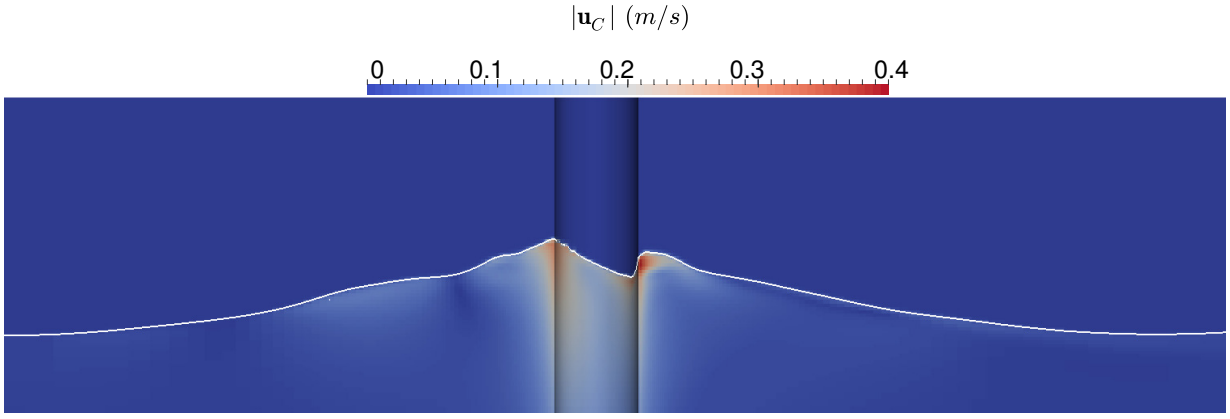

(c) GFM

Figure 5.12: Complementary velocity fields in the water when a wave crest pass the cylinder ($t = 7T$) obtained by different SWENSE formulations on the discretization No.4 (zoom).

- The complementary pressure fields obtained by the three SWENSE formulations agree well near the cylinder.

Computational time

The computational time of the three SWENSE formulations are measured and compared as shown in Tab. 5.6. The discretization No.4 with 0.67 million cells and 400 time steps per wave period are used. All the simulations are run with the same residual tolerances and are executed on 48 2.5GHz processors. The table represents the CPU time of each solver to run one wave period simulation. The relative time are normalized by the CPU time of the GFM formulation.

SWENSE Formulation	Computational Time/Wave period	Relative Time
Non conservative	1338s	1.71
Conservative	1614s	2.07
GFM	781s	1

Table 5.6: Comparison of the computational time of the three SWENSE formulations

The table shows that the GFM formulation is faster than the other two formulations and the non conservative formulation is slightly faster than the conservative formulation. Since the discretization and the residual criteria are the same for all the three solvers, the difference in the CPU time shows that the GFM version has the best convergence performance, due to the explicit treatment of the interface discontinuity. In the other two versions, the non conservative version is slightly better than the conservative version, this can be credit to the smaller spurious air velocity in the non conservative version (see Fig 5.9 and explication in Section 3.9.4). The conservative version generates the largest spurious air velocity and thus needs more efforts to converge.

5.1.3 Validation by comparing with reference data

In this part, the two-phase SWENSE method is validated by comparing with reference data on the same test case. The wave force on the cylinder with different wave steepnesses are calculated.

The discretization 4 mentioned in the previous section is used to make a compromise between accuracy and efficiency. The relative errors of the first to the fourth harmonic amplitudes with this discretization are 2.02%, 12.96%, 6.22%, and 4.00%. It contains 668000 cells, which corresponds to 1/8 of the discretization No.6. The total computational cost is only 1/16 (assuming the code has a ideal scability) of the finest configuration when the temporal refinement is taken into account.

On such a discretization, the three solvers produce close results. For this reason, only the solver with the non conservative formulation is used for this comparison.

Eight wave steepness are used ($ka \in \{0.06, 0.08, 0.10, 0.13, 0.15, 0.17, 0.20, 0.24\}$). The wavelength is invariant, only the wave height is changing. The mesh is modified in the vertical direction near the free surface so that a wave amplitude always contains the same number of cells.

Fourier analysis is applied to the time history of the wave force when the steady state has been achieved. Figure 5.15 and 5.16 present the simulation results and compare them

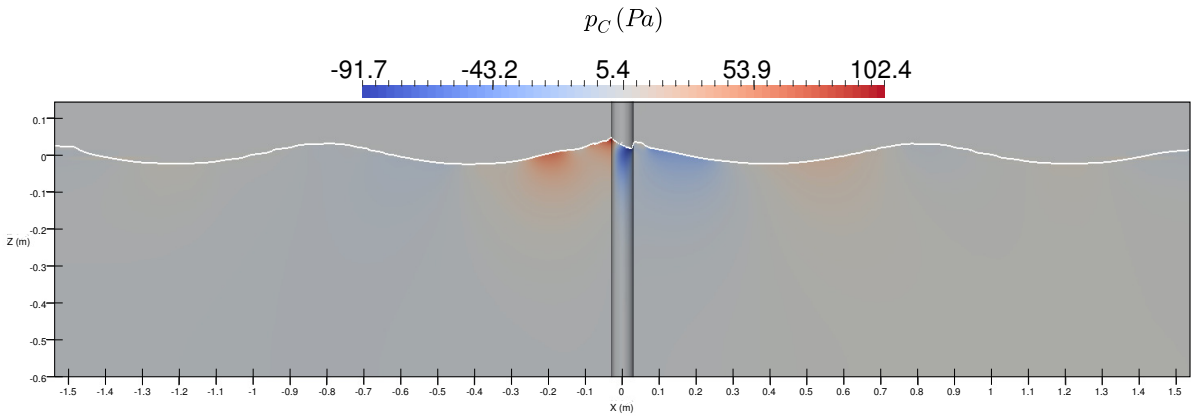

(a) Non Conservative

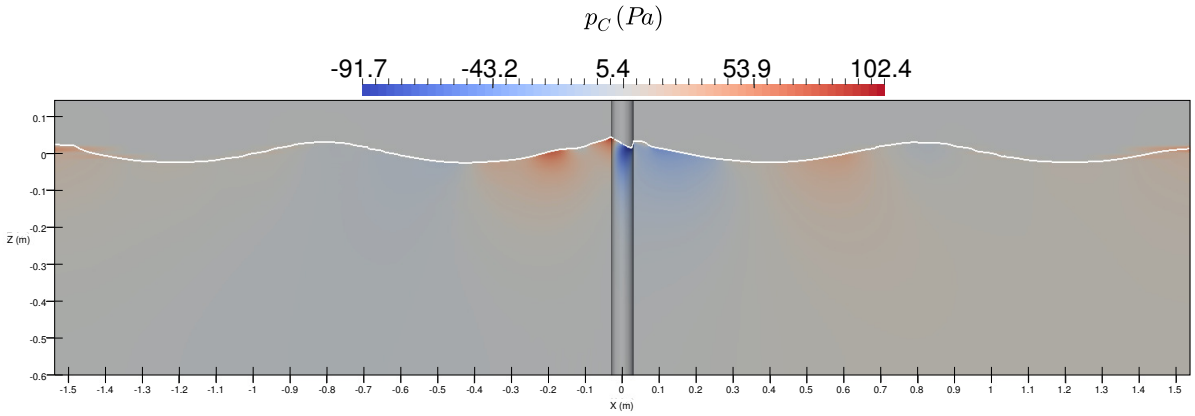

(b) Conservative

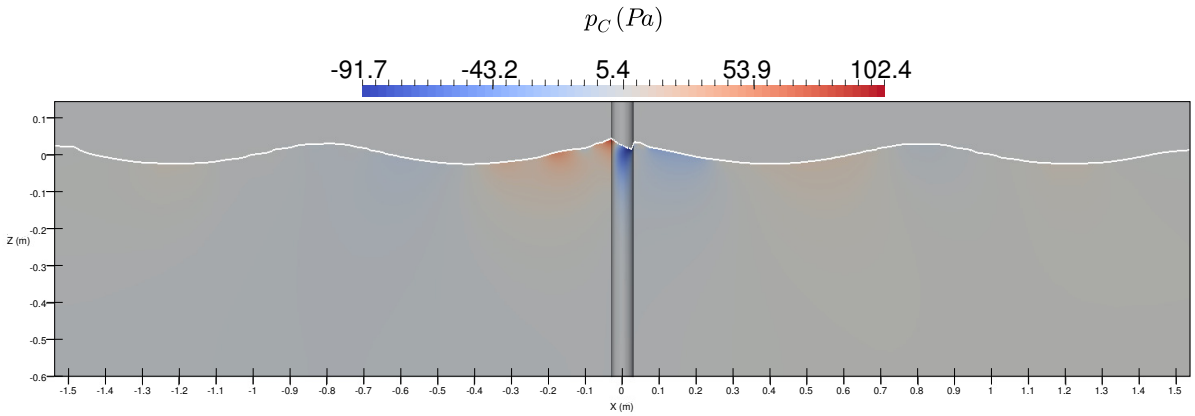

(c) GFM

Figure 5.13: Complementary pressure field in the entire computational domain when a wave crest pass the cylinder ($t = 7T$) obtained by different SWENSE formulations on the discretization No.4.

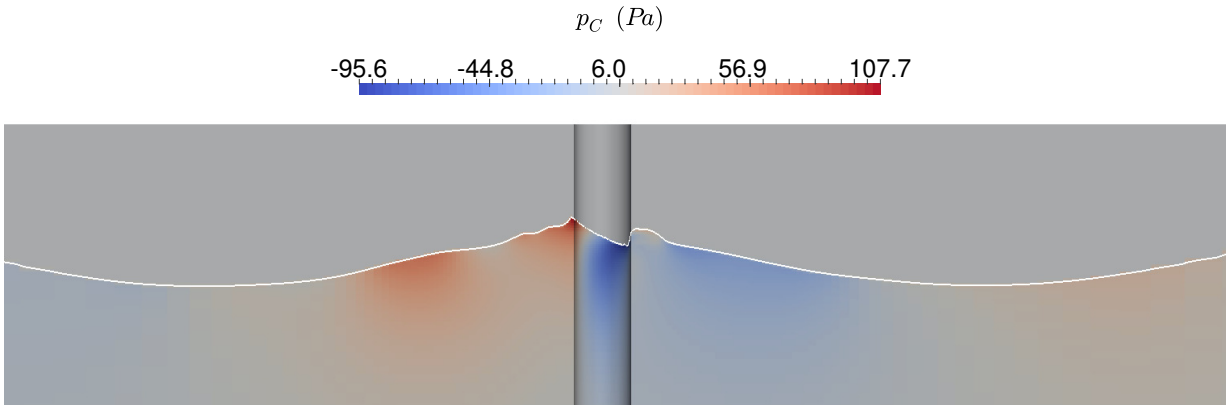

(a) Non Conservative

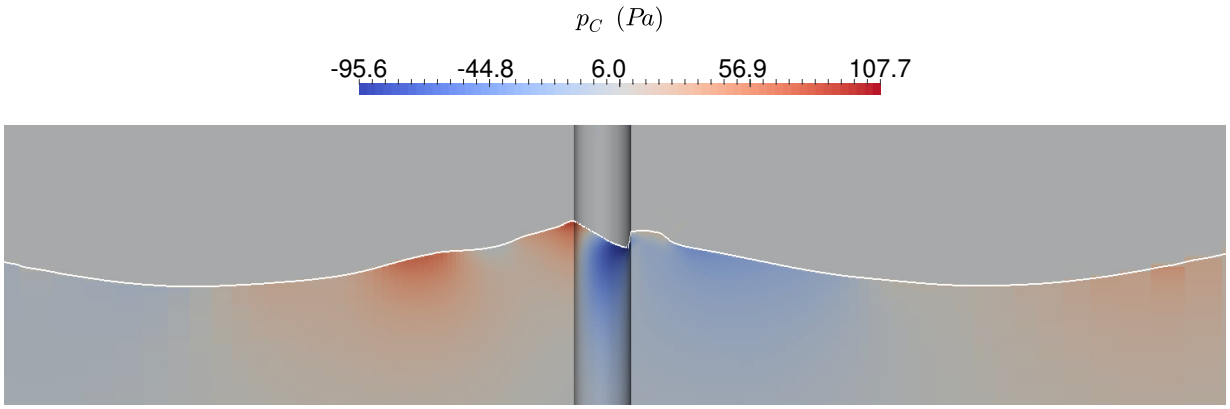

(b) Conservative

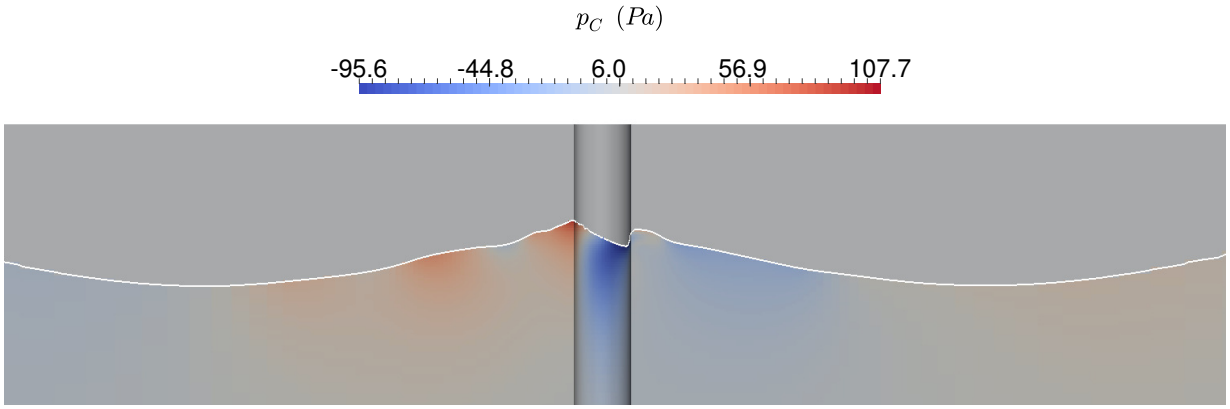

(c) GFM

Figure 5.14: Complementary pressure field in the entire computational domain when a wave crest pass the cylinder ($t = 7T$) obtained by different SWENSE formulations on the discretization No.4 (zoom).

with reference data. The first to fourth harmonic amplitude and their phase shift are shown. The results using the non conservative formulation SWENSE method are plotted as *foamStar-SWENSE*. The reference data used for the comparison are as follows:

- the third-order analytical solution of Malenica and Molin [84] (referred as Analytical);
- the experiment data of Huseby and Grue [68] (referred as EXP);
- numerical results of Ferrant [46, 47] and Shao *et al.* [114], using fully nonlinear potential flow theory.

The new solver *foamStar-SWENSE* is firstly validated by comparing with the analytic solution. At small wave steepnesses, the results of *foamStar-SWENSE* agree well with the analytic solution for both the amplitudes and the phase shifts.

Secondly, the numerical results based on the fully non-linear potential flow theory (Ferrant [47] and Shao *et al.* [114]) are used to validate *foamStar-SWENSE* when the wave is small. These simulations are both carried out with a computational domain similar to the present test case, *i.e.*, cylindrical mesh and ignores the side walls. For the first harmonic amplitude, *foamStar-SWENSE* is close to the potential flow solvers at small wave steepness ($ka < 0.1$); larger differences are observed when the steepness is larger ($0.1 < ka < 0.15$). In these region, the neglect of flow seperation in the potential flow solver may explain this difference [79]. For higher order harmonic amplitudes, *foamStar-SWENSE* is in good agreement with the potential flow solvers. Moreover, an excellent agreement is also observed when the phase shifts are compared. For larger waves ($ka > 0.15$), the local increase of the wave steepness may lead to numerical difficulties for the fully non-linear potential theory codes, so both the results of Ferrant [47] and of Shao *et al.* [114] stop before $ka = 0.15$. The local wave breaking can be observed in the present simulation. Figure 5.17 shows the free surface near the cylinder. The free surface is colored by the elevation (η) normalized by the incident wave amplitude (a). The incident wave steepness is $ka = 0.24$ for this case. The figures are snapped between $t = 6T$ to $t = 7T$ with an interval of $0.2T$. The incident waves travels from the left to the right. Local wave breaking may be observed at $t = 6.2T$ and $t = 6.8T$.

When comparing with the experimental data, an excellent agreement is achieved for the first harmonic amplitude. The overall discrepancy is less than 2%. For higher-order components, the differences between the simulated results and the experimental data become remarkable, but are still close. For the second harmonic amplitudes, both *foamStar-SWENSE* and the experiment show a same decreasing trend when the wave steepness becomes larger. The numerical results are approximately 20% larger than the experimental data. For the third and fourth harmonic amplitudes, the comparison is better when the wave steepnesses are higher. For small wave steepness, it is indeed more difficult since the higher-order forces are very small. The oscillations appearing in the experimental data show this difficulty. With respect to the phase shifts, apparent differences exist between the experimental data and all the other results. In consideration of the difference getting larger while the order increases, it is possible that the beginning time of the experiment and the calculations are different. Another source for the discrepancy between the experiment and the simulations may come from the computational domain size: the experiment was conducted in a narrow wave tank where the width $b = 0.5m \approx 0.65\lambda$. In the numerical simulations, the lateral walls are not modeled, but a larger domain ($r = 2\lambda$) is used to reproduce an open sea condition. The reflected waves occurred in the experiment are not considered in the numerical simulations.

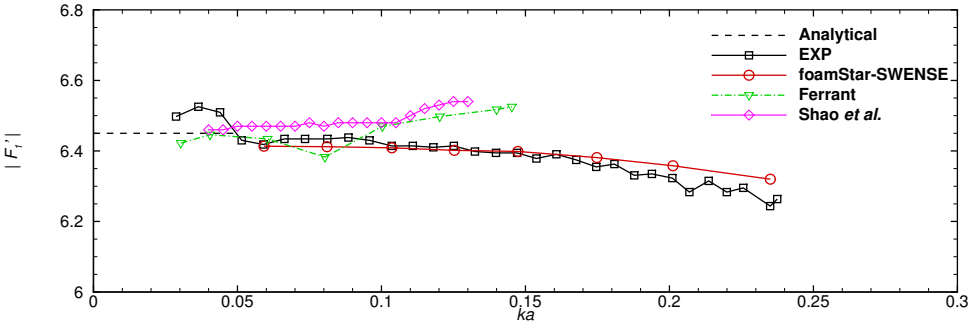

(a) First harmonic amplitudes

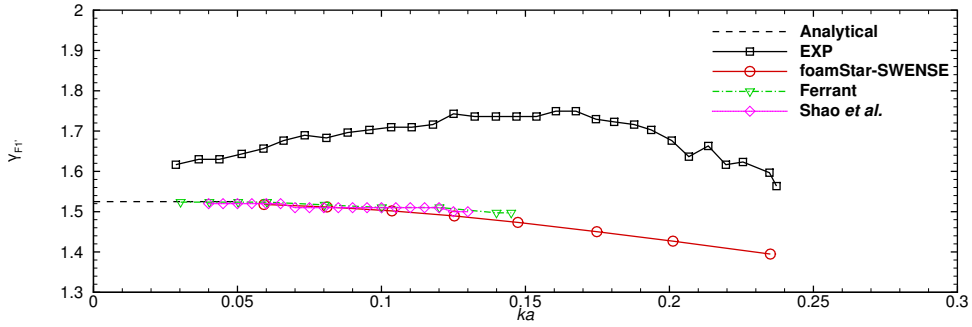

(b) First harmonic phases

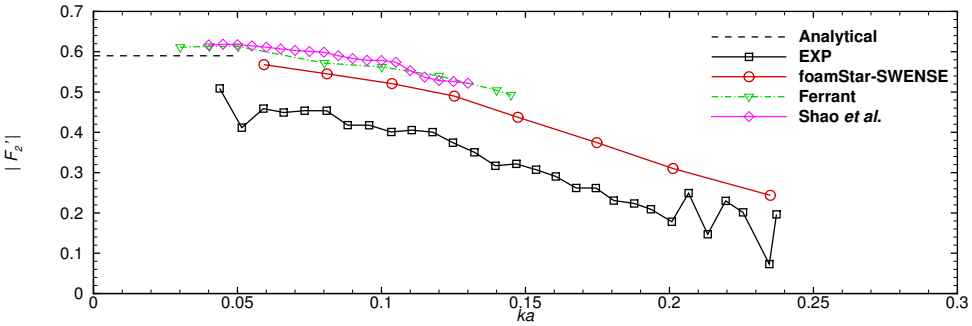

(c) Second harmonic amplitudes

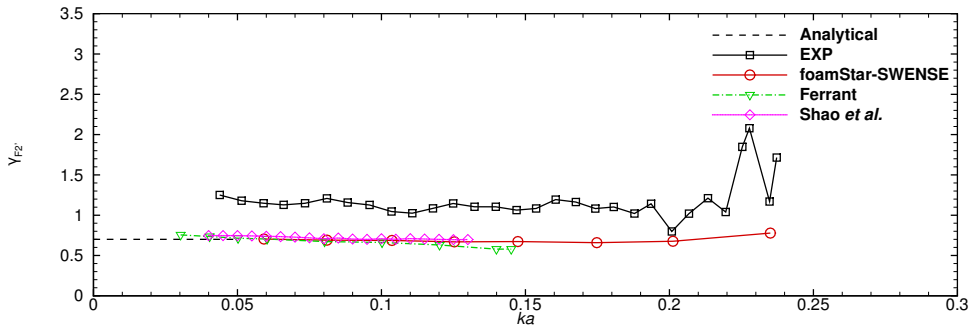

(d) Second harmonic phases

Figure 5.15: Comparison of the first and the second harmonics of horizontal forces on vertical circular cylinder in regular waves.

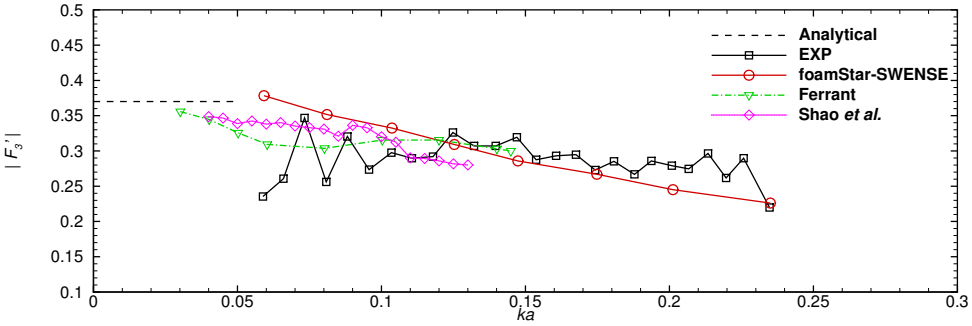

(a) Third harmonic amplitudes

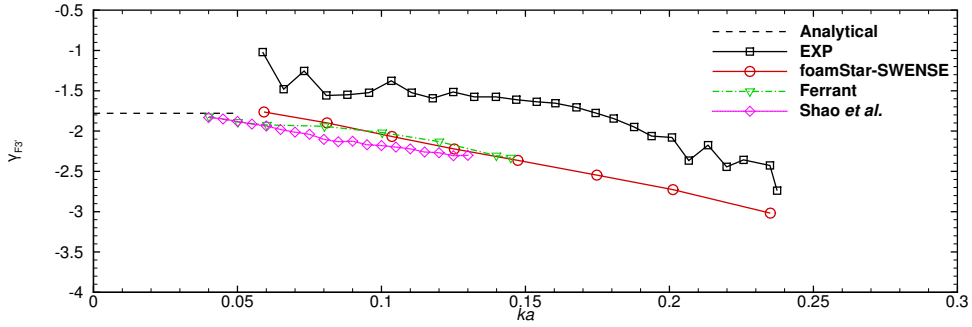

(b) Third harmonic phases

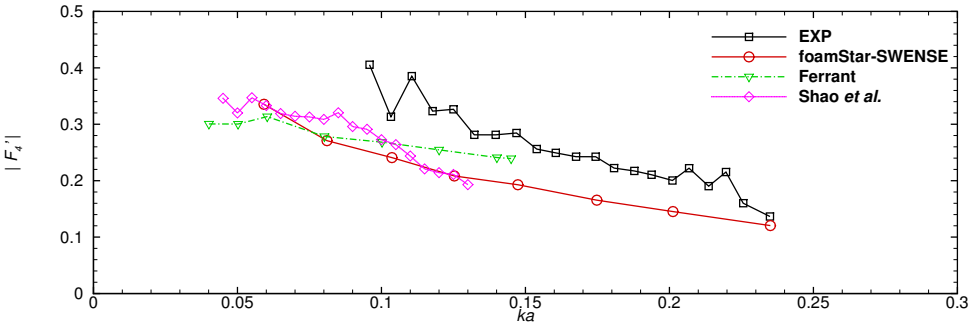

(c) Fourth harmonic amplitudes

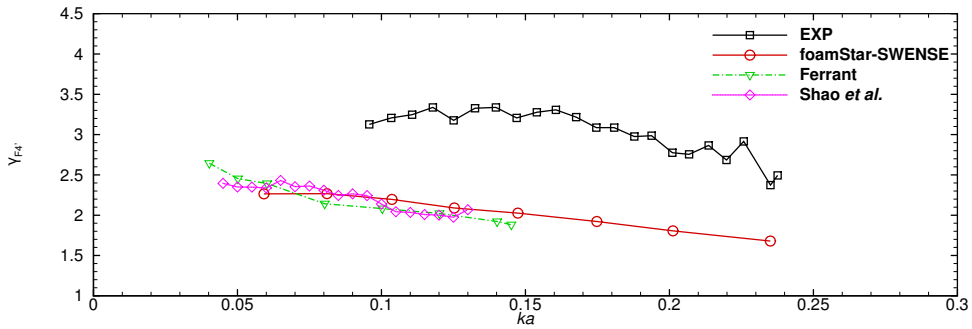

(d) Fourth harmonic phases

Figure 5.16: Comparison of the third and the fourth harmonics of horizontal forces on vertical circular cylinder in regular waves.

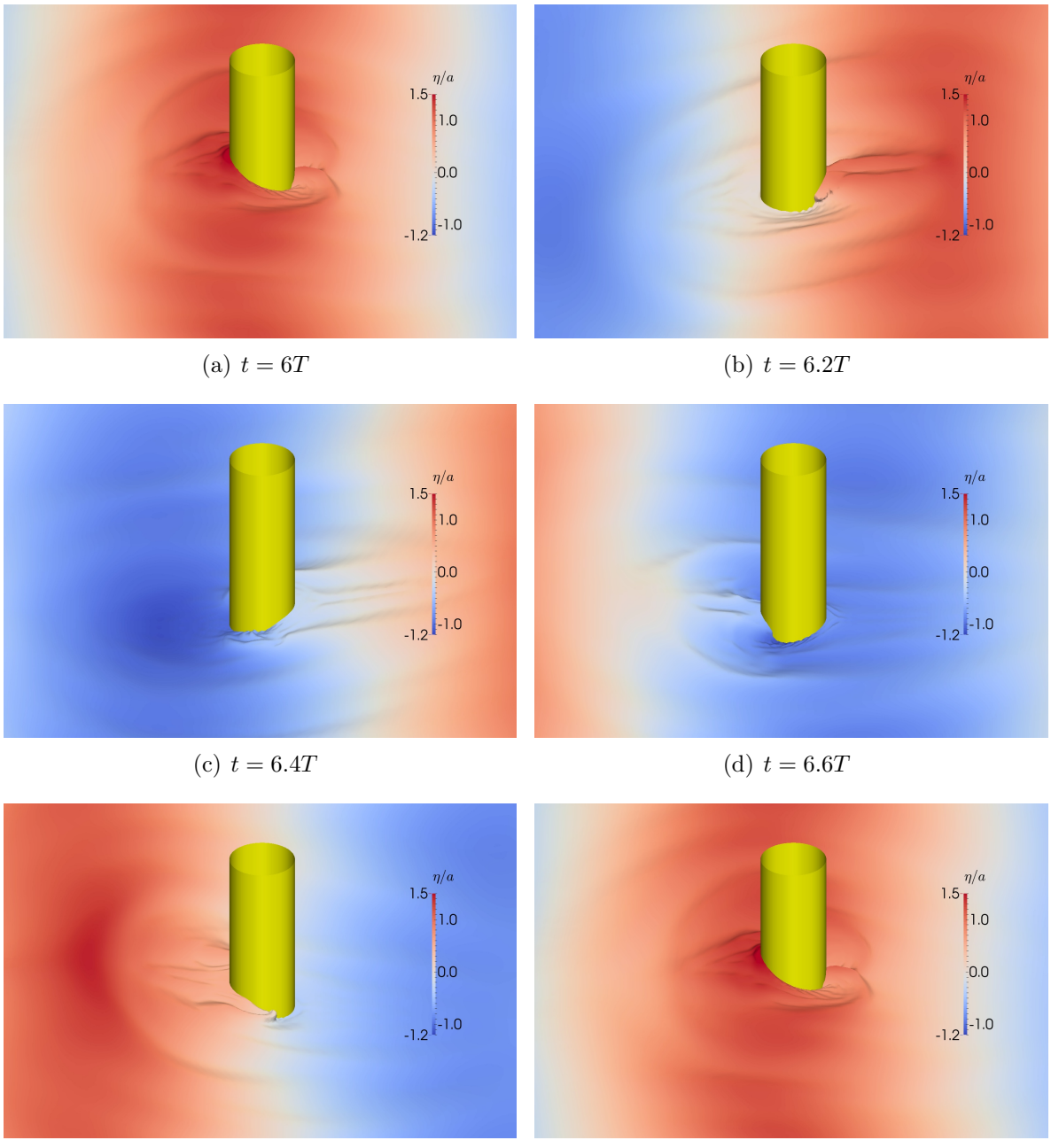

(a) $t = 6T$ (b) $t = 6.2T$

(c) $t = 6.4T$ (d) $t = 6.6T$

(e) $t = 6.8T$ (f) $t = 7T$

Figure 5.17: Free surface near the cylinder (incident wave steepness $ka = 0.24$).

To conclude, the comparison with the analytical solution, the results from potential flow solvers, and the experimental data shows that the proposed two-phase SWENSE method is able to predict the wave force on a simple structure correctly. The typical cylindrical mesh with coarse cells in the far-field can be used without influencing the accuracy of the simulation.

5.2 CALM buoy in regular and irregular waves

This part aims to demonstrate the ability of two-phase SWENSE method in dealing with a more complex wave-structure simulation. Both the structure geometry and the wave condition are more complex in this case than in the previous one.

- Geometry: The structure studied is a Catenary Anchor Leg Mooring (CALM) buoy [107]. This structure contains a thin heave plate. This geometry makes the mesh generation more complex than the cylinder case: locally refined unstructured mesh is used to represent the geometry. Moreover, more violent free surface deformation (wave breking) and larger viscous effect are expected in this case than in the cylinder case.
- Wave condition: Both regular and irregular wave conditions are used. The experimental condition for the irregular waves are obtained with the *HOS-NWT* solver [4, 38], and reconstructed onto the CFD mesh.

In this test case, the non conservative SWENSE formulation is used to represent the two-phase SWENSE method. The solver implementing this formulation is referred to as *foamStar-SWENSE*. The two-phase Navier-Stokes solver used here is *foamStar*. The regular wave simulations are run with both solvers. The results of the simulations are used to :

- Compare the accuracy of both solvers against the experimental data;
- Compare the computational efficiency of both solvers;
- Compare the flow details obtained by both solvers to validate the SWENSE method in a more detailed way.

The irregular wave simulation is run only with *foamStar-SWENSE* and compared with the experimental data to validate the coupling between the SWENSE and the HOS solver in a real wave-structure interaction problem and test the stability of the solver in a longtime simulation.

5.2.1 Geometry and wave parameters

The test case reproduces an experiment carried out in the ocean engineering basin of Ecole Centrale de Nantes (50m long, 30m wide and 5m deep). It deals with a fixed Catenary Anchor Leg Mooring(CALM) buoy [107] exposed in regular and irregular waves.

The buoy has a truncated cylinder form with a thin skirt near the bottom to provide additional damping forces through vortex shedding, as shown in Figure 5.18(a). The geometry of the buoy is detailed in Table 5.7. The horizontal and vertical forces on the buoy and the free surface elevation at three points around it are measured to validate the CFD results (see Figure 5.18(b)).

Regular and irregular wave conditions are chosen from the experiment. The information on the waves is listed in Table 5.8. The wave steepnesses are moderate. The irregular waves in the experiment are generated with the JONSWAP spectrum ($T_p = 2.0$s, $H_s = 0.12m$, $\gamma = 3$).

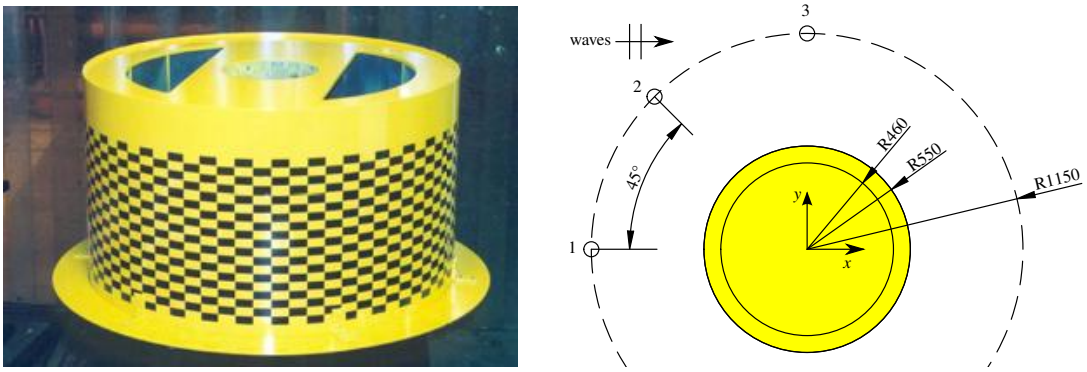

(a) CALM Buoy Model (b) Wave Gauge Positions

Figure 5.18: Experiment setup for CALM buoy case.

Parameter	Value
Radius	$0.460\,m$
Height overall	$0.560\,m$
Skirt radius	$0.550\,m$
Skirt thickness	$0.004\,m$
From the bottom to the skirt	$0.04\,m$
Draft	$0.25\,m$

Table 5.7: Geometry characteristics of the CALM buoy model.

Regular waves		Irregular waves	
T	1.80 s	T_p	2.00 s
H	0.16 m	H_s	0.12 m
$kH/2$	0.1	$k_pH_s/2$	0.06

Table 5.8: Wave conditions for the CALM buoy in wave case

5.2.2 Computational domain and meshes

Two types of mesh are used in this test case, including a cylindrical one and a rectangular one.

The cylindrical mesh is typically used by the SWENSE solvers. In this kind of mesh, the cells are refined near the structure to capture the wave-structure interaction, and gradually enlarged in the far-field to reduce the computational cost. The cylindrical configuration is used in this section for the simulation with *foamStar-SWENSE* both in regular and irregular wave cases.

However, the cylindrical mesh cannot be used by *foamStar*, since the incident wave propagation in conventional two-phase solvers requires fine meshes in the entire computational domain. The cylindrical mesh has coarse cells in the far-field, which deteriorates the incident waves even before they reach the structure. For this reason, a series of rectangular mesh with uniform background mesh is made for *foamStar*. The rectangular configuration is also used by *foamStar-SWENSE* for the comparison purpose.

The computational domain is defined with the regular wave characteristics (λ, H) hereafter.

Cylindrical configuration

A 3D cylindrical mesh is used. The origin of the coordinate system is located at the center of the computational domain and on the free surface at rest. The x axis points to the wave propagation direction, and z axis points upward. The domain radius is equal to 2λ. The depth of the computational domain is the same as in the experimental wave tank $z_{min} = -5m$. The top of the computational domain is 0.5m above the free surface position at rest. A longitudinal symmetry plane is used. The cells near the structure are refined in the radius direction to capture the flow details. They are gradually enlarged in the far-field to reduce the total number of cells (see Fig. 5.19). The discretization details are listed in Table 5.9. In the far-field, the relaxation zone with a length of 1.5λ is used to absorb the disturbed wave field, leaving a pure CFD zone with one wave length $r \in (-0.5\lambda, 0.5\lambda)$.

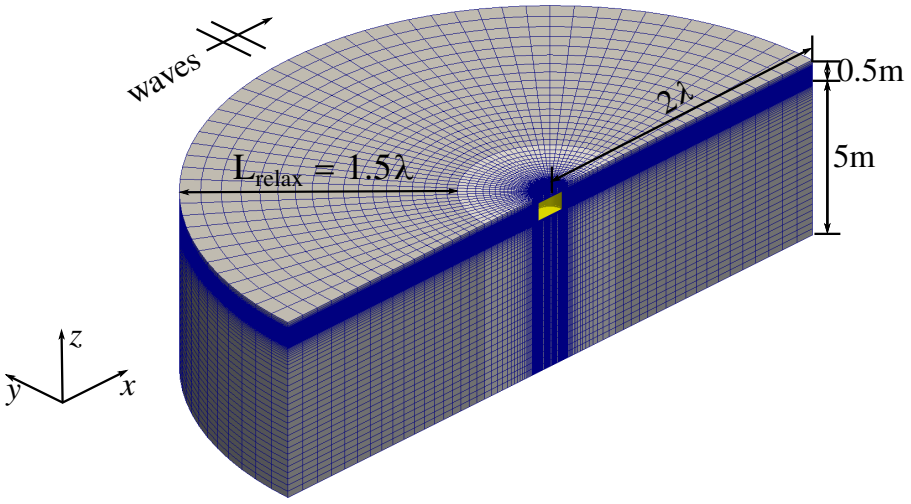

(a) Global view

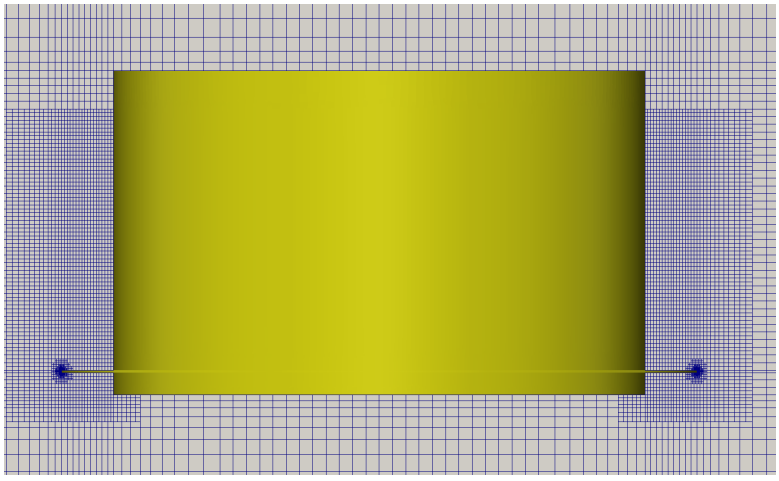

(b) Local mesh near the buoy

Figure 5.19: Cylindrical mesh layout for CALM buoy in waves

Parameter	Value
$\lambda/\Delta R_{near}$	400
$\lambda/\Delta R_{far}$	10
$180°/\Delta\theta$	96
$H/\Delta z$	16
Total Cells	0.72 M

Table 5.9: Mesh information for cylindrical computational domain

Rectangular configuration

A rectangular computational domain is defined to generate uniform Cartesian background meshes for the incident wave propagation. The meshes are also refined near the structure to have a same cell density similar to the cylindrical configuration (see Fig. 5.20). Three configurations: 20x, 40x, and 80x are used with 20, 40, and 80 cells per wave length in the x direction. The mesh in the y direction is less refined than in the x direction to reduce the total number of cells. The differences between the configurations are only in the far-field. The mesh density near the buoy is kept invariant.

The details of the different meshes are summarized in Table 5.10.

Mesh	$\lambda/\Delta x$	$\lambda/\Delta y$	$H/\Delta z$	Number of cells
20x	20	10	16	1.3 M
40x	40	10	16	1.5 M
80x	80	20	16	2.5 M

Table 5.10: Mesh configurations for CALM buoy in regular waves

In the far-field, both solvers use the same relaxation zones with a length of 1.5λ at inlet, outlet, and the side. Both solvers blend the CFD solutions to the incident wave fields in these zones. For *foamStar*, the relaxation zones are used to generate waves and absorb the scattered waves to prevent reflections. For *foamStar-SWENSE*, the complementary fields are diminished to zero in the far-field to avoid reflections.

5.2.3 Regular waves

The experimental condition with regular waves ($T = 1.8s, H = 0.16m, kH/2 = 0.1$) is reproduced by both *foamStar-SWENSE* and *foamStar* with stream function wave theory. The cylindrical configuration is used only by *foamStar-SWENSE*. The rectangular configurations are used by both solvers. The different discretizations of the rectangular computational domain are used to test how the SWENSE method is helpful in reducing the number of cells in the far-field and maintain the incident waves' accuracy. All the simulations use the same temporal discretization corresponding to 360 time steps per wave period.

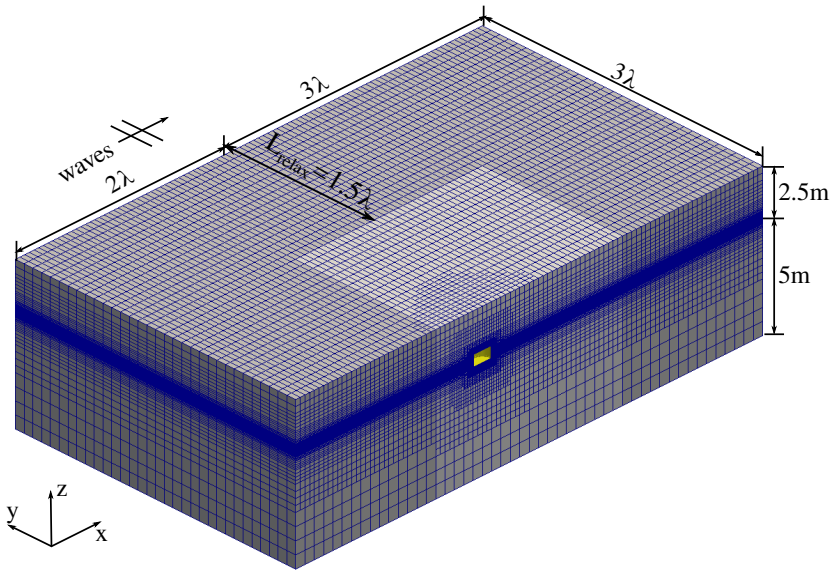

(a) Global view

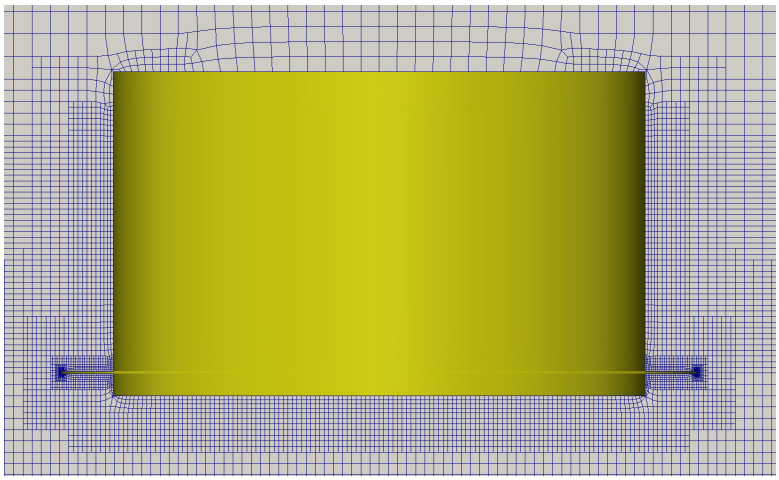

(b) Local mesh near the buoy

Figure 5.20: Rectangular mesh layout for CALM buoy in waves

Comparison of the accuracy

During the simulations, the wave forces (F_x and F_z for the horizontal and the vertical force) and free surface elevations (η_1, η_2, η_3 at the three wave probes) are recorded during 7 periods. The time history is transformed into the frequency domain with the moving window Fourier analysis and averaged over the periodic regime (similar to Section 5.1.2). The first and second harmonic amplitudes of these quantities are extracted and compared (denoted with the superscript (1) and (2)).

The amplitudes of wave force are normalized with $ak\rho g\nabla$, where the $a = H/2$ is the amplitude of the waves, k the wave number and ∇ the displacement volume of the buoy at the design draft. The free surface elevations are normalized by a, the amplitude of the waves. The

normalized results are shown in Table 5.11.

Harmonic Amplitudes		$F_x^{(1)}$	$F_x^{(2)}$	$F_z^{(1)}$	$F_z^{(2)}$	$\eta_1^{(1)}$	$\eta_1^{(2)}$	$\eta_2^{(1)}$	$\eta_2^{(2)}$	$\eta_3^{(1)}$	$\eta_3^{(2)}$
Experiment		1.390	0.170	1.180	0.015	1.220	0.065	1.210	0.040	1.040	0.035
foamStar	80x	1.359	0.168	1.098	0.010	1.195	0.060	1.180	0.036	1.002	0.045
		-2.23%	-1.18%	-6.95%	-33.33%	-2.05%	-7.69%	-2.48%	-10.00%	-3.65%	28.57%
	40x	1.328	0.165	1.075	0.011	1.172	0.057	1.164	0.035	0.983	0.041
		-4.46%	-2.94%	-8.90%	-26.67%	-3.93%	-12.31%	-3.80%	-12.50%	-5.48%	17.14%
	20x	1.202	0.130	1.018	0.017	1.063	0.057	1.057	0.037	0.924	0.039
		-13.53%	-23.53%	-13.73%	13.33%	-12.87%	-12.31%	-12.64%	-7.50%	-11.15%	11.43%
foamStar-SWENSE	80x	1.383	0.182	1.152	0.014	1.211	0.060	1.198	0.032	1.035	0.051
		-0.50%	7.06%	-2.37%	-6.67%	-0.74%	-7.69%	-0.99%	-20.00%	-0.48%	45.71%
	40x	1.376	0.181	1.144	0.012	1.208	0.060	1.195	0.032	1.028	0.051
		-1.01%	6.47%	-3.05%	-20.00%	-0.98%	-7.69%	-1.24%	-20.00%	-1.15%	45.71%
	20x	1.360	0.183	1.134	0.011	1.199	0.059	1.185	0.039	1.020	0.051
		-2.16%	7.65%	-3.90%	-26.67%	-1.72%	-9.23%	-2.07%	-2.50%	-1.92%	45.71%
	Cylind.	1.357	0.181	1.146	0.020	1.187	0.065	1.176	0.031	1.010	0.050
		-2.37%	6.47%	-2.88%	33.33%	-2.70%	0.00%	-2.81%	-22.50%	-2.88%	42.86%

Table 5.11: Comparison between CFD results and experimental data

To analyze the results, let's focus on the first harmonic amplitude of the horizontal wave force ($F_x^{(1)}$), and check the results of both *foamStar* and *foamStar-SWENSE* with different meshes.

- 80x: The results of both solvers are in good agreement. *foamStar* gives slightly smaller predictions on the first harmonic amplitudes. The *foamStar-SWENSE*'s results has a better agreement with the experiment.
- 40x: According to ITTC's recommendation, 40 cells per wave length is the minimum requirement for wave simulations by CFD [72]. With this discretization, *foamStar-SWENSE* is able to predict the wave force and elevation correctly with an accuracy of 1% compared with the experiment. This difference is about 4% for *foamStar*.
- 20x: This discretization is known to be too coarse to simulate waves in CFD. The coarse mesh causes excessive numerical diffusion and damps the incident waves. For this reason *foamStar* gives smaller predictions. However, *foamStar-SWENSE*'s results are still about 2% different from the experimental data.
- Cylindrical: This configuration has large cells in the far-field, and the mesh is gradually refined towards the domain center. With 0.72 million of cells, the results of *foamStar-SWENSE* is almost as accurate as the result of *foamStar* with 80x.
- Other quantities show a similar behavior.

Comparison of the flow details

To ensure the accuracy of the simulation, especially to validate the result of *foamStar-SWENSE* on the coarse mesh, the flow details of the simulation are compared.

Figures 5.21 to 5.24 plot the velocity field, the pressure field, and the Q-criteria [60] obtained by *foamStar* and *foamStar-SWENSE* with 80x and 20x, respectively. The Q-criteria is a description of vortex. Figure 5.24 plots the contour of $Q = 50s^{-2}$ and is colored by the total pressure. The flow details are snapped at the same moment where the incident wave crest passes the cylinder center. The white line in Fig. 5.21 to 5.23 represents the water free surface calculated with $\alpha = 0.5$.

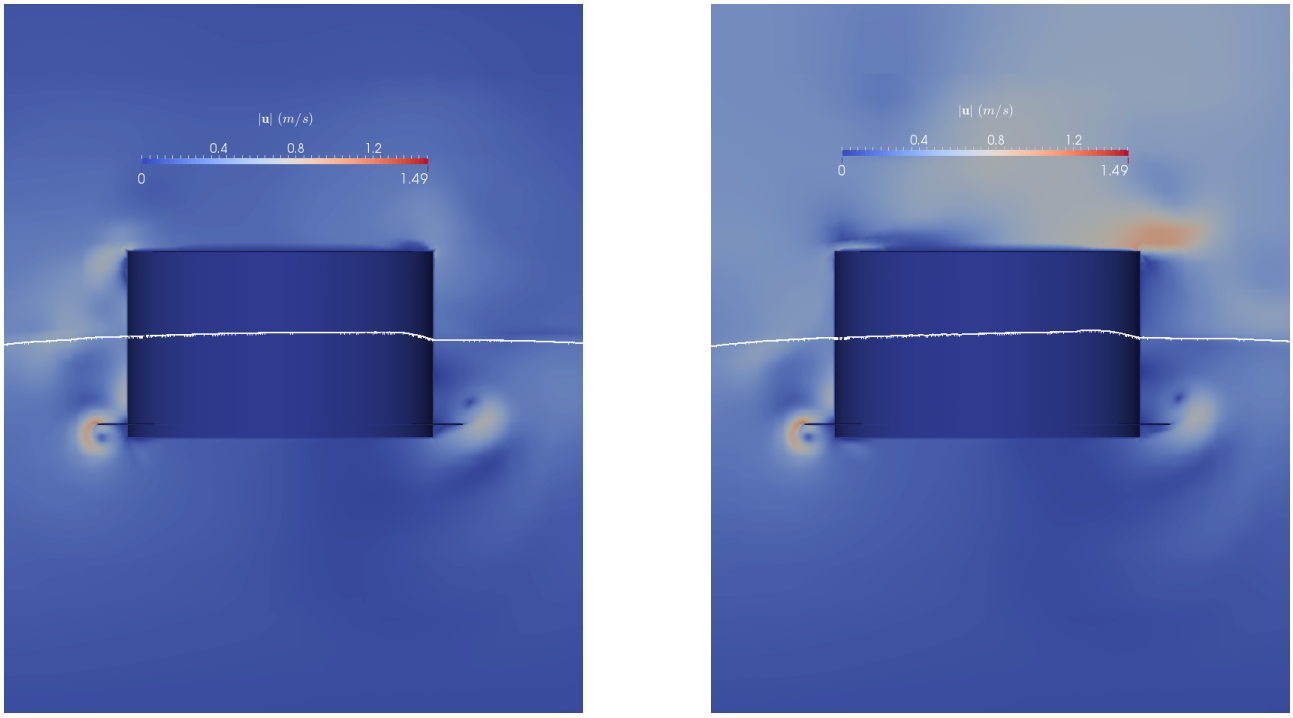

(a) *foamStar* 80x (b) *foamStar-SWENSE* 20x

Figure 5.21: Comparison of the velocity field when a wave crest passes the buoy

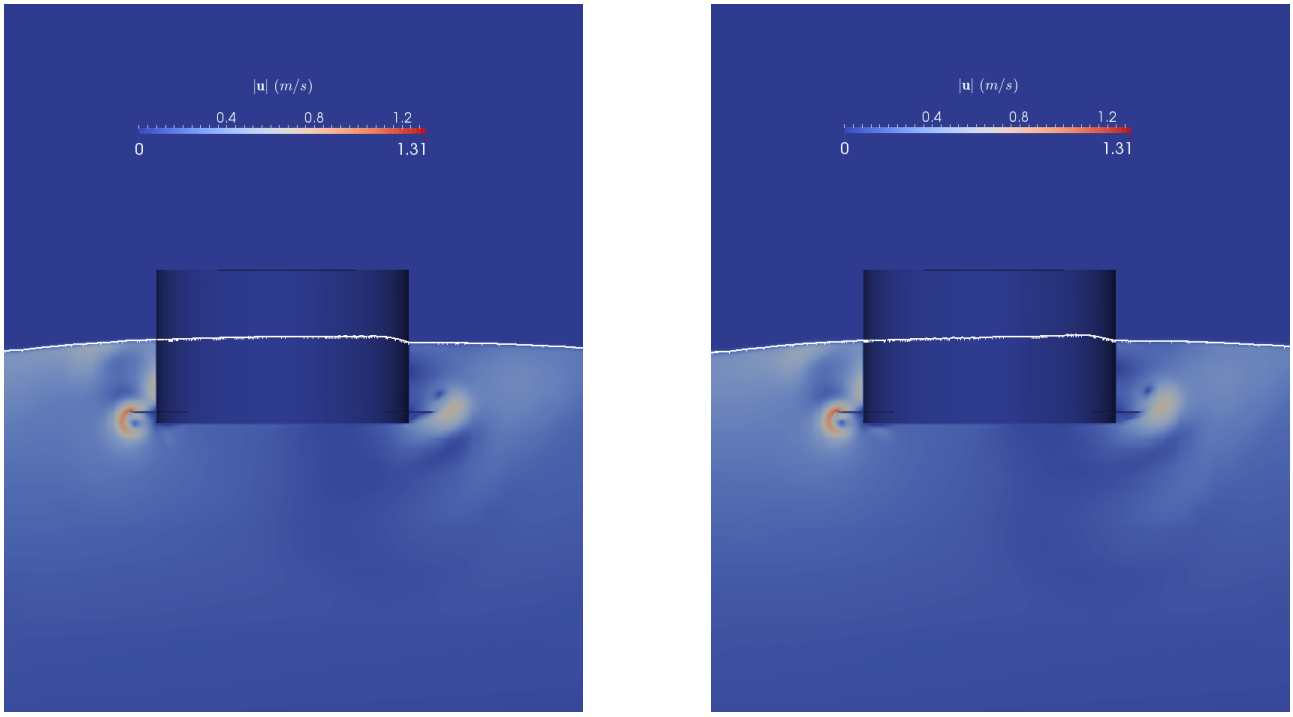

(a) *foamStar* 80x (b) *foamStar-SWENSE* 20x

Figure 5.22: Comparison of the velocity field in the water when a wave crest passes the buoy

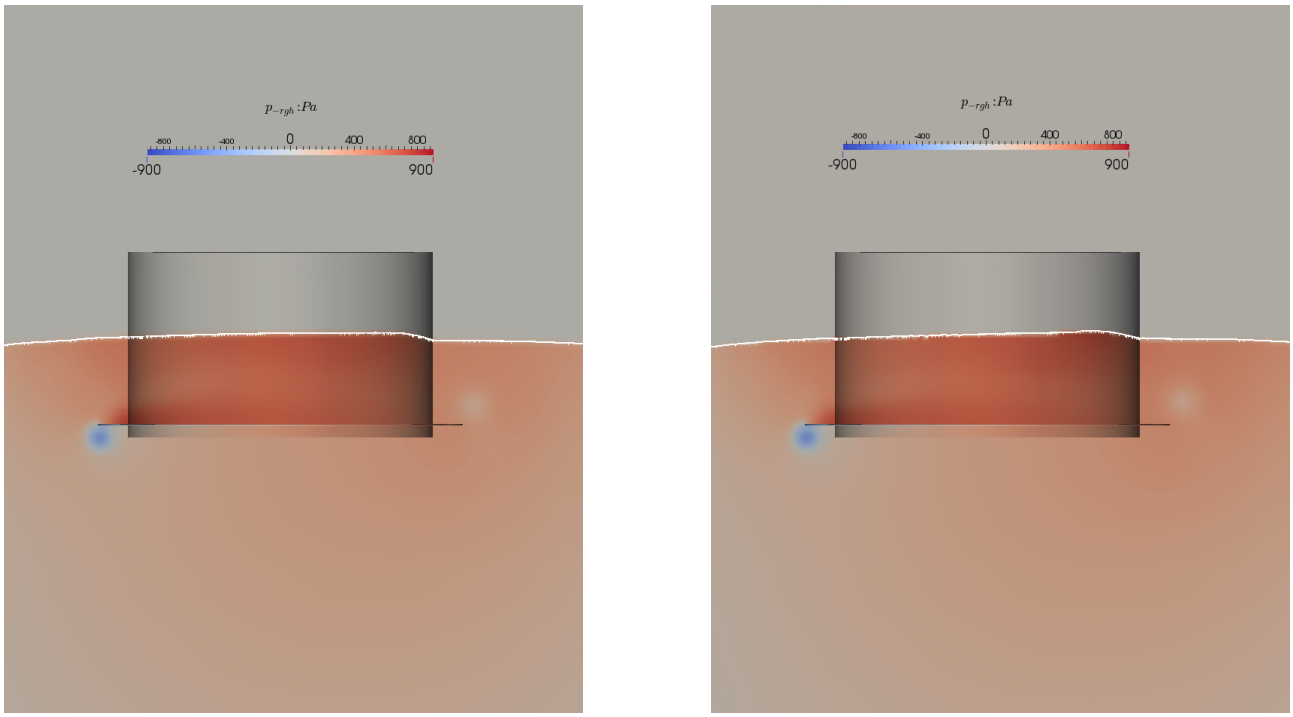

(a) *foamStar* 80x (b) *foamStar-SWENSE* 20x

Figure 5.23: Comparison of the dynamic pressure field ($p\_{\rho gh}$) when a wave crest passes the buoy

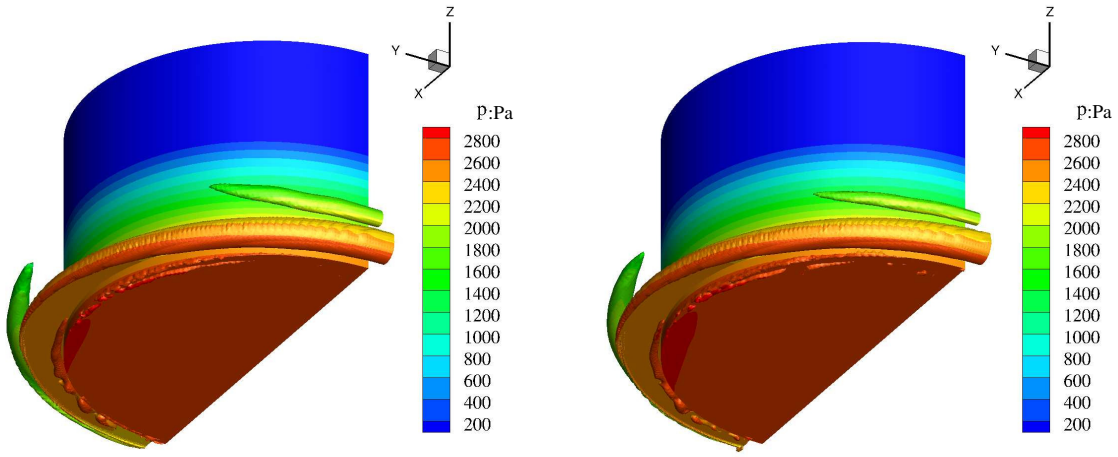

(a) *foamStar* 80x (b) *foamStar-SWENSE* 20x

Figure 5.24: Comparison of the iso-surfaces of Q-criteria = $50s^{-2}$ and pressure field when a wave crest passes the buoy

Excellent agreements are observed expect on the velocity in the air. The velocity field in the water, the free surface position, the dynamic pressure field, and the Q-criteria are in excellent agreement. Note that the good agreement of the dynamic pressure field is not only valid in the water. Figure 5.23 plots the dynamic pressure field in the entire domain including both the water and the air. This good comparison of pressure, while the air velocity fields are different, is due to the small density of the air. The small air density makes the variation of the pressure field in the air much smaller than in the water.

The velocity in the air is different in the SWENSE solver and in the NS solver. This discrepancy comes from the extension of incident wave velocity in the air. This extension creates an oscillatory wind in the air as the incident field. However, the air effects are often negligible in the wave-structure interaction problems for marine and offshore applications. Figure 5.25 compares the total force (in both the water and the air) and the force in the water on the buoy. The figure is zoomed over one wave period to check the details. The two forces are almost identical, showing that the air effects are negligible, and thus justify the assumption adopted when extending the incident velocity in the air, *i.e.*, the incident air velocity is not problematic for most wave-structure interaction problems.

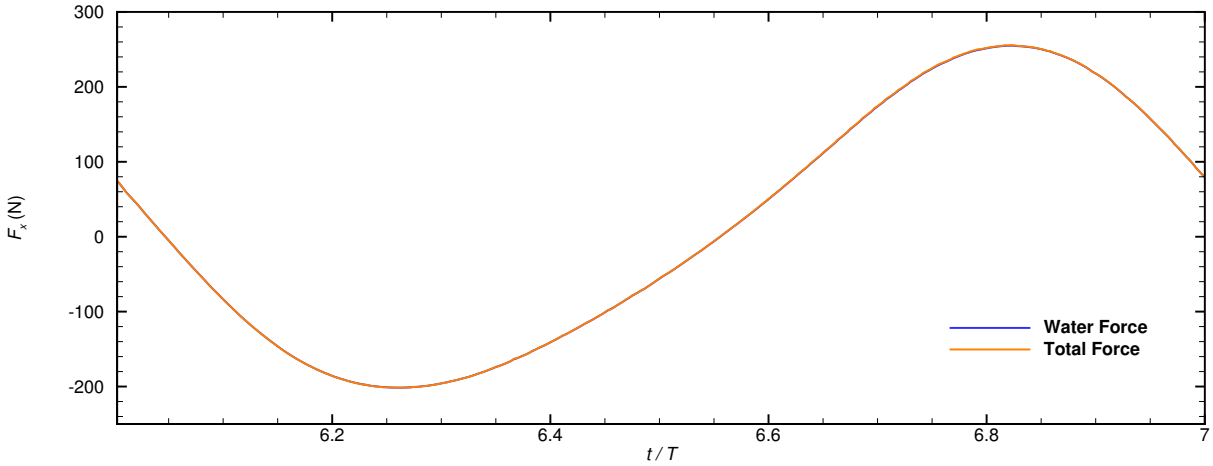

Figure 5.25: Comparison of the total force and the force in the water.

Comparison of the computational cost

The computational time required by *foamStar-SWENSE* and *foamStar* are tested, the results are listed in Tab 5.12. The computation is done with 24 2.5GHz processors. The wall-clock time per wave period is compared.

The computational time of *foamStar* and *foamStar-SWENSE* are comparable when they use the same mesh. But considering *foamStar-SWENSE* with 20x or the cylindrical mesh can obtain the same level of accuracy of *foamStar* using 80x, an acceleration rate of between 1.71 (with 20x) to 4.28 (with the cylindrical mesh) is expected. Note that the present test case uses the non conservative two-phase formulation without the Ghost Fluid Method to treat the interface jump condition. This speed up is directly due to the use of SWENSE method.

Mesh	Number of cells	Computational time / wave period	
		foamStar	*foamStar-SWENSE*
Cylind.	0.72 M	-	2417s
20x	1.3 M	6030s	6031s
40x	1.5 M	6808s	6782s
80x	2.5 M	10364s	9939s

Table 5.12: Comparison of the computational time used by *foamStar* and *foamStar-SWENSE*

5.2.4 Irregular waves

This section aims to demonstrate how the SWENSE method performs in an irregular wave case, and to test the zero-padding interpolation technique mentioned in Sect. 4.3 to couple the HOS solvers and the CFD solver. An irregular wave case of the experiment is reproduced with *foamStar-SWENSE*. The simulation is long and contains large wave groups in order to test the stability of the present SWENSE solver. The force on the buoy is recorded and compared with the experimental data.

Incident waves

In the experiment, the irregular waves are unidirectional, generated by JONSWAP spectrum ($T_p = 2.0$s, $H_s = 0.12m$, $\gamma = 3$). The open-source higher-order spectral method code, *HOS-NWT*, is used to simulate the incident wave propagation in the experimental wave tank. The motion of the wave-makers from the experiment is provided to the HOS solver to calculate the incident wave field in the entire computational domain in a fast and accurate manner.

Computational Domain

The incident waves generated by *HOS-NWT* is mapped to a cylindrical mesh located near the buoy. The cylindrical mesh is same as mentioned in the previous section. The computational domain of this test case is illustrated by Fig. 5.26.

Relaxation zones are used in the CFD computation to prevent wave reflections at the computational domain. This configuration represents an open sea condition. However, in the experiment, the waves are reflected from the side walls and the absorption beach. This reflection is not taken into account in the numerical simulation. The simulation reproduces the first 100s of the experiment. The time history of the wave force on the structure is recorded and compared to the experimental data.

Results

The comparison of the simulation results and the experimental data are shown in Figure 5.27(a) and Figure 5.27(b). The time history of the horizontal and vertical wave forces are plotted respectively.

The results of *foamStar-SWENSE* show a very good agreement with the experimental data. In the beginning of the simulation where the wave-front does not reach the structure, the wave forces remain zero. After the arrival of wave front, the simulated wave forces are very close to the experimental data during the majority of the simulation time. Both the amplitudes and the phases are in good agreement.

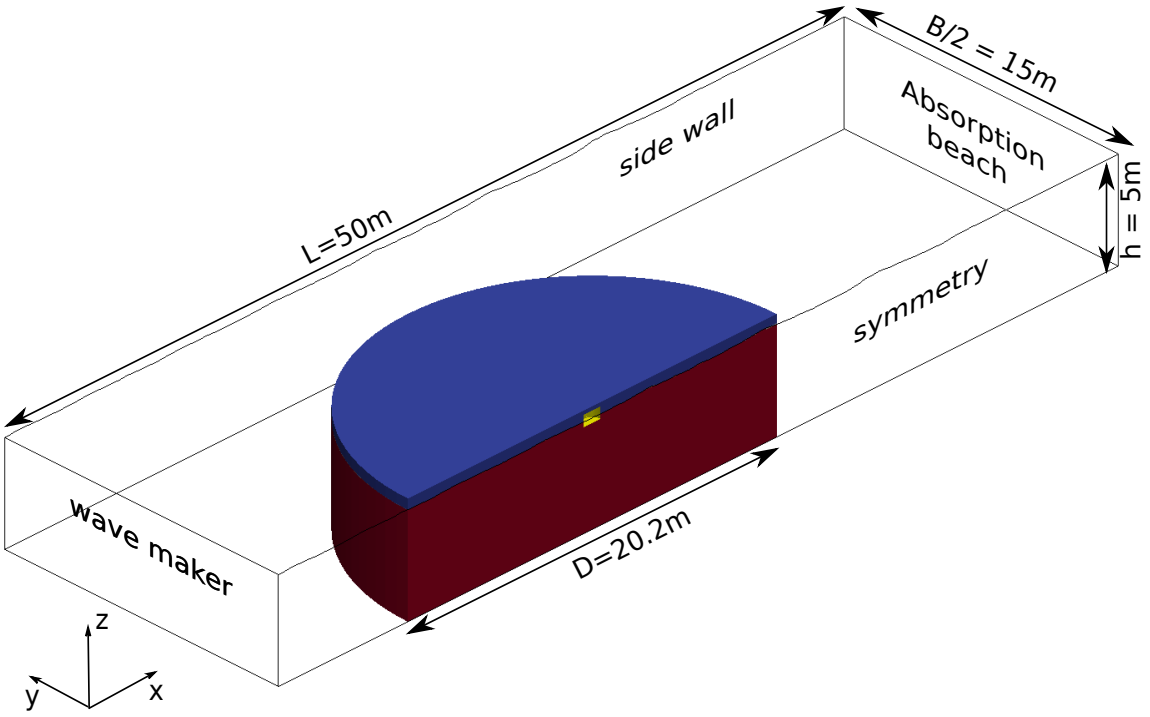

Figure 5.26: Computational domain of CALM buoy in irregular waves.

Figure 5.28 gives a focused view between $t = 61s$ and $t = 64s$, where a large wave group reaches the buoy. The time histories of forces, both in the horizontal and the vertical direction, are in good agreement with the experimental data. Note that the simulation results has a peak value slightly larger than the experimental data. It may due to the overprediction of wave crest related to the incident wave reconstruction from HOS method (see Section 4.4).

Flow details near the structure are provided in Fig. 5.29. The free surface (approximated by the contour of VOF field $\alpha = 0.5$) is plotted with the free surface elevation η. The time interval between each figure is $0.1s$. Violent free surface deformations are observed near the structure. At $t = 62.95s$, a large runup on the structure, which corresponds to the peak in the time history of force. After this instant, wave breaking is observed at $t = 63.1s$. In this case, the two-phase solver is able to deal with this phenomenon without special difficulties, showing the advantage of the present two-phase SWENSE method over the original single-phase SWENSE method.

After 70s, the results from the simulation starts to show a difference from the experimental data. The most apparent difference happens at about 85s, when the wave forces are small. This difference may originate from the reflected waves in the wave tank experiment. *foamStar-SWENSE* simply prevents all the wave reflection, but reflections on the side walls and the absorption beach indeed happen in the experiment. When the incident wave is large, the influence of the reflected waves can be hidden. This explains why the differences are more remarkable when the wave forces are small. The discrepancies on the small wave forces may also due to the insufficient spatial discretization as pointed out in Chapter 4.

The good agreement of the wave forces in the time history confirms the accuracy of the SWENSE method in dealing with complex wave conditions. This last test case also shows the

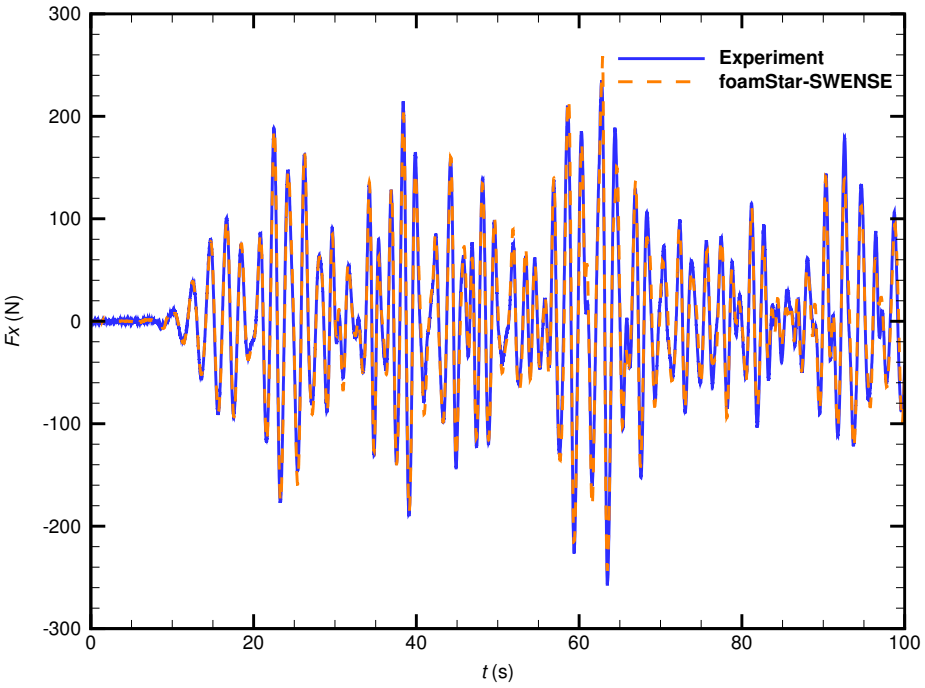

(a) Horizontal wave force on the CALM buoy in irregular waves

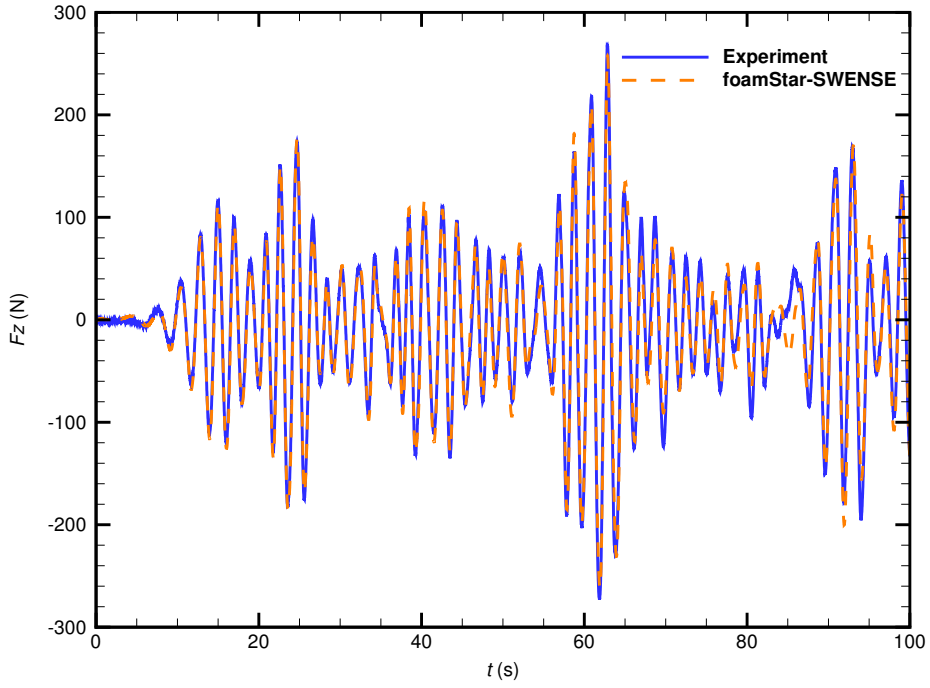

(b) Vertical wave force on the CALM buoy in irregular waves

Figure 5.27: Wave forces on the CALM buoy in irregular waves.

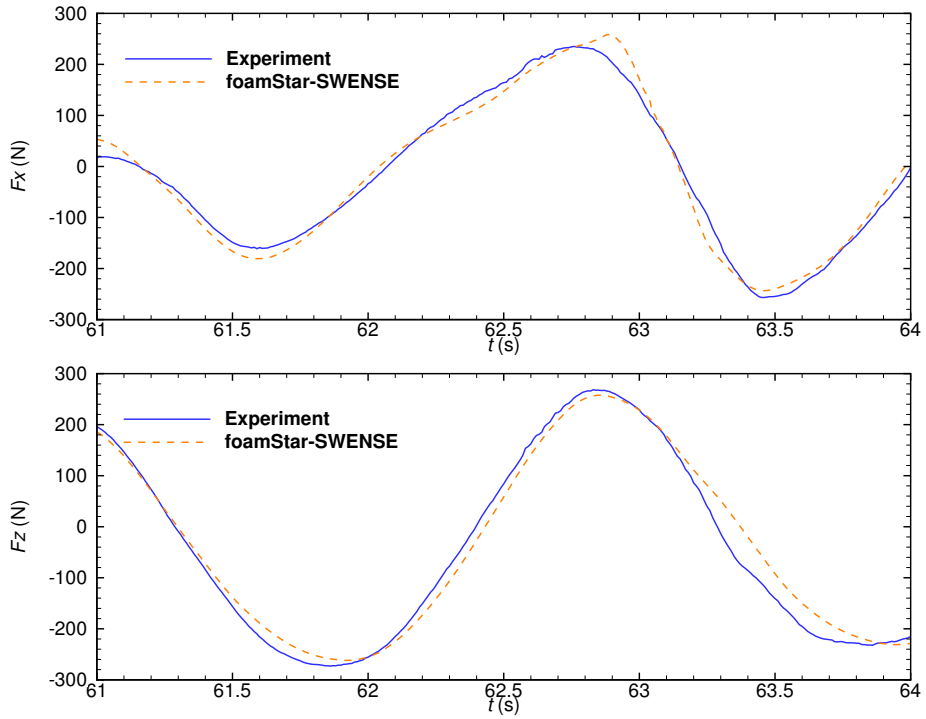

Figure 5.28: Wave forces on the CALM buoy in irregular waves.

advantages of the SWENSE method in reducing the computational cost:

- The size of the CFD computational domain is reduced. A large part of the wave tank is modeled efficiently by the potential wave solver, HOS-NWT;
- The number of cells in the CFD computational domain is reduced. Thanks to the explicit treatment of incident waves, coarse mesh in the far-field is able to produce the incident wave information accurately.

5.3 Summary

Two validation and application cases have been presented in this chapter.

Higher-order wave force on a vertical cylinder

The SWENSE method has been tested by calculating the wave loads on a vertical free-surface piercing cylinder.

A systematic mesh and time step refinement has been used to compare the convergence behavior of the three SWENSE formulations (the non conservative form, the conservative form, and the Ghost Fluid Method form). It is concluded that:

- The solvers with all the SWENSE formulations are able to produce correct converged results. The convergence order are all between 1 and 2.

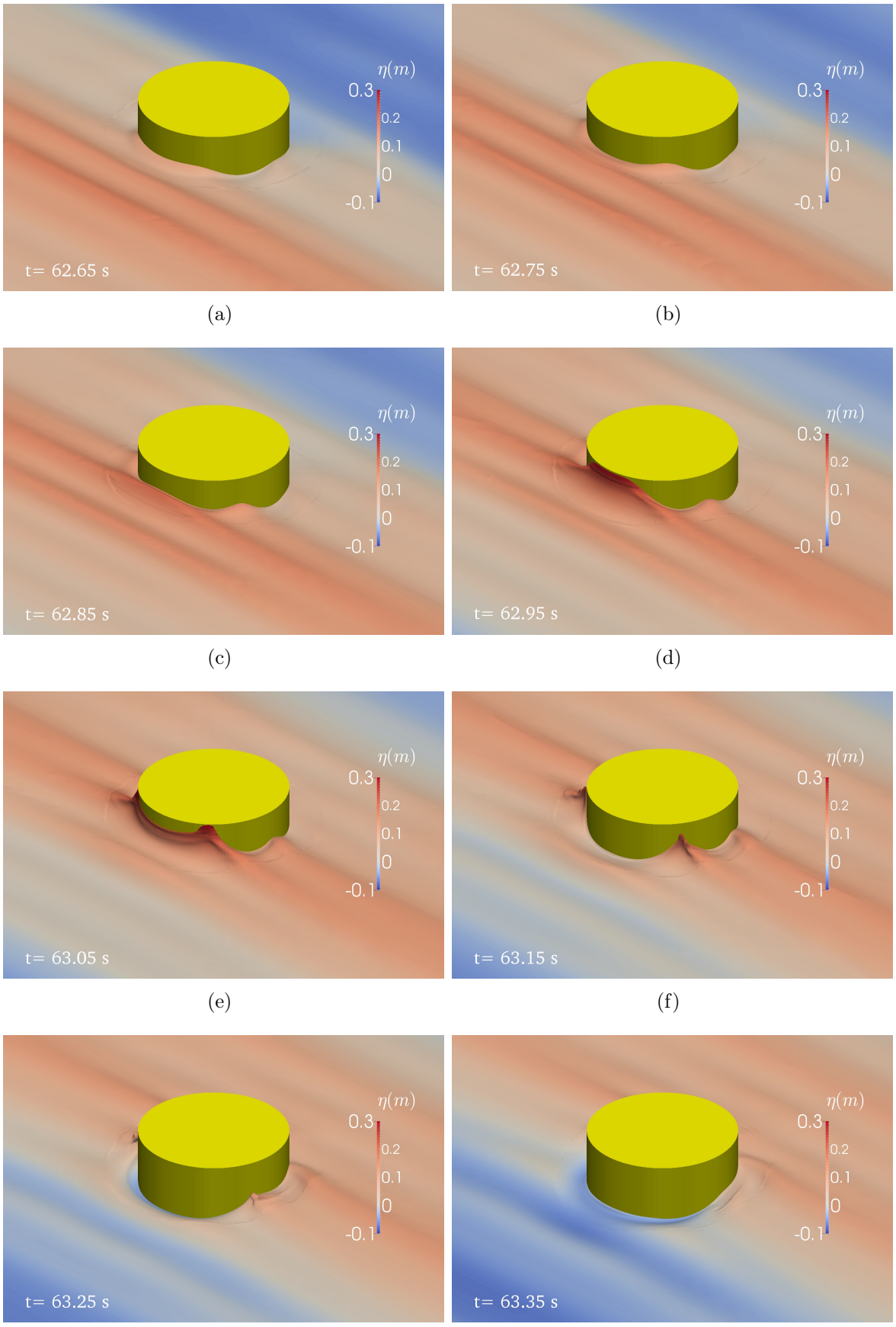

Figure 5.29: The free surface (contour of $\alpha = 0.5$) close to the buoy when a large wave group passes

- The relative errors show that the GFM formulation produces the most accurate results on coarse meshes; the non conservative formulation produces larger errors, while the conservative formulation produces the least accurate results on coarse meshes.
- All three formulations are able to produce very good results on the first harmonic force, even when the coarsest mesh is used, the dominant harmonic force has less than 10% difference than the finest discretization, while the computational cost is only 1/256 of the finest discretization. Showing the SWENSE method is able to produce a relatively good first order force with small computational cost.
- The higher harmonic force calculated with coarse mesh contains larger errors than the first harmonic force. Local mesh refinement near the structure may be needed to improve the accuracy on these harmonic components.

The efficiency of the three formulations has been studied. With the same setup, the Ghost Fluid Method formulation is the fastest, while the non conservative formulation and conservative formulation consumes 1.71 and 2.07 times more CPU time.

The comparison of the flow details shows a good agreement between the three formulations on the free surface elevation, the complementary pressure field, and the velocity field in the water. However, the conservative formulation creates larger air velocity than the other two formulations.

Still with this cylinder in wave test case, the SWENSE method has been validated by comparing with experimental data and reference numerical results. An excellent agreement on the first harmonic force is observed. The errors are less than 2% for all the wave steepnesses. The higher order components show also good agreement although the discrepancies are larger. The correctness of the two-phase SWENSE method is validated.

CALM buoy in regular and irregular waves

The ability of the two-phase SWENSE method in dealing with complex structure geometries has been validated by reproducing an experiment on a Catenary Anchor Leg Mooring (CALM) buoy.

The two-phase SWENSE method has been compared with a two-phase Navier-Stokes solver on the same numerical configurations (mesh and time step size). To make a fair comparison the GFM method version of the SWENSE method is not used, since it is not available in the conventional NS solver. A series discretization with different mesh sizes in the far-field are used. The results reveal that for conventional two-phase solver, fine mesh must be used in the entire computational domain to guarantee a good incident waves, while the two-phase SWENSE method is able to use coarse far-field mesh without much influence on the accuracy. To obtain the same level of accuracy, the two-phase SWENSE method is 1.71 to 4.28 times faster than the conventional method. This improvement comes directly from the use of SWENSE decomposition, without the Ghost Fluid Method.

The flow details obtained by the SWENSE method are validated by the NS solver's result. An excellent agreement has been shown on the velocity in the water and the pressure field, showing the correctness of the present mathematical models. The only difference is the velocity in the air. It has also been proven that the influence of this air velocity is negligible for the force calculation, and is thus acceptable for the present application scenario.

At last, the ability to deal with irregular waves has also been proven by reproducing an irregular wave case of the experiment. The wave forces calculated by the SWENSE solver

compares very well with the experimental data. The coupling of Higher-Order Spectral wave models and the SWENSE method to deal with the interaction of a structure and irregular waves has been validated. The results also show that the present two-phase method can deal with violent free surface deformation including the wave breaking phenomenon without special difficulties, which is a key advantage of the present two-phase SWENSE method over the original single-phase SWENSE method.

Chapter 6

Conclusion and perspectives

The objective of the present work is to develop a two-phase Spectral Wave Explicit Navier-Stokes Equations (SWENSE) method for two-phase CFD solvers to improve their efficiency in solving wave-structure interaction problems.

Before the present work, the SWENSE method was proposed [49] and had been developed for years in LHEEA Lab at Ecole Centrale de Nantes [48, 52, 81, 83, 91, 103]. It was used exclusively with a single-phase solver to solve the wave-structure interactions. The main advantage of the SWENSE method is that it allows the use of coarse mesh in the far-field without influencing the incident waves' accuracy. The accuracy and efficient of the SWENSE method has been validated and proved with the single-phase solver.

Due to the differences in the mathematical models between a single-phase CFD solver and a two-phase CFD solver, this method was not extended for two-phase solvers until the work of Vukčević [126, 127], in which the SWENSE method is extended to two-phase and implemented in OpenFOAM. However, the method proposed by Vukčević is different from the original SWENSE method: it kept all the incident wave solutions as source terms in the decomposed equations and evaluates them numerically on the CFD mesh and still requires a refined mesh to keep the incident wave accurate.

With this background, the objective of the present work is to develop a two-phase SWENSE method following the functional decomposition procedure used in the original SWENSE method.

6.1 Summary

This work has been documented in this thesis as follows.

Chapter 2 has provided a minimum theoretical background before developing the two-phase SWENSE method. The principal idea of the SWENSE method has been explained. It clarifies that the SWENSE governing equations should be derived by subtracting the Euler equations from the Navier-Stokes equations. It reveals that the resulting SWENS equations has the advantage in solving the incident wave propagation problem, *i.e.*, the CFD solution does not affect the incident wave solution: the complementary fields remains zero in the pure incident wave propagation scenario. This property should be inherited by the two-phase SWENSE method. The theoretical background of the spectral wave models is outlined. The information related to simulating two-phase flow is also provided, such as the two-phase Navier-Stokes equations, the Finite Volume method. The solution method in OpenFOAM is outlined.

The development of the mathematical models of the SWENSE method has been shown in Chapter 3. The definition zone of the Euler equations and the incident wave solution are exten-

ded in the air. The incident velocity field is extended directly in the air to ensure the continuity across the free surface. The incident pressure field is modified to solve the density-mismatch problem. A modified Euler equation is proposed to take into account this pressure modification. The two-phase SWENS equations are developed following the functional decomposition procedure by subtracting the modified Euler equations from the Navier-Stokes equations. Since the two-phase Navier-Stokes equations exist both in the conservative form and the non conservative form, the resulting two-phase SWENSE methods are in two forms as well. Another version using the Ghost Fluid Method [45, 67, 96, 126] are also presented to improve the accuracy and stability on the water-air interface. In a mathematical point of view, all the three forms of the governing equations are equivalent. They all inherit the property of the original SWENSE method, *i.e.*, being able to simulate the incident waves accurately with coarse CFD resolutions. The GFM form relies on special discretization operators to handle the interface discontinuity. The numerical discretization procedure of these equations and their implementation in OpenFOAM are shown. The first two versions of the governing equations requires only standard numerical discretization schemes. The GFM discretization operators developed by Vukčević [127] in the navalHydroPack [13] are used to implement the GFM version of the two-phase SWENSE solver.

Also in Chapter 3, a regular wave propagation test case with periodic boundary conditions has been conducted to test the proposed SWENSE formulations. It shows that the SWENSE methods can always produce more accurate results than a conventional Navier-Stokes solver if they use a same mesh, showing that the present two-phase SWENSE method is successful in reducing the errors in the incident wave propagation problem.

However, the wave solution may be different from the analytical solution due to the numerical error on the interface pressure term. Due to this error, the conservative formulation is prone to generate larger spurious air velocity than the non conservative formulation. The use of the Ghost Fluid method is able to reduce this numerical error drastically, and thus provide incident waves with the best quality. Fortunately, this problem caused by the numerical error is serious only if a periodic computational domain is used since the numerical errors can accumulate. This error can be absorbed by the wave generation and absorption boundary conditions in practical wave-structure applications. In the test case with wave generation and absorption boundary conditions, all the three SWENSE formulations are able to produce accurate incident wave results for a long simulation time.

Chapter 4 explains the difficulties in reconstructing the incident wave solution on the CFD mesh from a HOS wave model. The commonly used interpolation technique creates interpolation errors, since the spatial interval in a HOS grid is too large. A new interpolation method is proposed. The improvement is achieved through a refinement of the HOS grid at the post-processing stage. A zero-padding procedure extends the modal spectrum and translate the spectrum on a refined HOS grid with the Inverse Fast Fourier Transform algorithm. With this method, the interpolation accuracy can be improved drastically. The reconstruction error on the velocity divergence field can be reduced to by 2 orders of magnitude. With this method, the reconstructed velocity field can be used to transport the volume fraction field without breaking its boundedness. The ability to simulate irregular waves by the two-phase SWENSE method is tested. The CFD simulation is stable and compares well with the target value even after a long simulation time.

The validation of the two-phase SWENSE method is presented in Chapter 5.

The three SWENSE formulations have been tested and compared by calculating the higher-

order wave forces on a 3D vertical cylinder.

The convergence behavior of present implementation in OpenFOAM is compared in the first place. It is found that all the SWENSE formulations are able to produce converged results. The order of convergence is checked by the first four harmonic amplitudes of the wave force. All the three formulations are converging with an order between 1 and 2, which is consistent with the numerical schemes used in OpenFOAM.

By comparison of the three different SWENSE method, it is found that the GFM formulation produces the most accurate results on coarse meshes; the non conservative formulation produces larger errors, while the conservative formulation produces the least accurate results on coarse meshes. With the same setup, the GFM formulation is the fastest, while the non conservative formulation and conservative formulation consumes 1.71 and 2.07 times more CPU time. It may be concluded that the Ghost Fluid Method is helpful in improving the efficiency and the accuracy on coarse mesh.

It is worth noting that all the three formulations are able to predict first harmonic force well, even with very coarse mesh. The first harmonic force on a mesh with 88000 cells has less than 10% difference than on the finest mesh with 5.5 million cells, while the mesh size is only 1/64, showing the SWENSE method is very suitable to produce a good first order force with small computational cost. This property may be useful in the early stage design and optimization applications where the absolute accuracy is less important or the number of calculations is extremely high.

Still with this cylinder in wave test case, the SWENSE method has been validated by comparing with experimental data and reference numerical results. An excellent agreement on the first harmonic force is observed. The errors are less than 2% for all the wave steepnesses. The higher order components show also good agreements for all the wave steepnesses although the discrepancies are larger. The correctness of the two-phase SWENSE method is validated.

The Catenary Anchored Leg Mooring (CALM) buoy test case shows the ability of the two-phase SWENSE method in dealing with a more complex geometry. The two-phase SWENSE method produces good results comparing with the experimental data. The comparison between the SWENSE solver and the Navier-Stokes solver (both without GFM) shows that the two-phase SWENSE method is 1.71 to 4.28 times faster than the conventional method to achieve a same level of accuracy thanks to the use coarse mesh in the far-field. This test case also confirms that directly extending the incident velocity field in the air has negligible influence on the wave force on the structure, so that the present method can be applied to the majority of wave-structure interaction problems as long as the problems do not focus on the air effects.

At last, the coupling of Higher-Order Spectral wave models and the SWENSE method to deal with the irregular waves has been validated. A very good agreement between the SWENSE method results and the experimental data is found. The results also show that the present two-phase method can deal with violent free surface deformation including the wave breaking phenomenon without special difficulties, which is a key advantage of the present two-phase SWENSE method over the original single-phase SWENSE method.

6.2 Conclusion

To conclude, the SWENSE method has been extended for two-phase CFD solvers.

The incident velocity field is extended directly in the air. The incident pressure field is modified according to the real free surface position given by the simulation. This extension

makes the solution in the air not physically correct to earn a continuous velocity field across the free surface. This extension is valid for classical wave-structure interaction problem, as long as the air effects are not the focus.

Three versions of two-phase SWENSE governing equations are proposed, including:

- Non conservative form
- Conservative form
- Ghost Fluid Method (GFM) form

Comparing with the conventional two-phase Navier-Stokes solvers, solvers implementing any of the three SWENSE formulations will require less computational resources to achieve the same accuracy.

The comparison between the three formulations leads to the following conclusion.

The non conservative form and the conservative form use standard numerical discretization schemes and can be adopted by most two-phase solvers with minimal efforts. With the present test cases, the non conservative form shows a better performance than the conservative form. The conservative form prones to generate more momentum in the air phase and creates larger numerical error in both wave propagation and wave-structure interaction problems. The GFM form relies on special discretization operators to handle the interface discontinuity, but if the Ghost Fluid method can be adopted, both efficiency and accuracy can be enhanced.

An improved interpolation method to map the results of Higher-Order Spectral (HOS) wave models onto the CFD mesh is proposed. The method refines the HOS grid by adding zero-amplitude components to the wave spectrum. The refinement is done in the reconstruction stage, without increasing the computational cost of the HOS simulations. The efficiency is ensured by using the Fast Fourier Transform algorithm. A substantial improvement on the interpolation accuracy is achieved.

The test cases show the present method can be applied to calculate the wave load on simple and complex structure exposed in either regular or irregular waves. Comparing to conventional two-phase Navier-Stokes solver, the present two-phase method can achieve the same level of accuracy with smaller computational cost (speed up 1.71 to 4.28 times in present test case); comparing to the original single-phase SWENSE method, the present method can handle wave breaking phenomenon without special difficulties.

6.3 Proposals for future work

The present work provides a thorough description of the SWENSE method for two-phase CFD solvers. Three versions of governing equations are proposed to facilitate the implementation of this method in most two-phase CFD solvers without extensive efforts. The majority of numerical implementation are based on open source codes: OpenFOAM [14], HOS-Ocean [5], HOS-NWT [4], and Grid2Grid [3]. The reader is encouraged to reproduce this work following the implementation details presented in this thesis.

The proposals for future works are given as follows.

6.3.1 6DoF motion and dynamic mesh

The present work is only limited to the calculation of the wave force on a fixed structure. However, in most marine and offshore applications, a moving structure is of interest, *e.g.*, seakeeping, maneuvering, added resistance in waves, *etc.* The next step of the work is to extend the two-phase SWENSE method to deal with moving structures. This work can be done straightforwardly in OpenFOAM by using the existing dynamic mesh module. The behavior of the three versions of governing equations shall be tested with a dynamic mesh. More validation cases are necessary.

6.3.2 Level-Set

In the present version, the interface capturing is achieved through the Volume of Fluid Method [65]. This method is mass conservative but the interface is always smeared into several cells. Moreover, due to the boundedness of the VOF field, it can not be decomposed into an incident part and a complementary part. The transport of the VOF field may create numerical errors which should not happen in a pure incident wave propagation case (in the point of view of SWENSE). Note that the present two-phase SWENSE method is not limited to the VOF technique. The use of other interface capturing approaches can be straightforward. Two approaches have been proposed to use the Level-Set method within the SWENSE method [102, 126]. In the work [102] the Level-Set governing equation is also decomposed so that it equals zero for the pure incident wave propagation case. It helps to keep the incident wave propagation correct on coarse mesh. However, it requires a re-distancing procedure. This re-distancing procedure maybe removed with the implicit re-distancing method proposed in [126]. This work will be more interesting if the solver has a higher-order accuracy, since the Level-Set method is more accurate in such condition.

Chapter 7

Résumé substantiel en Français

Introduction générale

L'objectif de cette thèse est de développer une nouvelle approche de simulation numérique pour étudier les interactions houle-structure dans le domaine de l'ingénierie océanique et navale. L'approche numérique est basée sur une nouvelle formulation diphasique de la formulation Spectral Wave Explicit Navier-Stokes Equations (SWENSE), qui relie des modèles de houle basés sur la théorie potentielle et des codes de calcul diphasiques des équations Navier-Stokes.

Avant les travaux actuels, la méthode SWENSE monophasique avait été proposée [49] et développée au laboratoire LHEEA de l'Ecole Centrale de Nantes [48, 52, 81, 83, 91, 103]. Le principal avantage de la méthode SWENSE est qu'il permet aux codes CFD d'utiliser des maillages grossiers dans le champ lointain sans influencer la précision de la houle incidente. La précision et l'efficacité de la méthode SWENSE ont été validés avec des codes CFD monophasiques.

En raison des différences importantes entre les modèles mathématiques des codes monophasiques et diphasiques, la méthode SWENSE n'avait pas été étendue à ces solveurs diphasiques jusqu'au travail de Vukčević [126, 127]. Cependant, la méthode proposée par Vukčević diffère de la méthode SWENSE initiale : tous les termes issus des houles incidentes sont gardés comme termes sources dans les équations décomposées. Par conséquent, ces termes doivent être évalués numériquement sur le maillage CFD et nécessitent donc un maillage raffiné pour conserver la précision des houles incidentes.

Dans ce contexte, l'objectif du travail présenté ici consiste à développer une méthode diphasique de SWENSE en suivant la procédure de la décomposition fonctionnelle utilisée dans la méthode d'origine.

Afin d'atteindre cet objectif, la thèse apporte les contributions spécifiques suivantes:

1. De nouveaux modèles mathématiques de SWENSE sont dérivés pour les codes CFD diphasiques avec capture d'interface. Les équations sont proposées sous trois formes,

   - Forme non-conservative;
   - Forme conservative;
   - Forme Ghost Fluid Method (GFM [128]).

   Les deux premières formes utilisent des schémas de discrétisation numérique standard et peuvent être adoptées par la plupart des codes de calcul diphasiques sans difficultés

majeures. La forme GFM est une amélioration des deux formes précédentes en terme de précision et de stabilité de l'interface. Elle s'appuie sur des opérateurs de discrétisation spécifiques pour gérer la discontinuité de l'interface [127].

2. Une technique de reconstruction permettant d'évaluer efficacement les résultats des modèles de houle de type High-Order Spectral (HOS) sur des maillages CFD est proposée. Cette technique améliore la qualité du champ des houles incidentes après sa reconstruction sur le maillage CFD, sans augmenter le coût de calcul des simulations HOS. L'efficacité de la reconstruction est garantie par l'utilisation de l'algorithme Fast Fourier Transform (FFT).

Résumé par chapitre

La thèse contient six chapitres. Le contenu de ces chapitre est la suivant.

Chapitre 1 : Introduction

Le Chapitre 1 constitue l'introduction générale de la thèse et détaille le contexte d'application du présent travail. La nécessité d'accélérer les codes CFD pour l'étude des interactions houle-structure est expliquée. Une étude bibliographique sur la méthode d'accélération est ensuite fournie, qui se concentre sur le couplage de la théorie des écoulements potentiels et visqueux. Deux types de stratégie de couplage sont identifiés. Le premier est la décomposition de domaine (DD) et le second est la décomposition fonctionnelle (FD-functional decomposition). En général, les méthodes FD présentent plus d'avantages que les méthodes DD puisqu'elles permettent l'utilisation d'un maillage CFD grossier dans le champ lointain pour les problèmes d'interaction houle-structure. La méthode SWENSE est ensuite introduite en tant que méthode de type FD. Le concept de la méthode SWENSE, c'est-à-dire la décomposition du problème total en un problème de houle incidente et un problème complémentaire, est expliquée. L'historique de la méthode SWENSE est donné, puis la nécessité de développer une nouvelle méthode SWENSE pour les solveurs CFD diphasiques est avancée.

Chapitre 2 : Modèles mathématiques et méthodes numériques

Le Chapitre 2 rappelle tout d'abord un certain nombre d'éléments theoriques, utiles dans la suite du développement. Il précise que les équations SWENS - les équations gouvernant les champs comlémentaires - doivent être dérivées en soustrayant les équations d'Euler aux équations de Navier-Stokes. Avec un problème simplifié de propagation d'une onde incidente comme exemple, l'avantage des équations SWENS est démontré par le fait que la résolution du maillage en CFD n'affecte pas la propagation de l'onde incidente : les champs complémentaires restent nuls dans le scénario de propagation de houle seule. Cette propriété doit être conservée par la méthode SWENSE diphasique à développer.

Ce chapitre décrit aussi les deux modèles de houle, le modèle High-Order Spectral (HOS) [37] et le modèle de la fonction de courant [41], utilisés dans cette thèse. Ces deux modèles sont basés sur la théorie potentielle et résolus numériquement par une méthode spectrale. Ces modèles sont choisis car ils sont à la fois précis et efficaces. De plus, la cinématique des houles incidentes peut facilement être étendue au-dessus de la surface incidente. Une telle propriété

est très utile pour la méthode SWENSE, lorsque les surfaces libres de l'écoulement incidentes et de l'écoulement totale sont différentes.

Les modèles mathematiques des solveurs diphasiques sont également fournies, y compris les équations diphasiques de Navier-Stokes, la méthode des volumes finis, ainsi que les méthodes numériques dans OpenFOAM sont également présentés dans ce chapitre.

Chapitre 3 : Methode SWENSE diphasique

Ce chapitre présente les principaux travaux de recherche de cette thèse concernant le développement de la méthode SWENSE pour les écoulements diphasiques. Ce chapitre est divisé en trois parties, comprenant

- Sects. 3.1 - 3.7: les formulations mathématiques de la méthode SWENSE diphasique;
- Sect. 3.8 : l'implémentation des solveurs SWENSE diphasique dans OpenFOAM;
- Sect. 3.9: un exemple de test de propagation d'ondes.

Tout d'abord, les formulations mathématiques de la méthode SWENSE diphasique sont présentées dans la Sect. 3.1 - 3.6. Cette partie explique les difficultés rencontrées pour étendre la méthode SWENSE originelle (monophasique) à la configuration diphasique et propose une solution pour surmonter ces difficultés.

Dans la Sect. 3.1, les différences entre un code monophasique et un code diphasique sont identifiées. Les exigences et les défis liés au développement des modèles mathématiques pour la méthode SWENSE diphasique sont expliqués.

La Sect. 3.2 montre une première tentative de développement des équations SWENS diphasiques, où la procédure de décomposition fonctionnelle de la méthode SWENSE monophasique est appliquée directement. Cependant, les équations obtenues ne conservent pas les avantages de la méthode SWENSE et sont donc abandonnées. Ensuite, la raison d'un tel échec est analysée.

Afin de surmonter ces difficultés, la Sect. 3.3 propose une étape supplémentaire avant d'appliquer la décomposition fonctionnelle. Dans cette étape, les équations d'Euler, décrivant les champs incidents, sont reformulées.

Dans la Sect. 3.4 les équations diphasiques de SWENS sont dérivées en utilisant les équations d'Euler reformulées, à la fois sous la forme conservative et sous la forme non conservative. Les propriétés des équations dérivées sont analysées.

Dans la Sect. 3.5, la méthode GFM est utilisé pour améliorer la stabilité de l'interface, en dérivant la troisième forme du nouveau schéma SWENSE diphasique.

La Sect. 3.6 explique les conditions aux limites utilisées dans la méthode SWENSE diphasique. La plupart de ces conditions sont identiques avec la méthode monophasique. Seule la condition limite sur la frontière au dessus du domaine, qui représente une connection ouverte avec l'atmosphère, est nouvelle, car elle n'est pas requise par la méthode monophasique. Différentes définitions possibles de cette condition aux limites et leurs influences sont discutées.

Ces sections (Sect. 3.1 - 3.6) expliquent le développement des nouvelles formulations mathématiques de la méthode SWENSE diphasique dans cette thèse. Dans la Sect. 3.7, la méthode proposée est comparée à une autre méthode SWENSE diphasique, développée par Vukčević *et al.* [127].

La seconde partie contient uniquement la Sect. 3.8. Dans cette section, les modèles mathématiques sont implémentés dans OpenFOAM pour développer un code SWENSE diphasique, dénommé *foamStar-SWENSE*.

La dernière partie de ce chapitre (Sect. 3.9) teste la méthode SWENSE diphasique avec cas-test illustrant la propagation de houle seule. *foamStar-SWENSE* est comparé à *foamStar* et à une solution potentielle. Une comparaison entre la forme conservative, la forme non conservative et la forme GFM est également fournie. On montre que les méthodes SWENSE peuvent toujours produire des résultats plus précis qu'un code de Navier-Stokes s'ils utilisent un même maillage. Ceci prouve que que la méthode SWENSE diphasique permet de réduire les erreurs dans le problème de la propagation de houle seule.

Cependant, la solution obtenue peut être différente de la solution analytique en raison de l'erreur numérique sur le terme de pression d'interface. En raison de cette erreur, la formulation conservative est susceptible de générer une vitesse de l'air parasite supérieure à celle de la formulation non conservative. L'utilisation de GFM est capable de réduire considérablement cette erreur numérique et de fournir ainsi des houles incidentes avec la meilleure qualité. Heureusement, ce problème causé par l'erreur numérique n'est important que si un domaine périodique est utilisé car les erreurs numériques peuvent s'accumuler. Cette erreur peut être controlée par les conditions aux limites d'absorption et de génération d'onde dans les applications pratiques d'interaction houle-structure. Dans le cas-test avec des conditions limites d'absorption et de génération, les trois formulations de SWENSE sont capables de produire des résultats des houles incidentes précises pendant une longue période de simulation.

Chapitre 4 : Reconstruction du champ incident sur le maillage CFD

Ce chapitre est consacré à la reconstruction du champ de houle obtenu par la méthode spectrale sur le maillage CFD. Cette reconstruction est nécessaire car la méthode spectrale exprime les résultats avec une description modale, tandis que les codes CFD ont besoin des informations spatiales sur l'ensemble d'un maillage quelconque. La reconstruction peut être réalisée de deux manières:

- Evaluation directe analytique (pour des houles régulières) : les informations sur les houles incidentes dans une cellule du maillage sont évaluées en substituant le temps et les coordonnées aux fonctions modales;

- Interpolation (pour des houles irrégulières) : les résultats de la méthode spectrale sont d'abord transformés par la transformation de Fourier rapide inverse sur une grille rectangulaire grossière, puis interpolés sur le maillage CFD.

Ce chapitre explique les difficultés pour reconstruire la solution des houles irregulières obtenues par la méthode spectrale de type HOS. La technique d'interpolation couramment utilisée crée des erreurs d'interpolation, car l'intervalle spatial dans la grille HOS est trop grand.

Une nouvelle méthode d'interpolation est proposée. L'amélioration est obtenue par un raffinement de la grille HOS au stade du post-traitement. Une procédure de remplissage à zéro (zero-padding) étend le spectre modal et le traduit sur une grille HOS raffinée avec l'algorithme Inverse Fast Fourier Transform (IFFT). Avec cette méthode, la précision d'interpolation peut être considérablement améliorée. L'erreur de reconstruction du champ de divergence de vitesse peut être réduite de ainsi 2 ordres de grandeur.

La capacité de simuler des houles irrégulières par la méthode SWENSE diphasique est testée. Le test est stable et se compare bien au champs de référence même après une longue période de simulation.

Chapitre 5 : Validation et applications

Après avoir démontré la capacité de la méthode SWENSE diphasique proposée à la propagation des houles incidentes aux chapitres 3 et 4, ce chapitre vise à prouver la validité et l'efficacité de cette nouvelle méthode pour résoudre le problème de l'interaction houle-structure.

La principale différence entre un problème d'interaction houle-structure et la propagation des houles incidentes réside dans le fait que des structures apparaissent dans le domaine de calcul et perturbent les houles incidentes. Des champs complémentaires non nuls sont attendus traduisant cette interaction. La méthode SWENSE diphasique devrait permettre de calculer correctement les champs complémentaires.

Deux cas-tests sont utilisés pour tester la méthode SWENSE diphasique.

Cylindre vertical dans des houles régulières

Le premier est un problème simple et classique d'interaction houle-structure. On cherche à calculer les composantes d'ordre élevé des efforts de houle sur un cylindre vertical fixé au fond. Ce cas-test est utilisé pour:

- Etudier et comparer les propriété de convergence des trois formulations diphasique proposées dans cette thèse;
- Comparer le temps de calcul des trois formulations diphasique;
- Valider la méthode SWENSE diphasique en comparant les résultats des simulations SWENSE avec des données expérimentales et d'autres résultats numériques.

On constate tout d'abord que toutes les formulations SWENSE sont capables de produire des résultats convergents. L'ordre de convergence est vérifié sur les quatre premières amplitudes harmoniques des efforts dus à la houle. Les trois formulations convergent avec un ordre compris entre 1 et 2, ce qui est cohérent avec les schémas numériques utilisés dans OpenFOAM.

En comparant les trois formes des équations SWENS, il est apparu que la formulation GFM produisait les résultats les plus précis sur les maillages grossiers; la formulation non conservative produit des erreurs un peu plus importantes, tandis que la formulation conservative produit les résultats les moins précis sur des maillages grossiers. Avec la même configuration, la formulation GFM est la plus rapide, tandis que la formulation non conservative et la formulation conservative consomment 1,71 fois et 2,07 fois plus de temps de calcul. On peut en conclure que la GFM est utile pour améliorer l'efficacité et la précision quand des maillages grossiers sont utilisés.

Il est à noter que les trois formulations sont capables de bien prédire la première harmonique de la force, même avec un maillage très grossier. La première harmonique sur un maillage de 88 000 cellules a une différence inférieure à 10 % par rapport au maillage le plus fin comportant 5,5 millions de cellules, alors que la taille du maillage n'est que de 1/64, montrant que la méthode SWENSE est très appropriée pour produire une bonne estimation des forces de premier ordre avec un faible coût de calcul. Cette propriété peut être utile dans les applications de conception et d'optimisation à un stade préliminaire où la précision requise est moins importante et/ou le nombre de calculs à réaliser est extrêmement élevé.

Toujours avec ce cas-test, la méthode SWENSE a été validée en comparant les résultats avec des données expérimentales et des résultats numériques de référence. Un excellent accord sur la première harmonique de la force est observé. Les erreurs sont inférieures à 2 % pour toutes les cambrures (*i.e.*, non-linéarités) de houles. Les composantes d'ordres élevés montrent

également un bon accord pour toutes les cambrures des houles, bien que les écarts soient plus importants. La validité de la nouvelle méthode est confirmée.

Bouée CALM dans les houles régulières et irrégulières

Le deuxième cas-test représente un scénario d'application réel. La structure étudiée est une bouée d'ancrage caténaire (CALM-Catenary Anchor Leg Mooring [107]). La simulation reproduit les conditions expérimentales dans lesquelles la bouée est fixée dans sa position hydrostatique et exposée à des houles régulières et irrégulières. Des déferlements des houles et des effets visqueux importants sont attendus. Ce cas est utilisé pour :

- Valider et tester la robustesse de la méthode SWENSE dans le traitement d'une géométrie complexe ;
- Démontrer l'efficacité de la méthode SWENSE diphasique en la comparant à la méthode de Navier-Stokes diphasique originelle ;
- Valider la méthode SWENSE diphasique en comparant les détails de l'écoulement avec la méthode de Navier-Stokes diphasique originelle ;
- Valider la modélisation de houle irrégulière avec le modèle de houle HOS.

La nouvelle méthode produit de bons résultats en comparaison avec les données expérimentales. La comparaison entre le code SWENSE et le code Navier-Stokes (tous deux sans GFM) montre que la méthode SWENSE est 1,71 à 4,28 fois plus rapide que la méthode Navier-Stokes pour atteindre le même niveau de précision, grâce à l'utilisation d'un maillage grossier dans le champ lointain. Ce cas-test confirme également que l'extension directe du champ de vitesse incidente dans l'air a une influence négligeable sur l'évaluation de la force générée par les houles sur la structure, de sorte que la méthode actuelle peut être appliquée à la majorité des problèmes d'interaction houle-structure tant que ces problèmes ne se concentrent pas sur les effets de l'air.

Enfin, le couplage des modèles de houle HOS et de la méthode SWENSE pour traiter les houles irrégulières a été validé. Un très bon accord entre les résultats de la méthode SWENSE et les données expérimentales est trouvé. Les résultats montrent également que la méthode actuelle peut traiter une déformation de surface libre violente, y compris le phénomène de déferlement, sans difficultés particulières, ce qui constitue un avantage majeur de la méthode actuelle par rapport à la méthode SWENSE monophasique d'origine.

Chapitre 6 : Conclusion et perspectives

Ce chapitre présente le résumé et les conclusions de la thèse. Les perspectives de recherche future sont également brièvement discutées.

Conclusion

En conclusion, la méthode SWENSE a été étendue avec succès pour des codes CFD diphasiques.

Le champ de vitesse incident est directement étendu dans l'air. Le champ de pression incident est modifié en fonction de la position réelle de la surface libre, donnée par la simulation diphasique. Cette extension rend la solution dans l'air non physique, mais elle génére un champ de vitesse continu sur la surface libre, propriété essentielle pour la formulation SWENSE. Cette

extension est valable pour le problème classique d'interaction houle-structure, tant que les effets de l'air ne sont pas importants.

Trois formes des équations SWENS diphasique sont proposées, notamment:

- Forme non-conservative ;
- Forme conservative ;
- Forme Ghost Fluid Method (GFM).

Comparés aux codes Navier-Stokes diphasiques classiques, les codes SWENSE mettant en œuvre l'une des trois formulations SWENSE consommeront moins de ressources de calcul pour obtenir une même précision.

Les cas-test montrent que la méthode SWENSE peut être appliquée pour calculer les efforts de houle sur une structure exposée à des houles régulières ou irrégulières. Comparée au code conventionnel Navier-Stokes, la méthode actuelle peut atteindre le même niveau de précision avec un coût de calcul moindre (accélération de 1,71 à 4,28 fois dans un cas classique) ; En comparant à la méthode SWENSE monophasique d'origine, la méthode diphasique peut gérer le phénomène de déferlement des houles sans difficultés particulières.

La comparaison entre les trois formulations conduit à la conclusion suivante. La forme non-conservative et la forme conservative utilisent des schémas de discrétisation numérique standard et peuvent être adoptées par la plupart des codes diphasiques de façon relativement simple. Sur les cas-tests choisis, la forme non-conservative montre une meilleure performance que la forme conservative. La forme conservative a une tendance à générer plus d'erreurs numériques dans l'air. La forme GFM s'appuie sur des opérateurs de discrétisation spéciaux pour gérer la discontinuité d'interface, mais si la GFM peut être adoptée, l'efficacité et la précision peuvent être améliorées.

Une méthode d'interpolation permettant d'évaluer les résultats des modèles de houle obtenus par la méthode HOS sur le maillage CFD est proposée. La méthode raffine la grille HOS en ajoutant des composantes modales d'amplitude zéro à la description spectrale des houles. Le raffinement est effectué au stade de la reconstruction, sans augmenter le coût de calcul des simulations HOS. L'efficacité est garantie par l'utilisation de FFT. Une amélioration substantielle de la précision d'interpolation est obtenue.

Perspectives

Le présent travail fournit une description détaillée de la méthode SWENSE pour les solveurs CFD diphasiques. Trois versions des équations sont proposées pour faciliter la mise en œuvre de cette méthode dans la plupart des solveurs CFD. La majorité des implémentations numériques sont basées sur des codes source ouverts (open-source) : OpenFOAM [14], HOS-Ocean [5], HOS-NWT [4] et Grid2Grid [3]. Le lecteur est invité à reproduire ce travail en suivant les détails de mise en œuvre présentés dans cette thèse.

Les propositions pour les travaux futurs sont les suivantes.

Mouvement 6DDL et maillage dynamique

Le présent travail se limite au calcul des efforts dus aux houles sur une structure fixe. Cependant, dans la plupart des applications marines et offshore, on s'intéresse aux structures flottantes avec vitesse d'avance pour des problèmes de tenue à la mer, de manœuvrabilité, de résistance

ajouté sur houle, *etc.* La prochaine étape du travail consiste à étendre la méthode actuelle aux structures en mouvement. Ce travail peut être effectué directement dans OpenFOAM en utilisant le module de maillage dynamique. Le comportement des trois versions des équations SWENS doit être testé avec un maillage dynamique. Différents de cas de validation seront nécessaires.

Level-Set

Dans la version actuelle, la capture d'interface est réalisée via la méthode VOF (Volume of Fluid)[65]. Cette méthode est conservative en masse mais l'interface est toujours diffusée sur plusieurs cellules. De plus, la nature de la méthode VOF ne permet pas la décomposition en une partie incidente et une partie complémentaire. Le transport du champ VOF peut créer des erreurs numériques qui ne devraient pas apparaître dans un cas de propagation de houle incidente (du point de vue de SWENSE). Cependant, la méthode SWENSE diphasique actuelle ne se limite pas à la technique VOF. L'utilisation d'autres approches de capture d'interface est possible. Deux approches ont été proposées pour utiliser la méthode Level-Set dans la méthode SWENSE [102, 126]. Dans la mise en oeuvre présenté par Reliquet [102], l'équation VOF est également décomposée de sorte qu'elle soit égale à zéro pour le cas de propagation de houle seule. Cela aide à maintenir la précision de la propagation de houle incidente sur un maillage grossier. Cependant, cela nécessite une procédure de re-distanciation. Cette re-distanciation peut être supprimée avec la méthode implicite proposée dans [126]. Ce travail sera plus intéressant pour les solveurs d'ordre élevé, car la méthode Level-Set est plus précise dans de telles conditions.

Bibliography

[1] ANSYS marine and offshore CFD simulation: hydrodynamics and wave impact analysis. https://www.ansys.com/products/fluids/multiphase-flows/marine-and-offshore-cfd-simulation. Accessed: 2018-08-15.

[2] FINE/Marine product description. https://www.numeca.com/product/finemarine. Accessed: 2018-08-15.

[3] Grid2Grid: HOS wrapper for C++/Fortran CFD solvers. https://github.com/LHEEA/Grid2Grid. Accessed: 2018-08-15.

[4] Numerical wave tank based on High-Order Spectral method . https://github.com/LHEEA/HOS-NWT, . Accessed: 2018-08-15.

[5] High-Order Spectral method for oceanic simulations. https://github.com/LHEEA/HOS-ocean, . Accessed: 2018-08-15.

[6] NEMOH-presentation. https://lheea.ec-nantes.fr/logiciels-et-brevets/nemoh-presentation-192863.kjsp. Accessed: 2018-08-15.

[7] OpenFOAM user guide. https://www.openfoam.com. Accessed: 2018-08-15.

[8] ReFRESCO. http://www.marin.nl/web/Facilities-Tools/CFD/ReFRESCO.htm. Accessed: 2018-08-15.

[9] SIMULIA XFlow high fidelity CFD based on Lattice-Boltzmann method. https://www.3ds.com/products-services/simulia/products/xflow/marine-offshore. Accessed: 2018-08-15.

[10] Star-CCM+ product description. https://mdx.plm.automation.siemens.com/marine. Accessed: 2018-08-15.

[11] WAMIT technical description. https://www.wamit.com/techdescription.htm. Accessed: 2018-08-15.

[12] CFDShip-Iowa. http://www.iihr.uiowa.edu/shiphydro/cfd-code. Accessed: 2018-08-15.

[13] Naval hydro pack, specialist in numerical marine hydrodynamics. http://navalhydro.wikkiltd.co.uk/. Accessed: 2018-08-30.

[14] About OpenFOAM . https://www.openfoam.com. Accessed: 2018-08-15.

[15] B. Alessandrini and G. Delhommeau. Simulation of three-dimensional unsteady viscous free surface flow around a ship model. International Journal for Numerical Methods in Fluids, 19(4):321–342, 1994.

[16] M. Amini Afshar. Numerical wave generation in OpenFOAM®. Master's thesis, Chalmers University of Technology, 2010.

[17] A. Babarit and G. Delhommeau. Theoretical and numerical aspects of the open source BEM solver NEMOH. In 11th European Wave and Tidal Energy Conference, 2015.

[18] K. Bai and R. Yeung. Numerical solutions to free-surface flow problems. In 10th Symposium on Naval Hydrodynamics, 1974.

[19] E. Berberović, N. P. van Hinsberg, S. Jakirlić, I. V. Roisman, and C. Tropea. Drop impact onto a liquid layer of finite thickness: dynamics of the cavity evolution. Physical Review E, 79(3):036306, 2009.

[20] B. Biausser, P. Fraunié, S. T. Grilli, and R. Marcer. Numerical analysis of the internal kinematics and dynamics of 3-D breaking waves on slopes. International Journal of Offshore and Polar Engineering, 14(04), 2004.

[21] H. B. Bingham and H. Zhang. On the accuracy of finite-difference solutions for nonlinear water waves. Journal of Engineering Mathematics, 58(1-4):211–228, 2007.

[22] E. Campana, A. Di Mascio, P. Esposito, and F. Lalli. Viscous-inviscid coupling in free surface ship flows. International Journal for Numerical Methods in Fluids, 21(9):699–722, 1995.

[23] P. M. Carrica, R. V. Wilson, and F. Stern. Unsteady RANS simulation of the ship forward speed diffraction problem. Computers & Fluids, 35(6):545 – 570, 2006.

[24] H. C. Chen and S. K. Lee. Interactive RANS/Laplace method for nonlinear free surface flows. Journal of Engineering Mechanics, 122(2):153–162, 1996.

[25] H.-C. Chen and S.-K. Lee. RANS/Laplace calculations of nonlinear waves induced by surface-piercing bodies. Journal of Engineering Mechanics, 125(11):1231–1242, 1999.

[26] L. Chen, J. Zang, A. Hillis, G. Morgan, and A. Plummer. Numerical investigation of wave–structure interaction using OpenFOAM. Ocean Engineering, 88:91 – 109, 2014.

[27] Y. Chen and K. J. Maki. A velocity decomposition approach for three-dimensional unsteady flow. European Journal of Mechanics-B/Fluids, 62:94–108, 2017.

[28] Y. Choi, M. Gouin, G. Ducrozet, B. Bouscasse, and P. Ferrant. Grid2Grid : HOS Wrapper Program for CFD solvers. ArXiv e-prints.

[29] Y. Choi, B. Bouscasse, S. Seng, G. Ducrozet, L. Gentaz, and P. Ferrant. Generation of regular and irregular waves in Navier-Stokes CFD solvers by matching with nonlinear potential wave solution at the boundary. In 37th International Conference on Ocean, Offshore and Arctic Engineering, 2018.

[30] E. D. Christensen, H. Bredmose, and E. A. Hansen. Transfer of Boussinesq waves to a Navier-Stokes solver: application to wave loads on an offshore wind turbine foundation. In 28th International Conference on Ocean, Offshore and Arctic Engineering, 2009.

[31] G. Colicchio, M. Greco, and O. M. Faltinsen. A BEM-Level Set domain-decomposition strategy for non-linear and fragmented interfacial flows. International Journal for Numerical Methods in Engineering, 67(10):1385–1419, 2006.

[32] S. S. Deshpande, L. Anumolu, and M. F. Trujillo. Evaluating the performance of the two-phase flow solver interFoam. Computational Science & Discovery, 5(1):014016, 2012.

[33] DNVGL. Offshore Standard DNV-OS-C105: Structural design of TLPS. 2015.

[34] D. G. Dommermuth. The laminar interactions of a pair of vortex tubes with a free surface. Journal of Fluid Mechanics, 246:91–115, 1993.

[35] D. G. Dommermuth and D. K. Yue. A High-Order Spectral method for the study of nonlinear gravity waves. Journal of Fluid Mechanics, 184:267–288, 1987.

[36] G. Ducrozet. Modélisation des processus non-linéaires de génération et de propagation d'états de mer par une approche spectrale. PhD thesis, Université de Nantes; Ecole Centrale de Nantes (ECN), 2007.

[37] G. Ducrozet, F. Bonnefoy, D. Le Touzé, and P. Ferrant. HOS-Ocean: Open-source solver for nonlinear waves in open ocean based on High-Order Spectral method. Computer Physics Communications.

[38] G. Ducrozet, F. Bonnefoy, D. Le Touzé, and P. Ferrant. A modified High-Order Spectral method for wavemaker modeling in a numerical wave tank. European Journal of Mechanics-B/Fluids, 34:19–34, 2012.

[39] G. Ducrozet, F. Bonnefoy, D. Le Touzé, and P. Ferrant. HOS-Ocean: Open-source solver for nonlinear waves in open ocean based on High-Order Spectral method. Computer Physics Communications, 203:245 – 254, 2016.

[40] G. Ducrozet, F. Bonnefoy, and Y. Perignon. Applicability and limitations of highly nonlinear potential flow solvers in the context of water waves. Ocean Engineering, 142: 233–244, 2017.

[41] G. Ducrozet, F. Bonnefoy, B. Bouscasse, M. Gouin, and P. Ferrant. CN-Stream: Open-source library for nonlinear regular waves using stream function theory. Computer Physics Communications, in prep.

[42] L. Eça and M. Hoekstra. A procedure for the estimation of the numerical uncertainty of CFD calculations based on grid refinement studies. Journal of Computational Physics, 262:104–130, 2014.

[43] D. O. Edmund, K. J. Maki, and R. F. Beck. A velocity-decomposition formulation for the incompressible Navier-Stokes equations. Computational Mechanics, 52(3):669–680, 2013.

[44] O. M. Faltinsen, J. N. Newman, and T. Vinje. Nonlinear wave loads on a slender vertical cylinder. Journal of Fluid Mechanics, 289:179–198, 1995.

[45] R. P. Fedkiw, T. Aslam, B. Merriman, and S. Osher. A non-oscillatory Eulerian approach to interfaces in multimaterial flows (the Ghost Fluid Method). Journal of Computational Physics, 152(2):457–492, 1999.

[46] P. Ferrant. Computation of higher order diffraction effects using a fully nonlinear simulation method. In 11th International Workshop on Water Waves and Floating Bodies, 1996.

[47] P. Ferrant. Fully nonlinear interactions of long-crested wave packets with a three dimensional body. In 22nd ONR Symposium on Naval Hydrodynamics, pages 403–415, 1998.

[48] P. Ferrant, L. Gentaz, B. Alessandrini, R. Luquet, C. Monroy, G. Ducrozet, E. Jacquin, and A. Drouet. Fully nonlinear potential/RANSE simulation of wave interaction with ships and marine structures. In 27th International Conference on Offshore Mechanics and Arctic Engineering.

[49] P. Ferrant, L. Gentaz, B. Alessandrini, and D. Le Touzé. A potential/RANSE approach for regular water wave diffraction about 2-D structures. Ship Technology Research, 50 (4):165–171, 2003.

[50] J. H. Ferziger and M. Peric. Computational methods for fluid dynamics. Springer Science & Business Media, 2012.

[51] M. M. Francois, S. J. Cummins, E. D. Dendy, D. B. Kothe, J. M. Sicilian, and M. W. Williams. A balanced-force algorithm for continuous and sharp interfacial surface tension models within a volume tracking framework. Journal of Computational Physics, 213(1): 141–173, 2006.

[52] L. Gentaz, R. Luquet, B. Alessandrini, and P. Ferrant. Numerical simulation of the 3D viscous flow around a vertical cylinder in non-linear waves using an explicit incident wave model. In 23rd International Conference on Offshore Mechanics and Arctic Engineering.

[53] F. Gibou, R. Fedkiw, and S. Osher. A review of level-set methods and some recent applications. Journal of Computational Physics, 2017.

[54] M. Gouin. Modélisation déterministe d'états de mer à grande échelle en profondeur variable. PhD thesis, Ecole Centrale Nantes (ECN), 2016.

[55] M. Gouin, G. Ducrozet, and P. Ferrant. Development and validation of a non-linear spectral model for water waves over variable depth. European Journal of Mechanics-B/Fluids, 57:115–128, 2016.

[56] M. Gouin, G. Ducrozet, and P. Ferrant. Propagation of 3D nonlinear waves over an elliptical mound with a High-Order Spectral method. European Journal of Mechanics-B/Fluids, 63:9–24, 2017.

[57] S. Grilli, R. Gilbert, P. Lubin, S. Vincent, D. Astruc, D. Legendre, M. Duval, O. Kimmoun, H. Branger, and D. Devrard. Numerical modeling and experiments for solitary wave shoaling and breaking over a sloping beach. In 14th International Offshore and Polar Engineering Conference, 2004.

[58] S. Guignard, S. T. Grilli, R. Marcer, and V. Rey. Computation of shoaling and breaking waves in nearshore areas by the coupling of BEM and VOF methods. In 9th International Offshore and Polar Engineering Conference, 1999.

[59] Z. Hafsia, M. B. Hadj, H. Lamloumi, and K. Maalel. Internal inlet for wave generation and absorption treatment. Coastal Engineering, 56(9):951–959, 2009.

[60] G. Haller. An objective definition of a vortex. Journal of Fluid Mechanics, 525:1–26, 2005.

[61] J. A. Hamilton and R. W. Yeung. Viscous and inviscid matching of three-dimensional free-surface flows utilizing shell functions. Journal of Engineering Mathematics, 70(1-3): 43–66, 2011.

[62] F. H. Harlow and J. E. Welch. Numerical calculation of time-dependent viscous incompressible flow of fluid with free surface. The Physics of Fluids, 8(12):2182–2189, 1965.

[63] D. J. Harvie, M. Davidson, and M. Rudman. An analysis of parasitic current generation in Volume of Fluid simulations. Applied Mathematical Modelling, 30(10):1056–1066, 2006.

[64] P. Higuera, J. L. Lara, and I. J. Losada. Realistic wave generation and active wave absorption for Navier–Stokes models: Application to OpenFOAM®. Coastal Engineering, 71:102–118, 2013.

[65] C. W. Hirt and B. D. Nichols. Volume of Fluid (VOF) method for the dynamics of free boundaries. Journal of Computational Physics, 39(1):201 – 225, 1981.

[66] C. Hu and M. Kashiwagi. A cip-based method for numerical simulations of violent free-surface flows. Journal of Marine Science and Technology, 9(4):143–157, 2004.

[67] J. Huang, P. M. Carrica, and F. Stern. Coupled Ghost Fluid/two-phase Level Set method for curvilinear body-fitted grids. International Journal for Numerical Methods in Fluids, 55(9):867–897, 2007.

[68] M. Huseby and J. Grue. An experimental investigation of higher-harmonic wave forces on a vertical cylinder. Journal of fluid Mechanics, 414:75–103, 2000.

[69] A. Iafrati and E. Campana. A domain decomposition approach to compute wave breaking (wave-breaking flows). International Journal for Numerical Methods in Fluids, 41(4):419–445, 2003.

[70] A. Iafrati, A. Di Mascio, and E. Campana. A Level Set technique applied to unsteady free surface flows. International Journal for Numerical Methods in Fluids, 35(3):281–297, 2001.

[71] R. I. Issa. Solution of the implicitly discretised fluid flow equations by operator-splitting. Journal of computational physics, 62(1):40–65, 1986.

[72] ITTC. Practical guidelines for ship CFD applications ITTC recommended procedures and guidelines 7.5-03-02-03, 2014.

[73] N. G. Jacobsen, D. R. Fuhrman, and J. Fredsøe. A wave generation toolbox for the open-source CFD library: OpenFOAM®. International Journal for Numerical Methods in Fluids, 70(9):1073–1088, 2012.

[74] C. F. Janssen, M. Krafczyk, and S. Grilli. Modeling of wave breaking and wave-structure interactions by coupling of fully nonlinear potential flow and Lattice-Boltzmann models. In 20th International Offshore and Polar Engineering Conference, 2010.

[75] H. Jasak. Error analysis and estimation for the Finite Volume method with applications to fluid flows. PhD thesis, Imperial College London (University of London), 1996.

[76] D. D. Joseph. Potential flow of viscous fluids: Historical notes. International Journal of Multiphase Flow, 32(3):285–310, 2006.

[77] K. Kim, A. I. Sirviente, and R. F. Beck. The complementary RANS equations for the simulation of viscous flows. International Journal for Numerical Methods in Fluids, 48 (2):199–229, 2005.

[78] C. Lachaume, B. Biausser, P. Fraunié, S. T. Grilli, and S. Guignard. Modeling of breaking and post-breaking waves on slopes by coupling of BEM and VOF methods. In 13th International Offshore and Polar Engineering Conference, 2003.

[79] Z. Li, L. Gentaz, G. Ducrozet, and P. Ferrant. Calculation of high-order wave loads on a vertical circular cylinder using the SWENSE method. In 32th International Workshop on Water Waves and Floating Bodies, 2017.

[80] X. Lu, D. D. J. Chandar, Y. Chen, and J. Lou. An overlapping domain decomposition based near-far field coupling method for wave structure interaction simulations. Coastal Engineering, 126:37–50, 2017.

[81] R. Luquet, L. Gentaz, P. Ferrant, and B. Alessandrini. Viscous flow simulation past a ship in waves using the SWENSE approach. In ONR Conference.

[82] R. Luquet, B. Alessandrini, P. Ferrant, and L. Gentaz. RANSE analysis of 2D flow about a submerged body using explicit incident wave models. In Numerical Towing Tank Symposium, 2003.

[83] R. Luquet, P. Ferrant, B. Alessandrini, G. Ducrozet, and L. Gentaz. Simulation of a TLP in waves using the SWENSE scheme. In 17th International Offshore and Polar Engineering Conference, 2007.

[84] Š. Malenica and B. Molin. Third-harmonic wave diffraction by a vertical cylinder. Journal of Fluid Mechanics, 302:203–229, 1995.

[85] A. D. Mascio, R. Broglia, and R. Muscari. On the application of the single-phase Level Set method to naval hydrodynamic flows. Computers & Fluids.

[86] A. Mehmood, D. I. Graham, K. Langfeld, and D. M. Greaves. OpenFOAM Finite Volume method implementation of a fully nonlinear potential flow model for simulating wave-structure interactions. In 25th International Ocean and Polar Engineering Conference, 2015.

[87] A. M. Miquel, A. Kamath, M. Alagan Chella, R. Archetti, and H. Bihs. Analysis of different methods for wave generation and absorption in a CFD-based numerical wave tank. ArXiv e-prints, 2018.

[88] H. Miyata, T. Sato, and N. Baba. Difference solution of a viscous flow with free-surface wave about an advancing ship. Journal of Computational Physics, 72(2):393–421, 1987.

[89] B. Molin. Hydrodynamique des structures offshore. Editions Technip, 2002.

[90] C. Monroy. Simulation numérique de l'interaction houle-structure en fluide visqueux par décomposition fonctionnelle. PhD thesis, Ecole Centrale de Nantes (ECN), 2010.

[91] C. Monroy, G. Ducrozet, P. Roux de Reilhac, L. Gentaz, and P. Ferrant. RANS simulations of ship motions in regular and irregular head seas using the SWENSE method. In 19th Conference of the International Society for Offshore and Polar Engineering, Osaka, Japan, 2008.

[92] C. Monroy, S. Seng, and S. Malenica. Développements et validation de l'outil CFD OpenFOAM pour le calcul de tenue à la mer. In 15th Journées de l'Hydrodynamique, 11 2016.

[93] F. Moukalled, L. Mangani, and M. Darwish. The Finite Volume Method in Computational Fluid Dynamics An Advanced Introduction with OpenFOAM and Matlab. Springer, 2016.

[94] J. Newman and C.-H. Lee. Boundary-Element methods in offshore structure analysis. Journal of Offshore Mechanics and Arctic Engineering, 124(2):81–89, 2002.

[95] P. J. Oliveira and R. I. Issa. Numerical aspects of an algorithm for the Eulerian simulation of two-phase flows. International Journal for Numerical Methods in Fluids, 43(10-11): 1177–1198, 2003.

[96] S. Osher and R. P. Fedkiw. Level Set methods: an overview and some recent results. Journal of Computational Physics, 169(2):463–502, 2001.

[97] S. Osher and J. A. Sethian. Fronts propagating with curvature-dependent speed: Algorithms based on Hamilton-Jacobi formulations. Journal of Computational Physics, 79 (1):12 – 49, 1988.

[98] S. Patankar. Numerical heat transfer and fluid flow. CRC Press, 1980.

[99] B. T. Paulsen, H. Bredmose, and H. B. Bingham. An efficient domain decomposition strategy for wave loads on surface piercing circular cylinders. Coastal Engineering, 86: 57–76, 2014.

[100] B. T. Paulsen, H. Bredmose, H. B. Bingham, and N. G. Jacobsen. Forcing of a bottom-mounted circular cylinder by steep regular water waves at finite depth. Journal of Fluid Mechanics, 755:1–34, 2014.

[101] P. Queutey, E. Guilmineau, M. Visonneau, J. Wackers, and G. Deng. RANS and Hybrid RANS-LES simulations around the Japan Bulk Carrier of the Tokyo 2015 CFD Workshop. In 19th Numerical Towing Tank Symposium, 10 2016.

[102] G. Reliquet. Simulation numérique de l'interaction houle/carène par couplage d'une méthode spectrale HOS avec un algorithme de capture d'interface. PhD thesis, Ecole Centrale de Nantes, 2013.

[103] G. Reliquet, A. Drouet, P. Guillerm, E. Jacquin, L. Gentaz, and P. Ferrant. Simulation of wave-body interaction using a single-phase level set function in the SWENSE method. In ASME 2013 32nd International Conference on Ocean, Offshore and Arctic Engineering. American Society of Mechanical Engineers, 2013.

[104] C. Rhie and W. L. Chow. Numerical study of the turbulent flow past an airfoil with trailing edge separation. AIAA Journal, 21(11):1525–1532, 1983.

[105] M. M. Rienecker and J. D. Fenton. A Fourier approximation method for steady water waves. Journal of Fluid Mechanics, 104:119–137, 1981.

[106] W. J. Rosemurgy, R. F. Beck, and K. J. Maki. A velocity decomposition formulation for 2D steady incompressible lifting problems. European Journal of Mechanics-B/Fluids, 58: 70–84, 2016.

[107] Rousset, JM. and Ferrant, P. Model tests for Principia R&D. Technical Report CTR1 - JIP Calm Buoy 2, Laboratoire de Mécanique des Fluides de l'Ecole Centrale de Nantes (UMR CNRS 6598), 2005.

[108] M. Rudman. A volume-tracking method for incompressible multifluid flows with large density variations. International Journal for Numerical Methods in Fluids, 28(2):357–378, 1998.

[109] H. Rusche. Computational fluid dynamics of dispersed two-phase flows at high phase fractions. PhD thesis, Imperial College London (University of London), 2003.

[110] B. Seiffert, M. Hayatdavoodi, and R. C. Ertekin. Experiments and computations of solitary-wave forces on a coastal-bridge deck. Part I: Flat plate. Coastal Engineering, 88: 194–209, 2014.

[111] B. R. Seiffert and G. Ducrozet. Simulation of breaking waves using the High-Order Spectral method with laboratory experiments: wave-breaking energy dissipation. Ocean Dynamics, 68(1):65–89, 2018.

[112] B. R. Seiffert, G. Ducrozet, and F. Bonnefoy. Simulation of breaking waves using the High-Order Spectral method with laboratory experiments: Wave-breaking onset. Ocean Modelling, 119:94–104, 2017.

[113] J. A. Sethian and P. Smereka. Level set methods for fluid interfaces. Annual Review of Fluid Mechanics, 35(1):341–372, 2003.

[114] Y. L. Shao and O. M. Faltinsen. A harmonic polynomial cell (HPC) method for 3D Laplace equation with application in marine hydrodynamics. Journal of Computational Physics, 274:312 – 332, 2014.

[115] E. Shirani, N. Ashgriz, and J. Mostaghimi. Interface pressure calculation based on conservation of momentum for front capturing methods. Journal of Computational Physics, 203(1):154–175, 2005.

[116] M. Siddiqui, M. Greco, G. Colicchio, and O. M. Faltinsen. Validation of damaged ship hydrodynamics by a domain decomposition approach using the Harmonic Polynomial Cell method and OpenFOAM. In 33th International Workshop on Water Waves and Floating Bodies, 2018.

[117] B. Sirakov, E. Greitzer, and C. Tan. A note on irrotational viscous flow. Physics of Fluids, 17(10):108102, 2005.

[118] F. Stern, J. Yang, Z. Wang, H. Sadat-Hosseini, M. Mousaviraad, S. Bhushan, and T. Xing. Computational ship hydrodynamics: nowadays and way forward. International Shipbuilding Progress, 60(1-4):3–105, 2013.

[119] M. Sussman and E. Fatemi. An efficient, interface-preserving Level Set redistancing algorithm and its application to interfacial incompressible fluid flow. SIAM Journal on Scientific Computing, 20(4):1165–1191, 1999.

[120] M. Sussman, E. Fatemi, P. Smereka, and S. Osher. An improved Level Set method for incompressible two-phase flows. Computers & Fluids, 27(5-6):663–680, 1998.

[121] Y. Tahara and F. Stern. A large-domain approach for calculating ship boundary layers and wakes and wave fields for nonzero Froude number. Journal of Computational Physics, 127(2):398–411, 1996.

[122] G. Tryggvason, B. Bunner, A. Esmaeeli, D. Juric, N. Al-Rawahi, W. Tauber, J. Han, S. Nas, and Y. J. Jan. A front-tracking method for the computations of multiphase flow. Journal of Computational Physics, 169(2):708–759, 2001.

[123] H. Udaykumar, H. C. Kan, W. Shyy, and R. Tran-Son-Tay. Multiphase dynamics in arbitrary geometries on fixed cartesian grids. Journal of Computational Physics, 137(2): 366–405, 1997.

[124] G. Vaudor, T. Ménard, W. Aniszewski, M. Doring, and A. Berlemont. A consistent mass and momentum flux computation method for two phase flows. Application to atomization process. Computers & Fluids, 152:204–216, 2017.

[125] H. K. Versteeg and W. Malalasekera. An introduction to computational fluid dynamics: the finite volume method. Pearson Education, 2007.

[126] V. Vukčević. Numerical modelling of coupled potential and viscous flow for marine applications. PhD thesis, University of Zagreb, 2016.

[127] V. Vukčević, H. Jasak, and Š. Malenica. Decomposition model for naval hydrodynamic applications, part i: Computational method. Ocean Engineering, 121:37–46, 2016.

[128] V. Vukčević, H. Jasak, and I. Gatin. Implementation of the Ghost Fluid Method for free surface flows in polyhedral Finite Volume framework. Computers & fluids, 153:1–19, 2017.

[129] R. Wemmenhove. Numerical simulation of two-phase flow in offshore environments. PhD thesis, University Groningen, 2008.

[130] B. J. West, K. A. Brueckner, R. S. Janda, D. M. Milder, and R. L. Milton. A new numerical method for surface hydrodynamics. Journal of Geophysical Research: Oceans, 92(C11):11803–11824, 1987.

[131] P. F. White, Y. Chen, K. J. Maki, and R. F. Beck. Velocity decomposition analysis of free surface flow. In 32th International Workshop on Water Waves and Floating Bodies, 2017.

[132] G. Wu and R. Taylor. Time stepping solutions of the two-dimensional nonlinear wave radiation problem. Ocean Engineering, 22(8):785–798, 1995.

[133] Y. Zhang, M. Peszynska, and S. Yim. Coupling of viscous and potential flow models with free surface for near and far field wave propagation. International Journal of Numerical Analysis and Modeling, 4(3):256–82, 2013.

UNIVERSITE BRETAGNE SCIENCES LOIRE POUR L'INGENIEUR

CENTRALE NANTES

Titre : Méthode SWENSE bi-phasique : application à l'étude des interactions houle-structure

Mots clés : interaction houle-structure; couplage théorie potentielle et visqueuse; SWENSE; décomposition fonctionnelle ; écoulement bi-phasique; OpenFOAM.

Résumé : Cette thèse propose un algorithme efficace pour la simulation numérique des interactions houle-structure avec des solveurs CFD bi-phasiques. L'algorithme est basé sur le couplage de la théorie potentielle et des équations bi-phasiques de Navier-Stokes. C'est une extension de la méthode Spectral Wave Explicit Navier-Stokes Equations (SWENSE) pour les solveurs CFD bi-phasiques avec une technique de capture d'interface. Dans cet algorithme, la solution totale est décomposée en une composante incidente et une composante complémentaire. La partie incidente est explicitement obtenue avec des méthodes spectrales basées sur la théorie des écoulements potentiels ; seule la partie complémentaire est résolue avec des solveurs CFD, représentant l'influence de la structure sur les houles incidentes. La décomposition assure la précision de la cinématique des houles incidentes quel que soit le maillage utilisé par les solveurs CFD. Une réduction significative de la taille du maillage est attendue dans les problèmes typiques des interactions houle-structure. Les équations sont présentées sous trois formes : la forme conservative, la forme non conservative et la forme Ghost of Fluid Method. Les trois versions d'équations sont implémentées dans OpenFOAM et validées par une série de cas de test.
Une technique d'interpolation efficace pour reconstruire la solution des houles irrégulières donnée par la méthode Higher-Order Spectral (HOS) sur le maillage CFD est également proposée.

Title : Two-phase Spectral Wave Explicit Navier-Stokes Equations Method for wave-structure interactions

Keywords : Wave-structure interaction; Potential and viscous flow coupling; SWENSE; functional decomposition; two-phase flow ; OpenFOAM

Abstract: This thesis proposes an efficient algorithm for simulating wave-structure interaction with two-phase Computational Fluid Dynamics (CFD) solvers. The algorithm is based on the coupling of potential wave theory and two-phase Navier-Stokes equations. It is an extension of the Spectral Wave Explicit Navier-Stokes Equations (SWENSE) method for generalized two-phase CFD solvers with interface capturing techniques. In this algorithm, the total solution is decomposed into an incident and a complementary component. The incident solution is explicitly obtained with spectral wave models based on potential flow theory; only the complementary solution is solved with CFD solvers, representing the influence of the structure on the incident waves. The decomposition ensures the accuracy of the incident wave's kinematics regardless of the mesh in CFD solvers. A significant reduction of the mesh size is expected in typical wave-structure interaction problems.
The governing equations are given in three forms: the conservative form, the non-conservative form, and the Ghost of Fluid Method (GFM) form. The three sets of governing equations are implemented in OpenFOAM and validated by a series of wave-structure interaction cases. An efficient interpolation technique to map the irregular wave solution from a Higher-Order Spectral (HOS) Method onto the CFD grid is also proposed.